

VOLUME 78

OCTOBER 10, 1974

NUMBER 21

JPCHAx

THE JOURNAL OF
PHYSICAL
CHEMISTRY

PUBLISHED BIWEEKLY BY THE AMERICAN CHEMICAL SOCIETY

THE JOURNAL OF PHYSICAL CHEMISTRY

BRYCE CRAWFORD, Jr., *Editor*
WILMER G. MILLER, *Associate Editor*
ROBERT W. CARR, Jr., **FREDERIC A. VAN-CATLEDGE**, *Assistant Editors*

EDITORIAL BOARD: A. O. ALLEN (1970-1974), C. A. ANGELL (1973-1977),
F. C. ANSON (1974-1978), V. A. BLOOMFIELD (1974-1978), J. R. BOLTON (1971-1975),
L. M. DORFMAN (1974-1978), M. FIXMAN (1970-1974), H. S. FRANK (1970-1974),
R. R. HENTZ (1972-1976), W. J. KAUZMANN (1974-1978), R. L. KAY (1972-1976),
D. W. McCLURE (1974-1978), R. M. NOYES (1973-1977), J. A. POPLER (1971-1975),
B. S. RABINOVITCH (1971-1975), H. REISS (1970-1974), S. A. RICE (1969-1975),
F. S. ROWLAND (1973-1977), R. L. SCOTT (1973-1977), A. SILBERBERG (1971-1975),
J. B. STOTHERS (1974-1978), W. A. ZISMAN (1972-1976)

AMERICAN CHEMICAL SOCIETY, 1155 Sixteenth St., N.W., Washington, D. C. 20036

Books and Journals Division

JOHN K CRUM *Director*
RUTH REYNARD *Assistant to the Director*

CHARLES R. BERTSCH *Head, Editorial Processing Department*
D. H. MICHAEL BOWEN *Head, Journals Department*
BACIL GUILLEY *Head, Graphics and Production Department*
SELDON W. TERRANT *Head, Research and Development Department*

©Copyright, 1974, by the American Chemical Society. Published biweekly by the American Chemical Society at 20th and Northampton Sts., Easton, Pa. 18042. Second-class postage paid at Washington, D. C., and at additional mailing offices.

All manuscripts should be sent to *The Journal of Physical Chemistry*, Department of Chemistry, University of Minnesota, Minneapolis, Minn. 55455.

Additions and Corrections are published once yearly in the final issue. See Volume 77, Number 26 for the proper form.

Extensive or unusual alterations in an article after it has been set in type are made at the author's expense, and it is understood that by requesting such alterations the author agrees to defray the cost thereof.

The American Chemical Society and the Editor of *The Journal of Physical Chemistry* assume no responsibility for the statements and opinions advanced by contributors.

Correspondence regarding accepted copy, proofs, and reprints should be directed to *Editorial Processing Department*, American Chemical Society, 20th and Northampton Sts., Easton, Pa. 18042. Department Head: CHARLES R. BERTSCH. Assistant Department Head: MARIANNE C. BROGAN. Assistant Editor: CELIA B. MCFARLAND. Editorial Assistant: JOSEPH E. YURVATI.

Advertising Office: Centcom, Ltd., 50 W. State St., Westport, Conn. 06880.

Business and Subscription Information

Send all new and renewal subscriptions with payment to: Office of the Controller, 1155 16th Street, N.W., Washington, D. C. 20036. Subscriptions should be renewed promptly to avoid a break in your

series. All correspondence and telephone calls regarding changes of address, claims for missing issues, subscription service, the status of records, and accounts should be directed to *Manager, Membership and Subscription Services*, American Chemical Society, P.O. Box 3337, Columbus, Ohio 43210. Telephone (614) 421-7230.

On changes of address, include both old and new addresses with ZIP code numbers, accompanied by mailing label from a recent issue. Allow four weeks for change to become effective.

Claims for missing numbers will not be allowed (1) if loss was due to failure of notice of change in address to be received before the date specified, (2) if received more than sixty days from date of issue plus time normally required for postal delivery of journal and claim, or (3) if the reason for the claim is "issue missing from files."

Subscription rates (1974): members of the American Chemical Society, \$20.00 for 1 year; to nonmembers, \$60.00 for 1 year. Those interested in becoming members should write to the Admissions Department, American Chemical Society, 1155 Sixteenth St., N.W., Washington, D. C. 20036. Postage to Canada and countries in the Pan-American Union, \$5.00; all other countries, \$6.00. Air freight rates available on request. Single copies for current year: \$3.00. Rates for back issues from Volume 56 to date are available from the Special Issues Sales Department, 1155 Sixteenth St., N.W., Washington, D. C. 20036.

Subscriptions to this and the other ACS periodical publications are available on microfilm. Supplementary material not printed in this journal is now available in microfiche form on a current subscription basis. For information on microfilm or microfiche subscriptions, write Special Issues Sales Department at the address above.

THE JOURNAL OF
PHYSICAL CHEMISTRY

Volume 78, Number 21 October 10, 1974

JPCA_x 78(21) 2073-2182 (1974)

ISSN 0022-3654

- Kinetics of Nitric Oxide Catalyzed Decomposition of Nitryl Chloride and Its Related Nitrogen Isotope Exchange Reactions R. A. Wilkins, Jr., M. C. Dodge, and I. C. Hisatsune* 2073
- Characteristic Energy Loss, Luminescence, and Luminescence Excitation Spectra of Methane and Other Alkane Solids under Low-Energy Electron Impact Timothy Huang and William H. Hamill* 2077
- Luminescence Probe Analysis of Ionic States of Cyclopentane, Cyclohexane, and *n*-Hexane Solids under Low-Energy Electron Impact Timothy Huang and William H. Hamill* 2081
- Rate Constants for the Reactions of Ozone with Ethene and Propene, from 235.0 to 362.0 K John T. Herron* and Robert E. Huie 2085
- Pulse Radiolytic Investigations of OHCH₂O₂ Radicals Joseph Rabani,* Dina Klug-Roth, and Arnim Henglein 2089
- Formation of Ions and Excited States in the Pulse Radiolysis of Benzonitrile A. Kira and J. K. Thomas* 2094
- Reactivity of the Carbonate Radical in Aqueous Solution. Tryptophan and Its Derivatives Schoen-nan Chen and Morton Z. Hoffman* 2099
- Indirect Measurements for the Time Dependence of the Hydrated Electron . . . Charles D. Jonah 2103
- Raman Spectroscopic Study of Binary Systems. I. Molecular Association in the Ammonia Hexadeuteriobenzene Liquid System John H. Roberts* and Bertin J. De Bettignies 2106
- Electron Paramagnetic Resonance of a Nitroxide Adsorbed on Silica, Silica-Alumina, Alumina, and Decationated Zeolites G. P. Lozos and B. M. Hoffman* 2110
- Infrared Spectroscopic Studies of the Surface Bond of Carbon Dioxide on Uranium Oxides Carlos Colmenares 2117
- Absolute Quantum Yields of ²E_g → ⁴A_{2g} Luminescence in K₃(Co,Cr)(CN)₆ Powders Francesco Castelli and Leslie S. Forster* 2122
- Solvent and Temperature Effects in the Photoionization of Tetramethyl-*p*-phenylenediamine Richard A. Holroyd* and Robert L. Russell 2128
- Electron Spin Resonance of Palladium(I). IV. Mixed-Ligand Complexes of Palladium(I) Michihiro Nakamura* and Shizuo Fujiwara 2136
- Oxygen-17 Anisotropic Dipolar Interaction in the Carbonyl Group of Semiquinones E. Melamud and Brian L. Silver* 2140
- A Theoretical Interpretation of the Rotational Barrier in Benzophenone Ketyl Fernando Bernardi, Maurizio Guerra, and Gian Franco Pedulli* 2144
- Thermal Electron Transfer Reactions in Polar Solvents Neil R. Kestner,* Jean Logan, and Joshua Jortner 2148
- Unimolecular Reactions and Energy Partitioning. Three- and Four-Centered Elimination Reactions of Chemically Activated 1,1,2-Trichloroethane-*d*₀, -*d*₁, and -*d*₂ K. C. Kim and D. W. Setser* 2166

ห้องสมุด กรมวิทยาศาสตร์
001 7518

COMMUNICATIONS TO THE EDITOR

- Infrared Spectra of Methane Adsorbed on NaA, CaA, and NaX Zeolites
..... E. Cohen de Lara* and Y. Delaval 2180
- Solvated Electrons from Excited (λ 185 nm) *p*-Dioxane
..... Clemens von Sonntag* and Heinz Bandmann 2181

There is no supplementary material for this issue.

* In papers with more than one author, the asterisk indicates the name of the author to whom inquiries about the paper should be addressed.

AUTHOR INDEX

- | | | | |
|----------------------------|---------------------------|----------------------|---------------------------|
| Bandmann, H., 2181 | Guerra, M., 2144 | Kestner, N. R., 2148 | Rabani, J., 2089 |
| Bernardi, F., 2144 | Hamill, W. H., 2077, 2081 | Kim, K. C., 2166 | Roberts, J. H., 2106 |
| Castelli, F., 2122 | Henglein, A., 2089 | Kira, A., 2094 | Russell, R. L., 2128 |
| Chen, S., 2099 | Herron, J. T., 2085 | Klug-Roth, D., 2089 | |
| Colmenares, C., 2117 | Hisatsune, I. C., 2073 | Logan, J., 2148 | Setser, D. W., 2166 |
| De Bettignies, B. J., 2106 | Hoffman, B. M., 2110 | Lozos, G. P., 2110 | Silver, B. L., 2140 |
| de Lara, E. C., 2180 | Hoffman, M. Z., 2099 | | Thomas, J. K., 2094 |
| Delaval, Y., 2180 | Holroyd, R. A., 2128 | Melamud, E., 2140 | |
| Dodge, M. C., 2073 | Huang, T., 2077, 2081 | Nakamura, M., 2136 | von Sonntag, C., 2181 |
| | Huie, R. E., 2085 | Pedulli, G. F., 2144 | Wilkins, R. A., Jr., 2073 |
| Forster, L. S., 2122 | Jonah, C. D., 2103 | | |
| Fujiwara, S., 2136 | Jortner, J., 2148 | | |

THE JOURNAL OF PHYSICAL CHEMISTRY

Registered in U. S. Patent Office © Copyright, 1974, by the American Chemical Society

VOLUME 78, NUMBER 21 OCTOBER 10, 1974

Kinetics of Nitric Oxide Catalyzed Decomposition of Nitryl Chloride and Its Related Nitrogen Isotope Exchange Reactions

R. A. Wilkins, Jr., M. C. Dodge, and I. C. Hisatsune*¹

Department of Chemistry, Davey Laboratory, The Pennsylvania State University, University Park, Pennsylvania 16802

(Received April 4, 1974)

The kinetics of the reaction $\text{NO} + \text{NO}_2\text{Cl} \rightarrow \text{NOCl} + \text{NO}_2$ have been investigated by rapid-scan infrared spectroscopy. The experimental rate constant $k = 1.41 \times 10^9 \exp(-6.89 \text{ kcal}/RT) M^{-1} \text{ sec}^{-1}$ is in reasonable agreement with an earlier colorimetric value reported in the literature, but the use of isotopic nitric oxide has now established the reaction mechanism to be a chlorine atom transfer. Rate constants for nitrogen isotope exchange reactions $^{15}\text{NO} + \text{NOCl} \rightarrow \text{NO} + ^{15}\text{NOCl}$ and $^{15}\text{NO}_2 + \text{NO}_2\text{Cl} \rightarrow \text{NO}_2 + ^{15}\text{NO}_2\text{Cl}$ have also been determined to be $k = 4.26 \times 10^9 \exp(-10.48 \text{ kcal}/RT) M^{-1} \text{ sec}^{-1}$ and $k = 4.45 \times 10^{11} \exp(-15.60 \text{ kcal}/RT) M^{-1} \text{ sec}^{-1}$, respectively, but these reactions were unimportant in the isotope reaction $^{15}\text{NO} + \text{NO}_2\text{Cl}$. The analysis of the data from the latter reaction required consideration of only the known rapid equilibria $2\text{NO}_2 \rightleftharpoons \text{N}_2\text{O}_4$ and $^{15}\text{NO} + \text{NO}_2 \rightleftharpoons \text{NO} + ^{15}\text{NO}_2$.

Introduction

Freiling, Johnston, and Ogg² reported some years ago the kinetics of a fairly rapid homogeneous reaction between nitric oxide and nitryl chloride with the stoichiometry given by eq 1. The rate of this reaction, monitored by the growth



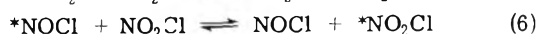
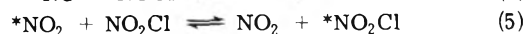
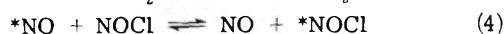
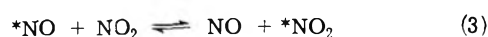
in absorbance at 436 nm where both nitrogen dioxide and nitrosyl chloride absorb, was found to be first order with respect to each reactant. In the temperature range of 1–71° and with reactant pressures varied from 0.1 to 18 Torr and diluted in nitrogen (0.2–384 Torr), the experimental second-order rate constant was $k_1 = 0.83 \times 10^8 \exp(-6.9 \text{ kcal}/RT) M^{-1} \text{ sec}^{-1}$ or $k_1 = 7.23 \times 10^3 M^{-1} \text{ sec}^{-1}$ at 25°. Although these investigators were not able to establish whether the bimolecular reaction 1 proceeded through an oxygen atom exchange or a chlorine atom exchange, they suggested that a study of this reaction with isotopic nitrogen compounds may remove the ambiguity in the mechanism. However, before such a study can be made, it is necessary to consider several reactions which may affect the interpretation of the nitrogen isotope distribution among the various molecular species.

Reaction 1 does not go to completion but reaches an equilibrium state. The rate of the reverse reaction



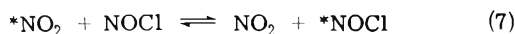
has been deduced indirectly by Martin and Kohnlein³ from an investigation of the oxidation of nitrosyl chloride by chlorine dioxide in a temperature range of –20 to +8°. Reaction 2 was inferred to be first order in each reactant and to have a second-order rate constant of $k_2 = 1.92 \times 10^7 \exp(-10.0 \text{ kcal}/RT) M^{-1} \text{ sec}^{-1}$. At 25° $k_2 = 0.889 M^{-1} \text{ sec}^{-1}$ so reaction 1 is faster than reaction 2 by about 4 orders of magnitude. Thus, the equilibrium represented by $K_{1,2} = k_1/k_2$ is far to the product side as was found by Ray and Ogg.⁴ The latter authors measured $K_{2,1} (=k_2/k_1)$ directly by infrared spectroscopy and found it to be $(1.01 \pm 0.33) \times 10^{-4}$ at 25°. The ratio of the kinetic rate constants, on the other hand, gives $K_{2,1} = 1.23 \times 10^{-4}$.

Whether the nitric oxide or the nitryl chloride in reaction 1 is labeled with the ¹⁵N atom (hereafter denoted by *N), once the reaction is initiated the following isotope-exchange reactions, all involving transfer of a single atom, need to be considered.



Leifer⁵ was the first to attempt the study of reaction 5, but he found the reaction too fast to follow at -35° by ordinary infrared spectroscopy. More recently, mass spectroscopic studies have shown that the bimolecular rate constant for reaction 3 was $2.2 \times 10^7 M^{-1} \text{sec}^{-1}$ at 23° on the basis of oxygen atom exchange⁶ and $2.5 \times 10^7 M^{-1} \text{sec}^{-1}$ at 25° from nitrogen atom exchange.⁷ Thus, reaction 3 is very fast, and this suggests that it will not be useful to follow the production of isotopic nitrogen dioxide in reaction 1. The exchange reaction 4 was found by Kuhn and Butkiewicz,⁸ also, to be too fast for ordinary infrared spectroscopy. Nevertheless, these authors were able to conclude that the rate-determining step in this reaction must involve the chlorine atom transfer. Reactions 5 and 6 have not been considered previously.

After the present study was completed and while this article was being prepared, Sharma and Sood⁹ reported a mass spectroscopic study of nitrogen and oxygen isotopic exchange reactions in a system consisting initially of NO_2 , NOCl , and NO . Although these authors were unable to establish the mechanism of reaction 1, they interpreted their data on the basis of reactions 1–4 and the two atom transfer reaction



From the data taken in a temperature range of 0 – 23° , they deduced that $k_2 + k_7 = 1.78 \times 10^5 \exp(-6.66 \text{ kcal}/RT) M^{-1} \text{sec}^{-1}$ and $k_4 = 1.64 \times 10^6 \exp(-6.25 \text{ kcal}/RT) M^{-1} \text{sec}^{-1}$. Our work reported here shows that these rate constants as well as the proposed mechanism of Sharma and Sood are not reasonable.

Experimental Section

The purification methods and sources of nitric oxide, oxygen, nitrogen, and chlorine have been described previously.¹⁰ The source of $*\text{NO}$ was the sample recovered from an earlier work on isotopic nitrogen oxyhalides¹¹ and oxyacids.¹² This gas had been reduced over copper wool at 300° . The preparations of nitrogen dioxide,¹⁰ nitrosyl chloride,¹⁰ and nitryl chloride¹¹ have also been described before.

Gas transfers were made in a conventional glass vacuum line having stopcocks lubricated with Fluorolube GR-90 grease (Fisher Scientific Co.). The pressures of the reactive gases were measured with an oil manometer containing Kel-F No. 3 oil (3M Co.).

All kinetics were followed by infrared spectroscopy. A Perkin-Elmer Model 112 with calcium fluoride prism was used for slow reactions while a Perkin-Elmer Model 108 rapid-scan spectrometer (calcium fluoride prism) was employed for the fast reactions. The operating characteristics of the latter instrument as well as its associated reaction cell system and constant-temperature housing unit have been described previously.^{10,13}

Results and Discussion

In addition to studies with isotopic nitrogen oxides and oxyhalides, we reexamined the kinetics of reaction 1 with normal compounds by rapid-scan infrared spectroscopy.¹⁴ A rate of 30 scans/sec in the 1700-cm^{-1} region was sufficient to follow the concentration changes in NO_2Cl , NOCl , and NO_2 , individually or all simultaneously. Our reactant pressures, which were limited by the reaction cell filling time of 0.15 ± 0.02 sec and to absorbances below 0.9, ranged from 1.52 to 28.6 Torr for NO and from 1.76 to 6.61

TABLE I: Second-Order Rate Constant for the Reaction $\text{NO} + \text{NO}_2\text{Cl} \rightarrow \text{NOCl} + \text{NO}_2$ at 24°

Ir band followed	$10^{-4}k_1$, $M^{-1} \text{sec}^{-1}$	No. of determinations
NOCl (1792 cm^{-1})	1.17 ± 0.19	10
NO_2Cl (1692 cm^{-1})	1.20 ± 0.17	6
NO_2 (1596 cm^{-1})	1.33 ± 0.31	6

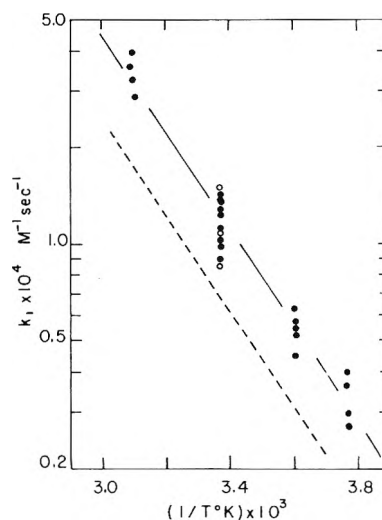


Figure 1. Temperature dependence of the second-order rate constant for the reaction $\text{NO} + \text{NO}_2\text{Cl} \rightarrow \text{NOCl} + \text{NO}_2$: solid line, this study, $k_1 = 10^{9.15} \exp(-6.89 \text{ kcal}/RT) M^{-1} \text{sec}^{-1}$ with all data points given equal weights; dotted line, $k_1 = 10^{8.92} \exp(-6.9 \text{ kcal}/RT) M^{-1} \text{sec}^{-1}$ from ref 2; opened circle points are from kinetic runs in which NO_2 , NO_2Cl , and NOCl were followed simultaneously, while only NOCl was followed for the closed circle data points.

Torr for NO_2Cl . Nitrogen at a pressure of about 470 Torr was used as the diluent gas. We verified experimentally that the reaction rate was not affected by the diluent gas and also by added NO_2 or NOCl . Changing the reaction cell window from CaF_2 to AgCl produced no observable difference, and identical rates, within experimental error limits, were obtained by following the infrared band of NOCl , NO_2 , or NO_2Cl . The second-order rate constants determined from the concentration changes in these species and their standard deviations are summarized in Table I. Since the NOCl infrared band was the most intense and least overlapped with the other bands, it permitted the kinetics to be followed over longer reaction times and was used in the temperature dependence study of the rate of reaction 1. The Arrhenius plot of our data in the range of -8 to $+51^\circ$ is shown in Figure 1. Here, the data points represented by closed circles are from kinetic runs in which only the NOCl band was followed. In this case, the maximum range of the rate constants at room temperature was from 0.89×10^4 to $1.31 \times 10^4 M^{-1} \text{sec}^{-1}$. However, when NOCl , NO_2Cl , and NO_2 were followed simultaneously, the maximum limits of the k_1 values were from 0.80×10^4 to $1.78 \times 10^4 M^{-1} \text{sec}^{-1}$. The latter high value was from the NO_2 band which is broad, is weaker than those of the other species, and overlaps severely with the atmospheric water band.^{13,14} Also, the correction for the nitrogen dioxide-dinitrogen tetroxide equilibrium introduced additional uncertainties in the rate constants determined from the NO_2 absorption band. The solid line in Figure 1 corresponds to a least-squares fitted frequency factor of $\log A_1 = 9.15 \pm 0.24$

($M^{-1} \text{ sec}^{-1}$ units) and an activation energy of $E_1 = 6.89 \pm 0.32$ kcal/mol where all data points were given equal weights. These parameters give a second-order rate constant of $k_1 = 1.24 \times 10^4 M^{-1} \text{ sec}^{-1}$ at 25° . The dotted line shown in Figure 1 represents the results reported by Freiling, *et al.*² Although there is excellent agreement in the activation energies obtained from the two sets of data, our frequency factor is 1.70 times larger. The source of this discrepancy is not apparent, but it may very well be experimental uncertainties associated with the two different spectroscopic techniques. We note from this figure that the lower error limit in our data may be close to the results of Freiling, *et al.*, and moreover, in the analysis of the latter data, extinction coefficients of NO_2 and NOCl and equilibrium constant data for N_2O_4 , each from a different literature source, were required.

We attempted to study the exchange reaction 3 in the temperature range of -15 to $+27^\circ$ with our rapid-scan spectrometer, but we found the equilibrium to be established within the cell-filling time. Thus, we were only able to estimate a lower limit of k_3 of $10^6 M^{-1} \text{ sec}^{-1}$. This lower limit, even in the absence of any other literature data on reaction 3, is sufficient to point out the futility of following the growth of $^*\text{NO}_2$ in a study of reaction 1 with isotopic reactants.

Reaction 4, on the other hand, could be followed readily with our spectrometer, and a typical kinetic run at 21.0° is illustrated in Figure 2. Here, 28.0 Torr of NO , 15.7 Torr of which was $^*\text{NO}$, was mixed with 2.82 Torr of NOCl and 485 Torr of nitrogen. The P branch of the $^*\text{NOCl}$ band at 1764 cm^{-1} and the R branch of the NOCl band at 1810 cm^{-1} were scanned together at 6 scans/sec. After equilibrium was established, the observed pressures of NOCl and $^*\text{NOCl}$ were 1.46 and 1.36 Torr, respectively. The data from the kinetic run were analyzed in terms of a simplified rate equation

$$\begin{aligned} -d[\text{NOCl}]/dt &= d[^*\text{NOCl}]/dt \\ &= k_4[^*\text{NO}][\text{NOCl}] - k_4[\text{NO}][^*\text{NOCl}] \end{aligned} \quad (8)$$

where the equilibrium constant was taken as unity although a value of 1.01 has been reported for the temperature range of -50 to $+25^\circ$.¹⁵ The values of the second-order rate constant k_4 determined in this manner are summarized in Table II. The resulting Arrhenius parameters are $\log A_4 = 9.63 \pm 0.14$ ($M^{-1} \text{ sec}^{-1}$ units) and $E_4 = 10.48 \pm 0.15$ kcal/mol. At 25° , k_4 is $87.8 M^{-1} \text{ sec}^{-1}$ so reaction 1 is over 2 orders of magnitude faster than reaction 4.

The rate of reaction 5 was also very slow, and it was studied with an ordinary infrared spectrometer. The second-order rate constants for this reaction at three different temperatures are summarized in Table III. A simplifying assumption that both the forward and the reverse rate constants were the same and equal to k_5 was used in the interpretation of the experimental data. The two values of k_5 listed for 24.5° were obtained by repeatedly scanning the NO_2Cl and $^*\text{NO}_2$ infrared bands during the reaction. At other temperatures only the changes in absorbance of a single infrared band were followed as a function of time. The rate constant k_5 in the Arrhenius form is $4.45 \times 10^{11} \exp(-15.6 \text{ kcal}/RT) M^{-1} \text{ sec}^{-1}$ and has a value of $1.61 M^{-1} \text{ sec}^{-1}$ at 25° . Reaction 5, therefore, is not important in the study of reaction 1 with isotopic reactants. It seemed reasonable to us to expect reaction 6 to be slow also, so it was

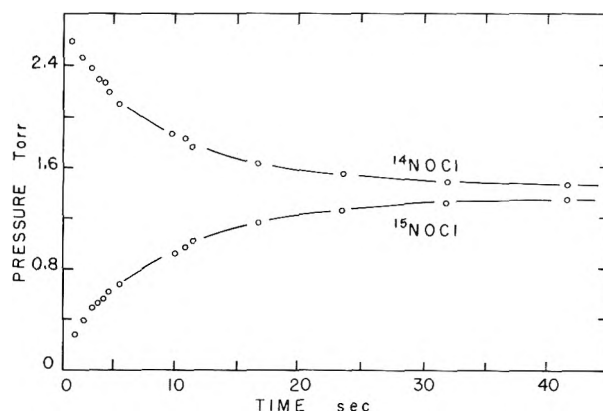


Figure 2. Time dependence of the nitrogen isotope exchange reaction $^{15}\text{NO} + \text{NOCl} \rightarrow \text{NO} + ^{15}\text{NOCl}$. Initial pressures [^{15}NO] = 15.7 Torr, [NO] = 12.3 Torr, and [NOCl] = 2.82 Torr; final pressures [NOCl] = 1.46 Torr and [$^{15}\text{NOCl}$] = 1.36 Torr; reaction temperature 21.0° .

TABLE II: Second-Order Rate Constant for the Reaction $^{15}\text{NO} + \text{NOCl} \rightarrow \text{NO} + ^{15}\text{NOCl}$

Temp, $^\circ\text{C}$	$k_4, M^{-1} \text{ sec}^{-1}$	
	$^{14}\text{NOCl}$	$^{15}\text{NOCl}$
-14	6.71	6.52
0	16.9	16.9
21	66.2	66.2
25	77.1	74.2
57	454	470
60	633	603

TABLE III: Second-Order Rate Constant for the Reaction $^{15}\text{NO}_2 + \text{NO}_2\text{Cl} \rightarrow \text{NO}_2 + ^{15}\text{NO}_2\text{Cl}$

Temp, $^\circ\text{C}$	Initial pressures, Torr			$k_5, M^{-1} \text{ sec}^{-1}$
	$^{14}\text{NO}_2\text{Cl}$	$^{15}\text{NO}_2$	$^{14}\text{NO}_2$	
24.5	6.34	4.90	2.86	1.66, 1.25
38.5	4.29	6.32	2.20	4.77
50.0	3.67	7.91	2.85	11.6

not studied nor was it found necessary to interpret the nitrogen isotope distribution in reaction 1.

A single kinetic run of reaction 1 with isotopic $^*\text{NO}$ was made at 24.0° . In this run the initial pressures of [$^*\text{NO}$], [NO], and [NO_2Cl] were 1.82, 0.60, and 3.65 Torr, respectively. Nitrogen was used as a diluent, and its pressure was 464 Torr. The same infrared absorption peaks followed in the study of reaction 4 were recorded at 30 scans/sec, and these peak absorbances converted into pressures are plotted in Figure 3. We note in this figure that the slope $d[^*\text{NOCl}]/d[\text{NOCl}]$ is approximately 2 initially and that $^*\text{NOCl}$ is definitely forming at a faster rate than is NOCl . Moreover, this slope decreases as the reaction approaches equilibrium after about 2 sec. The observed equilibrium pressures of the reaction products were [$^*\text{NOCl}$] = 1.09 Torr, [NOCl] = 1.27 Torr, [$^*\text{NO}_2$] = 0.73 Torr, and [NO_2] = 1.66 Torr. The expected total pressure of nitrosyl chloride in the reaction was 2.42 Torr while 2.36 Torr was actually observed. If the second-order rate constant for reaction 1 is assumed to be the same for both isotopic nitric oxides, the initial portion of the data displayed in Figure 3 can be fitted reasonably well with $k_1 = 0.96 \times 10^4 M^{-1} \text{ sec}^{-1}$. On the other hand, our Arrhenius parameters give $k_1 = 1.2 \times 10^4$

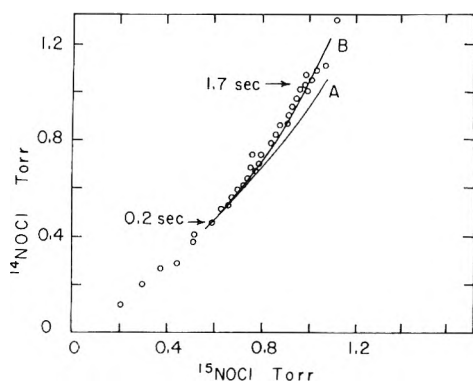


Figure 3. Isotopic composition of NOCl during the reaction $\text{NO} + \text{NO}_2\text{Cl} \rightarrow \text{NOCl} + \text{NO}_2$ at 24.0° . Initial pressures $[\text{NO}] = 1.82$ Torr, $[\text{NO}_2\text{Cl}] = 3.65$ Torr, and $[\text{N}_2] = 464$ Torr.

$M^{-1} \text{sec}^{-1}$. These results not only verify the internal consistency of our data but they show conclusively that reaction 1 is a bimolecular reaction involving the chlorine atom exchange.

The experimental data displayed in Figure 3 were analyzed further in terms of the following rate equations based on reaction 1 and equilibrium reaction 3.

$$d[\text{NOCl}]/dt = k_1[\text{NO}][\text{NO}_2\text{Cl}] \quad (9a)$$

$$d[*\text{NOCl}]/dt = k_1[*\text{NO}][\text{NO}_2\text{Cl}] \quad (9b)$$

$$d[\text{NO}_2]/dt = k_1[\text{NO}][\text{NO}_2\text{Cl}] + k_1[*\text{NO}][\text{NO}_2\text{Cl}] + k_{-3}[\text{NO}][*\text{NO}_2] - k_3[*\text{NO}][\text{NO}_2] \quad (10a)$$

$$d[*\text{NO}_2]/dt = k_3[*\text{NO}][\text{NO}_2] - k_{-3}[\text{NO}][*\text{NO}_2] \quad (10b)$$

Under our experimental conditions, the bimolecular association of NO_2 to form N_2O_4 has a rate constant¹⁶ of about $7 \times 10^6 M^{-1} \text{sec}^{-1}$ and an assumption of equilibrium between these two nitrogen oxides is a reasonable one. Thus, in the equations expressing the conservation of mass of isotopic nitrogen atoms, for example, $[\text{NO}] = [\text{NO}]_0 - [\text{NO}_2] + [*\text{NOCl}] - 2[\text{N}_2\text{O}_4] - [*\text{NNO}_4]$, the equilibrium was considered to have been established and a value¹⁷ of 115 Torr was taken for the ratio $[\text{NO}_2]^2/[\text{N}_2\text{O}_4]$. This simplification reduces the number of dependent variables to 4 and greatly facilitates the computations involving the four simultaneous differential equations (9) and (10). Numerical solutions to these differential equations were computed by the method of Runge-Kutta¹⁸ with Δt taken as 0.01 sec and by starting at a reaction time of 0.20 sec, indicated in Figure 3, where the filling of the reaction cell is already completed. The initial reactant concentrations were those listed earlier, and at $t = 0.20$ sec we observed $[\text{NOCl}] = 0.442$ Torr, and $d[\text{NOCl}]/d[*\text{NOCl}] = [\text{NO}]/[*\text{NO}] = 1.085$. The rate constant k_3 was varied from 1×10^4 to $2 \times 10^7 M^{-1} \text{sec}^{-1}$ but other constants were fixed at $k_1 = 0.96 \times 10^4 M^{-1} \text{sec}^{-1}$ for both isotopic NO and $k_3/k_{-3} = 1.040$ for reaction 3.¹⁵ If $k_3 = 1 \times 10^4 M^{-1} \text{sec}^{-1}$, the calculated concentration ratio curve A clearly deviates from

the experimental points as shown in Figure 3. However, $k_3 = 1 \times 10^6$ and $2 \times 10^7 M^{-1} \text{sec}^{-1}$ gave indistinguishable results, and both gave good fit of the experimental data as shown by curve B in the figure. Thus, it appears that equilibrium reaction 3 and $2\text{NO}_2 \rightleftharpoons \text{N}_2\text{O}_4$ both are established throughout the progress of reaction 1.

Our rate constant of $k_4 = 4.26 \times 10^9 \exp(-10.48 \text{ kcal}/RT) M^{-1} \text{sec}^{-1}$ obtained directly by following both NOCl and $*\text{NOCl}$ in the exchange reaction 4 disagrees completely with the value of $1.64 \times 10^6 \exp(-6.25 \text{ kcal}/RT) M^{-1} \text{sec}^{-1}$ deduced indirectly from a complex reaction system by Sharma and Sood.⁹ Not only does the frequency factor reported by these authors appear unusually low for a chlorine atom metathetical reaction,¹⁹ but also the mechanism from which k_4 was derived appears incomplete. If $k_2 + k_7$ was $2.3 M^{-1} \text{sec}^{-1}$ at 25° as these authors claim, then the elementary bimolecular reaction 5 whose rate constant is $1.6 M^{-1} \text{sec}^{-1}$ should have entered the mechanism. Even reaction 6 may be necessary in this case. The value of $k_2 + k_7 = 1.78 \times 10^5 \exp(-6.66 \text{ kcal}/RT) M^{-1} \text{sec}^{-1}$ also is in serious disagreement with $k_2 = 1.92 \times 10^7 \exp(-10.0 \text{ kcal}/RT) M^{-1} \text{sec}^{-1}$ found by Martin and Kohnlein.³ We have examined a kinetic system involving reaction 2 but we found no evidence of a low activation energy path to the product NO_2Cl and our results confirm those of Martin and Kohnlein.¹⁴ Perhaps a modification of the mechanism of Sharma and Sood may give rate constants which are more reasonable.

Acknowledgment. This work was supported by Grant AP-18 from the Office of Air Programs, Environmental Protection Agency.

References and Notes

- (1) To whom correspondence should be addressed.
- (2) E. C. Freiling, H. S. Johnston, and R. A. Ogg, Jr., *J. Chem. Phys.*, **20**, 327 (1952).
- (3) H. Martin and E. Kohnlein, *Z. Phys. Chem. (Frankfurt am Main)*, **17**, 375 (1958).
- (4) J. D. Ray and R. A. Ogg, Jr., *J. Chem. Phys.*, **31**, 168 (1959).
- (5) E. Leifer, *J. Chem. Phys.*, **8**, 301 (1940).
- (6) F. S. Klein, W. Spindel, and M. J. Stern, *J. Chim. Phys. Physicochim. Biol.*, **60**, 148 (1963).
- (7) H. D. Sharma, R. E. Jarvis, and K. Y. Wong, *J. Phys. Chem.*, **74**, 923 (1970).
- (8) L. P. Kuhn and C. Butkiewicz, *J. Phys. Chem.*, **65**, 1084 (1961).
- (9) H. D. Sharma and S. P. Sood, *J. Phys. Chem.*, **78**, 402 (1974). There is a notation error in this paper that may cause some confusion. The Arrhenius parameters for k_2 and k_3 should be interchanged.
- (10) I. C. Hisatsune and L. Zafonte, *J. Phys. Chem.*, **73**, 2980 (1969).
- (11) D. L. Bernitt, R. H. Miller, and I. C. Hisatsune, *Spectrochim. Acta, Part A*, **23**, 237 (1967).
- (12) G. E. McGraw, D. L. Bernitt, and I. C. Hisatsune, *J. Chem. Phys.*, **45**, 1392 (1966).
- (13) I. C. Hisatsune, *Kagaku No Ryoiki*, **23**, 148 (1969).
- (14) R. A. Wilkins, Jr., Ph.D. Thesis, The Pennsylvania State University, 1973.
- (15) G. M. Begun and W. H. Fletcher, *J. Chem. Phys.*, **33**, 1083 (1960).
- (16) T. Carrington and N. Davidson, *J. Phys. Chem.*, **57**, 418 (1953).
- (17) I. C. Hisatsune, *J. Phys. Chem.*, **65**, 2249 (1961).
- (18) IBM Application Program, System/360 Scientific Subroutine Package, Version III, "Programmer's Manual," 5th ed, International Business Machine Corp., New York, N.Y., 1970, p 333.
- (19) A. F. Trotman-Dickenson and G. S. Milne, *Nat. Stand. Ref. Data Ser., Nat. Bur. Stand.*, **No. 9** (1967).

Characteristic Energy Loss, Luminescence, and Luminescence Excitation Spectra of Methane and Other Alkane Solids under Low-Energy Electron Impact

Timothy Huang and William H. Hamill*

Department of Chemistry and the Radiation Laboratory,¹ University of Notre Dame, Notre Dame, Indiana 46556 (Received April 2, 1974)

Publication costs assisted by the U. S. Atomic Energy Commission

Characteristic energy losses under low-energy electron impact have been observed for methane at 2.5, 6–14, and 23 eV. The latter may be due to a collective excitation. Electron impact at 25 V excites luminescence at 220 (very weak), 360, 440, and 500 nm. The 360- and 495-nm emissions onset under ~18-V electron impact. Propane, *n*-octane, and *n*-decane resemble methane in most respects. The emissions of methane (excepting 220 nm) are attributed to CH which may be produced by recombination of CH₂⁺ and e⁻, provided ground-state CH₂⁺ does not react with CH₄ in the low-temperature solid. The emissions of other alkanes under low-energy electron impact may arise from comparable mechanisms.

Introduction

The fluorescence of liquid alkanes at ~200 nm has been studied in detail by Lipsky and his group.² The lifetime of this emission is approximately proportional to the number of carbon atoms for linear alkanes, amounting to several nsec.³ Thermoluminescence (or recombination luminescence) of ⁶⁰Co-irradiated 3-methylpentane at 77°K contains a weak band at 230 nm, the principal emission appearing as a rather asymmetric band with a maximum at ~400 nm but tailing considerably to the red.⁴ This emission can also be induced at 77°K by fast optical bleaching of matrix-trapped electrons, when its lifetime is 4.4 sec.⁵

Thin-film alkanes at 77°K luminesce under low-energy electron impact.⁶ In addition to weak emissions at ~200 and ~300 nm there are bands at ~380 and ~500 nm, the later being the stronger.

A limited examination of thermoluminescence of several ⁶⁰Co-irradiated alkanes at $\geq 77^\circ\text{K}$ shows that the emission spectra are usually dominated by a single broad peak at ~420 nm, as in 3-methylpentane. In isopentane, however, there are peaks at ~300, ~390, and ~580 nm. In neopentane there are peaks at ~330, 390, and ~490 nm.⁷

The work reported here was undertaken when preliminary observations showed that thin-film methane at 25°K luminesced under low-energy electron impact. Since the possibility of describing the excitations and emissions of methane and its daughter species is attractive, the study was continued. Propane, *n*-octane, and *n*-decane were included for comparison.

Experimental Section

The experimental procedures for measuring characteristic electron energy loss spectra⁸ and luminescence spectra under low-energy electron impact have been described. A closed-cycle refrigerator has been added for measurements below ~300°K as well as a PAR Model 124A lock-in amplifier. Films were ≥ 200 Å thick and they were maintained at 10⁻⁹ Torr following deposition. Electron currents were ~10⁻⁹ A for characteristic energy loss spectra. The cathode potential was modulated by 0.3 eV at 10³ Hz and the current transmitted by the sample to the anode; I_1 was differentiated to produce the spectrum dI_1/dV vs. eV.

The luminescence was measured by photon counting.

Spectra were measured with a Bausch and Lomb high-intensity monochromator. The electron current incident on the film was 10⁻⁸ A.

Results

The characteristic energy loss spectrum of methane appears in Figure 1. The zero of energy can be estimated very roughly from a loss maximum by electron impact of the low-pressure gas at 12 eV.⁹ The small peak following the first or electron injection peak is much better resolved, however, and is considered to correlate with the resonance at 2.48 eV reported by Pisanias, *et al.*¹⁰ The bulk electron affinity of the film is given by the position of the first peak¹¹ and it is 1.1 eV. The broad peak at ~23.5 eV is attributed tentatively to a collective excitation.

The characteristic energy loss spectrum of propane (not shown) contains no resolved structure and the zero of energy cannot be established. By retarding potential analysis of back-scattered electrons, for 2-eV initial energy, a strong resonance was observed at 0.7 eV. Such losses have been attributed previously to temporary negative ion states.¹¹

The luminescence emission spectra of methane at 25°K and of propane at 40°K for 25-eV excitation appear in Figure 2. The intensity at 220 nm was reexamined for 10-eV excitation (to avoid ion-molecule reactions). The counts were 251 and 172 during 170 sec. This difference is probably real but it is too weak for adequate characterization. The 500-nm emissions of methane and propane are very similar, indicating a common emitter.

The emission spectra of *n*-octane in Figure 3 and of *n*-decane in Figure 4 resemble those for other alkanes reported previously.⁶ An asymmetry at ~500 nm noted previously is now seen, for *n*-octane, to arise from a somewhat lower energy band. The signal was phase-shifted and at 6 kHz the nominal lifetime was 46 μsec but the decay was not simply exponential since the lifetime depended upon the frequency. There may be two simple exponential components but this could not be established. The low-energy emission of *n*-decane behaved similarly. The luminescence at 500 nm from methane and propane was too weak for this type of measurement.

The electron-impact excitation spectra for 200-nm fluorescence from *n*-octane and *n*-decane appear in Figure 5.

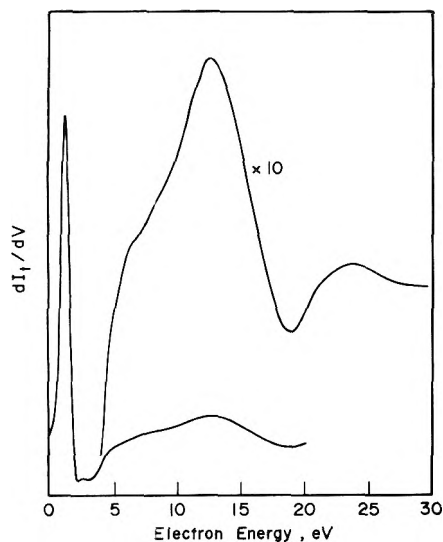


Figure 1. Dependence of the electron current, I_e , transmitted by a thin film of CH_4 on the incident electron energy, eV.

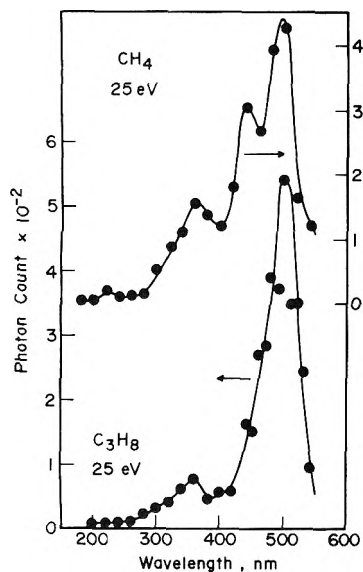


Figure 2. Luminescence spectra of CH_4 at 25°K and of C_3H_8 at 40°K at 25-eV incident electron energy.

The onset approximates that observed under uv excitation.²

The electron-impact excitation spectra for 360- and 340-nm emissions from methane at 26°K and *n*-decane at 70°K appear in Figure 6.

The excitation spectra for ~ 500 -nm emissions of methane at 26°K , propane at 40°K , and *n*-octane and *n*-decane at 70°K appear in Figure 7. Excepting that for *n*-octane, the spectra are remarkably similar. That for methane is also very similar to the excitation spectrum for the 360-nm emission in Figure 6. For *n*-octane and *n*-decane the rising intensity of low-energy emissions correlates with decreasing intensity of the 200-nm emission.

The dependence of 490-nm emission intensity for *n*-octane on temperature appears in Figure 8. If the quenching is activated, the activation energy is 0.012 eV. The other octane emissions were too weak for lifetime measurements.

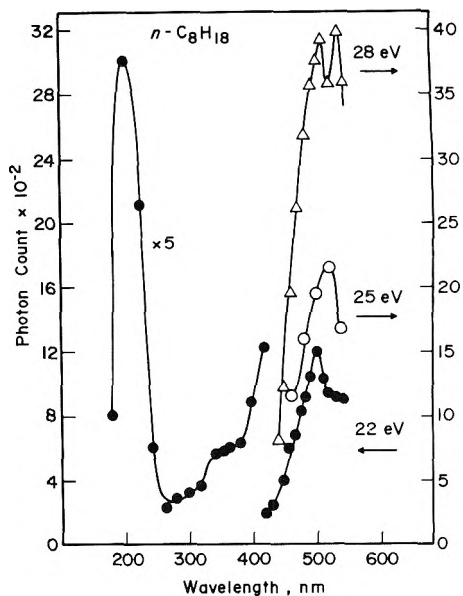


Figure 3. Luminescence spectrum of *n*- C_8H_{18} at 70°K and 22-, 25-, and 28-eV incident electron energy.

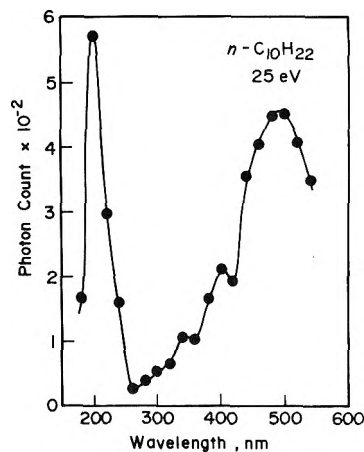


Figure 4. Luminescence spectrum of *n*- $\text{C}_{10}\text{H}_{22}$ at 75°K and 25-eV incident electron energy.

Discussion

The 2.5-eV resonance of methane observed by Pisanias, *et al.*,¹⁰ has been attributed to a compound negative ion state. The corresponding weak resonance in Figure 1 resembles similar events at ~ 2.5 eV for other alkanes.^{8,11} The resonance at 0.7 eV for propane is matched by a corresponding loss for almost all higher alkanes, but the methane spectrum exhibits no such event. It has been noted previously that such low-lying losses are weak or undetectable for those alkanes which have high electron mobilities in the liquid state.¹¹

Five higher alkanes provided evidence of a broad energy loss at ~ 23 eV and this was attributed tentatively to a collective excitation.¹¹ The event at ~ 23.5 eV for methane appears to be similar. A prominent peak at ~ 21 eV in the energy loss function of liquid water has been attributed to a collective electronic excitation.¹² Since methane and water are isoelectronic, the 23.5-eV event in methane can be interpreted similarly.

The energy distribution of injected electrons is described by the first peak of Figure 1 and this should be considered

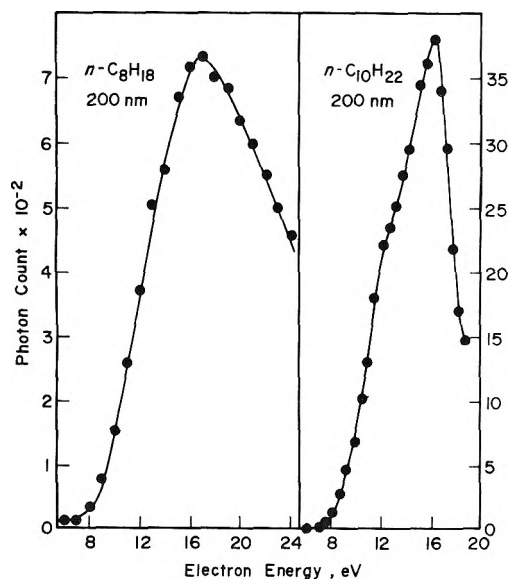


Figure 5. Excitation spectra of $n\text{-C}_8\text{H}_{18}$ and $n\text{-C}_{10}\text{H}_{22}$ for 200-nm fluorescence by electron impact at 70°K.

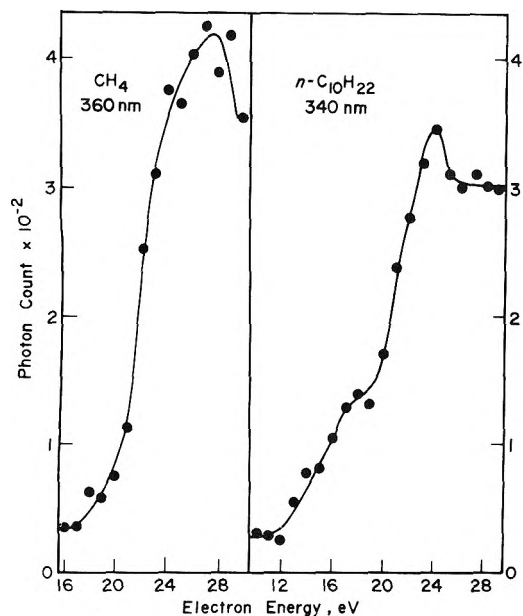


Figure 6. Excitation spectra of emissions at 360 nm from CH_4 at 26°K and 340 nm from $n\text{-C}_{10}\text{H}_{22}$ at 70°K.

for interpretations of luminescence excitation spectra. The high-energy component of the electron energy extends ~ 0.6 eV above the center of the distribution.

Methane is the simplest system to consider, but excitation at $\lesssim 13$ eV introduces formidable complications arising from ion-molecule reactions. Wexler and Jesse¹³ observed consecutive ion-molecule reactions of methane by mass spectrometry to the sixth and seventh generations, *e.g.*, as high as $\text{C}_5\text{H}_{11}^+$. The following examples suffice for the present purpose: CH_5^+ and C_2H_6^+ from CH_4^+ ; C_2H_4^+ and C_2H_5^+ from CH_3^+ ; C_2H_3^+ and C_3H_5^+ from CH_2^+ ; C_2H_2^+ and C_3H_3^+ from CH^+ .

The emissions will be tentatively attributed to states of CH for which the electronic term values are known to be 2.88 eV for $^2\Delta$, 3.23 eV for $^2\Sigma^-$, and 3.96 eV for $^2\Sigma^+$. The lowest state, $^4\Sigma^-$, has not been observed.¹⁴

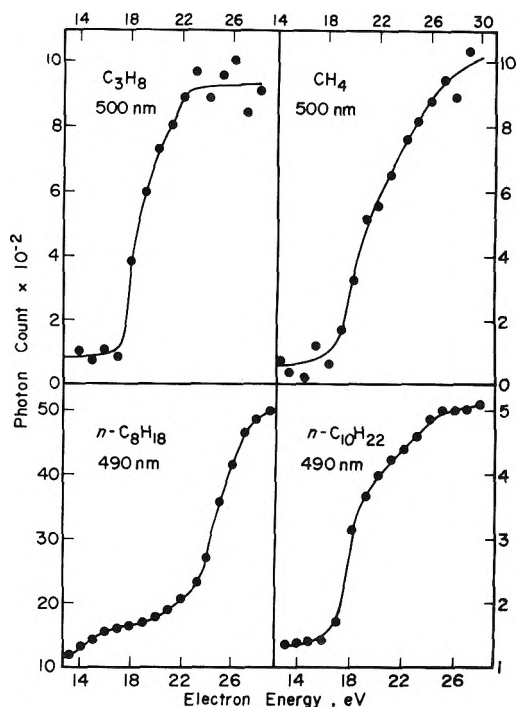


Figure 7. Excitation spectra of ~ 500 -nm emissions from CH_4 at 26°K, C_3H_8 at 40°K, and $n\text{-C}_8\text{H}_{18}$ and $n\text{-C}_{10}\text{H}_{22}$ at 70°K.

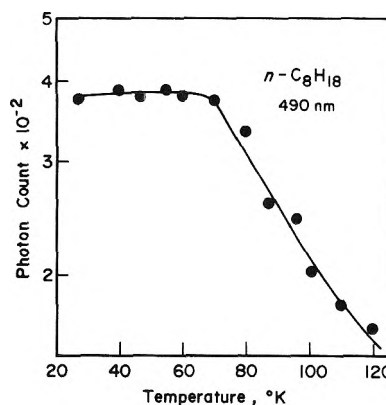


Figure 8. Dependence of 490-nm intensity for $n\text{-C}_8\text{H}_{18}$ on temperature.

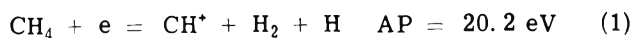
The three principal emissions of methane in Figure 2 have high-energy limits at ~ 2.8 , 3.1, and 4.3 eV, in rough agreement with term values of CH. If the most probable final states of the vertical transitions in the solid are assigned one quantum of vibrational energy (0.36 eV), then the assumed emission maxima are predicted at 2.52, 2.87, and 3.60 eV. There are no data for optically excited emissions from solid methane. The maxima in Figure 2 appear at 2.54, 2.82, and 3.45 eV.

The slow 500-nm emissions of n -octane and n -decane are in qualitative agreement with a 480-nsec lifetime for emissions of $\text{CH } ^2\Delta \rightarrow ^2\Pi$ in the gas phase.¹⁵

The 360- and 500-nm emissions of methane onset at an excitation energy of ~ 18.5 eV, the zero point having been established by Figure 1. There is one excited state of CH_4^+ at 19.4 eV in the gas phase¹⁶ or ~ 17.4 eV in the solid.¹⁷ The primary process is considered to be dissociation from a vibrationally excited state of this ion. The emitting states of CH would then arise from one or more ion-electron recom-

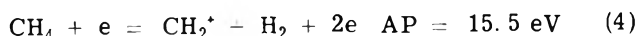
binations. If the recombination energies are estimated to be ~ 2 eV less exoergic in the solid state than under vacuum,¹⁷ then even second-generation ions have insufficient energy to yield excited CH. Later generation ions have still less energy. This suggests that one of the primary ions may be unreactive in the low-temperature solid. Both CH_4^+ and CH_3^+ can be eliminated from consideration because their ionization and appearance potentials (AP) are too low.

Processes 1 and 2 cannot be ruled out since the conver-

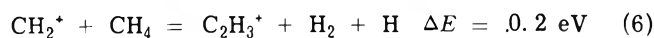


sion to C_2H_2^+ by reaction 3 is only slightly exoergic at $\text{CH}^+ + \text{CH}_4 = \text{C}_2\text{H}_2^+ + \text{H}_2 + \text{H} \quad \Delta E = -0.5 \text{ eV} \quad (3)$

at 298°K,¹⁵ and CH^+ might be stabilized. It may be doubted, however, that CH can survive charge recombination which is exoergic by 11 eV. Processes 4 and 5 are acceptable be-



cause $\text{AP}(4) \cong 13.5 \text{ eV}$ and $\text{AP}(5) \cong 17.7 \text{ eV}$ in the solid and conversion of CH_2^+ to C_2H_3^+ by reaction 6 may be en-



doergic at 26°K. Consequently CH_2^+ may survive until recombination occurs at $\sim 10^{-12}$ sec. Finally, the recombination process 7 should produce emitting states of CH for



$\Delta E(7) \cong -4 \text{ eV}$ in the solid.

The general resemblance of the luminescence spectra of several alkane thin-film solids and their somewhat similar high-energy excitation onsets indicate that common species may be largely responsible. This would require that $\text{AP}(\text{CH}_2^+) \cong 13 \text{ eV}$ for the 340-nm emission from *n*-decane in Figure 6. A rearranged *n*-decane ion to produce CH_2^+ and *n*-nonane requires 14.7 eV¹⁵ under vacuum or an estimated 12.7 eV in the solid. The much stronger excitation which onsets at $\sim 19 \text{ eV}$ may correspond to formation of CH_2^+ , H, and C_9H_{19} . Alternatively, ions with alkylidene structures, RCH^+ , can produce excited CH upon recombination.

It can be seen from Figure 5 that the 200-nm fluorescence of *n*-octane and *n*-decane is excited strongly throughout the energy range where there is efficient ionization,¹⁷ whether direct or indirect. It has been shown that charge pair formation dominates the characteristic electron energy loss spectrum of *n*-nonane at $>12 \text{ eV}$.¹¹ Consequently it appears that charge recombination may contribute efficiently to 200-nm luminescence.

No significance is attributed to the relative intensities in

Figure 5 because excitonic diffusion would make them very sensitive to thickness, surface condition, and structural defects. The other emitters are self-trapped. In all studies of thin films the emphasis has been placed on energy levels, not on cross sections for electron-impact excitations. The dependence of luminescence intensity on electron energy may have limited significance, however.

The slow decrease of 200-nm luminescence at $>17 \text{ eV}$ for *n*-octane is matched by a slow increase of 490-nm luminescence intensity in Figure 7. The abrupt decrease of 200 nm fluorescence from *n*-decane at 16 eV correlates with a sharply increased intensity of the 490-nm band at 17 eV. The onset of the 340-nm band for *n*-decane at 12 eV correlates with a shoulder in the 200-nm band at 12 eV. Such effects may arise from ion fragmentation at higher energy which terminates molecular emission and initiates that for fragments.

It should be noted that there are two regimes of excitation for *n*- $\text{C}_{10}\text{H}_{22}$ in Figure 6, the lower onsets at 12 eV and the higher at $\leq 19 \text{ eV}$. The lower may arise from the analog of reaction 4 for CH_4 ; the higher, for reaction 5. The higher onset is obscured by the weak lower excitation and it may lie at $\sim 17 \text{ eV}$ by analogy with the 490-nm excitation in Figure 7, where the two excitations are better resolved.

Emissions at ~ 350 and $\sim 500 \text{ nm}$ continue to increase in the region of collective excitations. One possibility is that the two types of excitation are not connected and that the latter are relatively weak and therefore do not compete appreciably. Another possibility is that collective excitations subsequently convert to upper ionic states.

References and Notes

- (1) The Radiation Laboratory of the University of Notre Dame is operated under contract with the U. S. Atomic Energy Commission. This is AEC Document No. COO-38-943.
- (2) W. Rothman, F. Hirayama, and S. Lipsky, *J. Chem. Phys.*, **58**, 1300 (1973).
- (3) M. S. Henry and W. P. Helman, *J. Chem. Phys.*, **56**, 5734 (1972).
- (4) K. Funabashi, C. Hebert, and J. L. Magee, *J. Phys. Chem.*, **75**, 3221 (1971).
- (5) P. B. Merkle and W. H. Hamill, *J. Chem. Phys.*, **53**, 3414 (1970).
- (6) K. Hiraoka and W. H. Hamill, *J. Phys. Chem.*, **77**, 1616 (1973).
- (7) H. Ogura, unpublished results.
- (8) K. Hiraoka and W. H. Hamill, *J. Chem. Phys.*, **57**, 3870 (1972).
- (9) H. H. Brongersma, Ph.D. Thesis, University of Leiden, 1968.
- (10) M. N. Pisanias, L. G. Christophorou, and J. G. Carter, Report ORNL-TM-3904, Oak Ridge National Laboratory, Oak Ridge, Tenn., Aug 1972.
- (11) K. Hiraoka and W. H. Hamill, *J. Chem. Phys.*, **59**, 5749 (1973).
- (12) J. M. Heller, R. N. Hamm, R. D. Birkhoff, and L. R. Painter, *J. Chem. Phys.*, to be submitted for publication.
- (13) S. Wexler and N. Jesse, *J. Amer. Chem. Soc.*, **84**, 3425 (1962).
- (14) G. Herzberg, "Molecular Spectra and Molecular Structure," Vol. 1, D. Van Nostrand, Princeton, N. J., 1950.
- (15) P. Erman and J. Brzozowski, *Nucl. Instrum. Methods*, **110**, 471 (1973).
- (16) J. L. Franklin, J. G. Dillard, H. M. Rosenstock, J. T. Herron, K. Draxl, and F. H. Field, *Nat. Stand. Ref. Data Ser., Nat. Bur. Stand.*, **No. 26** (1969).
- (17) T. Huang and W. H. Hamill, *J. Phys. Chem.*, **78**, 2081 (1974).

Luminescence Probe Analysis of Ionic States of Cyclopentane, Cyclohexane, and *n*-Hexane Solids under Low-Energy Electron Impact

Timothy Huang and William H. Hamill*

Department of Chemistry and the Radiation Laboratory,¹ University of Notre Dame, Notre Dame, Indiana 46556 (Received April 2, 1974)

Publication costs assisted by the U. S. Atomic Energy Commission

Thin films (~ 200 Å) of cyclopentane, cyclohexane, and *n*-hexane at 60°K doped with 1% benzene or toluene luminesce under low-energy electron impact. Bands appear at ~ 200 , ~ 275 , and ~ 380 nm due to alkane fluorescence and to the aromatic hydrocarbon fluorescence and phosphorescence, respectively. For benzene in cyclohexane the 370-nm luminescence excitation spectrum has peaks at 7.8, ~ 10 , ~ 13 , 14.5, 15.9, 17.6, and 19.1 eV. The spectrum for toluene in cyclohexane is very similar and comparable spectra were obtained for *n*-hexane. For benzene in cyclopentane the excitation peaks appeared at 8.5, 9.3, 11.0, 11.9, 13.5, 14.7, and 16.7 eV. The principal mechanism of excitation appears to be ionization of a molecule of the matrix, positive hole migration and trapping by the impurity, charge recombination to form an excited molecule of the additive, and luminescence. The luminescence excitation spectrum of the probe detects only those positive-hole states which can migrate and be trapped prior to recombination. The spectra indicates that the energy band width for migration is rather narrow.

Introduction

Characteristic energy losses measured by slow electron impact on solid alkanes are usually poorly resolved, both for excited neutral states and for ionic states.^{2,3} A comparable effect is observed optically.

The luminescence bands of alkane solids under electron impact which appear at ~ 200 , ~ 290 , ~ 370 , and ~ 490 nm provide some additional information.⁴ The 200-nm band has been thoroughly investigated by Lipsky's group⁵ and will not be considered further.

The other emissions of alkanes under electron impact arise from ionic states and are probably due to fragments, which may include CH.⁶ Their excitation spectra contain no resolved structure.

A further possible approach to the problem of resolving the electronic structure of alkane solids is to add a positive-hole trap which will generate a suitable recombination luminescence. The excitation luminescence spectrum would then describe the delocalized positive ion (or hole) energy levels. Preliminary experiments with 1% benzene in cyclohexane showed adequate intensities of benzene fluorescence and phosphorescence and well-resolved luminescence excitation spectra. Fragmented ions would contribute little to benzene luminescence since they are localized. They do contribute an overlapping luminescence, but it is weak for excitation below ~ 18 eV.

Experimental Section

The apparatus and general procedures have been described.^{2,3,6} Samples of 1 mol % benzene or toluene in cyclopentane, cyclohexane, or *n*-hexane were admitted to the high-vacuum system and maintained at 2×10^{-7} Torr for 480 sec. Film thickness would approximate 200 Å. The substrate was held at 60°K unless otherwise specified. The photon-counting period was 14 sec at each energy. First-derivative excitation spectra, dL/dV vs. eV , were obtained from the luminescence intensity L by the photon count difference at voltages V and $V + 0.5$.

A high-intensity Bausch and Lomb monochromator was

used for all measurements except those for benzene in cyclopentane for which a Corning 7-54 filter isolated the combined 280-nm fluorescence and 380-nm phosphorescence.

Results

The luminescence spectra for *n*-hexane and cyclohexane doped with benzene at 15-eV incident electron energy appear in Figure 1. The 200-nm band is due to alkane fluorescence. The bands at ~ 275 and ~ 380 nm correspond to the fluorescence and phosphorescence of benzene, although a weak admixture of alkane emissions^{3,6} cannot be excluded. The spectrum of toluene-doped cyclohexane for similar conditions appears in Figure 2. There is no evidence of excimer emissions and the activators are presumed to be homogeneously dispersed. This is to be expected for deposition at 60°K.

The excitation spectrum of 390-nm emission by electron impact for toluene-doped cyclohexane appears in Figure 3 (above) together with that for 370-nm emission from benzene-doped cyclohexane (below). The results from photoionization spectroscopy (PS) of cyclohexane⁷ are shown by bars at the top of Figure 3, but with an arbitrary zero of energy. The electron energy scale is zeroed to the first (injection) peak of the energy loss spectrum.³ This choice will be correct if the electron affinity of the solid is zero and if there is negligible charge trapping in the film. The ionization potentials from photoelectron spectroscopy can be brought into register with the excitation peaks for electron impact by applying a constant shift of -2.0 eV. There is one "extra" excitation peak (or shoulder) for the solids at 14.5 eV, but this is not unexpected for electron impact because of different selection rules.

The excitation spectrum for 280-nm luminescence of benzene-doped cyclohexane in Figure 4 can be correlated with the results of photoelectron spectroscopy except that the luminescence associated with the ground state of $C_6H_{12}^+$ is even weaker than before and a peak cannot be located reliably. Correlations are based therefore on the three strongest peaks at 10.3, 15.9, and 17.0 eV. There is

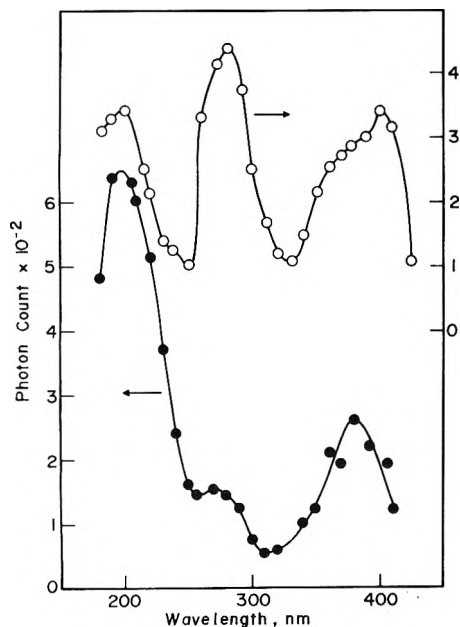


Figure 1. Emission spectra of 1% benzene in cyclohexane (O) and in *n*-hexane (●), both at 60°K and at 15-eV incident electron energy.

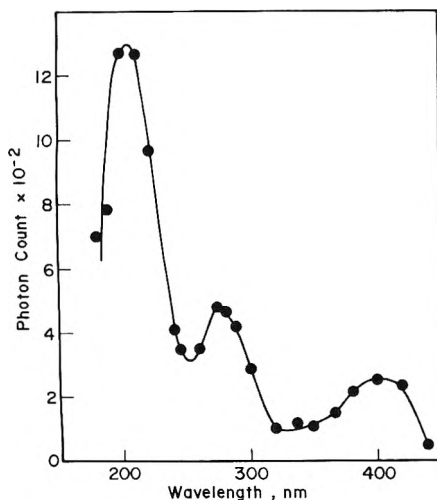


Figure 2. Emission spectra of 1% toluene in cyclohexane at 60°K and at 15 eV incident electron energy.

“extra” structure at ~14.6 eV, as in Figure 3. The results for cyclohexane are summarized in Table I.

Considered together, these three excitation spectra support the interpretation that they correspond to the ionic states of cyclohexane. Their energy levels lie about 2.0 eV lower in the solid state than under vacuum.

The excitation spectrum of benzene-doped cyclopentane appears in Figure 5. Luminescence below ~8-eV electron energy was also observed in *n*-hexane but not in cyclohexane. Possible correlations with data from photoelectron spectroscopy appear as bars at the top.

The excitation spectrum of 390-nm luminescence from benzene-doped *n*-hexane appears in Figure 6. The peak at 6.3 eV coincides with a resolved resonance in the characteristic energy loss spectrum.² The other peaks occur at 8.8, 10.1, 11.8, 13.3, 15.3, and 16.8 eV. These results do not correlate with those for excitation of benzene phosphorescence

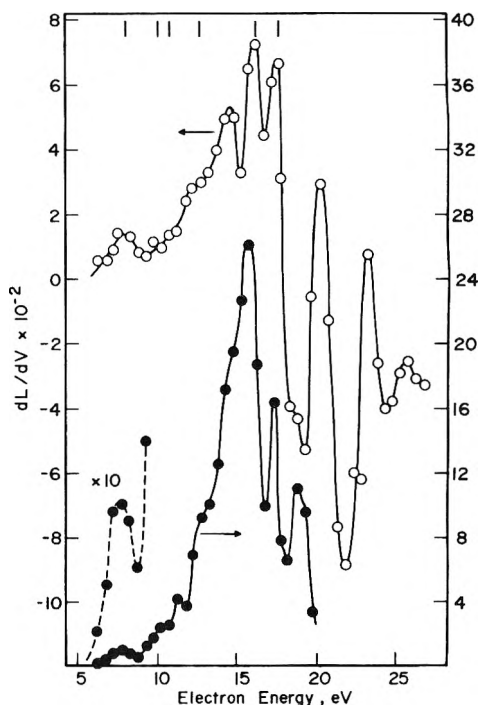


Figure 3. Excitation spectra of 390-nm emission from 1% toluene in cyclohexane (O) and 370-nm emission from 1% benzene in cyclohexane (●). Data from photoionization spectroscopy are shown by bars after shifts of -2.0 eV.

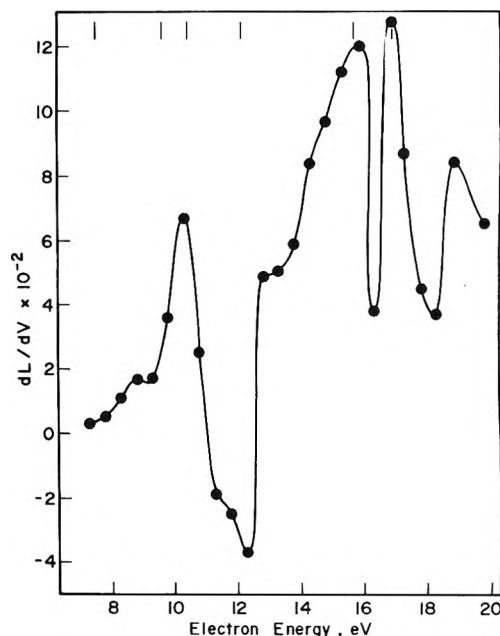


Figure 4. Excitation spectrum of 280-nm luminescence for 1% benzene in cyclohexane.

in cyclohexane. This supports the interpretation that they represent states of the lattice. There are no results from photoelectron spectroscopy for comparison.

Discussion

The luminescence spectra in Figures 1 and 2 do not permit an estimate of the extent of quenching 200-nm alkane fluorescence by benzene. In liquid cyclohexane 1% of benzene quenches about 80% of the fluorescence.⁸ Whatever

TABLE I: Ionization Potentials of Cyclopentane and Cyclohexane (eV)

c-C ₅ H ₁₀ ^a (solid, C ₆ H ₆ , 280 nm + 370 nm)	c-C ₅ H ₁₀ ^b (vapor, PS)	Shift, c-C ₅ H ₁₀	c-C ₆ H ₁₂ ^c (solid, C ₆ H ₅ CH ₃ , 390 nm)	c-C ₆ H ₁₂ ^c (solid, C ₆ H ₆ , 370 nm)	c-C ₆ H ₁₂ ^d (solid, C ₆ H ₆ , 280 nm)	c-C ₆ H ₁₂ ^b (vapor, PS)	c-C ₆ H ₁₂ ^e (vapor, PS)	Shift c-C ₆ H ₁₂
8.5	10.49	2.0	7.8	7.8		9.81	9.88	2.0
9.3					~9	(11.88)	(11.33)	
11.0			~10.3	~10	10.3	(12.74)	12.22	1.9
11.9	13.89	2.0	~12.8	~13	~13.2	14.50	14.37	~1.4
13.5	15.91	2.4	14.7	~14.5	~14.6			
14.7			16.3	15.9	15.9	(18.04)		~2.0
16.7	18.27	1.5	17.8	17.6	17.0	(19.34)	19.43	2.0
			~18.8	19.0	19.0			
			19.9					
			23.3					
			25.9					

^a From Figure 5. ^b From ref 7. Values in parentheses are uncertain. ^c From Figure 3. ^d From Figure 4. ^e M. I. Al-Joboury and D. W. Turner, *J. Chem. Soc.*, 4434 (1964).

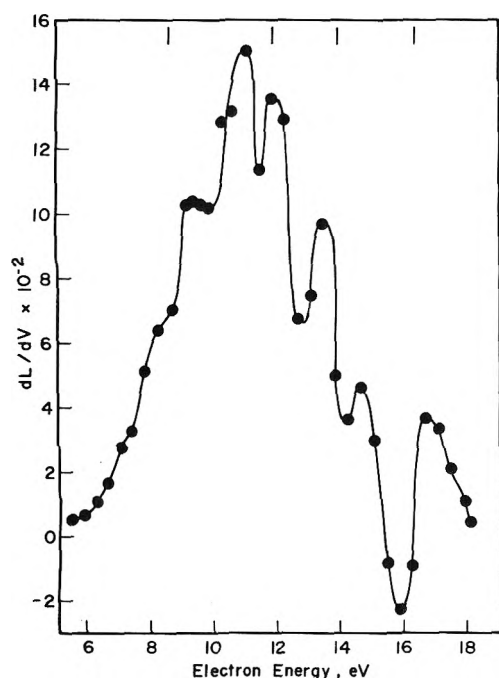


Figure 5. Excitation spectrum of the combined fluorescence and phosphorescence of benzene in cyclopentane.

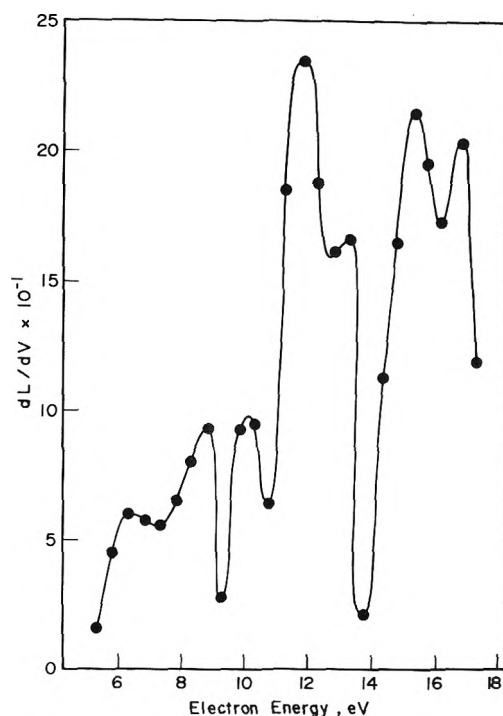


Figure 6. Excitation spectrum of 390-nm luminescence for 1% benzene in *n*-hexane.

the effect may be in the solid state, it need not concern us further. Alkane emissions at ~280, ~350, and ~490 nm are excited strongly only at ~18 eV or more.² Consequently the ~275- and ~380-nm bands of Figures 1 and 2 under 15-eV excitation are due entirely, or nearly so, to the fluorescence and phosphorescence of benzene and toluene. Under 25-eV excitation there is strong emission at ~500 nm from benzene-doped cyclohexane and there are relatively weak bands at 280 and 380 nm. It is quite impossible to determine how much of the latter is due to the very similar emissions of alkanes, but it will be shown that this is not critical. The emissions of alkanes probably arise from fragment ions; *i.e.*, they are self-trapped holes,⁶ and their fate would not be sensitive to addition of 1% benzene.

The excitation peaks of Figures 3–6 are those of benzene and toluene luminescence alone for electron energy below ~18 eV. Those at or above ~18 eV do not at all resemble the structureless alkane luminescence excitation spectra and these peaks can also be attributed to excitation of ben-

zene and toluene emissions. The differences between the two types of spectra can be seen more readily by differentiating the excitation spectra for the 200-nm band of *n*-C₁₀H₂₂ and the 490-nm band of *n*-C₈H₁₈ from the preceding article.⁶ These spectra appear in Figure 7. The intensities of other bands were too weak for this purpose.

The clue to understanding the excitations of Figures 3–6 is provided by comparison with the results from photoelectron spectroscopy in Table I and Figures 3–6. If all of the ionization potentials of cyclohexane and cyclopentane in the low-pressure vapor are decreased by approximately the same amount in the solid, then it should be possible to bring them into register with those luminescence excitations which result from positive-hole trapping, that is from initially delocalized ionic states in the solid. The correlation which has been chosen in Figures 3 and 4 requires a uniform shift of -2.0 eV which can be shown to arise largely from the electronic polarization of the solid for the posi-

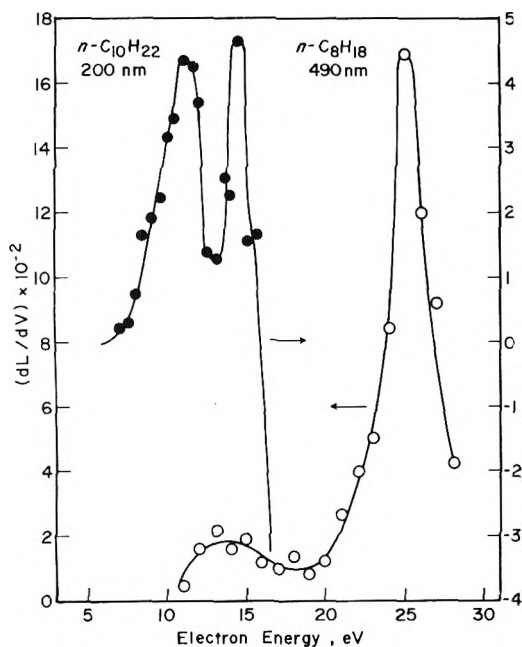


Figure 7. Comparison of two types of excitation for 200-nm emission from $n\text{-C}_8\text{H}_{18}$ and for 390-nm emission from benzene-doped $n\text{-C}_6\text{H}_{14}$.

tive-hole state. The shift for cyclopentane in Figure 5 was also -2.0 eV but the uncertainty is greater due to the limited number of measurements.

All luminescence excitation peaks for cyclohexane and cyclopentane systems above ~ 7.5 eV are considered to correlate with energy levels of $c\text{-C}_6\text{H}_{12}^+$ and $c\text{-C}_5\text{H}_{10}^+$ in the solid. The mechanism for luminescence of the doped systems is then positive-hole formation and migration, trapping by benzene or toluene, charge recombination, and luminescence.

The lowest energy of the conducting state of an electron in an insulator, liquid or solid, is commonly represented by V_0 which should not be confused with the zero-point potential energy U_0 . Referred to a vacuum zero, V_0 is the negative of the bulk electron affinity, $-A$. The latter is the least total energy change for (thermal) electron injection and consequently $-A = T_0 + U_0$. It is commonly assumed that $T_0 = 0$ or that the zero-point kinetic energy of an electron in the conducting state is zero. This is incorrect, possibly by 1 eV or more.^{9,10}

For a properly zeroed energy scale of a characteristic energy loss spectrum the first (electron injection) peak is located at A .³ The zero of energy was arbitrarily located at the first peak ($A \cong 0$ for these alkanes in the liquid state¹¹), and the first ionization potential I_s in the solid, e.g., at 7.8 eV in Figure 3, is correctly described by $I_s = (7.8 + A)$ eV. Since I_s is related to the gas-phase ionization potential I_g by $I_s = I_g - A + P_h$ where P_h is the electronic polarization energy of the positive hole, it follows that $P_h = 7.8 + 2A - I_g$. For $A \cong 0$,¹¹ $P_h \cong -2.0$ eV.

The striking feature of Figures 3–6 is the relatively well-resolved structure of the ionizing excitations which is not observed optically nor is it observed by energy loss spectra for electron impact, in the gas phase or the solid. It was not observed for the excitation of the luminescence from neat benzene⁴ or from many undoped alkane solids using the same apparatus and procedures.^{6,12} The well-resolved structure will be attributed to the mechanism of energy mi-

gration since this is not required for luminescence from undoped solids.

A wide band of vibronic states for each electronic term of alkane ions must be accessible to excitation by electron impact and there should be efficient charge exchange between any of them and a molecule of benzene or toluene. In fact, the half-width of resolved excitation peaks is only ~ 0.8 eV while the electron energy half-width is ~ 0.6 eV. It must be assumed then that many of these vibrationally excited states are not conducting, i.e., that the conducting states lie within a relatively narrow band of energies for each electronic term. This suggests that efficient hole conduction is limited to 0–0, or near 0–0, electron transfers between ion-molecule pairs.

The facts also require assuming that vibrationally excited ions do not become conducting as they cool since this would obliterate the selective effect which is observed. By the time an ion has dissipated its vibrational energy, both its configuration and the lattice have somewhat relaxed and the hole should be self-trapped. Electron tunneling to the impurity from nonadjacent donor molecules will not be prompt. At 60°K in solid alkanes there can be no randomized or free charge pairs and the lifetimes of coulombically correlated charge pairs are limited by recombination to $\sim 10^{-12}$ sec. Hole migration by hopping probably contributes little. There remains a short-range band-like conduction with nearest-neighbor charge-transfer time of $\sim 10^{-15}$ sec which cannot couple effectively to vibrationally excited states. (This is an estimated value for cyclohexane which is based upon a band-model calculation for octacosane ($\text{C}_{28}\text{H}_{58}$) for which $\Delta t \cong 10^{-14}$ sec was found.¹³ Scaling from $d = 35.6$ Å for octacosane for hole migration end to end along the chains to $d \cong 5$ Å for migration across the stacked cycloalkane rings gives $\Delta t \cong 10^{-15}$ sec.) Consequently, well-resolved ionizations may be selectively detected and higher hole states must retain their electronic identity during migration since electronic relaxation would lead to considerable vibrational excitation.

Comparable effects have been observed previously¹² in Ti^+ -doped alkali halides above the optical band gap where the mechanism may also be hole trapping followed by recombination. The luminescence excitation spectrum under electron impact was better resolved than the characteristic energy loss spectrum. It is interesting that exciton states of the ionic lattice were also better resolved by the same technique.

The distinct excitation peak for benzene phosphorescence from n -hexane at 6.5 eV in Figure 6 is attributed to energy transfer from a triplet state of n -hexane at this energy. Excitations of alkanes by low-energy electron impact were observed by Brongersma and Oosterhoff with onsets about 1.0 eV below optical values.¹⁴ For cyclopropane and cyclooctane the values were 5.9 and 6.0 eV and they were attributed to excitation of triplet states. Characteristic losses have been observed for several solid alkanes at ~ 6 eV, but only for n -hexane was the energy loss adequately resolved,^{2,4} and that determined its choice in this work. There is also a resolved resonance at 6 eV for chemical decomposition of n -hexane at 77°K under electron impact which was considered to be due to a vibrationally excited triplet state.¹⁵

References and Notes

- (1) The Radiation Laboratory of the University of Notre Dame is operated under contract with the U. S. Atomic Energy Commission. This is AEC Document No. COO-38-944.

- (2) K. Hiraoka and W. H. Hamill, *J. Chem. Phys.*, **57**, 3870 (1972).
 (3) K. Hiraoka and W. H. Hamill, *J. Chem. Phys.*, **59**, 5749 (1973).
 (4) K. Hiraoka and W. H. Hamill, *J. Phys. Chem.*, **77**, 1616 (1973).
 (5) W. Rothman, F. Hirayama, and S. Lipsky, *J. Chem. Phys.*, **58**, 1300 (1973).
 (6) T. Huang and W. H. Hamill, *J. Phys. Chem.*, **78**, 2077 (1974).
 (7) M. J. Dewar and S. D. Worley, *J. Chem. Phys.*, **50**, 668 (1969).
 (8) F. Hirayama and S. Lipsky, *J. Chem. Phys.*, **51**, 3616 (1969).
 (9) O. Klemperer, "Electron Physics," Butterworths, London, 1961, p. 164.
 (10) For solid xenon with $A \cong 0.6$ eV the inner potential is 5.5 eV for 20-eV electron injection. Consequently $T_0 \cong 5$ eV: A. Ignatiev and T. N. Rhodin, *Phys. Rev. B*, **8**, 893 (1973).
 (11) R. A. Holroyd and M. Allen, *J. Chem. Phys.*, **54**, 5014 (1971).
 (12) K. Hiraoka and W. H. Hamill, *J. Chem. Phys.*, **58**, 3686 (1973).
 (13) W. L. McCubbin, *Trans. Faraday Soc.*, **59**, 769 (1963).
 (14) H. H. Brongersma and L. J. Oosterhoff, *Chem. Phys. Lett.*, **3**, 437 (1969).
 (15) T. Matsushige and W. H. Hamill, *J. Phys. Chem.*, **76**, 1255 (1972).

Rate Constants for the Reactions of Ozone with Ethene and Propene, from 235.0 to 362.0 K

John T. Herron* and Robert E. Huie

Institute for Materials Research, National Bureau of Standards, Washington, D. C. 20234 (Received June 12, 1974)

Publication costs assisted by the National Bureau of Standards

The rate constants for the reactions of ozone with ethene and propene have been measured over the temperature range 235.0–362.0 K, using a stopped-flow system coupled to a beam-sampling mass spectrometer. The rate constants found, at a total pressure of about 500 N m⁻², in the presence of molecular oxygen, were $k(\text{C}_2\text{H}_4) = (5.42 \pm 3.19) \times 10^9 \exp(-2557 \pm 167/T) \text{ cm}^3 \text{ mol}^{-1} \text{ sec}^{-1}$ and $k(\text{C}_3\text{H}_6) = (3.70 \pm 1.42) \times 10^9 \exp(-1897 \pm 109/T) \text{ cm}^3 \text{ mol}^{-1} \text{ sec}^{-1}$.

Introduction

Although there have been numerous studies of the kinetics of the ozone-olefin reactions at room temperature (see Stedman, Wu, and Niki¹ and references therein), there are few data available at other temperatures, the only extensive set of data being that of DeMore² on C₂H₂ (243–283 K), C₂H₄ (178–233 K), and C₃H₆ (183–193 K). We report here data on the kinetics of the reaction of ozone with C₂H₄ and C₃H₆ over the temperature range 235.0–362.0 K.

Experimental Section

The experiments were carried out using a stopped-flow reactor, shown in Figure 1, coupled to a beam-sampling mass spectrometer.^{3,4} Ozone, produced in an ozonizer and stored at -78° on silica gel, was mixed with reactant olefin and carrier gas (Ar or O₂) and was allowed to flow into a 350-cm³ glass reactor. Flow into and out of the reactor was controlled by stainless steel solenoid valves, which could be closed simultaneously to entrap the premixed reacting gases. The contents of the reactor were monitored by means of a beam-sampling mass spectrometer through a 100-μm diameter orifice. A modulated ion signal was obtained by mechanically chopping the beam, and a phase-sensitive detection technique was used. The output of the phase-sensitive amplifier was digitized, sampled at a preselected interval, and stored on a paper tape using a high-speed punch. The reactor was double-walled so that fluid could be circulated to cool or heat the reactor. The temperature of the reactor was measured by means of a copper-

constantan thermocouple inserted into the reactor through a "well" (see Figure 1). The temperature of the circulating heat-exchange liquid was also measured using a copper-constantan thermocouple or an immersion thermometer. The two temperatures were identical under all experimental conditions. The uncertainty in temperature measurement was less than 0.5 K and resulted primarily from potentiometer reading error. The total pressure was about 500 N m⁻² and was measured by means of a capacitance manometer. The sensitivity of the mass spectrometer to the olefins was determined for each run using two different gas mixtures of known composition (2–5% olefin in O₂).

Results

For the reaction of ozone with an olefin A



$$-d[\text{O}_3]/dt = k_1[\text{O}_3][\text{A}] \quad (1)$$

and if $[\text{A}] \gg [\text{O}_3]$, then

$$\ln [\text{O}_3] = k_1[\text{A}]t + c$$

where $k_1[\text{A}]$ is effectively the first-order rate constant for the decay of ozone in excess olefin. The ozone decay data, in digital form, corrected for any background ion signal at m/e 48, were fitted to eq 1 using a weighted linear least-squares routine. The weighting function used was $W = (N - B)^2/(N + B)$, where N is the signal intensity and B is the background correction. The slopes from these fits are the first-order rate constants given in Tables I and II. The stat-

TABLE I: Rate Data for the Reaction of Ozone with Ethene

T, K	$10^9[C_2H_4]_0,$ mol cm ⁻³	$10^9[O_3]_0,$ mol cm ⁻³	$10^2k^{1st},$ sec ⁻¹
235.0	0.0	0.16	0.258 ± 0.009
	3.32	0.12	0.350 ± 0.015
	7.72	0.17	0.350 ± 0.016
	14.0	0.15	0.461 ± 0.017
	27.8	0.14	0.671 ± 0.019
	39.9	0.16	0.784 ± 0.020
	$k = (1.35 \pm 0.08) \times 10^5$ cm ³ mol ⁻¹ sec ⁻¹		
266.9	0.0	0.19	0.267 ± 0.010
	2.33	0.20	0.342 ± 0.011
	5.18	0.17	0.467 ± 0.014
	8.79	0.20	0.591 ± 0.018
	12.31	0.19	0.683 ± 0.027
	17.13	0.19	0.853 ± 0.024
	20.87	0.18	0.988 ± 0.032
$k = (3.48 \pm 0.09) \times 10^5$ cm ³ mol ⁻¹ sec ⁻¹			
286.2	0.0	0.12	0.380 ± 0.010
	1.82	0.12	0.488 ± 0.017
	3.73	0.14	0.601 ± 0.025
	6.30	0.13	0.659 ± 0.021
	9.24	0.13	0.909 ± 0.025
	14.6	0.11	1.29 ± 0.03
	26.3	0.14	1.83 ± 0.03
$k = (5.62 \pm 0.22) \times 10^5$ cm ³ mol ⁻¹ sec ⁻¹			
309.4	0.0	0.15	0.264 ± 0.009
	1.84	0.16	0.600 ± 0.012
	3.79	0.16	0.830 ± 0.018
	5.62	0.16	1.09 ± 0.02
	7.41	0.16	1.29 ± 0.02
	9.21	0.17	1.59 ± 0.02
	11.3	0.16	1.88 ± 0.02
	14.5	0.15	2.29 ± 0.03
$k = (1.41 \pm 0.03) \times 10^6$ cm ³ mol ⁻¹ sec ⁻¹			
332.4	0.0	0.11	0.337 ± 0.008
	2.12	0.12	0.917 ± 0.023
	3.19	0.28	1.18 ± 0.01
	3.31	0.02	1.13 ± 0.06
	3.56	0.12	1.29 ± 0.03
	6.02	0.12	1.77 ± 0.03
	6.35	0.27	1.86 ± 0.02
	6.46	0.02	1.83 ± 0.09
	8.67	0.11	2.43 ± 0.04
	11.08	0.02	2.75 ± 0.11
	11.19	0.26	2.85 ± 0.03
11.69	0.13	2.90 ± 0.04	
$k = (2.31 \pm 0.05) \times 10^6$ cm ³ mol ⁻¹ sec ⁻¹			
362.0	0.0	0.15	0.445 ± 0.008
	1.55	0.12	1.39 ± 0.02
	2.52	0.19	1.94 ± 0.03
	4.74	0.19	3.10 ± 0.04
	6.45	0.14	3.93 ± 0.07
	9.07	0.20	5.24 ± 0.07
	$k = (5.44 \pm 0.11) \times 10^6$ cm ³ mol ⁻¹ sec ⁻¹		

ed uncertainties are the standard errors of the slopes from the least-squares fit. First-order rate constants were mea-

TABLE II: Rate Data for the Reaction of Ozone with Propene

T, K	$10^9[C_3H_6]_0,$ mol cm ⁻³	$10^9[O_3]_0,$ mol cm ⁻³	$10^2k^{1st},$ sec ⁻¹
250.0	0.0	0.16	0.258 ± 0.009
	1.24	0.12	0.378 ± 0.027
	3.16	0.15	0.632 ± 0.020
	4.73	0.14	0.859 ± 0.029
	6.44	0.15	1.04 ± 0.02
	8.78	0.17	1.36 ± 0.03
	17.2	0.13	2.41 ± 0.03
	$k = (1.25 \pm 0.01) \times 10^6$ cm ³ mol ⁻¹ sec ⁻¹		
	266.9	0.0	0.19
2.85		0.18	1.16 ± 0.02
4.82		0.19	1.76 ± 0.03
7.60		0.17	2.43 ± 0.04
9.57		0.18	3.11 ± 0.05
11.6		0.17	3.56 ± 0.05
$k = (2.91 \pm 0.06) \times 10^6$ cm ³ mol ⁻¹ sec ⁻¹			
286.2	0.0	0.12	0.380 ± 0.010
	1.31	0.11	0.914 ± 0.026
	2.31	0.11	1.29 ± 0.03
	3.64	0.12	2.00 ± 0.03
	5.55	0.12	2.95 ± 0.05
	7.36	0.14	3.63 ± 0.05
	$k = (4.44 \pm 0.09) \times 10^6$ cm ³ mol ⁻¹ sec ⁻¹		
309.4	0.0	0.15	0.264 ± 0.009
	1.92	0.16	1.93 ± 0.04
	3.02	0.16	2.85 ± 0.04
	4.81	0.15	4.53 ± 0.07
	6.69	0.15	5.99 ± 0.09
	8.79	0.15	7.55 ± 0.10
	$k = (8.50 \pm 0.11) \times 10^6$ cm ³ mol ⁻¹ sec ⁻¹		
332.4	0.0	0.11	0.337 ± 0.080
	1.71	0.10	2.14 ± 0.03
	2.18	0.025	2.69 ± 0.12
	2.43	0.24	2.91 ± 0.03
	2.80	0.10	3.23 ± 0.05
	4.55	0.10	5.11 ± 0.07
	4.89	0.017	5.87 ± 0.39
	5.48	0.23	6.11 ± 0.06
	6.24	0.11	6.93 ± 0.11
	$k = (1.06 \pm 0.01) \times 10^7$ cm ³ mol ⁻¹ sec ⁻¹		
362.0	0.0	0.15	0.445 ± 0.008
	1.10	0.14	3.20 ± 0.05
	1.89	0.18	4.81 ± 0.06
	2.82	0.18	7.00 ± 0.08
	3.89	0.16	9.24 ± 0.14
	$k = (2.30 \pm 0.03) \times 10^7$ cm ³ mol ⁻¹ sec ⁻¹		

sured over a range of olefin concentrations, keeping $[A]_0 > 10[O_3]_0$. Second-order rate constants at a particular temperature were determined as the slope of a plot of the first-order rate constant against the olefin concentration. The olefin concentration was corrected for effusion to a weighted midpoint of the reaction, $(N/N_0)^2 = 1/2$. The correction factor was typically less than 1% and never exceeded 6%.

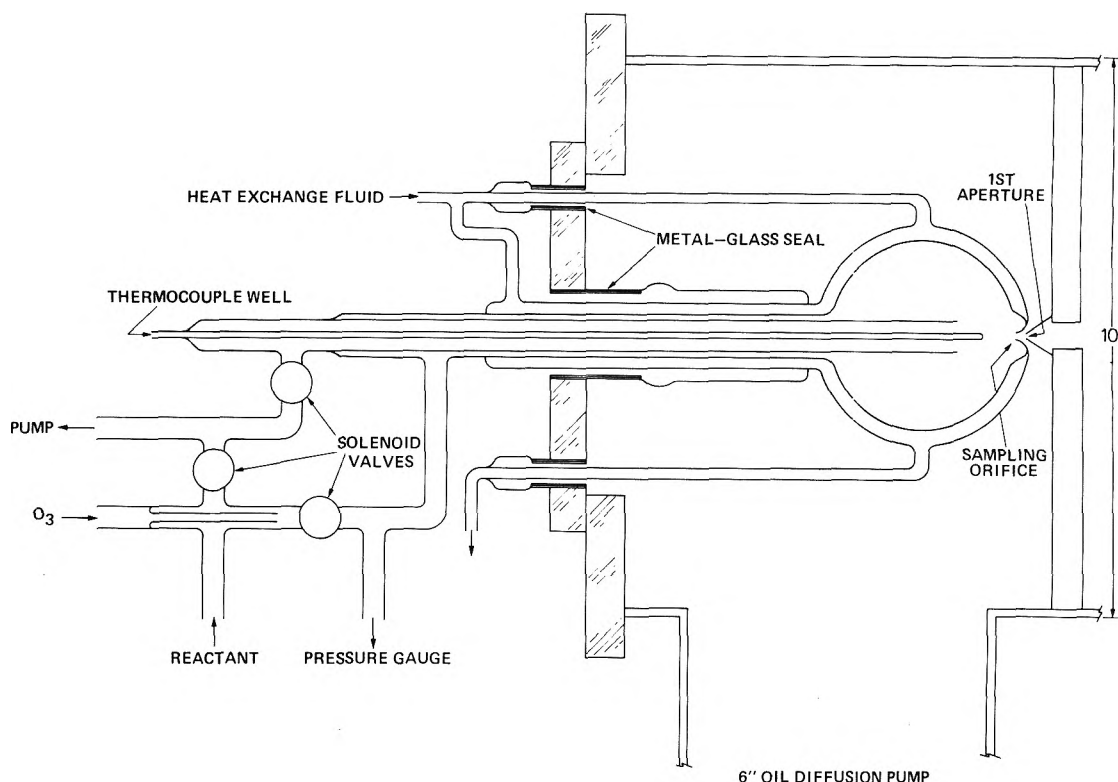


Figure 1. Stopped-flow reactor.

The second-order rate constants are shown in Arrhenius form in Figure 2. The error bars reflect both the uncertainty in the values from the least-squares standard error and an additional 5% uncertainty resulting from the calibration procedure. A least-squares fit of the data to the Arrhenius expression, weighted by the squares of the relative uncertainties of the second-order rate constants, gave

$$k(\text{C}_2\text{H}_4) = (5.42 \pm 3.19) \times 10^9 \exp(-2557 \pm 167/T) \text{ cm}^3 \text{ mol}^{-1} \text{ sec}^{-1}$$

$$k(\text{C}_3\text{H}_6) = (3.70 \pm 1.42) \times 10^9 \exp(-1897 \pm 109/T) \text{ cm}^3 \text{ mol}^{-1} \text{ sec}^{-1}$$

All the data used in the determination of these rate constants were obtained in the presence of about 400 N m^{-2} of oxygen, which was used as the carrier gas. In most experiments the concentration of ozone was kept between about 1 and $2 \times 10^{-10} \text{ mol cm}^{-3}$ and the olefin concentration was varied. In the rate measurements at 332.4 K , however, measurements were made over a tenfold range of ozone concentrations. The first-order rate constants were found to be independent of ozone concentration.

In the initial studies on the kinetics of the olefin reactions in which argon was used as a carrier gas, we obtained results which were nonreproducible and led to rate constants much higher than those reported by other workers at room temperature and atmospheric pressure.¹ Since it is known^{5,6} that free radicals are products of ozone-olefin reactions at low pressures, it seemed likely that secondary reactions of free radicals and ozone were the source of the anomalous results. In flow tube experiments under similar conditions, Niki⁷ has observed that oxygen has a strong effect on the course of the reaction. This suggested the possi-

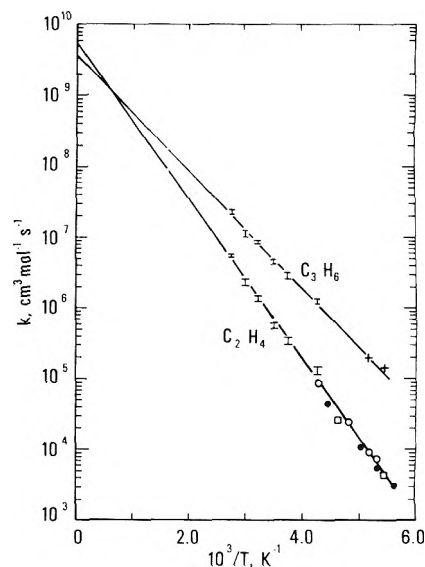


Figure 2. Arrhenius plot for the reactions of ozone with ethene and propene; data with error bars are from this work; other points are from ref 2: open circles, added oxygen; closed circles, inert gas, atmospheric pressure; open squares, inert gas, atmospheric pressure, and added oxygen; crosses, conditions not specified.

bility of scavenging the reactive free radicals with molecular oxygen.

Figure 3 shows the effect of added O_2 on the apparent second-order rate constant for the reaction of ozone with propene at room temperature. Similar results are found for other olefins. The effect of added O_2 is dramatic and appears to confirm the hypothesis that free radicals produced in the initial ozone-olefin reaction react rapidly with ozone. In the presence of excess O_2 , the radicals are scavenged and the true rate constant is obtained.

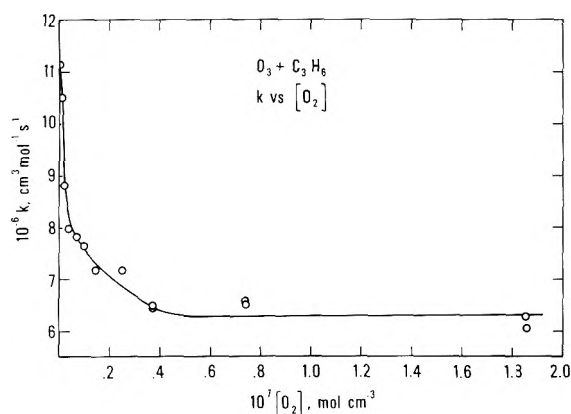


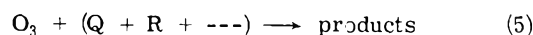
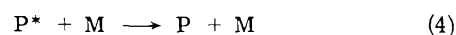
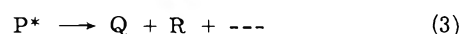
Figure 3. Effect of molecular oxygen on the apparent rate constant for the reaction of ozone with propene at 298 K and 450 N m^{-2} total pressure.

Discussion

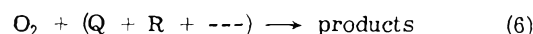
The results obtained in this work can be compared with those of DeMore,² which are shown in Figure 2. In the work of DeMore, the reactions were carried out in an 86-cm^3 cell, following the ozone concentration by absorption at 253.7 nm . Measurements were made with added inert gases or O_2 at total pressure in excess of atmospheric or at lower total pressures ($1.3\text{--}4 \text{ kN m}^{-2}$) with added O_2 . As can be seen from Figure 2, our Arrhenius lines fit the data of DeMore very closely. Recent measurements by Stedman, *et al.*,¹ at room temperature and atmospheric pressure (with and without O_2) in which the ozone decay was monitored using a chemiluminescence ozone detector also give results in good agreement with the present values. Thus, Stedman, *et al.*, reported $k(C_2H_4) = 9.34 \times 10^5 \text{ cm}^3 \text{ mol}^{-1} \text{ sec}^{-1}$ and $k(C_3H_6) = 7.53 \times 10^6 \text{ cm}^3 \text{ mol}^{-1} \text{ sec}^{-1}$ while we calculate from our Arrhenius expression $k(C_2H_4) = 1.02 \times 10^6 \text{ cm}^3 \text{ mol}^{-1} \text{ sec}^{-1}$ and $k(C_3H_6) = 6.36 \times 10^6 \text{ cm}^3 \text{ mol}^{-1} \text{ sec}^{-1}$.

The agreement in all cases is close and strongly supports our interpretation of the role of molecular oxygen at low pressures. These observations, together with the observations of other workers that O_2 has no effect on the rate constant for ozone loss at atmospheric pressure, suggest the

general mechanism for these reactions

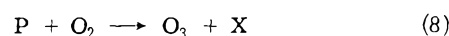
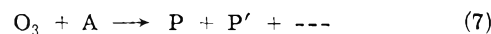


where P^* is not necessarily the initially formed adduct but could be formed by its subsequent rearrangement. At low pressures reaction 3 is favored followed by reaction 5. At high pressures reaction 4 is favored and reaction 3 and 5 are unimportant. With added O_2 at low pressures



and again reaction 5 is unimportant.

An alternative explanation for the reduction of the rate constant with added O_2 is



where P is an oxygen-containing free radical.

However, this mechanism is incompatible with the observations of Wu, *et al.*,¹ which showed that the stoichiometry of the reactions at atmospheric pressure with respect to reactant consumption was 1:1 with or without O_2 . Also as noted above the rate constants are unaffected by O_2 . Thus reaction 8 is very unlikely.

Acknowledgments. This work was supported in part by the Climatic Impact Assessment Program, Office of the Secretary, U. S. Department of Transportation, and the Measures for Air Quality Program, National Bureau of Standards.

References and Notes

- (1) D. H. Stedman, C. H. Wu, and H. Niki, *J. Phys. Chem.*, **77**, 2511 (1973).
- (2) W. B. DeMore, *Int. J. Chem. Kinet.*, **1**, 209 (1969).
- (3) R. E. Huie and J. T. Herron, *Chem. Phys. Lett.*, **27**, 411 (1974).
- (4) J. T. Herron and R. E. Huie, *Int. J. Mass Spectrom. Ion Phys.*, in press.
- (5) B. E. Saltzman, *Ind. Eng. Chem.*, **50**, 677 (1958).
- (6) R. Atkinson, B. J. Finlayson, and J. N. Pitts, Jr., *J. Amer. Chem. Soc.*, **95**, 7592 (1973).
- (7) H. Niki, private communication, 1974.

Pulse Radiolytic Investigations of OHCH₂O₂ RadicalsJoseph Rabani,*¹ Dina Klug-Roth,²¹Department of Physical Chemistry, The Hebrew University, Jerusalem 91000, Israel

and Arnim Henglein

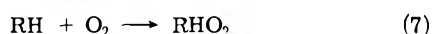
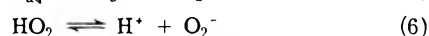
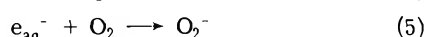
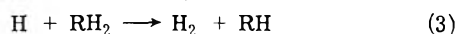
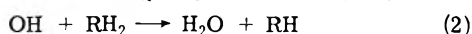
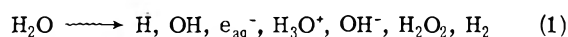
²Bereich Strahlenchemie, Hahn-Meitner-Institut, 1 Berlin 39, West Germany (Received March 13, 1974)

Publication costs assisted by the Hahn-Meitner-Institut

Methanol radicals CH₂OH react with oxygen and produce peroxy radicals O₂CH₂OH, $k_{\text{CH}_2\text{OH}+\text{O}_2} = (4.2 \pm 0.5) \times 10^9 \text{ M}^{-1} \text{ sec}^{-1}$. O₂CH₂OH ionizes to form O₂CH₂O⁻ which quickly decomposes to CH₂O and O₂⁻. The ionization is catalyzed by OH⁻ and by HPO₄²⁻. $k_{\text{O}_2\text{CH}_2\text{OH}+\text{OH}^-} = (1.8 \pm 0.9) \times 10^{10} \text{ M}^{-1} \text{ sec}^{-1}$ and $k_{\text{O}_2\text{CH}_2\text{OH}+\text{HPO}_4^{2-}} \approx 2 \times 10^6 \text{ M}^{-1} \text{ sec}^{-1}$ were measured. The spontaneous ionization rate constant $k_{\text{O}_2\text{CH}_2\text{OH} \rightarrow \text{O}_2\text{CH}_2\text{O}^- + \text{H}^+} < 3 \text{ sec}^{-1}$ was estimated. The pK of O₂CH₂OH was estimated to be higher than 6, and probably >8.8. Previous reports of more accurate determinations of pK values of peroxy radicals should be reconsidered, in view of the possible instability of the basic form of the peroxy radicals. The absorption spectrum of O₂CH₂OH was determined. $\epsilon_{1070 \text{ M}^{-1} \text{ cm}^{-1}}$ was measured at 248 nm. At relatively high pulse intensities, formation of O₂⁻ from O₂CH₂OH is inhibited, and a second-order process which competes with the unimolecular formation of O₂⁻ from O₂CH₂O⁻ is proposed.

Introduction

The method of pulse radiolysis has been extensively used to study the mechanism of reactions of peroxy radicals.³⁻¹⁰ The superoxide radicals HO₂ and O₂⁻ are produced by the reduction of oxygen. H atoms,⁴ e_{aq}⁻,³ and CO₂⁻^{5,11} have been found so far to reduce oxygen and to produce a superoxide radical. Many organic free radicals were found to produce addition products with oxygen.^{6-10,12} Thus, the general reaction sequence for radiation-induced peroxy radical formation in O₂-containing solutions, in the absence of electron scavengers, is represented by eq 1-7. RH₂ repre-



sents organic compounds which might be dehydrogenated by H atoms and OH radicals (alcohols, aldehydes, chloral hydrate, etc.).

The fate of the organic peroxy radicals is not fully understood. Thus, peroxy radicals from alcohols were reported to decay *via* a bimolecular process.^{6a} The products were assumed to be hydrotetroxides^{6a} or tetroxides.¹² It has been suggested that in some cases hydrotetroxides may be strongly dissociated into HO₂.⁸ However, the exact nature of the products of the bimolecular decay process of peroxy radicals is still a matter for speculation.

The effect of pH on the optical absorbance and decay kinetics shows, in several instances, rather a great complexity. While peroxy radicals from cyclohexane^{6a} and from diethyl ether^{6a} do not show acid-base properties, peroxy radicals from alcohols,^{6,7} chloral hydrate,⁸ formaldehyde,¹⁰ lactate,⁹ glycolate,⁹ lactamide,⁹ glycine anhydride,⁹ and *N*-

acetylglycylglycine⁹ were reported to ionize in the pH range 5-10.

To make things still more complicated, esr measurements suggested the formation of HO₂ radicals under conditions where evidence for organic peroxy radicals was also presented.³

In view of this, we felt that a systematic investigation of peroxy radicals would be desirable. In a previous paper,¹³ the formation and decay of peroxycyclopentyl radicals, C₅H₉O₂, have been reported. These radicals, formed from C₅H₉, were shown to be stable with respect to decomposition to O₂⁻. Their investigation demonstrated the possibility of relying on careful optical methods, so as to discriminate between O₂⁻ and organic peroxy radicals.

In the present paper we report a similar research on HOCH₂O₂ radicals. We have carefully investigated their absorption spectrum and compared it to the spectrum of O₂⁻, above the pK of HO₂ (pK = 4.8^{4,5}). At low pulse intensities, and in the presence of a base, we could measure the rate of the ionic dissociation of HOCH₂O₂ to ⁻OCH₂O₂. Finally, spectroscopic and kinetic measurements indicate that ⁻OCH₂O₂ quickly decomposes to yield O₂⁻.

Experimental Section

The linear accelerators, at the Hahn-Meitner-Institut (HMI), Berlin, and at The Hebrew University, Jerusalem, have been employed. The operational conditions were similar to those prevailing in previous works.^{5,13} Water-cooled Xe-Hg Osram lamps, 150 W (Jerusalem) and 450 W (Berlin), have been used. Scattered light was zero (Carl Zeiss M4QIII prism monochromator, Berlin) or less than 3% (Bausch & Lomb monochromator, Jerusalem). The Bausch & Lomb monochromator was used for the kinetic work only. Oscilloscopes, Tektronix 556 and 549 (memory), were employed, with W or 1A5 plug-in units. Triply distilled water was used for all the experiments. All chemicals were of high purity and used as received. All the solutions were saturated with gas mixtures of N₂O-O₂. The temperature was 22 ± 1°.

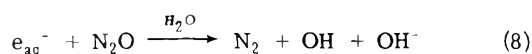
TABLE I: Ratios of Absorbance Changes at Various Wavelengths^a

λ , nm	$10^3 D_\infty^b$	$10^3 D_0^c$	D_0/D_0^{248d}	$D_\infty^\lambda/D_\infty^{248d}$	$D_{O_2^-}^\lambda/D_{O_2^-}^{248e}$
240	11.9	7.7	1.08	1.02	1.05
248	11.7	7.1	1.00	1.00	1.00
260	9.4	5.2	0.73	0.80	0.79
280	5.0	3.38	0.48	0.43	0.44
290	3.10	2.75	0.39	0.27	0.28
300	1.84	1.60	0.225	0.157	0.155

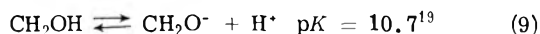
^a Conditions as in Figure 1. ^b Absorbance change after 150 μ sec. ^c Absorbance change extrapolated to the end of the electron pulse. ^d D^λ is the absorbance change at wavelength λ (nm). ^e Measured in formate solutions (this work), under the conditions of Figure 1 (10 mM formate instead of the methanol).

Results and Discussion

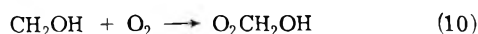
When an aqueous solution of $>0.05 M$ methanol is pulse irradiated, OH radicals react with methanol within less than 1 μ sec, according to reaction 2 ($k_2 = 5 \times 10^8 M^{-1} \text{sec}^{-1}$ for methanol¹⁴). When N_2O is also present, e_{aq}^- is efficiently converted into OH, according to reaction 8¹⁵ ($k_8^{16} =$



$8.7 \times 10^9 M^{-1} \text{sec}^{-1}$). H atoms react with O_2 under our conditions ($k_4^{17} = 2 \times 10^{10} M^{-1} \text{sec}^{-1}$ and $k_3^{18} = 2 \times 10^6 M^{-1} \text{sec}^{-1}$ for methanol). Thus, as a result of an electron pulse, CH_2OH and O_2^- radicals are produced within 1 μ sec, under our conditions, with a ratio 6:1. O_2^- is produced largely from reaction 4 followed by reaction 6 and partially by reaction 5 in competition with reaction 8. CH_2OH radicals are known to ionize according to equilibrium 9 and are ex-



pected to react with O_2 according to reaction 6,7 10. In Fig-



ure 1 we present the absorption spectrum of O_2CH_2OH , extrapolated to the end of the electron pulse. A different spectrum is observed 150 μ sec after the electron pulse and is also shown in Figure 1. This spectrum is practically identical with the known spectrum⁵ of O_2^- . The absorption observed in similar solutions containing 10 mM formate instead of methanol gave optical densities at 248 nm which were higher by 10%, as compared with the optical densities obtained after 150 μ sec in methanolic solutions. Despite this fact we consider the absorption after 150 μ sec observed in methanol solutions, identical with that of O_2^- radical ions. The small deviations (Figure 1) and the 10% difference are well within experimental error considering the fact that the work was carried out with two different monochromators and that the yields of O_2^- in solutions of formate might be somewhat different from the yield observed after 150 μ sec in the solutions of methanol. (Only 93% of the OH radicals react with methanol according to reaction 2 to produce CH_2OH . Seven per cent of the OH radicals produce CH_3O radicals²⁰ which perhaps do not contribute to the formation of O_2^- .)

Figure 1 leaves no doubt that the product of reaction 10 is different from O_2^- . Several measurements at some chosen wavelengths were carried out with particular accuracy and are summarized in Table I. This demonstrates, again, the formation of a product other than O_2^- at the end of reaction 10 which is presumably converted to O_2^- after 150

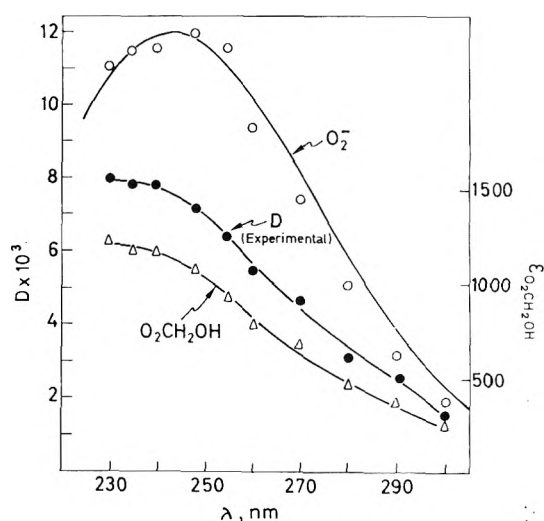
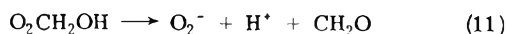


Figure 1. Optical absorption of O_2CH_2OH saturated with 29% O_2 and 71% N_2O (volume), at pH 8.0 ($6.3 \times 10^{-3} M$ phosphate buffer), $3 \times 10^{-2} M$ methanol, 22°, total radical concentration $1.65 \times 10^{-6} M$ /pulse, and light path 4 cm. Each point is an average of three to six determinations. ● shows the experimental absorbance, extrapolated to the end of the electron pulse. Δ shows the absorption of O_2CH_2OH , corrected for O_2^- (14% of the total radical concentration). The scale for $\epsilon_{O_2CH_2OH}$ was calculated assuming that 10% of the OH radicals produced CH_3O ,²⁰ the absorbance of which was neglected. ○ shows the optical absorption after 150 μ sec. The solid line represents the expected absorbance of O_2^- calculated from ref 5, neglecting the possible absorbance of CH_3O .²⁰

μ sec. The kinetics of the absorbance increase are shown in Figure 2. Under the conditions of Figure 2, the buildup of optical absorbance is first order and the overall process is proposed to be (11). As will be seen later, O_2CH_2OH de-



composes only slowly, if at all, to yield O_2^- directly. The O_2^- is actually produced from the ionized form of O_2CH_2OH , namely, $O_2CH_2O^-$. We will therefore refer to reaction 11 as "11" if the overall process of O_2 formation from O_2CH_2OH (which includes reactions 12 and 13) and as 11 if direct formation of O_2^- from the acid form of the radical is meant.

The Effect of pH. The effect of pH on the optical density extrapolated to the end of the electron pulse (D_0) and on the optical density observed at the end of process "11" (D_∞) is presented in Figure 3. D_0 shows only a small dependence, if any, on pH in the range 5.3–8.8. D_0 equals the absorbance of O_2CH_2OH plus the absorbance of O_2^- which is formed by (4) (followed by (6)) and (5) (in competition

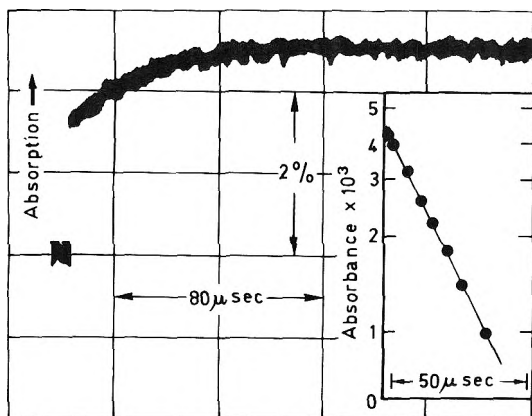


Figure 2. Oscilloscope trace representing the formation of O_2^- from $\text{O}_2\text{CH}_2\text{OH}$. Conditions are as in Figure 1; 248 nm.

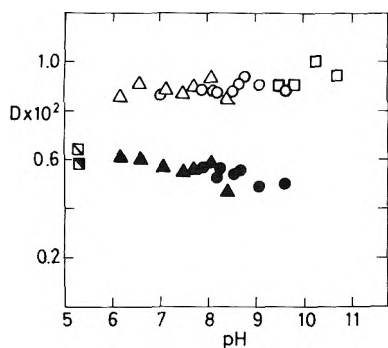


Figure 3. Effect of pH on D_0 and D_∞ at 248 nm D_0 and D_∞ measured or normalized to light path 4 cm; 0.1 M methanol equilibrated with 30% O_2 and 70% N_2O (by volume); open circles, triangles, and squares signify D_∞ ; closed or half-closed circles, triangles, and squares signify D_0 ; ● and ○, $[\text{HPO}_4^{2-}] + [\text{H}_2\text{PO}_4^-] = 3.5 \text{ mM}$; ▲ and △, $[\text{HPO}_4^{2-}] + [\text{H}_2\text{PO}_4^-] = 10 \text{ mM}$; □, no phosphate present (NaOH used for the adjustment of pH); ◻ and ◻, 18 mM $[\text{HPO}_4^{2-}] + [\text{H}_2\text{PO}_4^-]$.

with (8)). Above pH 8.8, process "11" becomes too fast and its time separation from reactions 2 and 7 is not good. Although it is still possible to carry out kinetic measurements for the rate of process "11," it is difficult to analyze quantitatively the significance of D_0 above pH 8.8. These results suggest that $\text{O}_2\text{CH}_2\text{OH}$ is not appreciably ionized below pH 8.8.

D_∞ depends little, if at all, on the pH in the range 6.6–10.7, under the conditions of Figure 3. Below pH 6.6, a significant decrease of D_∞ is observed. We interpret this as due to the inefficiency of process "11" at low pH's (this will be discussed later). The ratio D_∞/D_0 decreases at relatively high pulse intensities and at relatively low alkali (OH^- and HPO_4^{2-}) concentrations. The lowest pH at which D_∞ is still unchanged (6.6 in Figure 3) depends on $[\text{HPO}_4^{2-}]$ and on the pulse intensity. Under the conditions of Figure 3 we may assume that process "11" accounts for the fate of the great majority of the $\text{O}_2\text{CH}_2\text{OH}$ radicals.

Kinetic Measurements. Let us define " k_{11} " = $(d/dt) \ln(D_\infty - D_t)$. D_t is the optical density at time t . The effect of pH on " k_{11} ," at various phosphate concentrations, is presented in Figure 4. At a relatively low HPO_4^{2-} concentration, $\log "k_{11}"$ increases linearly with pH in the range 8–10, with a slope of 1. At higher [phosphate] there is a smaller effect of pH.

The results of Figure 4 can be explained if we assume that $\text{O}_2\text{CH}_2\text{OH}$ ionizes, at least in part, to form $\text{O}_2\text{CH}_2\text{O}^-$,

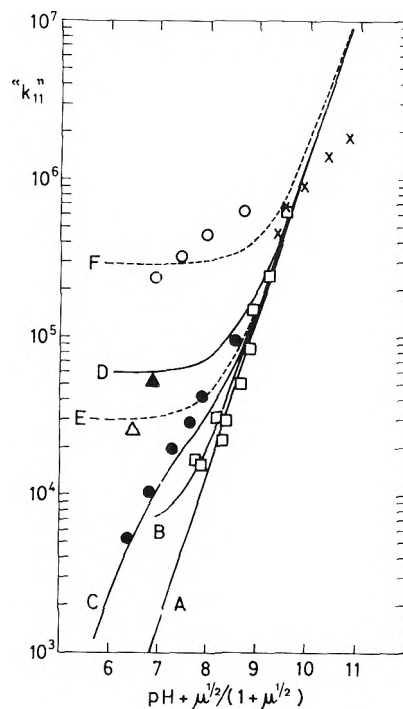
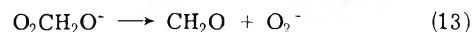
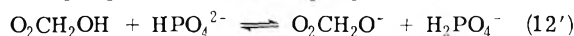
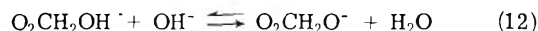


Figure 4. Effect of pH on " k_{11} ," with 30% O_2 and 70% N_2O (volume) and 0.1 M methanol; NaClO_4 was added whenever a constant ionic strength was kept: ●, $1.0 \times 10^{-2} \text{ M}$ ($\text{HPO}_4^{2-} + \text{H}_2\text{PO}_4^-$), ionic strength 0.03; □, $3.0 \times 10^{-3} \text{ M}$ HPO_4^{2-} , ionic strength 0.009; X, no phosphate present, ionic strength 0.01; O, 0.3 M HPO_4^{2-} , ionic strength 1.2; △, 0.03 M HPO_4^{2-} , ionic strength 1.2; ▲, 0.03 M HPO_4^{2-} , ionic strength 0.12. All curves were calculated using $k_{12} = 1.8 \times 10^{10} \text{ M}^{-1} \text{ sec}^{-1}$; solid curves, $k_{12}' = 2 \times 10^6 \text{ M}^{-1} \text{ sec}^{-1}$; dotted curves, $k_{12}' = 1 \times 10^6 \text{ M}^{-1} \text{ sec}^{-1}$; A, for solutions containing no phosphate ions; B, for $3 \times 10^{-3} \text{ M}$ HPO_4^{2-} ; C, for $1 \times 10^{-2} \text{ M}$ ($\text{HPO}_4^{2-} + \text{H}_2\text{PO}_4^-$), taking $\text{p}K_{\text{H}_2\text{PO}_4^-} = 6.8$ at ionic strength 0.03 M; D, for $3 \times 10^{-2} \text{ M}$ HPO_4^{2-} ; E, for $3 \times 10^{-2} \text{ M}$ HPO_4^{2-} , $k_{12}' = 1 \times 10^6 \text{ M}^{-1} \text{ sec}^{-1}$ used; F, for 0.3 M HPO_4^{2-} , $k_{12}' = 1 \times 10^6 \text{ M}^{-1} \text{ sec}^{-1}$ used.

which is able to produce O_2^- much faster than does $\text{O}_2\text{CH}_2\text{OH}$ (reactions 12 or 12' and 13). In fact, we find no



evidence for direct formation of O_2^- (or HO_2) from $\text{O}_2\text{CH}_2\text{OH}$ ($k_{11} < 10,000 \text{ sec}^{-1}$). Assuming that reaction 13 is much faster than (–12), (–12'), (12), or (12') (this will be discussed later), one obtains eq 14. The agreement of eq 14

$$"k_{11}" = k_{12}[\text{OH}^-] + k_{12}'[\text{HPO}_4^{2-}] \quad (14)$$

with the experimental data is demonstrated in Figure 4. The solid lines have been calculated taking $k_{12} = 1.8 \times 10^{10} \text{ M}^{-1} \text{ sec}^{-1}$ and $k_{12}' = 2 \times 10^6 \text{ M}^{-1} \text{ sec}^{-1}$. The pH of each of the solutions was measured, and pOH was calculated from eq 15, where μ is the ionic strength. The agreement of the

$$\text{pOH} = 14.1 - \text{pH} - \mu^{0.5}/(1 + \mu^{0.5}) \quad (15)$$

calculated $\log "k_{11}"$ vs. pOH with the experimental data supports the proposed mechanism. The deviations observed above pH 10 are due to the high rate of process "11" at high pH. Equation 14 is valid as long as process "11" is considerably slower than reaction 7. This is not the case in the higher pH range. In fact, at pH 10.7, reaction 7 is expected to be much slower than process "11"; i.e., " k_{11} "

TABLE II: Effect of pH, $[\text{HPO}_4^{2-}]$, and Pulse Intensity on D_∞/D_0 at 248 nm

pH	$[\text{HPO}_4^{2-}]$, M	Total [radicals] ^a $\times 10^6$, M	D_∞/D_0
8.25	3×10^{-3}	2.02	1.7 ^b
8.25	3×10^{-3}	5.13	1.6 ^b
8.25	3×10^{-3}	14.3	1.4 ^b
8.0	3×10^{-3}	1.48	1.5 ^b
8.0	3×10^{-3}	6.32	1.3 ^b
8.0	3×10^{-3}	17.1	1.0 ^b
7.5	5×10^{-3}	1.23	1.8 ^{c,d}
7.5	5×10^{-3}	5.15	1.6 ^{c,d}
7.5	5×10^{-3}	8.4	1.4 ^{c,d}
7.5	5×10^{-3}	12.8	1.2 ^{c,d}
7.5	5×10^{-3}	25.5	1.1 ^{c,d}
6.35	2×10^{-3}	0.57	1.4 ^c
6.35	2×10^{-3}	2.0	1.2 ^c
6.35	2×10^{-3}	8.0	0.9 ^c
6.25	3×10^{-4}	1.21	1.0 ^c
6.25	1.7×10^{-3}	1.34	1.3 ^c
6.0	3×10^{-3}	2.0	1.1 ^b
6.0	3×10^{-3}	6.0	0.7 ^b
6.0	3×10^{-3}	15.4	0.5 ^b
6.0	3×10^{-2}	2.0	1.6 ^b
6.0	3×10^{-2}	5.2	1.4 ^b
6.0	3×10^{-2}	14.3	1.1 ^b

^a $[\text{O}_2\text{CH}_2\text{OH}]_0$ (76 mol %) + $[\text{O}_2^-]_0$ (14 mol %) + $[\text{CH}_3\text{O}]_0$ (10 mol %); 0.1 M methanol unless otherwise stated; 30% (volume) O_2 and 70% (volume) N_2O . ^b At 256 nm, $\epsilon_{\text{O}_2^-} = 1800 \text{ M}^{-1} \text{ cm}^{-1}$, $\epsilon_{\text{O}_2\text{CH}_2\text{OH}} = 920 \text{ M}^{-1} \text{ cm}^{-1}$, and $\epsilon_{\text{CH}_3\text{O}}$ neglected. ^c At 248 nm, $\epsilon_{\text{O}_2^-} = 2000 \text{ M}^{-1} \text{ cm}^{-1}$, $\epsilon_{\text{O}_2\text{CH}_2\text{OH}} = 1070 \text{ M}^{-1} \text{ cm}^{-1}$, and $\epsilon_{\text{CH}_3\text{O}}$ neglected. ^d Using 0.05 M methanol.

seemingly becomes equal to $k_7[\text{O}_2]$. This was confirmed by the use of two different $[\text{O}_2]$'s, 4×10^{-4} and $1.3 \times 10^{-3} \text{ M}$, showing that under these conditions " k_{11} " is proportional to $[\text{O}_2]$. From these results, we find $k_7 = (4.2 \pm 0.5) \times 10^9 \text{ M}^{-1} \text{ sec}^{-1}$ for the reaction of methanol radicals with O_2 at pH 10.7. As CH_2OH radicals have $\text{p}K = 10.7$,¹⁹ reaction 7 at this pH may involve both CH_2OH and CH_2O^- . Adams and Willson²¹ measured $k_{10} = 4.8 \times 10^9 \text{ M}^{-1} \text{ sec}^{-1}$, which is similar to our value of k_7 . This is perhaps due to similar reactivities of CH_2OH and CH_2O^- toward O_2 . In the calculation of the various curves (Figure 4), it was assumed that H_2PO_4^- ions are not reactive. The agreement, in particular of curve C, with the data at low pH's, justifies that assumption. We used $\text{p}K_{\text{H}_2\text{PO}_4^-} = 6.8$ for these calculations, a value which we determined under our conditions.

The open circles and triangles were measured at ionic strength 1.2 M and in the presence of 0.9–1.2 N Na^+ ions. Under such conditions, HPO_4^{2-} associates with Na^+ ions.²² Under these circumstances, the disagreement with the calculated curves is not surprising. The effect of such high ionic strength on the ionization of water may be considerably different from that expressed by the term $\mu^{1/2}/(1 + \mu^{1/2})$. The increase of " k_{11} " with pH in 0.3 M HPO_4^{2-} solutions (open circles, Figure 4) indicates that reaction 12 cannot be neglected under these conditions. Probably the ionization of water supplies more OH^- than can be calculated from eq 15. Note that the dotted lines E and F (Figure 4) are calculated with $k_{12'} = 1 \times 10^6 \text{ M}^{-1} \text{ sec}^{-1}$. The association of HPO_4^{2-} with Na^+ may decrease $k_{12'}$.

It might be argued that reactions 12, 12', and 16 are fast and that equilibrium 12, 12', or 16 is established before O_2^-

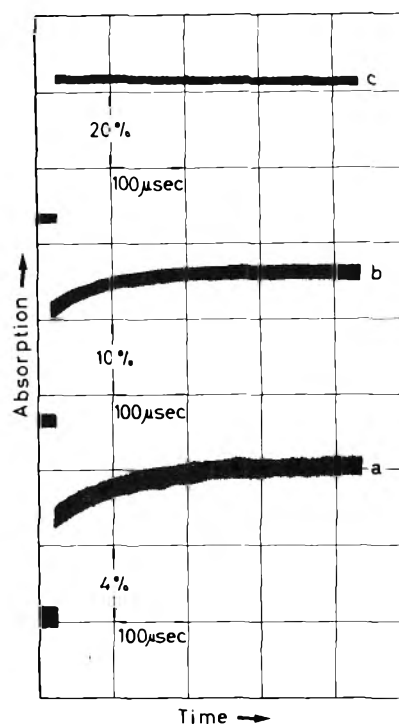
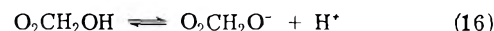


Figure 5. Oscilloscope traces representing the buildup of O_2^- absorption at various pulse intensities for solutions containing 0.1 M methanol and 30% O_2 and 70% N_2O (volume); pH 8.0, $[\text{HPO}_4^{2-}] = 3 \times 10^{-3} \text{ M}$, $[\text{H}_2\text{PO}_4^-] = 4.8 \times 10^{-4} \text{ M}$, light path 12.3 cm, 17.5°, λ 256 nm: (a) $[\text{O}_2\text{CH}_2\text{OH}] = 1.52 \times 10^{-6} \text{ M}$ initially formed, $[\text{O}_2^-] = 2.8 \times 10^{-7} \text{ M}$ initially formed; (b) $[\text{O}_2\text{CH}_2\text{OH}] = 4.7 \times 10^{-6} \text{ M}$ initially formed, $[\text{O}_2^-] = 8.7 \times 10^{-7} \text{ M}$ initially formed; (c) $[\text{O}_2\text{CH}_2\text{OH}] = 1.3 \times 10^{-5} \text{ M}$ initially formed, $[\text{O}_2^-] = 2.4 \times 10^{-6} \text{ M}$ initially formed. In the calculation of initial radical concentrations we used $\epsilon_{\text{O}_2\text{CH}_2\text{OH}} = 920 \text{ M}^{-1} \text{ cm}^{-1}$ and $\epsilon_{\text{O}_2^-} = 1800 \text{ M}^{-1} \text{ cm}^{-1}$ (14% of the radicals were O_2^- , 76% were $\text{O}_2\text{CH}_2\text{OH}$, and 10% were CH_3O —the absorption of which was neglected).



starts to build up according to reaction 13. Such an interpretation requires that equilibria 12, 12', and 16 are shifted to the left under the conditions of our experiments. The kinetic treatment leads to a linear dependency of $\log "k_{11}"$ on pOH with a slope of 1, which is observed in the experiments at low $[\text{HPO}_4^{2-}]$, when $[\text{OH}^-]$ is not too high (see Figure 4).

It is not difficult to rule out reaction 16 under our conditions. Reaction -16 is a typical protonation reaction, and one may assume $k_{-16} = (1-5) \times 10^{10} \text{ M}^{-1} \text{ sec}^{-1}$. In order that equilibrium 16 be shifted to the left under our conditions, $\text{p}K_{\text{O}_2\text{CH}_2\text{OH}} > 10$ must be assumed. This yields $k_{16} = K_{16}k_{-16} < 3 \text{ sec}^{-1}$. Since our measurements were carried out in the time range shorter than 1 msec, reaction 16 can be neglected under our conditions. The effect of $[\text{HPO}_4^{2-}]$ at the lower pH's shows that under these conditions, reaction 12' is the rate-determining step in the formation of O_2^- .

We cannot rule out the possibility that at a certain $[\text{OH}^-]$ and $[\text{HPO}_4^{2-}]$, reactions 12 and 12' may become fast enough so that reaction 13 may become rate determining in the formation of O_2^- . However, this does not occur under our conditions: the value of $k_{12'}$ obtained at high $[\text{HPO}_4^{2-}]$ is the same, within experimental error, as $k_{12'}$ values calculated from experiments at lower $[\text{HPO}_4^{2-}]$ (Figure 4). Deviations from line A (Figure 4) at high pH's, which might have been due to reaction 13 becoming rate determining,

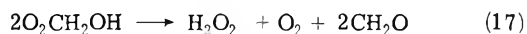
were shown to be due to the relative slowness of reaction 7. The results agree with a lower limit, $k_{13} > 10^7 \text{ sec}^{-1}$.

It is interesting to note that no accurate information about pK_{16} is obtained from Figure 4. As long as we may assume that reactions 12 and 12' are rate determining, any $pK_{16} > 6$ would be in agreement with our data. It cannot be less than 6; otherwise k_{16} can be shown to be higher than would be required by the slowness of O₂⁻ formation at pH ~6. It is of importance to note that all the results represented in Figure 4 were carried out under conditions where most, if not all, O₂CH₂OH radicals are eventually converted to O₂⁻ by process 11. This was tested for each of the experiments, by the comparison of D_{∞} with D_0 and with the absorbance observed in similar solutions containing formate ions instead of methanol.

We must assume relatively high errors in the determination of both k_{12} and k_{12}' , due to errors in the determination of pH and uncertainty in the ionic strength corrections. We consider $k_{12} = 1.8 \times 10^{10} \text{ M}^{-1} \text{ sec}^{-1}$ and $k_{12}' = 2 \times 10^6 \text{ M}^{-1} \text{ sec}^{-1}$ good to within a factor of 2. A factor of $\sim 10^4$ between k_{12} and k_{12}' is expected from the Brønsted equation for general basic catalysis.²³

The ratio $D_{\infty}^{248}/D_0^{248} = 1.6$ was determined at a relatively wide pH range, at low pulse intensities, such as used in Figure 4. The value 1.6 is a limiting value and is independent of [HPO₄²⁻] and of pulse intensity within some range. However, when the pH is below 6, the ratio $D_{\infty}^{248}/D_0^{248}$ decreases below 1.6. At sufficiently low pH, $D_{\infty}^{248}/D_0^{248} < 1$, namely, a decay of the initially formed absorbance is observed rather than a buildup. Under conditions where $D_{\infty}^{248}/D_0^{248} < 1.6$, the following effects were observed. (a) This ratio increased with pH at a constant [HPO₄²⁻] = $3 \times 10^{-3} \text{ M}$ and constant pulse intensity. (b) It increased with [HPO₄²⁻] at a constant pH and constant pulse intensity. (c) It decreased with the pulse intensity (up to a total of $1.5 \times 10^{-5} \text{ M}$ of radicals/pulse) at constant pH and [HPO₄²⁻], provided the pH was not above 8.5 and [HPO₄²⁻] was not above 30 mM. Typical results for the effect of pulse intensity are shown in Figure 5. The effect of pH and of [HPO₄²⁻] is demonstrated in Figure 3 and in Table II. The results show that process "11" has to compete with a second-order process, in which less O₂⁻ or no O₂⁻ whatsoever is produced. High [OH⁻] and [HPO₄²⁻] enhance process 11. High pulse intensities enhance the competing second-order process.

Second-order processes of peroxy radicals in acid solutions have been reported in several cases. It was shown that about one ion pair is formed during the second-order disappearance of two radicals.^{6a,8,10} No explanation which can satisfactorily account for all observed effects has as yet been given. A previous suggestion assuming formation of a hydrotetroxide from two peroxy radicals which is strongly dissociated in the O₄ chain cannot suit our present results.⁸ An alternative mechanism would be reaction 17 in competi-



tion with O₂⁻ formation either directly or indirectly (when OH⁻ or HPO₄²⁻ is present) from the peroxy radicals (process 11 or "11"). If k_{11} would be 5×10^3 – 10^4 sec^{-1} , reaction 11 could take place besides (17) and the rate of O₂⁻ build-up would essentially be determined by the rate of the disappearance of the radicals. More work is needed in order to test quantitatively this hypothesis in various systems.

Conclusions

The methanol radical CH₂OH reacts efficiently with O₂ and forms the peroxy radical O₂CH₂OH. This radical may ionize to O₂CH₂O⁻, which gives very quickly CH₂O and O₂⁻. The ionization is catalyzed by OH⁻ and by HPO₄²⁻. The radicals O₂CH₂OH as such seem to undergo, under our conditions, a bimolecular reaction rather than to produce O₂⁻ (or HO₂). Previous conclusions concerning the pK of O₂CH₂OH^{6,7} and other peroxy radicals⁹ may not be correct in view of the instability of O₂CH₂O⁻ and of similar radicals. A previous suggestion assuming strong homolysis in the O₄ chain of hydrotetroxides⁸ may not suit our results if an O₄ chain is formed in our system. More work is still called for on the fate of the bimolecular reaction products of O₂CH₂OH.

References and Notes

- (1) To whom correspondence should be addressed.
- (2) In part of the fulfillment of the requirements toward a Ph.D. degree at The Hebrew University.
- (3) G. Czapski, *Annu. Rev. Phys. Chem.*, **22**, 171 (1971).
- (4) J. Rabani and S. O. Nielsen, *J. Phys. Chem.*, **73**, 3736 (1969).
- (5) D. Behar, G. Czapski, L. M. Dorfman, J. Rabani, and H. A. Schwarz, *J. Phys. Chem.*, **74**, 3209 (1970).
- (6) (a) K. Stockhausen, A. Fojtik, and A. Henglein, *Ber. Bunsenges. Phys. Chem.*, **74**, 34 (1970); (b) M. Simic, P. Neta, and E. Hayon, *J. Phys. Chem.*, **73**, 3794 (1969).
- (7) M. Simic and E. Hayon, *Biochem. Biophys. Res. Commun.*, **50**, 364 (1973).
- (8) T. Eriksen, A. Henglein, and K. Stockhausen, *Trans. Faraday Soc.*, **69**, 337 (1973).
- (9) E. Hayon and M. Simic, *J. Amer. Chem. Soc.*, **95**, 6681 (1973).
- (10) K. Stockhausen and A. Henglein, *Ber. Bunsenges. Phys. Chem.*, **75**, 833 (1971).
- (11) A. Fojtik, G. Czapski, and A. Henglein, *J. Phys. Chem.*, **74**, 3204 (1970).
- (12) M. T. Downes and H. C. Sutton, *Trans. Faraday Soc.*, **69**, 263 (1973).
- (13) J. Rabani, M. Pick, and M. Simic, *J. Phys. Chem.*, **78**, 1049 (1974).
- (14) G. E. Adams, J. W. Boag, J. Currant, and B. D. Michael, "Pulse Radiolysis," M. Ebert, J. P. Keene, A. J. Swallow, and J. H. Baxendale, Ed., Academic Press, New York, N. Y., 1965, p 131.
- (15) F. S. Dainton and D. B. Peterson, *Nature (London)*, **186**, 878 (1960).
- (16) S. Gordon, E. J. Hart, M. S. Matheson, J. Rabani, and J. K. Thomas, *Discuss. Faraday Soc.*, **36**, 193 (1963).
- (17) H. Fricke and J. K. Thomas, *Radiat. Res. Suppl.*, **No. 4**, 35 (1964).
- (18) J. P. Sweet and J. K. Thomas, *J. Phys. Chem.*, **68**, 1363 (1964).
- (19) K. D. Asmus, A. Henglein, A. Wigger, and G. Beck, *Ber. Bunsenges. Phys. Chem.*, **70**, 756 (1966).
- (20) K. D. Asmus, H. Mockel, and A. Henglein, *J. Phys. Chem.*, **77**, 1218 (1973).
- (21) G. E. Adams and R. L. Willson, *Trans. Faraday Soc.*, **65**, 2981 (1969).
- (22) *Chem. Soc., Spec. Publ.*, **No. 17**, (1964).
- (23) R. P. Bell, "The Proton in Chemistry," Cornell University Press, Ithaca, N. Y., 1959.

Formation of Ions and Excited States in the Pulse Radiolysis of Benzonitrile

A. Kira and J. K. Thomas*

Department of Chemistry and the Radiation Laboratory,¹ University of Notre Dame, Notre Dame, Indiana 46556 (Received April 17, 1974)

Publication costs assisted by the U. S. Atomic Energy Commission

Transient ionic and excited species in liquid benzonitrile and solutions of solutes in benzonitrile were investigated using nanosecond pulse radiolysis. The radiolysis of several aromatic solutes gave rise to the cations of these solutes and the yields were determined to be 1.4 ions/100 eV. Anions of the solutes were also detected for all solutes apart from *trans*-stilbene. The effects of ammonia, sulfur hexafluoride, and nitrous oxide on the yield of ionic species suggest that the precursors of the solute ions are cations and anions of benzonitrile. Solute excited states are also observed, and the *G* values for the excited singlet and triplet states were determined to be 0.7 and 1.4, respectively. The mechanism of formation of the excited states is discussed.

Introduction

The radiolysis of liquid benzene gives rise to excited states with *G* values of 5.4–5.8/100 eV.^{2,3} The yield of observed ionic species is low, about 0.3 in pulse radiolysis experiments.⁴ High yields of excited states have been measured for toluene and several xylenes.² The exact mechanism of formation of the excited states has not been elucidated, although charge recombination and direct excitation by secondary electrons have been suggested. The yield of ionic species becomes more marked and the yield of excited states decreases in the radiolysis of some derivatives of benzene such as aniline⁵ and benzyl alcohol⁶ that contain polar groups. This suggests that in these compounds at least some of the excited states are formed *via* ionic processes, *i.e.*, by charge recombination. In order to investigate this possibility further, it is necessary to have further data on the relationship between the yields of ions and excited states in other polar arenes.

Benzonitrile is one of several compounds which may be used to study this problem, as prior work indicates that the pulse radiolysis of solutions of benzonitrile leads to the formation of both ions and excited states of solute molecules.^{7,8} The present study was undertaken to obtain quantitative data for the formation of transient ionic and excited species in the nanosecond pulse radiolysis of benzonitrile.

Experimental Section

The pulse radiolysis apparatus has been described in detail elsewhere.⁹ The samples were irradiated with pulses of 5-, 10-, and 15-nsec duration with a total dose of about 10^{20} eV $l^{-1}/5$ -nsec pulse. *G* values were calculated based on the absorption of hydrated electrons, in the radiolysis of water where $G(e_{aq}^-) = 3.3$ and ϵ is $11,700 M^{-1} cm^{-1}$ at λ 6000 Å, for e_{aq}^- .

The benzonitrile used was Kodak's Spectrograde reagent; distillation of the benzonitrile did not affect the data. Zone-refined perylene was purchased from J. Hinton; pyrene was purified by chromatography; *trans*-stilbene was recrystallized twice; Kodak's 1,1'-binaphthyl and Fluka's 1,2-benzanthracene were used without further purification. Nitrous oxide, sulfur hexafluoride, and ammonia were obtained from Matheson Co. All samples were bubbled with

nitrogen except when saturated with the gases mentioned earlier.

Results

Short-Lived Transients in Benzonitrile. The pulse radiolysis of benzonitrile leads to the transitory spectra shown in Figure 1, two typical decay curves are also shown in the figure. A long-lived absorption dominates the spectrum below 400 nm; a typical decay of the species is shown at 360 nm. A short-lived absorption spreads over the 400–600-nm spectral region, and its decay half-life is 10 nsec, in agreement with that for emission decay which is observed below 380 nm. Another species with a half-life of 30 nsec shows an absorption from 380 to 520 nm. This latter species with a rapid decay dominates the decay curve at 475 nm as shown in Figure 1. If the sample is saturated with ammonia ($\sim 0.1 M$) the band at 390 nm is enhanced. Sulfur hexafluoride (SF_6) ($\sim 0.1 M$) has little effect on the spectrum apart from a slight enhancement of the absorption at 400 nm. These data are also shown in Figure 1.

Pulse Radiolysis of Benzonitrile. The radiolysis of benzonitrile in cyclohexane solution gives rise to the absorption spectrum shown in Figure 2 with a maximum at 400 nm. A similar absorption maximum is observed in the radiolysis of methanolic solutions of benzonitrile. The radiolysis of benzonitrile in benzene solution gives rise to a broad absorption above 400 nm with a half-life of 10 nsec and an absorption with a 450-nm peak and a half-life of 200 nsec. The lifetime of the benzonitrile emission in benzene solution agrees with that of the short-lived 10-nsec absorption. The 400- or 410-nm bands in cyclohexane or methanol solution, respectively, are identified as the benzonitrile anion, a decision which is based on previous studies.¹⁰ The long-lived species in benzene solution could be ascribed to the triplet state of benzonitrile, since excited states are the dominant species observed in the radiolysis of benzene solutions. The short-lived absorption in benzene solution may be assigned to the excited singlet state or excimer of benzonitrile.

The transient spectrum in pure benzonitrile is considered to consist of the above ionic and excited-state components. However, it is difficult to separate and assign each absorption. Another difficulty in the assignment arises

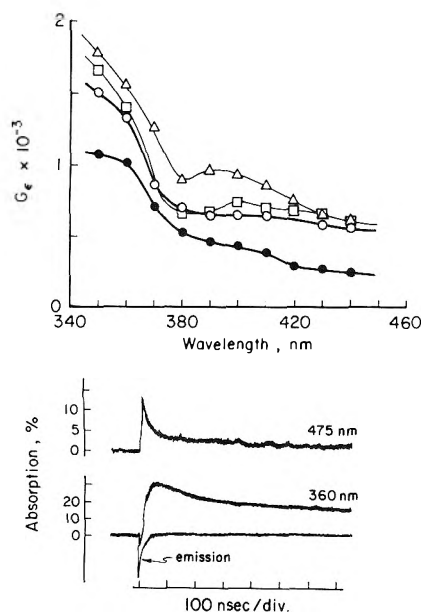


Figure 1. Upper part shows transient spectra in liquid benzonitrile: nitrogen bubbled, O; ammonia saturated, Δ ; SF₆ saturated, \square , at the end of pulse; nitrogen bubbled at 100 nsec, \bullet . Lower part shows oscilloscope traces for a nitrogen-bubbled sample.

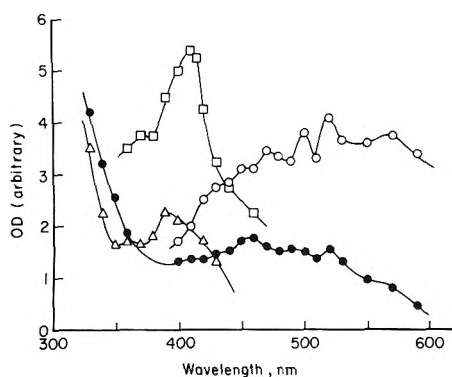


Figure 2. Transient spectra of benzonitrile solutions in benzene (O), cyclohexane (Δ), and methanol (\square) at the end of pulse and in benzene at 150 nsec (\bullet).

from the possibility that aggregated ions may be formed in pure liquid benzonitrile.

Formation of Solute Ions. Transitory spectra are observed in the pulse radiolysis of perylene, *trans*-stilbene, anthracene, pyrene, and 1,2-benzanthracene in benzonitrile solution and are shown in Figures 3–5.

Solutions of Perylene. In solutions of perylene, saturation with SF₆ removes an absorption band at 580 nm while a 545-nm peak remains. Nitrous oxide (N₂O) ($\sim 0.1 M$) does not affect the spectrum; while ammonia intensifies the 580-nm band. These results are consistent with the previous assignment^{11,12} that the maxima at 550 and 580 nm are due to the perylene cation and anion, respectively.

Solutions of Anthracene. In the radiolysis of anthracene in benzonitrile, ammonia slightly enhances the absorption near 660 nm and depresses a 740-nm peak due to the anthracene cation. This result indicates that the anthracene anion is also produced in the radiolysis of benzonitrile solutions, contrary to the previous report that only the anthracene cation was observed.⁸

Solutions of Pyrene. A 490-nm absorption is observed in

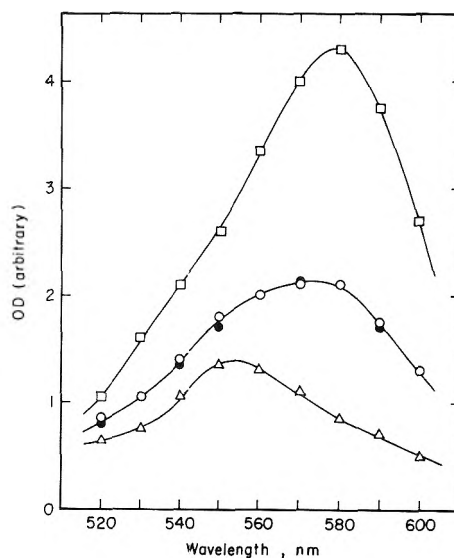


Figure 3. Transient spectra of perylene solutions in benzonitrile: nitrogen bubbled (300 nsec), O; N₂O saturated (300 nsec), \bullet ; SF₆ saturated (800 nsec), Δ ; ammonia saturated (800 nsec), \square . Perylene concentrations are 0.34–0.37 mM.

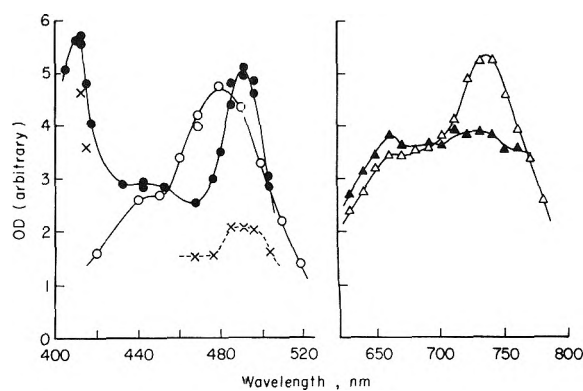


Figure 4. Transient spectra for aromatic solutes in benzonitrile: pyrene (10 mM) in nitrogen-bubbled, \bullet , and SF₆-saturated, X, solutions; *trans*-stilbene (10 mM) in nitrogen-bubbled solution, O; anthracene (10 mM) in nitrogen-bubbled, Δ , and ammonia-saturated, \blacktriangle , solutions.

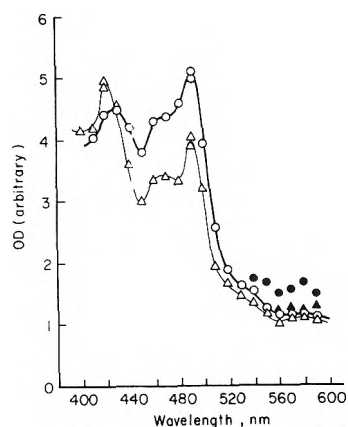


Figure 5. Transient spectra in 30 mM 1,2-benzanthracene solution: nitrogen bubbled, O, \bullet ; ammonia saturated, Δ , \blacktriangle . Open marks stand for 150 nsec and filled ones for the end of pulse.

the radiolysis of pyrene in benzonitrile and is attributed to the pyrene anion.^{11,12} The absorption of the pyrene cation

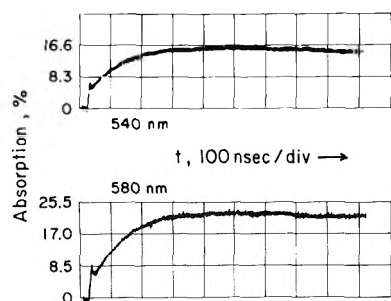


Figure 6. Growth in the transient absorption in a 3×10^{-4} M perylene solution.

which normally has a peak at 450 nm was not observed, probably because at this pyrene concentration the cation exists as the dimer cation.^{13,14}

Solutions of *trans*-Stilbene. The transient spectrum observed in the pulse radiolysis of *trans*-stilbene in benzonitrile is assigned to the *trans*-stilbene cation. This decision is based on previous assignments^{8,11} and the fact that the spectrum was not affected by oxygen and SF₆. The *trans*-stilbene anion which normally has an absorption peak at 480 nm was not detected.

Solutions of 1,2-Benzanthracene. The pulse radiolysis of 1,2-benzanthracene in benzonitrile gives rise to the spectrum shown in Figure 5. The 420-nm absorption peak is assigned to the anion,¹¹ as its intensity is increased by ammonia. The triplet state also has a peak at 430 nm which is about half as intense as the main triplet peak at 490 nm. Thus the observed 420–430-nm band is due to a composite spectrum of the anion and the triplet state of 1,2-benzanthracene. The absorption of the sample itself prohibited measurements below 400 nm, at wavelengths where the cation absorbs strongly.

The yield of the *trans*-stilbene cation extrapolated to infinite solute concentration was determined as 1.4 ions/100 eV; an extinction coefficient for the anion at λ 480 nm in acetone solution of 3.55×10^4 M⁻¹ cm⁻¹ was used.¹⁵ The yields of the anions at infinite solute concentration were estimated for pyrene and 1,2-benzanthracene using extinction coefficients of 5.1×10^4 M⁻¹ cm⁻¹ at λ 490 nm and 1.9×10^4 M⁻¹ cm⁻¹^{11b} at λ 430 nm, respectively. The 490-nm band of the pyrene anion is overlapped by the absorption of the dimer cation and the triplet state. If the optical density at 490 nm is regarded as being solely due to the anion, a G (anion) of 0.7 is obtained. The contribution of other species to the optical density at 490 nm is estimated to be about 30% based on the effect of SF₆ on reducing the anion yield. Accordingly, $G(\text{ion}) = 0.5$ is estimated. Similarly, a G value of ~ 0.5 is obtained for the 1,2-benzanthracene anion. Again the anion band at 420 nm is overlapped by the triplet absorption.

The curves in Figure 6 illustrate a growth of the ionic spectra at λ 580 and 540 nm after the irradiation pulse in perylene solutions. The rapid rise during the pulse is probably due to the transient from the solvent. Saturation with ammonia or SF₆ reduces the rate of the slow growth to about half that for the nitrogen-bubbled solution and retards the decay of the ions. The rate of growth in nitrogen-bubbled solutions was found to obey first-order kinetics. If the anion and cation have natural rate constants for decay of k_s^- and k_s^+ , respectively, and if the rate constants for reaction of the anion and cation with perylene are k^- and k^+ , respectively then

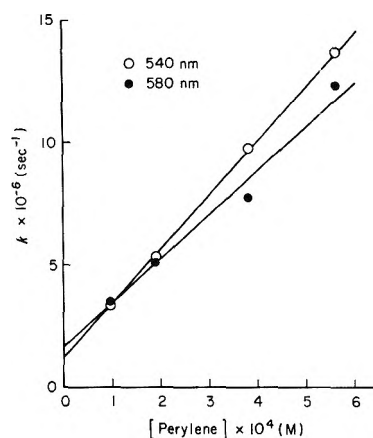


Figure 7. The change in the pseudo-first-order rate constant for the growth of perylene ions with the perylene concentration.

$$k = k_s^- + k^-[\text{perylene}]$$

and

$$k' = k_s^+ + k^+[\text{perylene}]$$

where k and k' are the observed total rates of reaction of the anion and cation, respectively. A plot of the pseudo-first-order rate constant *vs.* concentration is shown in Figure 7 and furnishes rate constants for scavenging of solvent ions by perylene, k^- and k^+ . And the rate constants for decay of the solvent ions where k_s^+ and k_s^- are the rate constants for decay of the cation C₆H₅CN⁺ and the anion C₆H₅CN⁻ of benzonitrile, respectively. Values of 2.2×10^{10} and 1.8×10^{10} M⁻¹ sec⁻¹ were obtained for k^+ and k^- for the cation and anion, respectively. Under experimental conditions where 7×10^{-5} M solvent ions were produced per pulse, values for k_s^- and k_s^+ of 1.3×10^6 and 1.7×10^6 sec⁻¹, were measured, respectively. The bimolecular rate constant for the neutralization of the cation and anion is then 2×10^{10} M⁻¹ sec⁻¹. This assumes that the ions do not also react in some other way.

Excited States of Solutes. Both excited singlet and triplet states of solutes are observed in the pulse radiolysis of solutions of benzonitrile. In the case of 1,2-benzanthracene, 1:2 BA shown in Figure 5, the 490- and 460-nm bands are assigned to the triplet state¹⁶ and the short-lived absorption in the 500–600-nm region is due to the excited singlet¹⁷ and/or the excimer. In a solution of 30 mM 1:2 BA, an emission was observed at wavelengths below 500 nm lasting for about 100 nsec after the pulse. The 420-nm absorption for pyrene in Figure 4 is assigned to the triplet state,¹⁶ a strong excimer emission was also observed in this solution.

The yields of triplet states of aromatic solutes were determined from the T–T absorption using extinction coefficients reported by Bensasson and Land.¹⁸ The changes in G values for the triplet states of 1,2-benzanthracene and naphthalene with concentration are shown in Figure 8. The yield at infinite solute concentration was obtained by extrapolating a Stern–Volmer plot of the data, a typical example of which is shown in Figure 9. G values thus extrapolated are 2.1 for 1,2-benzanthracene and naphthalene, 2.4 for 1,1'-binaphthyl, and 1.7 for pyrene. As shown in Figure 8, ammonia decreases the triplet yield, but N₂O and SF₆ do not affect the yield.

The yield of excited singlet states was determined by comparing the emission intensity for a solution of 1,1'-binaphthyl in benzonitrile with that in benzene, where a $G(\text{singlet}) = 1.6$ has been established.^{2–4} A Stern–Volmer

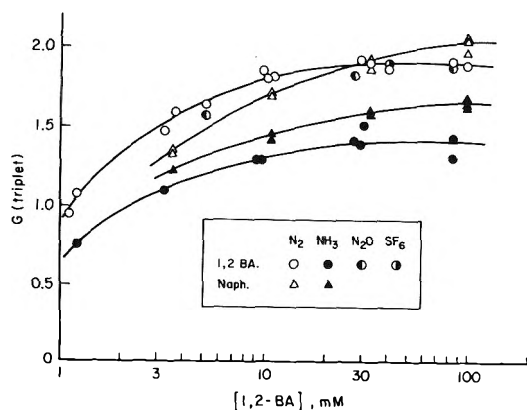


Figure 8. The change in G value for triplet states of 1,2-benzanthracene and naphthalene.

plot in Figure 9 furnishes a G value of 1.4 at infinite concentration. Since 1,1'-binaphthyl does not form an excimer,¹⁹ an intersystem crossing efficiency of 0.5² can be used at infinite concentration. Hence, the yield of the triplet 1,1'-binaphthyl produced by the intersystem crossing from the singlet is 0.7 expressed in G units. As the total $G(\text{triplet})$ in this system is 2.4, a yield of triplets of $G = 1.7$ is attributed to direct energy transfer from the triplet state of benzonitrile to the 1,1'-binaphthyl. This latter value is in agreement with the observed triplet yield for pyrene, where intersystem crossing is small at high concentrations due to excimer formation.²⁰

The rise of the emission of 1,1'-binaphthyl was too fast to be measured by the present apparatus. No delayed growth was observed in either the emission or the absorption of the excited singlet of 1,2-benzanthracene. A Stern-Volmer plot of the singlet energy transfer from benzonitrile to 1,1'-binaphthyl gives a rate constant ratio α/β . The rate constants α and β refer to the natural decay of the singlet state in benzonitrile in the absence of a quencher, and β is the singlet energy-transfer rate constant to 1,1'-binaphthyl. The value for α/β is 1.0×10^{-2} , and if β is about $10^{10} \text{ M}^{-1} \text{ sec}^{-1}$, α is 10^8 sec^{-1} which agrees with the decay rates of both of the species giving rise to the short-lived emission and absorption in pure benzonitrile. This is evidence supporting the assignment of a singlet excited state to this species.

The delayed growth in the triplet state generally results from the intersystem crossing in the solute molecule. However, in a 10^{-4} M *p*-terphenyl solution a triplet growth is observed for 100 nsec after the pulse and can be ascribed to energy transfer from the benzonitrile triplet to the *p*-terphenyl. Since the lifetime of the fluorescence of *p*-terphenyl is 0.95–2.8 nsec,²¹ the observed triplet growth is not due to intersystem crossing.

A Stern-Volmer plot of the triplet growth furnishes a ratio of α/β where α is the rate constant for the spontaneous decay of the solute triplet precursor and β is the rate constant for triplet energy transfer to the solute. For 1,1'-binaphthyl solutions, an α/β of $1.7 \times 10^{-3} \text{ M}$ was measured, and as the triplet energy rate constant to *p*-terphenyl β is measured as $10^{10} \text{ M}^{-1} \text{ sec}^{-1}$, the natural decay rate α is 10^7 sec^{-1} .

Discussion

The formation of solute cations in benzonitrile solution has already been reported.^{7,8,14} A $G(\text{ion})$ of 1.4 obtained in this study is considered to be a better yield for the ioniza-

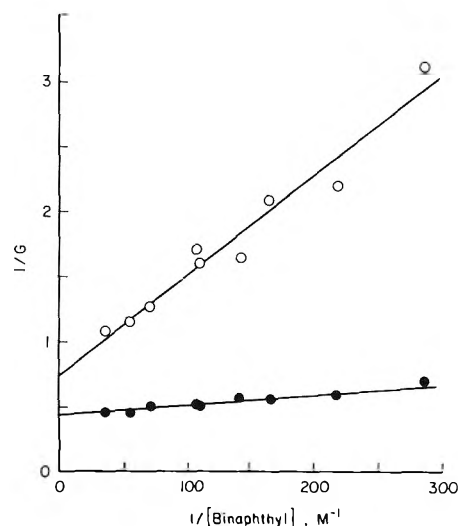
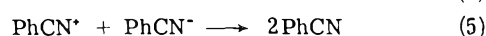
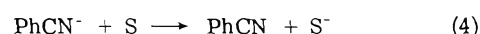


Figure 9. Stern-Volmer plots for the excited singlet (O) and triplet (●) states of 1,1'-binaphthyl.

tion in liquid benzonitrile than the previous value of 0.9.²² The latter value was evaluated from a measurement in 10 *mM* *trans*-stilbene solution where all the solvent ions were not measured. The fact that the anion yield $G > 0.5$ is lower than that of the cation $G = 1.4$ suggests that some process rapidly degrades the benzonitrile anion.

The fact that anions of anthracene, pyrene, perylene, and 1,2-benzanthracene are observed but the *trans*-stilbene anion is not detected suggests that the formation of solute anions in benzonitrile solution only takes place for solute molecules where the electron affinity is high.²³ Such selectivity implies that the solute anion is formed by a reaction of a solute molecule with the benzonitrile anion and not with an electron. The fact that the yield of the solute anion is decreased by SF_6 but not by N_2O also suggests that the direct precursor for the solute anion is not an electron but the benzonitrile anion. If the solute actually scavenged electrons to form the anion, N_2O as well as SF_6 should decrease the yield of the solute anion. The decrement in the anion yield in the presence of SF_6 could be due to a scavenging of benzonitrile anions by SF_6 , which has a large electron affinity (1.43 eV).²⁴ There is no proof for the existence of solvated electrons in benzonitrile. However benzonitrile does capture electrons both in cyclohexane and in methanol to form an anion, and it is reasonable to suggest that, in pure benzonitrile, anion formation is the major fate of electrons.

The above discussion leads to the reaction scheme shown by eq 1–5 for charged species in irradiated benzonitrile,



where PhCN denotes benzonitrile and S denotes a solute molecule. The benzonitrile cation could exist as a dimer cation; however, dimer anions have only been reported for anthracene under selected conditions.²⁵ A benzonitrile dimer anion may be formed in the pure liquid due to the high concentration. Although dimer or aggregated ions may

be the actual species involved in the system, the notations of eq 1-5 are used for simplicity.

The present study gives rate constants of 2.2×10^{10} and $1.8 \times 10^{10} M^{-1} \text{sec}^{-1}$ for reactions 3 and 4, respectively. From the pseudo-first-order rate constant of the ionic decay in pure benzonitrile and the concentration of ions, a crude estimate of the rate constant for reaction 5 turns out to be $2 \times 10^{10} M^{-1} \text{sec}^{-1}$, which is rather slower than the rate constant for the diffusion-controlled ion neutralization. This rate constant and the formation of perylene anions in $10^{-4} M$ solutions suggest that benzonitrile ions are distributed homogeneously within 5 nsec after the irradiation pulse. This indicates that fast-moving electrons ejected from benzonitrile molecules can move past many benzonitrile molecules and that the electrons are trapped outside the Onsager distance, $e^2/\epsilon kT$ (21 Å for benzonitrile), to form benzonitrile anions. The anion may also be formed within the Onsager distance although explicit data for such a process were not observed in this study. Some of the ejected electrons could return to the cation which itself may be very mobile and produce excited states. The increase in the yield of the anion in the presence of ammonia is probably due to the scavenging of benzonitrile cations by ammonia. If the benzonitrile cation is mobile, a rapid neutralization with the electron results. However scavenging of the solvent cation with ammonia will produce a different cation of lower mobility. Hence the rate of the neutralization process is decreased, and more anions are subsequently observed.

The depression of the triplet yield by ammonia can be explained by the scavenging of benzonitrile cations, which in turn are assumed to be responsible for the formation of excited states. An alternative explanation is that ammonia quenches the excited singlet of benzonitrile and/or of solutes and decreases the triplet yield. However, the data show that the decays of the fluorescence in pure liquid benzonitrile and of the fluorescence of 1,2-benzanthracene in benzonitrile solution are unaffected by ammonia. This tends to rule out the latter interpretation.

Excited singlet states of solutes are formed rapidly and with the irradiation pulse. This indicates that the excited singlet of benzonitrile is formed in less than 10^{-9} sec. As the apparent lifetime of neutralization of the benzonitrile cation and anion was measured to be about 10^{-6} sec, then this later neutralization process cannot be responsible for the formation of excited states. A corresponding neutralization of solute ions is even less plausible as the concentration of solute ions is even lower than that of benzonitrile ions. Possible mechanisms for the formation of excited

states are the recombination of electrons and benzonitrile cations and direct excitation by secondary electrons. Even under such extreme ion scavenging conditions as prevail in the present system, where the solvent itself is an effective electron scavenger, the initial rapid neutralization process still may occur, if the separation of the electron and cation is small.

The sum of the G values for ions and excited states in benzonitrile, of 4.5, is close to the G values reported for excited states in benzene. A similar correlation has been found for benzyl alcohol and toluene.⁶

Hence it is suggested that the initial act of the radiation leads to the ionization of benzonitrile giving cations and electrons. An initial rapid neutralization of these ions leads to excited states both singlet and triplet. A second process competes with the neutralization, namely, the escape of the electron from the solvent cation and subsequent formation of a solvated anion. Solute may react with the solvent ions to form solute cations and anions. Energy transfer from the solvent also leads to singlet and triplet excited states of the solute.

References and Notes

- (1) The Radiation Laboratory of the University of Notre Dame is operated under contract with the U. S. Atomic Energy Commission. This is AEC Document No. COO-38-946.
- (2) T. Gangwer and J. K. Thomas, *Radiat. Res.*, **54**, 192 (1973).
- (3) J. H. Baxendale and M. Fiti, *J. Chem. Soc., Faraday Trans. 2*, **68**, 218 (1972).
- (4) R. Cooper and J. K. Thomas, *J. Chem. Phys.*, **48**, 5097 (1968).
- (5) R. Cooper and J. K. Thomas, *J. Chem. Phys.*, **48**, 5103 (1968).
- (6) A. Kira and J. K. Thomas, *J. Chem. Phys.*, in press.
- (7) E. Hayon, *J. Chem. Phys.*, **53**, 2353 (1970).
- (8) A. Kira, S. Arai, and M. Imamura, *Int. J. Radiat. Phys. Chem.*, **5**, 127 (1973).
- (9) T. Kajiwara and J. K. Thomas, *J. Phys. Chem.*, **76**, 1700 (1972).
- (10) B. Chutny and A. J. Swallow, *Trans. Faraday Soc.*, **66**, 2847 (1970).
- (11) (a) T. Shida and W. H. Hamill, *J. Chem. Phys.*, **44**, 2375 (1966); (b) T. Shida, *J. Amer. Chem. Soc.*, **95**, 3473 (1973).
- (12) J. Jagur-Grodzinski, M. Feld, S. L. Yang, and M. Szwarc, *J. Phys. Chem.*, **69**, 628 (1965).
- (13) B. Badger and B. Brocklehurst, *Trans. Faraday Soc.*, **65**, 2588 (1969).
- (14) A. Kira, S. Arai, and M. Imamura, *J. Chem. Phys.*, **54**, 4890 (1971).
- (15) M. A. J. Rodgers, *Trans. Faraday Soc.*, **67**, 1029 (1971).
- (16) G. Porter and M. W. Windsor, *Proc. Roy. Soc., Ser. A*, **245**, 238 (1958).
- (17) R. McNeil, J. T. Richards, and J. K. Thomas, *J. Phys. Chem.*, **74**, 2290 (1970).
- (18) R. Bensasson and R. J. Land, *Trans. Faraday Soc.*, **67**, 1904 (1971).
- (19) D. L. Horrocks, *J. Chem. Phys.*, **52**, 1566 (1970).
- (20) W. Heinzelman and H. Labhart, *Chem. Phys. Lett.*, **4**, 20 (1969).
- (21) J. B. Birks, "Photophysics of Aromatic Molecules," Wiley-Interscience, London, 1970, p 130.
- (22) S. Tagawa, S. Arai, A. Kira, M. Imamura, Y. Tabata, and K. Oshima, *J. Polym. Sci., Part B*, **10**, 295 (1972).
- (23) Values of the electron affinity in literature scatter depending on the method of measurement and cannot be utilized for this discussion.
- (24) "Handbook of Chemistry and Physics," 53rd ed, CRC Press, Cleveland, Ohio, 1972, p E55.
- (25) T. Shida and S. Iwata, *J. Chem. Phys.*, **56**, 2858 (1972).

Reactivity of the Carbonate Radical in Aqueous Solution. Tryptophan and Its Derivatives¹

Schoen-nan Chen and Morton Z. Hoffman*

Department of Chemistry, Boston University, Boston, Massachusetts 02215 (Received June 17, 1974)

The rate constants for the reaction of CO_3^- and CO_3H radicals, generated in the flash photolysis of aqueous solutions of $\text{Co}(\text{NH}_3)_4\text{CO}_3^+$, with tryptophan and its derivatives have been measured as a function of pH. At 0.1 *M* solution ionic strength, *k* for indole-3-propionic acid, *N*-acetyltryptophan, and *N*-methyltryptophan follows a "titration" curve that represents the acid-base equilibrium of the radical ($\text{p}K_a = 9.6 \pm 0.3$). At 0.003 *M* ionic strength, the rate constants are the same for the three compounds, independent of pH, and equal to that for indole ($4.2 \times 10^8 \text{ M}^{-1} \text{ sec}^{-1}$) indicating that the mode of reaction is interaction of the radical with the aromatic system and that the intrinsic reactivity of the acidic and basic forms of the radical are the same. Amino-containing compounds show variation of the rate constant according to the $\text{p}K_a$ of the NH_3^+ group (tryptamine, tryptophanamide, tryptophan methyl ester, glycyltryptophan, glycyglycyltryptophan, tryptophylglycine, and tryptophan) with the rate constant being greater by almost a factor of 2 for NH_3^+ than for NH_2 . A small but significant enhancement of the rate is noted for amino compounds lacking the carboxylate group. A model is proposed wherein the reaction of the radical with the aromatic system is enhanced by interaction with the amino group which results in a transitory cooperative mechanism causing the radical to be in closer proximity to the reactive site.

Introduction

The carbonate radical (CO_3^-) can be generated in aqueous solution upon the reaction of OH radicals with CO_3^{2-} ($k = 4.2 \times 10^8 \text{ M}^{-1} \text{ sec}^{-1}$)² or CO_3H^- ($k = 1.5 \times 10^7 \text{ M}^{-1} \text{ sec}^{-1}$)² and thus may be an important component in biological systems which suffer radiolytic damage. Whereas the reactivity patterns of the primary radicals generated in the radiolysis of water (e_{aq}^- , OH, and H) are rather well known,³⁻⁵ the behavior of the CO_3^- radical has not been investigated in much detail. Despite the convenient absorption spectrum of the radical (λ_{max} 600 nm; $\epsilon_{600} 1.83 \times 10^3 \text{ M}^{-1} \text{ cm}^{-1}$),⁶ the use of pulse radiolysis is limited to a rather narrow pH range in alkaline solution because of the relatively low reactivity of OH with CO_3H^- , the $\text{p}K_a$ of CO_3H^- (10.36), the $\text{p}K_a$ of OH (11.9),² and the low reactivity of its conjugate base.² Thus, pulse radiolysis does not permit an examination of the radical's nature in biologically important neutral solution or as a general function of pH.

We have reported^{7,8} that the flash photolysis of $\text{Co}(\text{NH}_3)_4\text{CO}_3^+$ generates the CO_3^- radical permitting an evaluation of its acid-base properties ($\text{p}K_a = 9.6 \pm 0.3$ for CO_3H)^{9,10} and the rate constants for its reaction with biologically important molecules in neutral solution.¹¹ Among the compounds with which the radical reacts fairly rapidly ($k > 10^8 \text{ M}^{-1} \text{ sec}^{-1}$) are tryptophan and its derivatives.¹¹ In this paper we examine the reactivity of the radical as a function of pH with this group of compounds and attempt to identify the molecular parameters that give rise to the observed patterns.

Experimental Section

The flash photolysis apparatus used and the techniques employed have been described in detail as has been the preparation of $\text{Co}(\text{NH}_3)_4\text{CO}_3^+$.^{8,10,11} Solutions were prepared from triply distilled water containing $5 \times 10^{-5} \text{ M}$ complex and up to $2 \times 10^{-5} \text{ M}$ organic scavenger. The pH of the solution was controlled by combinations of KH_2PO_4 , K_2HPO_4 , and KOH solutions which gave a constant solution ionic strength of 0.003 *M* at pH < 11.5. Above that pH,

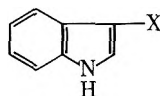
only KOH was used to establish the acidity and ionic strength of the solution. For an ionic strength of 0.1 *M*, NaClO_4 was used with a correction for the Na^+ effect on the pH measurement. The pH of the solutions was measured before and after the flash with a Beckman Expandomatic SS-2 pH meter and was not changed by the flash. All solutions were freshly prepared from the solid complex and were discarded after one flash. Inasmuch as CO_3^- radicals do not react with O_2 , the solutions were flashed without deoxygenation. Independently we demonstrated that the presence of air had no effect on the values of *k*.

The following compounds were used without further purification: tryptophan, tryptophan methyl ester, glycyltryptophan, tryptophylglycine, indole (Calbiochem); glycyglycyltryptophan, *N*-methyltryptophan, *N*-acetyltryptophan, tryptamine, and tryptophanamide (Cyclo Chemicals); indole-3-propionic acid (Matheson, Coleman, and Bell). The structures and known $\text{p}K_a$ values for these compounds are given in Table I.

The pseudo-first-order rate constant for the decay of the transient absorption at 600 nm was determined at a single scavenger concentration; the linear dependence of *k* on [scavenger] had already been established.^{10,11} The value of the second-order rate constant for the reaction of the radical with the scavenger was evaluated from at least four individual decays and is known to be $\pm 10\%$ at pH < 11.5. Above that pH, the bimolecular disappearance of the radical itself becomes competitive¹⁰ and the error in the scavenging rate constant increases ($\pm 25\%$).

Results

Figure 1 shows the dependence of $k(\text{CO}_3^- + \text{S})$ ¹² as a function of pH for three of the tryptophan derivatives which do not contain deprotonatable amino groups: indole-3-propionic acid, *N*-acetyltryptophan, and *N*-methyltryptophan. At low ionic strength (0.003 *M*) the value of $k = 4.2 \times 10^8 \text{ M}^{-1} \text{ sec}^{-1}$ is independent of pH. The rate constant in basic solution increases with increasing ionic strength which gives rise to the "titration curve" seen at $\mu = 0.1 \text{ M}$.

TABLE I: Structure and pK_a of Compounds

Name	X ^a	pK_a^b
Indole	-H	
Tryptophan	$-\text{CH}_2\text{CH}(\text{NH}_3^+)\text{CO}_2^-$	9.39 ^c
Indole-3-propionic acid	$-\text{CH}_2\text{CH}_2\text{CO}_2^-$	
<i>N</i> -Acetyltryptophan	$-\text{CH}_2\text{CH}(\text{CO}_2^-)\text{NHCOCH}_3$	
<i>N</i> -Methyltryptophan	$-\text{CH}_2\text{CH}(\text{CO}_2^-)\text{NHCH}_3$	
Tryptamine	$-\text{CH}_2\text{CH}_2\text{NH}_3^+$	9.3 ^d
Tryptophanamide	$-\text{CH}_2\text{CH}(\text{NH}_3^+)\text{CONH}_2$	7.50 ^c
Tryptophan methyl ester	$-\text{CH}_2\text{CH}(\text{NH}_3^+)\text{CO}_2\text{CH}_3$	7.6 ^d
Glycyltryptophan	$-\text{CH}_2\text{CH}(\text{CO}_2^-)\text{NHCOCH}_2\text{NH}_3^+$	8.06 ^c
Glycylglycyltryptophan	$-\text{CH}_2\text{CH}(\text{CO}_2^-)\text{NHCOCH}_2\text{NHCOCH}_2\text{NH}_3^+$	7.9 ^d
Tryptophylglycine	$-\text{CH}_2\text{CH}(\text{NH}_3^+)\text{CONHCH}_2\text{CO}_2^-$	7.6 ^d

^a Structures are written in the carboxylate form. ^b pK_a of the amino group. ^c Data taken from W. P. Jencks and J. Regenstein, "Handbook of Biochemistry," Chemical Rubber Co., Cleveland, Ohio, 1970, p J-150. ^d Deduced from this research.

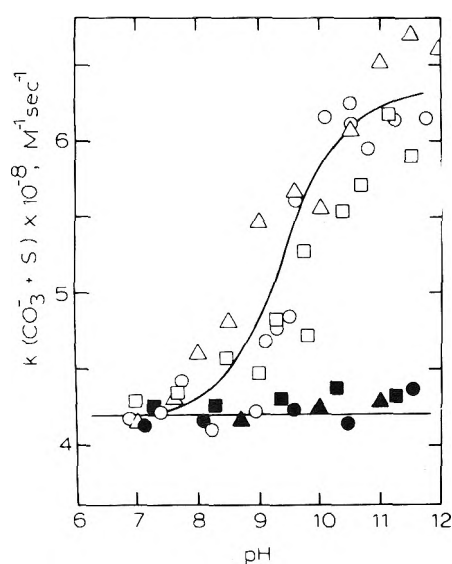


Figure 1. Dependence of $k(\text{CO}_3^- + \text{S})$ on pH for indole-3-propionic acid (Δ , \blacktriangle), *N*-acetyltryptophan (O, \bullet), and *N*-methyltryptophan (\square , \blacksquare). Open symbols correspond to 0.1 *M* solution ionic strength; filled symbols correspond to 0.003 *M* solution ionic strength.

The results for indole-3-propionic acid have already been published;¹⁰ the virtually identical behavior of the two *N*-substituted compounds is readily seen.

In Figure 2, the behavior of indole, tryptophan, and tryptophylglycine is illustrated. For comparison, the data for tryptophylglycine are given for high and low ionic strengths. It is in basic solution that the rate constant is affected by ionic strength. As seen at low ionic strength, the pH dependence of tryptophan reflects the pK_a of the amino group; indole shows pH- and μ -independent behavior.

The behavior of tryptamine, tryptophanamide, tryptophan methyl ester, glycyltryptophan, and glycylglycyltryptophan is shown in Figure 3 for $\mu = 0.003$ *M*. The pH-dependent values of the rate constant follow the same pattern as before reflecting the pK_a of the amino groups of the scavenger where known. Except for tryptamine and tryptophanamide, the values of k for all the amino-containing

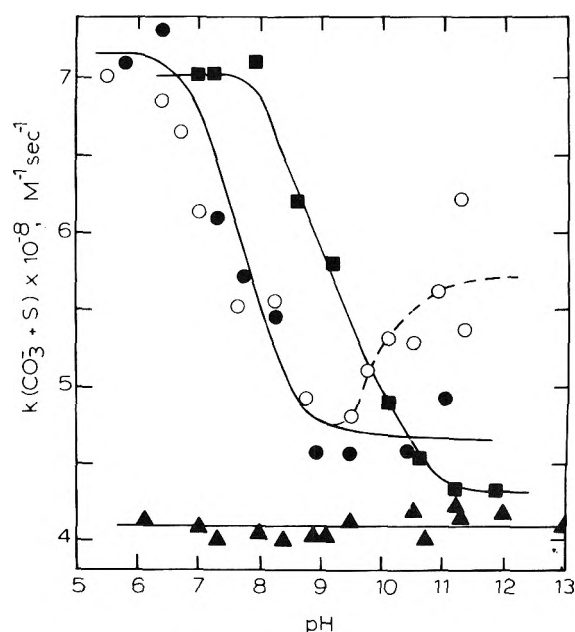


Figure 2. Dependence of $k(\text{CO}_3^- + \text{S})$ on pH for indole (\blacktriangle), tryptophan (\blacksquare), and tryptophylglycine (O, \bullet). Open symbols correspond to 0.1 *M* solution ionic strength; filled symbols correspond to 0.003 *M* solution ionic strength.

compounds in basic solution (deprotonated form) are practically the same as that of indole.

Discussion

The mode of reaction of CO_3^- radicals with scavengers is not known but certain possibilities are evident: (1) oxidative electron transfer from the scavenger to the radical, (2) addition of the radical to the molecule, and (3) hydrogen abstraction by the radical. In a pulse radiolysis study, Adams, *et al.*,¹³ determined the rate constant for the reaction of CO_3^- with tryptophan at pH 11.2 in 0.1 *M* Na_2CO_3 to be 4.4×10^8 $\text{M}^{-1} \text{sec}^{-1}$ and observed a transient absorption spectrum resulting from that reaction. The transient spectrum, showing absorption bands at 320 and 510 nm, was virtually identical with that generated by the action of OH radicals on tryptophan¹⁴ where radical addition to the

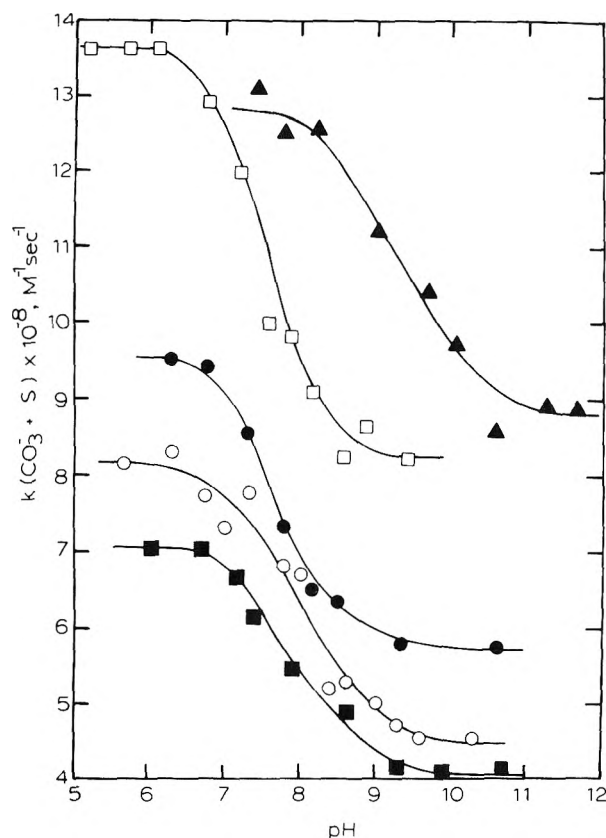


Figure 3. Dependence of $k(\text{CO}_3^{\cdot-} + \text{S})$ on pH for tryptophanamide (\square), tryptamine (\blacktriangle), tryptophan methyl ester (\bullet), glycytryptophan (\circ), and glycyglycyltryptophan (\blacksquare). Solution ionic strength was 0.003 M.

aromatic system appears to be the operative mechanism. In the work reported here, no attempt was made to resolve the spectrum of any transient species generated from the $\text{CO}_3^{\cdot-}$ radical attack.

The great similarity of the rate constants for these tryptophan derivatives, including indole, suggests that reaction in all cases is *via* a common mechanism involving the aromatic system. We have shown¹¹ that the reactivity of the radical with aliphatic amino acids and peptides is very low suggesting that direct attack on the side chain of the tryptophan derivatives is not probable. However, an *a priori* judgment of the reaction mode with the aromatic system, whether by electron transfer or radical addition, cannot be made.

Indole-3-propionic acid, *N*-acetyltryptophan, and *N*-methyltryptophan are all in their anionic form with a 1- charge across the pH range covered by this work. At low solution ionic strength the values of $k(\text{CO}_3^{\cdot-} + \text{S})$ are independent of pH but at high ionic strength a definite pH dependence is observed. We had shown previously¹⁰ that the behavior of indole-3-propionic acid was consistent with the pH dependence arising from a kinetic salt effect; plots of $\log k$ vs. the appropriate square root function of ionic strength were linear. The conclusion was drawn then and further reinforced by the coincidence of the behavior of the other two compounds that in neutral solution the radical exists as a neutral entity and as a 1- charged species in basic solution, specifically as CO_3H and $\text{CO}_3^{\cdot-}$ in acid-base equilibrium with an apparent $\text{p}K_a$ of 9.6. However, it must be further concluded from the results at low ionic strength

that the intrinsic reactivity of the two forms of the radical are the same with these compounds.

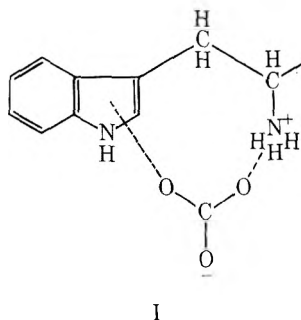
The reactivities of very few radicals have been examined as a function of their acid-base forms in aqueous solution. Among oxidizing radicals, the most analogous to the $\text{CO}_3^{\cdot-}$ radical is the OH radical ($\text{p}K_a = 11.9$)² which is far more reactive than is the $\text{O}^{\cdot-}$ radical⁴ and, in particular, is 20–500 times more reactive than $\text{O}^{\cdot-}$ with aromatic systems.¹⁵ The mode of attack of OH with aromatic systems has always been assumed⁴ to be direct addition although the possibility of electron transfer ($E^\circ_{\text{red}}(\text{OH}) = 2.8 \text{ V}$)¹⁶ leading to the same hydroxycyclohexadienyl product cannot be ignored. The behavior of NH_3^+ and NH_2 radicals toward aromatic systems is also different with NH_3^+ adding to benzene and NH_2 not giving an observable transient.¹⁷ However, the structure of these radicals is sufficiently different from that of $\text{CO}_3^{\cdot-}$ to make analysis based on these limited examples of dubious validity. Indeed, if $\text{CO}_3^{\cdot-}$ acted as an electron-transfer agent, one would expect its reactivity to be lower than that of the protonated form. However, if the reactivity mode were addition to the aromatic system and if the unpaired electron were on an oxygen atom different from the site of protonation, the similar reactivities of both forms of the radical could be rationalized.

The assumption is thus made at the start that the $\text{CO}_3^{\cdot-}$ radical interacts with the π system of the aromatic indole structure, forming initially, perhaps, a molecular complex. The reactivity of the radical with the non-amino-containing derivatives at low ionic strength is the same as that with indole ($k = 4.2 \times 10^8 \text{ M}^{-1} \text{ sec}^{-1}$); the rate constant is 10–100 times lower than the diffusion-controlled limit demonstrating that radical addition does not occur at every encounter and that steric restrictions are undoubtedly in effect. We also note that the limiting value of k in basic solution and low ionic strength for tryptophan, tryptophylglycine, glycytryptophan, and glycyglycyltryptophan is the same as for indole and the non-amino-containing compounds. This suggests that the mechanism of reaction for all those compounds is the same and that the steric and energetic barriers are comparable when the amino group is deprotonated or absent. The data for tryptophylglycine at high or low ionic strength are identical except at $\text{pH} > 9$ where the effect of ionic strength on the reactivity of the basic form of the radical becomes evident. Tryptophylglycine was especially chosen to test this effect because the $\text{p}K_a$ of its amino group was expected to be substantially lower than that for tryptophan; amino groups adjacent to the amide linkage are more acidic than ordinary amino groups (e.g., $\text{p}K_a$ of glycine is 9.6 but that of glycyglycine is 8.1).¹⁸ The three remaining compounds in Figure 3 show the same behavior as the other amino-containing derivatives except that the limiting value of k in basic solution is larger than that of indole.

The pH dependence of k at low solution ionic strength, which mirrors the $\text{p}K_a$ of the amino group, cannot arise from simple electrostatic effects. In addition to the identical behavior of the two forms of the radical seen at low ionic strength (Figure 1), the value of k for 1- charged species is the same as for neutral species. Similarly, although it is known that the electron density on the aromatic rings is affected by substitution,¹⁹ the possibility of transmission of an inductive effect through a multiatom chain, as in the case of the peptides, is rather remote. In addition, there does not appear to be any evidence favoring a static association of the protonated amino groups with

the aromatic system that could serve as an activating influence on the reactivity of the radical. We conclude that the attack by the radical involves a transitory cooperative mechanism involving the interaction of the radical with the protonated amino group.

Thus, when NH_3^+ is present, even in the cases of the flexible peptides, interaction of the radical with NH_3^+ , perhaps *via* hydrogen bonding and enhanced by the attraction of the electronegative oxygen atom of the radical to the positive charge on the amino group, allows the radical to be held in proximity to the aromatic system for a period of time longer than is the case in random collision (see structure I). The result is a sterically more effective collision



with a greater probability of ultimate reaction and a higher observed rate. Differences in the structures of the various derivatives that affect the charge distribution at the amino group would cause subtle changes in the radical reaction rate. Removal of the adjacent carboxylate group, as in tryptamine and tryptophanamide, would result in an increase of the effective charge of NH_3^+ and of the template effect. The intermediate behavior of the tryptophan methyl ester could be due to the nature of the ester linkage or hydrolysis during the reaction. The higher rate for the non-carboxylate-containing amino derivatives (as compared to indole) in basic solution suggests that some interaction occurs between the radical and the amino group even when the latter is deprotonated. Apparently when a carboxylate

group is present, as in the case of tryptophan, the basis for radical-amino group interaction is removed in basic solution.

While we recognize that the pH dependence of the rate constants for these reactions is not a large effect (no more than a factor of 2), the effect is outside of experimental error. The results do demonstrate that in the case of the CO_3^- radical, the rate constants for these less-than-encounter-controlled reactions are affected by small changes in the structure of the scavenger. Such structure-reactivity patterns would be extremely difficult to detect in the case of very reactive radicals, such as OH, which react on virtually every collision.

References and Notes

- (1) The support of this research by the National Science Foundation through Grant No. GP-40623X is gratefully acknowledged. Aspects of this research were reported at the 167th National Meeting of the American Chemical Society, Los Angeles, Calif., April 1974; No. PHYS 22.
- (2) J. L. Weeks and J. Rabani, *J. Phys. Chem.*, **70**, 2100 (1966).
- (3) E. J. Hart and M. Anbar, "The Hydrated Electron," Wiley-Interscience, New York, N. Y., 1970.
- (4) L. M. Dorfman and G. E. Adams, *Nat. Stand. Ref. Data Ser., Nat. Bur. Stand., No. 46* (1973).
- (5) P. Neta, *Chem. Rev.*, **72**, 533 (1972).
- (6) E. Hayon and J. J. McGarvey, *J. Phys. Chem.*, **71**, 1472 (1967).
- (7) V. W. Cope and M. Z. Hoffman, *J. Chem. Soc., Chem. Commun.*, 227 (1972).
- (8) V. W. Cope, S.-N. Chen, and M. Z. Hoffman, *J. Amer. Chem. Soc.*, **95**, 3116 (1973).
- (9) S.-N. Chen and M. Z. Hoffman, *J. Chem. Soc., Chem. Commun.*, 991 (1972).
- (10) S.-N. Chen, V. W. Cope, and M. Z. Hoffman, *J. Phys. Chem.*, **77**, 1111 (1973).
- (11) S.-N. Chen and M. Z. Hoffman, *Radiat. Res.*, **56**, 40 (1973).
- (12) The symbol CO_3^- will be used in this paper to designate the radical irrespective of its acidic or basic form unless the specific nature of the radical is essential for the discussion.
- (13) G. E. Adams, J. E. Aldrich, R. H. Bisby, R. B. Cundall, J. L. Redpath, and R. L. Willson, *Radiat. Res.*, **49**, 278 (1972).
- (14) R. C. Armstrong and A. J. Swallow, *Radiat. Res.*, **40**, 563 (1969).
- (15) M. Simic, M. Z. Hoffman, and M. Ebert, *J. Phys. Chem.*, **77**, 1117 (1973).
- (16) W. Latimer, "Oxidation Potentials," 2nd ed, Prentice-Hall, Englewood Cliffs, N. J., 1952.
- (17) M. Simic and E. Hayon, *J. Amer. Chem. Soc.*, **93**, 5982 (1971).
- (18) W. P. Jencks and J. Regenstein, "Handbook of Biochemistry," Chemical Rubber Co., Cleveland, Ohio, 1970, p J-150.
- (19) R. J. Sundberg, "The Chemistry of Indoles," Academic Press, New York, N. Y., 1970.

Indirect Measurements for the Time Dependence of the Hydrated Electron¹

Charles D. Jonah

Chemistry Division, Argonne National Laboratory, Argonne, Illinois 60439 (Received September 24, 1973;

Revised Manuscript Received June 6, 1974)

Publication costs assisted by the U. S. Atomic Energy Commission

Two indirect methods that have been used for determining the yield of the hydrated electron as a function of time, the steady-state concentration method and the Laplace transform method, have been examined. The experimental difficulty in measuring rate constants at high concentrations and the errors in neglecting certain intraspur reactions lead to errors which are consistent with the differences between the experimentally observed and the indirect measurements for the decay of the hydrated electron.

Experimental observations in the radiation chemistry of aqueous solution have, until recently, been fairly well explained by a diffusion kinetic model.² For instance, the diffusion model has accounted for the yields of H₂O₂, H₂, and H as a function of the concentrations of various additives.³ Further, it has satisfactorily predicted the dependence on linear energy transfer of the *G* value for water decomposition and of the *G* value for those hydrated electrons and other spur species which escape the spur to form a homogeneous solution.⁴ In addition, the diffusion model has been used to calculate the yield of the hydrated electron in pure water as a function of time after energy deposition.

With respect to this latter prediction it has not been possible until recently to measure directly hydrated electron yields at short times during the life of the spur, and therefore attempts have been made to determine the time dependence indirectly using high scavenger concentrations. These attempts have given results similar to those predicted by the Schwarz formulation of the diffusion model.⁵ However, recent direct experimental measurements of the time dependence of hydrated electron yields disagree with the predicted results.⁶ As a consequence of this disagreement, it appears worthwhile to examine the basis on which the indirect measurements are used to predict decays of the hydrated electron. In pursuit of this aim, two "experiments" were done. (1) The rate constant for e_{aq}⁻ + H⁺ was measured as a function of H⁺ concentration and combined with the previously measured time dependence of e_{aq}⁻ in pure water to reproduce the data of Koulkes-Pujo, *et al.*^{5a} (2) The Laplace transform technique as applied to radiation chemistry by Schuler^{5b} was tested theoretically using a model of Kuppermann.⁷

Experimental Section

The subnanosecond pulse radiolysis apparatus has been previously described.⁸ All decay curves were measured using 514.5-nm light from an argon ion laser. Solutions were made by diluting a stock 1 *M* perchloric acid solution with distilled water. Solutions were degassed by bubbling helium through them for at least 20 min before irradiation. Comparison runs were made either using tap water or without degassing solutions. No effects which could be ascribed to oxygen or other impurities were seen for times as long as 30 nsec, the maximum time used.

One series of experiments was run using 0.01–0.5 *M* acid concentration and a second similar series was run with suf-

ficient sodium chloride added to give a constant 1 *M* ion concentration.

Rate constants were extracted from the raw data using a nonlinear least-squares routine in which the effect of an RC type frequency response ($\omega = 50$ GHz, which is approximately equivalent to a 10–90% rise time of 50 psec) was incorporated into the fitting function. The results are plotted in Figure 1 where the error bars are ± 2 standard deviations. These data are similar to the rate constant dependence previously obtained by Hunt.⁹

Results and Discussion

It has often been implicitly assumed, that, if one knows the time dependence of a species' concentration without scavenger present, one can calculate the yield of a product from the reaction of that species with an added scavenger for various scavenger concentrations. With certain assumptions, Hummel has pointed out for hydrocarbons that if one had the yield of scavenger product as a function of scavenger concentration, one could obtain the time dependence of the reacting species without scavenger present.¹⁰ This technique has been applied to the radiation chemistry of water by Schuler.^{5b}

To calculate the yield as a function of concentration, Hummel¹⁰ proposed the equation

$$\int_0^{\infty} n(t)e^{-kct} dt = N_0 - N_s(c) \quad (1)$$

where $n(t) dt$ is the amount of (in this case) hydrated electron lost through spur processes between times t and $t + dt$ after formation; c is the concentration of the electron scavenger and k its rate constant with the hydrated electron; N_0 is the total amount of product formed as a function of concentration. To work with the amount of hydrated electron at time t , we can integrate by parts to get

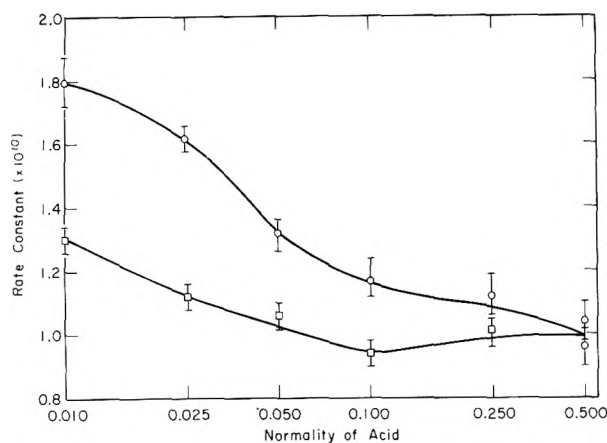
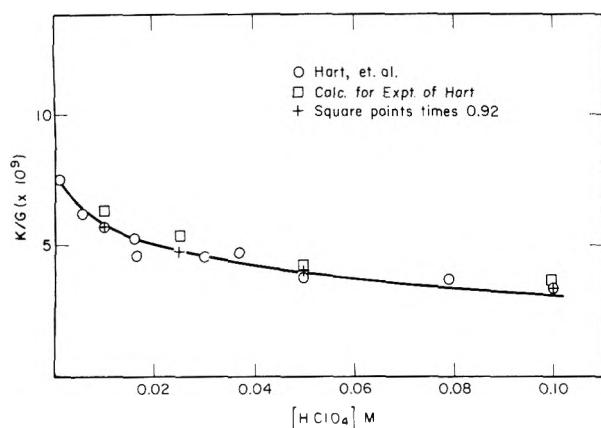
$$\int_0^{\infty} G(t)kce^{-kct} dt = N_s(c) \quad (1a)$$

where $G(t)$ is the amount of hydrated electron at time t ($dG/dt = -n(t)$). Equations 1 and 1a will be used interchangeably.

Koulkes-Pujo, *et al.*,^{5a} used a long electron pulse (0.5–3.0 μ sec) and integrated the amount of absorption during the pulse. The transient portion of the absorption is small, and the effects at the beginning and the end of the pulse approximately cancel so that one can consider their experi-

TABLE I: Fraction of Radical 1 (Radical 2) Reacting with the Scavenger as Calculated by Kuppermann⁷ and by Using Eq 1

[Scavenger], <i>M</i>	Spherical spur				Short track			
	Radical 1		Radical 2		Radical 1		Radical 2	
	Kuppermann	Eq 1	Kuppermann	Eq 1	Kuppermann	Eq 1	Kuppermann	Eq 1
1	0.970	0.955	0.925	0.894	0.895	0.833	0.797	0.727
0.1	0.891	0.868	0.801	0.770	0.633	0.570	0.494	0.436
0.01	0.813	0.797	0.709	0.694	0.396	0.356	0.285	0.254
10 ⁻³	0.772	0.765	0.669	0.663	0.257 ^a	0.237	0.179 ^a	0.166
10 ⁻⁴	0.758	0.753	0.656	0.653	0.190	0.174	0.133	0.121
10 ⁻⁵	0.752	0.751	0.652	0.651	0.150	0.141	0.105	0.098

^a Recalculated.

Figure 1. Second-order rate constant for the reaction $H^+ + e_{aq}^-$ in units of $M^{-1} \text{sec}^{-1}$. Circles are for pure $HClO_4$ and squares are for $HClO_4 + NaCl$ where the concentrations of ions is 1 *M*.

Figure 2. A plot of the rate constant for $H^+ + e_{aq}^-$ in $M^{-1} \text{sec}^{-1}$ divided by the yield of the hydrated electron in molecules/100 eV vs. acid concentration as measured by ref 5a. The circles and the line are from ref 5a; the squares are calculated using eq 1a, the initial yield of ref 8, and the time-proportional expression for the e_{aq}^- concentration ($0.723 + 0.277 \exp(-1.03 \times 10^8 t)$).

ment to give as the integrated intensity the product of pulse width and steady-state concentration.

It has been published that one can describe, in the time domain of 1–30 nsec, the total hydrated electron concentration in the absence of scavengers as proportional⁸ to $0.723 + 0.277 \exp(-1.03 \times 10^8 t)$. Using this and eq 1 with the data shown in Figure 1 we can determine the experimental

results which would be determined in the experiment of Koulkes-Pujo, *et al.*^{5a} The squares shown in Figure 2 are the results of these calculations. If the results of these calculations are multiplied by 0.92, the resulting values (shown by + in Figure 2) fall very nicely on the line drawn in ref 3. This could imply a systemic variation in rate constants and/or dosimetry between the two methods of 8%, excellent agreement between experiments done in greatly different ways.

Since the use of eq 1 has been one of the primary methods that has been used to determine indirectly the time evolution of the hydrated electron through the work of Schuler and coworkers with the Laplace transform techniques,^{5b,10} it seems of interest to study its validity for aqueous systems. A theoretical limitation to eq 1 appears from looking at the equivalent differential equation

$$\frac{d[e_{aq}^-]}{dt} = -kc[e_{aq}^-] + [e_{aq}^-] \frac{dG}{dt}/G \quad (2)$$

This equation could only be correct if all processes which destroy hydrated electrons in the spur are first order. This is clearly not the case since the reaction $e_{aq}^- + e_{aq}^-$ does occur.

To estimate the error involved in applying eq 1 to water, it is necessary to have an expression for $G(t)$ and $N_s(c)$ free from experimental error. One way to do this is to assume a model for the spur processes, solve the model exactly, and solve the model using the approximations of eq 1. Since diffusion kinetics has been useful in predicting the results of many radiation-chemical experiments, we shall test eq 1 within the framework of diffusion kinetics. To avoid great amounts of computation, the model of the reaction occurring was simplified. If only the primary species in water are considered, a reasonable basis for computation is the two radical-six radical pair spur calculated by Kuppermann.⁴ In this system, the two radicals R_1 and R_2 are prototypes of e_{aq}^- and OH. This model is particularly attractive since most of the data needed have been published. These calculations should give an order-of-magnitude value for the errors inherent in eq 1 for aqueous systems. To attempt to determine the magnitude of these effects for more nearly realistic systems would be of little value since the present best spur diffusion model calculations do not accurately predict the decay of the hydrated electron observed in pure water.⁶

Calculations were done using a program written by Fricke and Phillips which was modified for use with the Chemistry Division's Sigma 5 computer.¹¹ The program uses a finite-difference Crank-Nicolson predictor corrector technique for solving the parabolic partial differential equations.¹² The equations were solved to give the time de-

pendence of R_1 and R_2 with no scavengers present. To obtain the yield of scavenger product (1) the equations were solved with scavenger present and (2) the results with no scavenger present were used in eq 1 to calculate the product of the scavenger reaction. Thus we have the results for the exact solution of the model and the results arising from the use of eq 1.

In Table I is given the fraction of radical 1 (radical 2) that reacts with the scavenger, calculated either using diffusion theory or using eq 1. As one would expect, little difference is found for a spherical spur at low concentrations since the intraspur reactions are complete before there is much reaction with the scavenger. For the spherical spur with high concentrations of scavengers and for all short-track calculations, the inhomogeneous reactions compete with scavenger reactions and there is a substantial difference (as high as 10% for 0.1 M scavenger in a short track) between the exact value and that calculated using eq 1.

The differences calculated between the results of the diffusion kinetic model and the application of eq 1 are not expected to predict quantitatively the errors in the application of eq 1 to aqueous radiation chemistry; however since the essential features of the aqueous system are present, the differences should be qualitatively correct.

Conclusion

It has been shown in this paper that the use of scavenger techniques to determine the form of the hydrated electron time dependence at short times in pure water has limitations originating from both experimental and theoretical considerations. To measure scavenger rate constants over the wide time (concentration) range involved requires a measurement system of great bandwidth, in fact one sufficiently wide that it can measure the hydrated electron decay directly. Even if one has the appropriate rate con-

stant data, one finds that with high scavenger concentrations and with the effects of short tracks (which have been estimated to account for more than 20% of the energy deposited by 1-MeV electrons¹³), the predictions of eq 1 as applied to aqueous systems are only approximate. It appears then that the agreement of previous work that attempts to determine the time dependence of the hydrated electron with the predictions of the diffusion kinetic model is fortuitous. Specifically (1) the results of Koules-Pujo, *et al.*, said to agree with the diffusion kinetic model may be more correctly explained by a variable $k(e_{aq}^- + H^+)$ and a measured e_{aq}^- dependence which differs from that predicted by the model, and (2) the Laplace transform technique for going from product yield *vs.* scavenger concentration to the time dependence of the hydrated electron is not equivalent to an experimental measurement.

References and Notes

- (1) Work performed under the auspices of the U. S. Atomic Energy Commission.
- (2) I. G. Draganic and Z. D. Draganic, "The Radiation Chemistry of Water," Academic Press, New York N. Y., 1972, Chapter 6.
- (3) H. A. Schwarz, *J. Phys. Chem.*, **73**, 1928 (1969).
- (4) A. Kuppermann "Radiation Research, 1966," G. Sillinj, Ed., North Holland Publishing Co., Amsterdam, 1967, p 212.
- (5) (a) A. M. Koules-Pujo, B. D. Michael, and E. J. Hart, *Int. J. Radiat. Phys. Chem.*, **3**, 333 (1971); (b) T. G. Balkas, J. H. Fendler, and R. H. Schuler, *J. Phys. Chem.*, **74**, 4497 (1970).
- (6) J. W. Hunt, R. K. Wolff, M. J. Bronskill, C. D. Jonah, E. J. Hart, and M. S. Matheson, *J. Phys. Chem.*, **77**, 425 (1973).
- (7) A. Kuppermann, *Actions Chim. Biol. Radiat.*, **5**, 85 (1961).
- (8) C. D. Jonah, E. J. Hart, and M. S. Matheson, *J. Phys. Chem.*, **77**, 1838 (1973).
- (9) M. J. Bronskill, R. K. Wolff, and J. W. Hunt, *J. Chem. Phys.*, **53**, 4201 (1970).
- (10) A. Hummel, *J. Chem. Phys.* **49**, 4840 (1968).
- (11) D. L. Phillips and M. Gabriel, Internal Report, Program C146, Applied Mathematics Division, Argonne National Laboratory, Argonne, Ill., 1967.
- (12) S. H. Crandall, "Engineering Analysis," McGraw-Hill, New York, N. Y., 1956, Chapter 6.
- (13) A. Mozumder and J. L. Magee, *J. Chem. Phys.*, **45**, 3332 (1966).

Raman Spectroscopic Study of Binary Systems. I. Molecular Association in the Ammonia Hexadeuteriobenzene Liquid System

John H. Roberts*

Laboratoire des Métaux Alcalins dans l'Ammoniac Liquide, Equipe de Recherche Associée au CNRS, Faculté Libre des Sciences et Hautes Etudes Industrielle, 59046 Lille, France

and Bertin J. De Bettignies

Laboratoire de Spectroscopie Raman, C.5, Université des Sciences et Techniques de Lille, 59650 Villeneuve D'Ascq, France
(Received May 22, 1974)

Publication costs assisted by the Centre de Spectrochimie

The Raman spectra of solutions of ammonia and hexadeuteriobenzene have been measured at ambient temperature. Although ν' and ν_3 of ammonia decrease in intensity relative to ν_1 and $2\nu_4$, these bands have been observed in very dilute solutions by means of repetitive scanning of the spectrum with data accumulation. The results show there are no specific hydrogen-bonded interactions between ammonia molecules and hexadeuteriobenzene molecules, and the hydrogen-bonded structure of liquid ammonia breaks up as the ammonia is diluted with benzene. The results support the four-band resolution of the N-H stretching region of liquid ammonia and the application of the mixture model to liquid ammonia.

Introduction

There has been considerable interest in the structure of binary solvent systems.¹ Interest in systems with liquid ammonia has arisen because of the general problem of the structure of hydrogen-bonded liquids,²⁻⁴ radiation chemistry of the solvated electron in mixed systems,^{5,6} nmr studies of the structure of ammonia-containing systems,⁷ and the interpretation of the N-H stretching region of the Raman spectrum of liquid ammonia.^{3,8-10}

The ammonia-benzene system has been used as a medium for many organic reactions of great synthetic utility.¹¹ This is due to the formation of the solvated electron upon dissolution of alkali metals in liquid ammonia and the enhancement of the solubility of organic substrates by the addition of benzene to the system. In view of the interest in these reactions a structural study of the ammonia-benzene system seemed warranted.

Hydrogen-bonded liquid structures and the problem of mixture models *vs.* continuum models for the liquid state have been discussed in detail.¹ Recent spectroscopic studies of ammonia-containing systems have been interpreted in terms of mixture models.^{2-4,8,9,12} However, the interpretation of details of the N-H stretching region of the Raman spectrum of liquid ammonia has led to some controversy, even though there is generally good agreement in the experimental results from different laboratories.^{3,8-10,13,15} The resolution of the spectrum in this region into four bands has been accomplished mathematically by use of a computer program⁸ and by use of a Du Pont 310 curve analyzer.^{9,13,16} As in aqueous systems¹⁷ more bands are expected in the liquid state than in the gas due to the formation of various hydrogen-bonded species.^{2,3,8,9,16} The spectrum of liquid is further complicated by Fermi resonance between ν_1 , the symmetric stretching mode of ammonia molecules with C_{3v} symmetry, and a component of $2\nu_4$, the harmonic of the asymmetric bending mode.^{8,10,14,15}

Recent interest in the π -donor properties of benzene in hydrogen-bonded systems provides further reason to exam-

ine the ammonia-benzene system.^{18,19} Whereas water is miscible with ammonia but relatively insoluble in benzene, ammonia is miscible with both water and benzene. For this reason one could not *a priori* predict the relative strengths of the possible hydrogen-bond interactions in the ammonia-benzene system. The results of this study contribute to a better understanding of all of the above-mentioned phenomena.

Experimental Section

The ammonia used in these experiments was doubly distilled from a sodium-ammonia solution and was degassed by freezing and pumping on the solid. Spectroscopy grade hexadeuteriobenzene (Merck) was used directly or was used after distillation from sodium. The samples were prepared by placing a weighed quantity of hexadeuteriobenzene in a 6-mm o.d. Pyrex tube of 1-mm wall thickness. The sample was frozen and degassed on a vacuum line before ammonia was distilled into the tube, which was then sealed off and weighed.

The Raman spectra were recorded on an instrument comprising a Coderg double monochromator equipped with a rapid-scanning system and a system for data accumulations²⁰ using the 5145-Å line or the 4880-Å line of an argon ion laser, Spectraphysics Model 164 AC, as an excitation source. The system was calibrated with carbon tetrachloride and benzene, and the plasma lines of the laser and the spectra were recorded at ambient temperature.

Resolution of the experimental spectra into individual bands was accomplished by means of program RESOL⁸ or with a Du Pont 310 curve analyzer.

Results

Figure 1 shows the resolved Raman spectrum of the N-H stretching region of ammonia in a solution with a 9:1 mole ratio of NH_3 to C_6D_6 . In addition to the experimental envelope (squares) and the calculated bands (circles), an error curve is included which represents the difference between

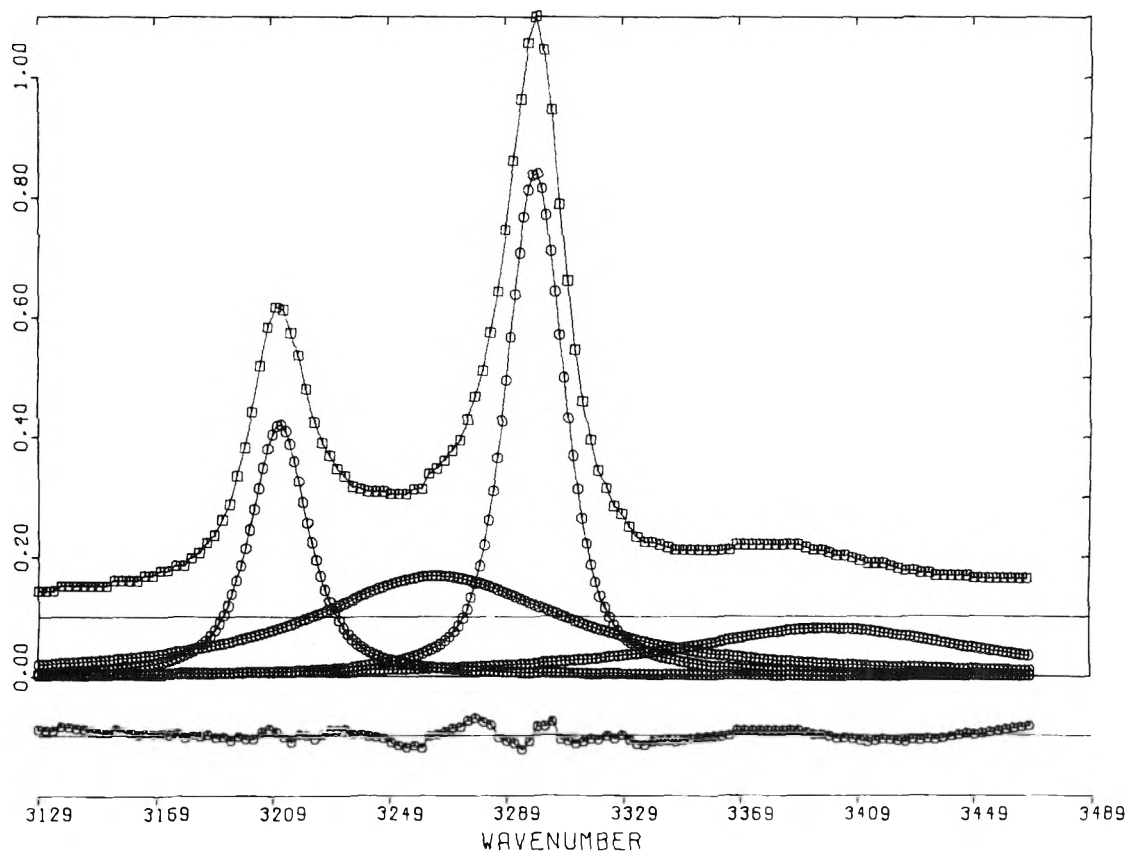


Figure 1. Resolved Raman spectrum of the N-H stretching region of a solution with a 9:1 mole ratio of NH_3 to C_6D_6 at 25° . See text for description of symbols.

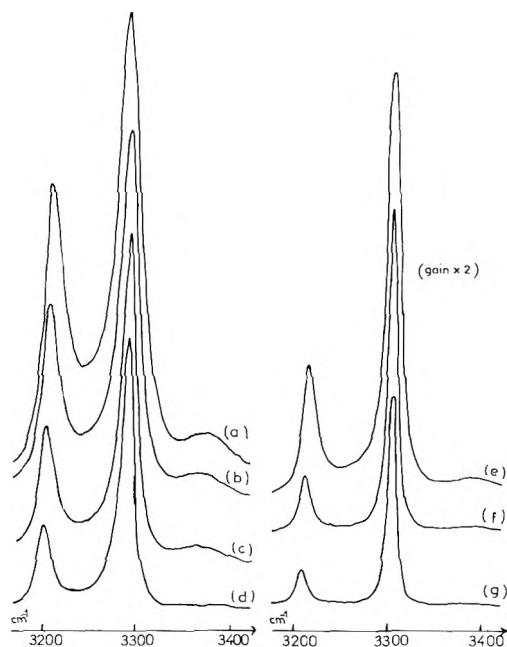


Figure 2. Experimental spectrum of the N-H stretching region at different concentrations: (a) pure NH_3 ; (b) 9 NH_3 :1 C_6D_6 ; (c) 3 NH_3 :1 C_6D_6 ; (d) 1.5 NH_3 :1 C_6D_6 ; (e) 1.3 C_6D_6 :1 NH_3 ; (f) 2.5 C_6D_6 :1 NH_3 ; (g) 5.6 C_6D_6 :1 NH_3 ; for (e), (f), and (g) the sensitivity is multiplied by 2.

the experimental curve and the calculated intensities. Previous workers have assigned the bands as follows: $2\nu_4$ at 3212 cm^{-1} , ν' at 3265 cm^{-1} , ν_1 at 3298 cm^{-1} , and ν_3 at 3388 cm^{-1} .⁸⁻¹⁰ ν' is the ν_1 band of ammonia molecules with C_s

TABLE I: Raman Stretching Frequencies^a of Ammonia

NH_3 : C_6D_6 mole ratio	$2\nu_4(\text{p})^b$	$\nu'(\text{p})$	$\nu_1(\text{p})$	$\nu_3(\text{dp})^c$	Mol % NH_3
	3212	3265	3298	3388	100
9:1	3210	3265	3299	3397	90
4.6:1	3210	3264	3300	3402	82
3:1	3211	3255	3301	3409	75
1.5:1	3213		3301		60
1:1.3	3213		3302		43
1:2.5	3210		3303		29
1:3.6	3208		3305		22
1:5.6	3210		3303		15

^a In cm^{-1} . ^b p = polarized. ^c dp = depolarized.

symmetry and has been labeled in this way to avoid confusion with ν_1 of ammonia molecules with C_{3v} symmetry. The spectrum of hexadeuteriobenzene has no bands in the $3100\text{--}3500\text{ cm}^{-1}$ region, which permits observation of the ammonia bands without interference. In none of the experiments performed on solutions of NH_3 and C_6D_6 was there any evidence that proton-deuterium exchange had occurred, as is observed for $\text{D}_2\text{O}\text{--}\text{NH}_3$ mixtures.⁴

Figure 2 shows the Raman spectrum of pure ammonia and of ammonia in several ammonia-hexadeuteriobenzene solutions. The evolution of the spectrum with decreasing ammonia concentration is dominated by the decrease in intensity of ν' and ν_3 relative to ν_1 and $2\nu_4$, which are in Fermi resonance. The frequency shifts, Table I, are small but regular as can be seen from Figure 3. Positions for ν' and ν_3 are not given for the more dilute solutions because the band

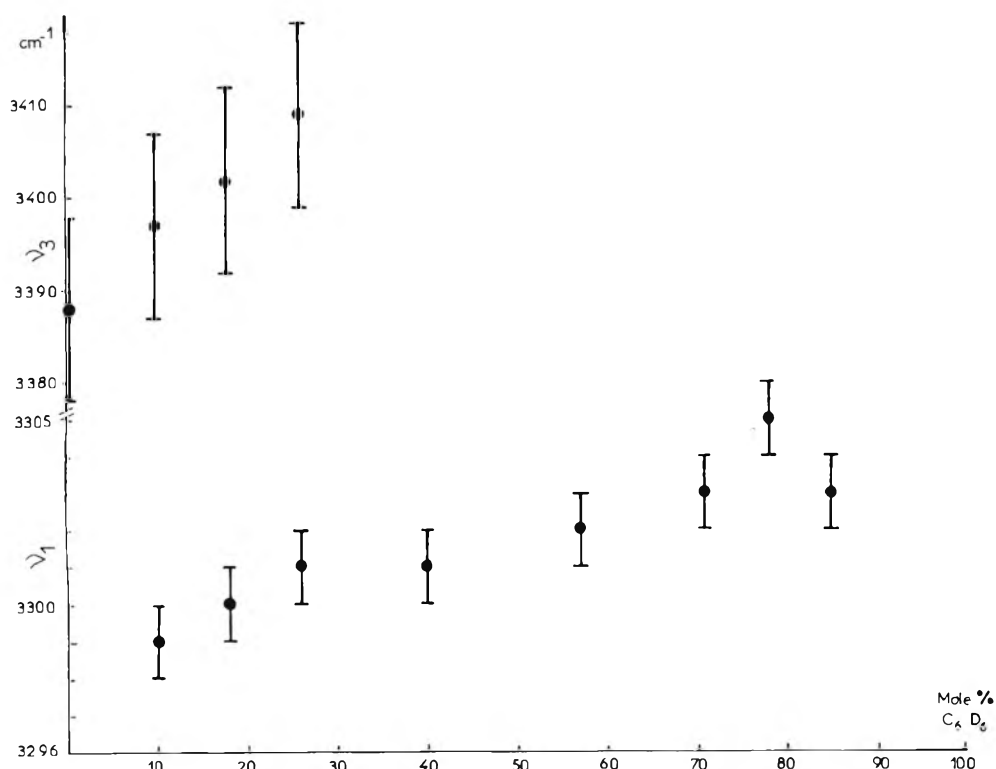


Figure 3. Change of the frequencies (in cm^{-1}) ν_3 and ν_1 of ammonia with the concentration of benzene.

maxima of these weak, broad bands are very difficult to determine with accuracy. A data accumulation system was used to observe ν_3 and ν' in the dilute solutions. With 36 scans ν_3 was observed in all the solutions studied, even though it was of very low intensity. The gradual decrease in ν' continues until in the most dilute solutions there is almost no intensity in the 3265-cm^{-1} region.

Also apparent in Figure 2 is the decrease in the half-widths of ν_1 and $2\nu_4$ with decreasing ammonia concentration, and in the solutions of very low ammonia concentration the spectrum resembles that of gaseous ammonia.²¹ Figure 4 shows the changes in half-widths of ν_1 and $2\nu_4$ with decreasing ammonia concentration. The bending modes of ammonia, which occur at lower frequencies, were obscured due to overlap with the bands of benzene. No significant changes were observed in the portion of the spectrum attributed to hexadeuteriobenzene.

Discussion

There are several possible types of interactions which could occur in the ammonia-benzene binary solvent system. Conceivably, there could be a specific interaction between an N-H of ammonia and the π -electron cloud of benzene similar to the C-H interaction with benzene systems.²²⁻²⁴ If this were the case, π -donor complexes of 1:1 and/or 1:2 benzene to ammonia ratios could be envisaged. Another possibility for a hydrogen-bond type interaction would be between the C-H of benzene and the lone pair on nitrogen of ammonia. Evidence for this type of association could best be obtained by observing ν_2 , the symmetric bending mode of ammonia which is particularly sensitive to interactions affecting the lone pair.^{12,25} Although ν_2 cannot be observed independently in any of the four (NH_3 , ND_3 , C_6D_6 , C_6H_6) binary systems due to the many intense ben-

zene bands in the $700\text{-}1100\text{-cm}^{-1}$ region, an interaction of this sort would also affect the stretching modes to some extent and this is not observed. Also, previous work has shown that at least three halogen atoms are required on the benzene ring before the remaining C-H groups are acidic enough to participate in C-H...N hydrogen bonds,²⁶ so this specific interaction would not be expected to occur in this system. Since there are no breaks in the plots of frequency shift of the bands as a function of concentration, Figure 3, it appears that definite ammonia-benzene complexes do not form in this system at ambient temperature, and thus no specific hydrogen-bonded interaction occurs between ammonia and hexadeuteriobenzene molecules.

It has recently been recognized that the N-H stretching region of the Raman spectrum of liquid ammonia consists of four bands^{3,8,9,13} and is further complicated by Fermi resonance.¹⁰ The fourth band, referred to here as ν' , appears at a frequency intermediate between ν_1 and $2\nu_4$, the bands which are in Fermi resonance. The features of the spectrum have been discussed in terms of the presence of two symmetry species of ammonia molecules in solution, and ν' has been attributed to the symmetric stretch of C_s ammonia molecules whose symmetry has been lowered from C_{3v} by the formation of a hydrogen bond of the type N-H...N.⁸

The results of this study show that as the concentration of ammonia in the ammonia-benzene system decreases, ν' decreases in intensity. This indicates that C_s ammonia is being converted into C_{3v} ammonia; *i.e.*, with increasing dilution by benzene the hydrogen-bonded structure of liquid ammonia breaks down and the ammonia molecules become isolated. The decrease in the half-widths of ν_1 and $2\nu_4$ are a result of the increased freedom of the unbound isolated ammonia molecules.²⁴ The trends in frequency shift of the N-H stretching bands, ν_1 and ν_3 , to higher frequency

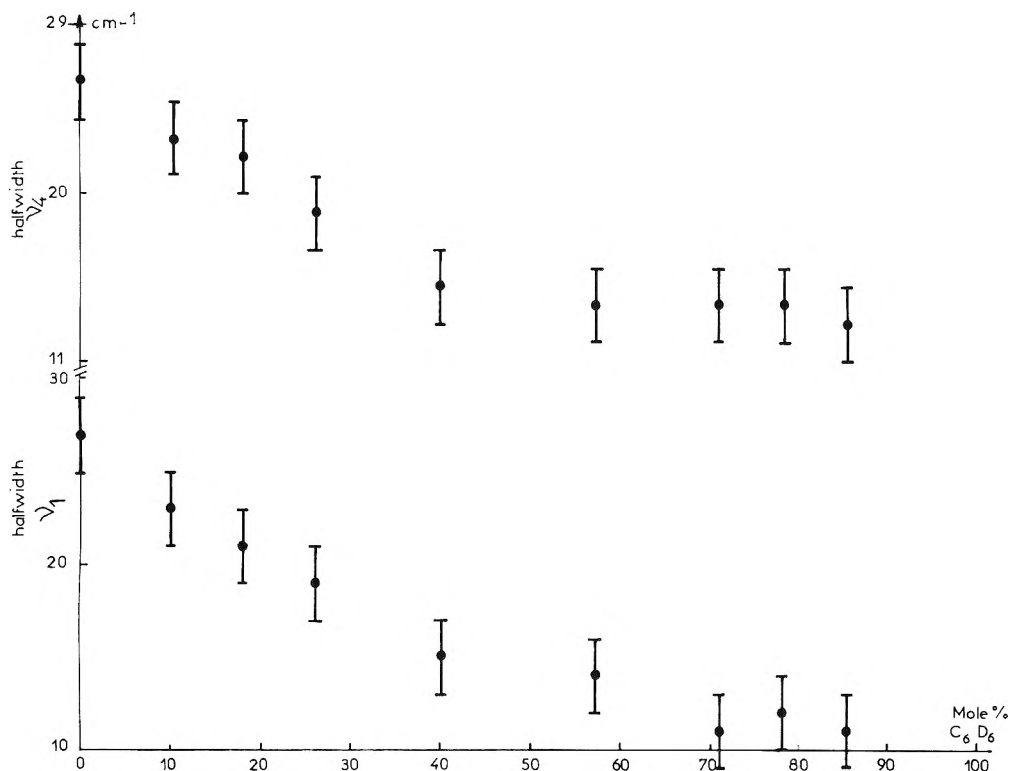


Figure 4. Influence of the concentration of C₆D₆ on the half-width (in cm⁻¹) of ν₁ and 2ν₄ of ammonia.

are also consistent with a structure-breaking effect as the ammonia becomes more dilute.²⁴ Indeed, the general evolution of the spectrum from pure liquid ammonia to a spectrum resembling gaseous ammonia in the solutions of low ammonia concentration supports this view.

Further evidence for this interpretation comes from the Raman spectrum of NH₃ in the NH₃-CCl₄ system.^{9,27} No hydrogen-bonded interactions between NH₃ and CCl₄ are detected as would be expected, and the breakup of the structure of liquid ammonia as a function of dilution by CCl₄ can easily be observed. The evolution of the spectrum in the N-H stretching region in the NH₃-CCl₄ system is analogous to that of the NH₃-C₆D₆ system.

Conclusions

No specific hydrogen-bonded interactions between ammonia molecules and benzene molecules are observed in this binary solvent system. As ammonia is diluted with benzene, the hydrogen-bonded structure of ammonia breaks up and the ammonia molecules become isolated. Changes in the N-H stretching region of the Raman spectrum support the resolution of this region into four bands. These results are further evidence for the mixture model of liquid ammonia.

Acknowledgments. We wish to thank the National Science Foundation and the Centre National de la Recherche Scientifique for the Exchange of Scientists Grant to J. H. R. We also wish to thank Dr. J. J. Lagowski for making program RESOL available to us and professor J. P. Mathieu for the use of his curve analyzer.

References and Notes

- (1) A. K. Covington and P. Jones, "Hydrogen-Bonded Solvent Systems," Taylor and Francis, London, 1968.
- (2) J. H. Roberts and J. J. Lagowski, "Electrons in Fluids," J. Jortner and N. R. Kestner, Ed., Springer-Verlag, Berlin, 1973.
- (3) J. H. Roberts, A. T. Lemley, and J. J. Lagowski, *Spectrosc. Lett.*, **5**, 271 (1972).
- (4) J. H. Roberts and J. J. Lagowski, Abstracts, 165th National Meeting of the American Chemical Society, Dallas, Tex., April 1973, No. PHYS 147.
- (5) U. Schindewolf, "Metal-Ammonia Solutions," J. J. Lagowski and M. J. Sienko, Ed., Butterworths, London, 1970.
- (6) J. L. Dye, M. G. De Backer, and L. M. Dorfman, *J. Chem. Phys.*, **52**, 6251 (1970).
- (7) M. Alei, Jr., and A. E. Florin, *J. Phys. Chem.*, **72**, 550 (1968).
- (8) A. T. Lemley, J. H. Roberts, K. R. Plowman, and J. J. Lagowski, *J. Phys. Chem.*, **77**, 2185 (1973).
- (9) D. J. Gardiner, R. E. Hester, and W. E. L. Grossman, *J. Raman Spectrosc.*, **1**, 81 (1973).
- (10) B. De Bettignies and F. Wallart, *C. R. Acad. Sci., Ser. B*, **271**, 640 (1970).
- (11) H. Smith, "Organic Reactions in Liquid Ammonia," Interscience, New York, N. Y., 1963.
- (12) J. Corset and J. Lascombe, *J. Chim. Phys. Physicochim. Biol.*, **64**, 665, 1707 (1966).
- (13) D. J. Gardiner, R. E. Mester, and W. E. L. Grossman, *J. Chem. Phys.*, **59**, 175 (1973).
- (14) T. Birchall and I. Drummond, *J. Chem. Soc. A*, 1859 (1970).
- (15) M. Schwartz and C. J. Wang, *J. Chem. Phys.*, **59**, 5258 (1973).
- (16) B. De Bettignies, unpublished results.
- (17) G. E. Walrafen, ref 1, p 9.
- (18) T. S. Pang and S. Ng, *Spectrochim. Acta, Part A*, **29**, 207 (1973).
- (19) A. S. Kertes and F. Grauer, *J. Phys. Chem.*, **77**, 3107 (1973).
- (20) F. Waliart, Thesis, Lille, 1970.
- (21) L. M. Lewis and W. V. Houston, *Phys. Rev.*, **44**, 903 (1933).
- (22) C. M. Huggins and G. C. Pimental, *J. Chem. Phys.*, **23**, 251 (1955).
- (23) L. W. Reeves and W. G. Schneider, *Can. J. Chem.*, **35**, 251 (1957).
- (24) G. C. Pimental and A. L. McClellan, "The Hydrogen Bond," W. H. Freeman, San Francisco, Calif., 1960.
- (25) K. R. Plowman and J. J. Lagowski, *J. Phys. Chem.*, **78**, 143 (1974).
- (26) A. Allerhand and P. Von R. Schleyer, *J. Amer. Chem. Soc.*, **85**, 1715 (1963).
- (27) J. H. Roberts and B. J. De Bettignies, to be submitted for publication.

Electron Paramagnetic Resonance of a Nitroxide Adsorbed on Silica, Silica-Alumina, Alumina, and Decationated Zeolites

G. P. Lozos and B. M. Hoffman*

Department of Chemistry, Northwestern University, Evanston, Illinois 60201 (Received May 28, 1974)

Publication costs assisted by the Petroleum Research Fund

Di-tert-butyl nitroxide (DTBN) has been adsorbed on silica, silica-alumina, alumina, and decationated Y and X zeolites. The surface epr spectra exhibit well-resolved nitrogen hyperfine splittings (hfs) from DTBN adsorbed at two distinct types of sites. One spectrum arises from DTBN hydrogen bonded to surface hydroxyls. The second arises from complexation with a surface Al^{3+} and exhibits ^{27}Al hfs. In some cases, the existence of a strongly acidic ($\text{Br}\phi\text{nsted}$) site is inferred. The trends in epr results observed upon comparing different surfaces are compared to trends in catalytic activity, and poisoning experiments with CO_2 give further connection with catalytic reactions. Surface nitroxides exhibit rotational and translational motion, and from observations of the manner in which they partition themselves between H bonding and complexation to Al^{3+} , the enthalpy change for transfer of a nitroxide from surface hydroxyl to aluminum coordination is positive and estimated to be $\sim +5$ kcal/mol.

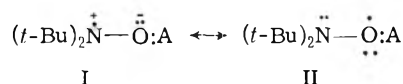
Introduction

An understanding of the structure and nature of the dative bonds formed in chemisorption is important in surface chemistry and heterogeneous catalysis. Chemisorption equilibria and thermodynamics can be determined by classical methods¹ but investigations of catalytic reaction mechanisms also demand a knowledge of surface interactions on a molecular level.

In recent years, continuing efforts have been made to obtain this knowledge by use of various nonclassical techniques.²⁻⁶ As one such method, electron paramagnetic resonance (epr) has been increasingly successful in extending our understanding of the microscopic properties of catalytic surfaces.⁷ These studies have the limitation that a paramagnetic species must be present but simultaneously the virtue that the unpaired spin is selectively observed. Diatomic radicals NO^8 and O_2^- ⁹ are particularly useful because of the sensitivity of their spectra to the strong local fields at a catalytic surface. Large organic radicals have been useful in studies of motional effects or as monitors of chemical reactions.¹⁰

It has recently been shown that the epr parameters of adsorbed aliphatic nitroxides are sensitive to the nature and strength of the perturbation caused by interaction with a surface. Evreinov, *et al.*, have reported studies of the adsorption of tetramethylpiperidine-*N*-oxyl from benzene or toluene solution onto γ -alumina, Ga_2O_3 , and NaX and NaY zeolites,¹¹ and we reported observations of *di-tert*-butyl nitroxide (DTBN) adsorbed from the gas phase onto silica and silica-alumina surfaces.¹²

The nitroxide, acting as a Lewis base, coordinates to an electron acceptor (A) through the nonbonding electrons of the nitroxide oxygen. The unpaired π electron does not directly participate in the dative bond but serves as a probe of the electronic structure of the complex. Coordination causes a redistribution in the N-O π -electron system which is equivalent to increasing the contribution of resonance



structure I: charge density shifts toward oxygen, and spin density shifts toward nitrogen.

The redistribution of spin density causes the parallel component of the nitroxide ^{14}N hyperfine splitting (hfs), A_N (see below), to increase and the change is monotonic with the strength of the interaction.¹³ The measured value of A_N thus forms the basis of a scale for measuring the electron-pair acceptor strengths of Lewis acids. Such a scale is of significance because reactivity in cracking or isomerization reactions is related to surface acidity.¹⁴ In some cases, hfs from the surface site can also be observed, unambiguously identifying the coordinating atom and giving further information about bonds between adsorbate and surface. Since nitroxides also form complexes with molecular Lewis acids in free solution,^{13,15-17} for the first time a radical may be used to compare the properties of a surface site with those of a well-defined solution species.

We have now studied *di-tert*-butyl nitroxide adsorbed on silica, silica-alumina, alumina, and decationated Y and X zeolites. The surface epr spectra exhibit well-resolved nitrogen hyperfine splittings from DTBN adsorbed at two distinct types of sites. One spectrum arises from DTBN hydrogen bonded to surface hydroxyls. The second arises from complexation with a surface aluminum and exhibits ^{27}Al hfs.

The trends in epr results observed upon comparing different surfaces are compared to trends in catalytic activity, and poisoning experiments with CO_2 give further connection with catalytic reactions. Surface nitroxides exhibit rotational and translational motion, and from observations of the manner in which they partition themselves between H bonding and aluminum complexation, we further obtain thermodynamic information about relative enthalpies of interaction.

Experimental Section

The catalysts used were silica-alumina catalysts F1-13 (13% alumina), F1-25 (25% alumina), and silica gel, grades 950 and 59, all from Grace Davison Chemical Co., γ -alumina (SB catapal) from Continental Oil, the ammonium form of the Y zeolite from Strem Chemicals, and 13X zeolite

from the Linde Co. The ammonium form of the 13X zeolite was prepared by exchange in either NH_4NO_3 or $\text{NH}_4\text{O}-\text{COCH}_3$ solution. DTBN was obtained from Eastman Organic Chemicals and purified by vacuum distillation.

Sample preparation employed a high-vacuum system. A 25–50-mg catalyst sample was placed in a 3-mm o.d. fused-silica tube with a Teflon valve, heated in oxygen for 8 hr, and then rehydrated with water vapor at room temperature for 12 hr. As noted below this treatment was varied for the zeolites. The solid was then heated under vacuum from room temperature to a desired activation temperature (T_A) between 110 and 500° over a period of 8 hr and held at the final temperature for at least 2 hr. For the zeolite catalysts this produced the decationated form. An ultimate pressure of 10^{-5} Torr was obtained. An epr spectrum of the activated catalyst was recorded for reference.

The nitroxide was stored under vacuum in a reservoir with a calibrated bulb. From a vapor pressure–temperature curve for DTBN,¹⁸ the calibrated bulb could be filled with a known pressure of DTBN by holding the reservoir at a fixed temperature (–18 to +25°). This vapor was transferred to the sample immersed in liquid nitrogen. Upon initial addition of DTBN a strong, unresolved, spin-exchanged signal was observed. To distribute the nitroxide evenly throughout the catalyst and eliminate high local concentration, the samples were warmed, in most cases at about 50°.

Epr spectra were taken on a Varian Associates X-band Model E-4 spectrometer. Using additional 80-Hz field modulation and phase lock amplifier, a second-derivative presentation was available. The microwave frequency was measured with a modified Sage Corp. tunable coherent synchronizer, a prescaler, and a Transitor Specialties digital frequency counter. Differential g values were also determined with reference to a saturated potassium carbonate solution of peroxyaminedisulfonate standard ($g = 2.0055$, $a_N = 13.09$ G)¹⁹ as described elsewhere.¹³ Unless noted, epr spectra were taken in liquid nitrogen (77°K). Variable-temperature studies employed a flow of gaseous N_2 (100–400°K).

Computer simulation of axial epr powder spectra were produced by a program which assumes a random orientation of spins and performs a numerical integration over an octant of the unit sphere utilizing a Gauss–Legendre integration over the polar angle theta. An anisotropic gaussian line width was used. Provisions were included for adding contributions from different species with specified relative concentration.^{19c}

Although single-crystal studies require a more complicated spin Hamiltonian,²⁰ a randomly oriented ensemble of nitroxide free radicals exhibits a “powder” spectrum, designated type I, which may be described with the axial spin Hamiltonian

$$\mathcal{H} = g_{\parallel}\beta H_z S_z + g_{\perp}\beta(S_x H_x + S_y H_y) + A_N S_z I_z + B_N(S_x I_x + S_y I_y)$$

Both A_N and g_{\parallel} were directly measured from appropriate spectral features. A_N is the parameter most sensitive to surface interactions. In order to emphasize the effects of these interactions, we frequently reference the measured values to that in the noninteracting solvent n -hexane ($A_N^{n\text{-hexane}} = 34.1$ G) and discuss below $\Delta A_N = A_N - 34.1$. Because of the lack of resolution in the “perpendicular” region, g_{\perp} and B_N , which was less than the line width em-

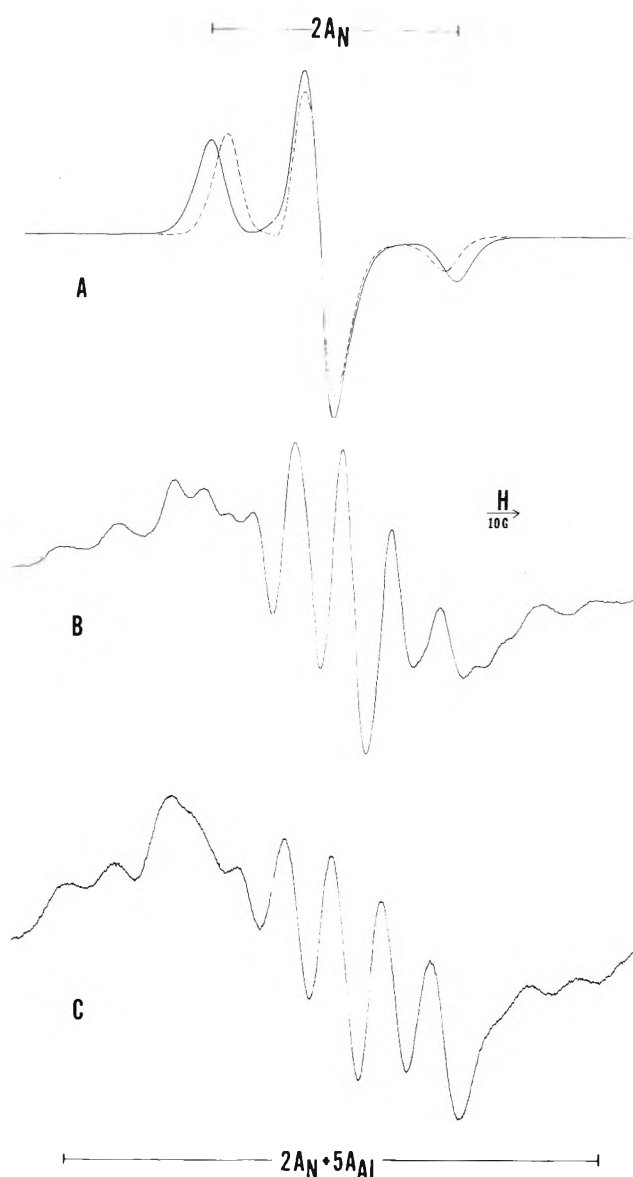


Figure 1. Epr of DTBN at 77°K: (A) type I spectrum on silica–alumina (—) and that in frozen toluene solution (---); (B) type II spectrum on silica–alumina; (C) spectrum of the AlCl_3 molecular complex.

ployed, were estimated by computer simulations. Neither could be determined very accurately. Simulation of type I spectra are excellent (see ref 16b), and $B_N = 6 \pm 1$ G gave acceptable results in all cases.

When the nitroxide interacts with a metal nucleus which has a magnetic moment, there is an added term in the spin Hamiltonian

$$\mathcal{H}' = A_M S_z I_z^M + B_M(S_x I_x^M + S_y I_y^M)$$

and each of the nitrogen hfs lines is split again. For ^{27}Al ($I = 5/2$) the multiplicity is 6, and such a spectrum is designated type II (Figure 1B). A_{Al} and A_N in type II spectra were frequently difficult to measure accurately since the lines in the outer wings were broad, leading to larger errors than for type I spectra. Since B_{Al} is large, splittings in the perpendicular region were well resolved and easily measured. A_N , A_{Al} , and B_{Al} obtained from the appropriate spectral features were refined with simulations. Complications arise from type I contribution of less than 10% to type II spectra,

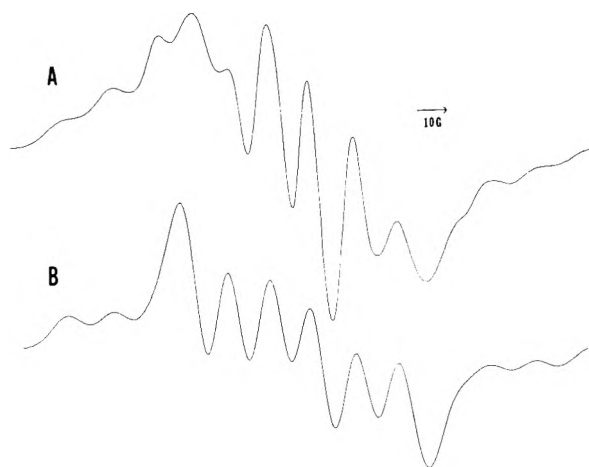


Figure 2. Type II epr spectrum and simulation of DTBN on silica-alumina (77°K): (A) first-derivative spectrum; (B) simulation with parameters in Table I and a gaussian line width of 11 G.

and this contribution was incorporated in simulations with some improvement. The best computer fit involving an axial spin Hamiltonian is illustrated in Figure 2. Uncertainties in measuring the epr parameters resulted both from the actual measurement errors and from a slight variation of parameters with sample and surface treatment whose cause was not apparent. Table I lists the larger of these uncertainties for each parameter.

Results

Silica. Silica samples were activated at either 125 or 500° with equivalent results. The nitroxide was added and distributed over the catalyst surface by gently heating while evacuating. When as few as 2×10^{14} molecules of nitroxide were added per milligram of sample, a strong epr signal of type I was observed. Grades 950 and 59 silica gel gave essentially the same results.

In these spectra, A_N was larger than that for a frozen solution of DTBN in an inert solvent (toluene) (Figure 1), indicating a surface interaction. The value of A_N is in the range found for H-bonded DTBN,¹³ and thus we attribute the spectrum to nitroxide hydrogen bonded to surface silanol groups. In particular, A_N is close to that observed for DTBN in solution with phenol. As with DTBN in hydrogen-bonding media, no splittings are resolved from the surface proton. Rehydrating with D₂O instead of H₂O before activation did not produce a decrease in line width, as would be expected if hfs from the hydrogen-bonded proton were a large contribution to the line width.

Only extended evacuation at high temperature could remove DTBN from silica. For example, in one experiment, heating a sample (3×10^{14} molecules of DTBN/mg of catalyst) at 600° while evacuating for 16 hr still left a strong signal reduced to 10% of its original value. Treatment with water vapor also did not change the spectrum, but a strong base such as pyridine displaced the adsorbed nitroxide, resulting in a room-temperature solution spectrum and liquid nitrogen powder spectrum typical for DTBN dissolved in pyridine ($a_N = 15.3$ G, $A_N = 35.2$ G). Pumping off pyridine resulted in the reappearance of the original spectrum indicating that excess pyridine is removed while the nitroxide stays behind.

Silica-Alumina. Pretreated samples were activated at 125, 215, 415, or 500°; both 13 and 25% alumina gave essen-

TABLE I: Spin-Hamiltonian Parameters for DTBN Complexed on Surfaces and in Solution^{a, b}

	Toluene	Phenol ^c	Silica, Silica-Alumina, Alumina	Decationated Y zeolite
Type I				
A_N	34.6 ^d	38.3 ^d	38.6	40-41
g_{\perp}	2.0079	2.0072	2.0072	2.0072
ΔA_N^e	0.5	4.2	4.5	~6.4
Type II				
	Alumina	Decationated Y zeolite	Silica-alumina	AlCl ₃
A_N	42.5	44.6	45.3	47.0
g_{\perp}	2.0058	2.0058	2.0058	2.0058
A_{Al}	14.6	14.8	16.4	14.6
B_{Al}	11.2	12.5	14.2 ^f	16.2
ΔA_N^g	8.4	10.5	11.2	12.9
a_{Al}^h	12.3	13.3	14.9	15.7
T_{Al}^i	2.3	1.5	1.5	-1.1

$$g_{\parallel} = 2.0023, B_N = 6 \pm 1 \text{ G}$$

^a Hfs constants in Gauss. Uncertainties in $A_1 = \pm 0.5$ and $g = \pm 0.0003$ unless indicated. $T = 77^\circ\text{K}$. ^b $g_{\parallel} = 2.0023 \pm 0.0002$ in all cases. ^c Reference 13. ^d ± 0.2 . ^e $\Delta A_N = A_N - 34.1$. ^f Corrected value from ref 12. ^g $a_{Al} = 1/3(A_{Al} + 2B_{Al})$; $T_{Al} = 2/3(A_{Al} - B_{Al})$.

tially the same results. Upon nitroxide addition, this catalyst, in contrast to pure silica, exhibited both the type I spectrum and also a type II spectrum with hyperfine splittings from both nitroxide ¹⁴N and surface ²⁷Al.

For samples activated at 215° or above, addition of relatively large amounts of nitroxide (2.5×10^{17} molecules/mg of catalyst) and distribution of the radical by warming (50-80°) under vacuum gave rise to the type I spectrum. The values of A_N were the same as those discussed above for DTBN on silica, but the apparent line width was greater, the result either of an underlying contribution from a type II spectrum (see below) or of a distribution of sites with slightly different A_N . At this level of loading, 10-15 times as many molecules of nitroxide had to be added to obtain the same signal strength as for silica.

With these samples ($T_A \geq 215^\circ$) addition of less nitroxide (8×10^{14} molecules/mg) and equilibration at room temperature gave a broadened type I spectrum. However, subsequent equilibration at 50-80° gave rise to a type II spectrum, but with an overall decrease of signal amplitude. Decomposition and signal loss increased with time and temperature of equilibration.

Spin Hamiltonian parameters for the type II spectrum are reported in Table I. A_N is substantially larger than for the type I spectra arising from surface hydrogen bonding. Because of the resolved hfs from an $I = 5/2$ nucleus, this spectrum is assigned to a nitroxide complexed with a surface aluminum ion. Table I includes for discussion below the calculated aluminum isotropic hfs, $a_{Al} = 1/3(A_{Al} + 2B_{Al})$, and dipolar interaction constant, $T_{Al} = 2/3(A_{Al} - B_{Al})$.

The type II spectrum is qualitatively similar to that for a frozen solution of the DTBN-AlCl₃ complex (Figure 1C). Some additional features of the surface spectrum can be partially accounted for by small contribution from a type I signal. Comparing the values of ΔA_N for complexed DTBN (Table I) shows the acceptor strength of the surface aluminum ions to be less than that of AlCl₃. The differences in

aluminum hfs further indicate that bonding in the two cases is not identical.

As indicated above, equilibration at 50–80° allows DTBN to migrate over the silica–alumina surface and preferentially bind to surface aluminum ions with at most a small proportion of the epr signal arising from H-bonding sites. If increasing amounts of DTBN are added to a given sample, both the epr signal strength and also the fraction of type I signal increase until a high-loading limit is reached where only the type I signal is observable. Further additions of nitroxide lead to spin exchange and loss of resolution. These results indicate that at 50–80° complexation to Al^{3+} is thermodynamically favored over H bonding to the surface.

Surprisingly, if a sample exhibiting a well-resolved type II spectrum is stored overnight in Dry Ice, the type I signal is restored. This change is reversible, for the type II signal returns after reequilibration at 50–80°. Thus, surface migration persists at –79° and at this temperature aluminum coordination is not thermodynamically favored.

Because the relative numbers of surface hydroxyl and aluminum sites is not known, the equilibrium constant for the transfer of DTBN from surface silanol to surface aluminum coordination is not available. However, equilibration at 323°K gives about 90% type II spectrum, but equilibration at 194°K (Dry Ice) gives about 90% type I spectrum. Thus, the enthalpy change (ΔH) for transfer to Al^{3+} is positive. An estimate of the value of ΔH may be obtained on the assumption that the number of both surface silanols and aluminum ions is greater than the number of bound nitroxides: $\Delta H \approx +5$ kcal/mol.

Only slight desorption of nitroxide from either type of site occurred upon evacuation at room temperature or 125°, but addition of pyridine (or methanol) removed all adsorbed nitroxide from the surface. Pumping off pyridine regenerated only a type I spectrum with the value of A_N given in Table I; pyridine presumably poisons the surface aluminum sites irreversibly. The regenerated type I spectrum exhibited slightly reduced line widths, perhaps because of a more uniform radical distribution or because pyridine poisoning removes an underlying type II contribution to the normal type I spectrum.

If a sample which exhibits the type II spectrum is exposed to air, the radical is destroyed and cannot be regenerated by evacuation. If instead water vapor is added, the nitroxide bound to Al^{3+} is displaced with little decrease in signal, and only a type I spectrum remains. Reevacuation cannot restore the type II signal and heating causes nitroxide decomposition.

CO_2 is known selectively to poison certain catalytic sites on alumina catalysts.²¹ A silica–alumina sample with DTBN coordinated to surface Al^{3+} was treated with 650 Torr of CO_2 and heated at 100° without displacing the bound radical. However, pretreatment of the activated catalyst with CO_2 before addition of the radical prevented DTBN from forming a surface aluminum complex. The catalyst had been activated for maximal surface aluminum site production ($T_A = 500^\circ$) and then treated with 650 Torr of CO_2 at room temperature and evacuated. Upon exposure to a low nitroxide dose, only the H-bonded type I spectrum was observed.

Activation at 125° should remove H bonded water leaving only those water molecules bound to surface aluminum ions. Such molecules act as strong Brønsted acids.^{3,14a,b} Interaction with such sites was not directly observed. How-

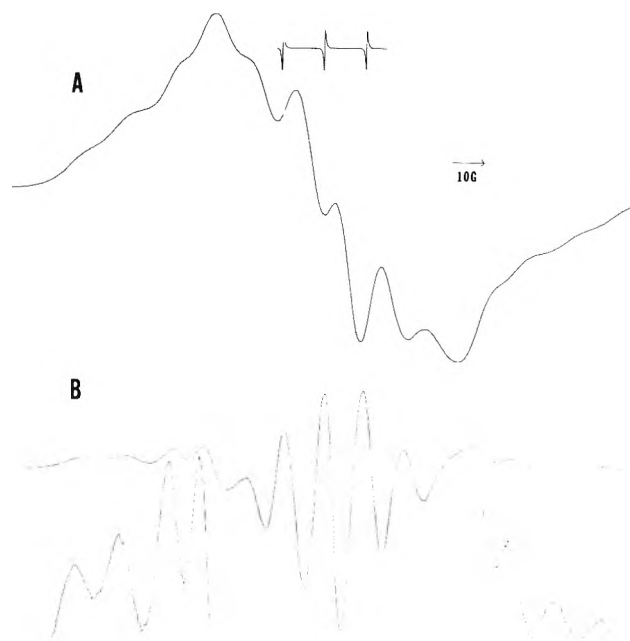


Figure 3. Type II epr spectrum of DTBN on alumina (77°K): (A) first-derivative spectrum with superimposed room-temperature spectrum of peroxyaminedisulfonate; (B) second-derivative spectrum with gain for parallel region increased three times.

ever, presumably because of reaction at these sites, decomposition of DTBN on samples with $T_A = 125^\circ$ is greater than for those activated at higher temperatures. When 3×10^{15} molecules of DTBN/mg of catalyst are added to such a sample, no signal is seen, and only with a total of 6×10^{15} molecules/mg is a weak type I spectrum detected. Evacuation at room temperature produced a very weak type II signal with a slight background of type I. The signals could be removed by pumping at room temperature or heating. It is particularly interesting that any type II signal could be seen and thus that some surface aluminum sites exist under such a mild treatment ($T_A = 125^\circ$).

Alumina. Samples were given the standard pretreatment and activated at 110 or 500°. For $T_A = 110^\circ$, loading with 7×10^{14} molecules of DTBN/mg of sample and warming at 50° gave only a strong type I signal with A_N and line width similar to those seen on silica–alumina. Thus, by epr, the Lewis acid property of the surface aluminol proton is not significantly different from that of silanol. Essentially no decomposition of DTBN occurred, in marked contrast to results for silica–alumina at a similar T_A . Treatment with pyridine gave the usual spectrum of DTBN in pyridine and, as for silica–alumina, evacuation restored the surface spectrum with decreased line width.

A sample activated at 500° showed no visible signal with 6×10^{15} molecules of DTBN/mg, but a total of 3×10^{16} molecules/mg gave a strong type I spectrum. Conversion to a type II spectrum without decomposition was achieved by heating (80–100°) under vacuum. Both ^{14}N and ^{27}Al hfs differed from those for the aluminum-coordinated nitroxide on silica–alumina (Table I). In particular, ΔA_N shows that the Al^{3+} of alumina is a poorer electron acceptor than that of silica–alumina. The line width in the parallel region was greater than for silica–alumina. To measure the poorly resolved parallel splittings, second-derivative epr detection was employed (Figure 3).

As with silica–alumina, surface migration of DTBN on

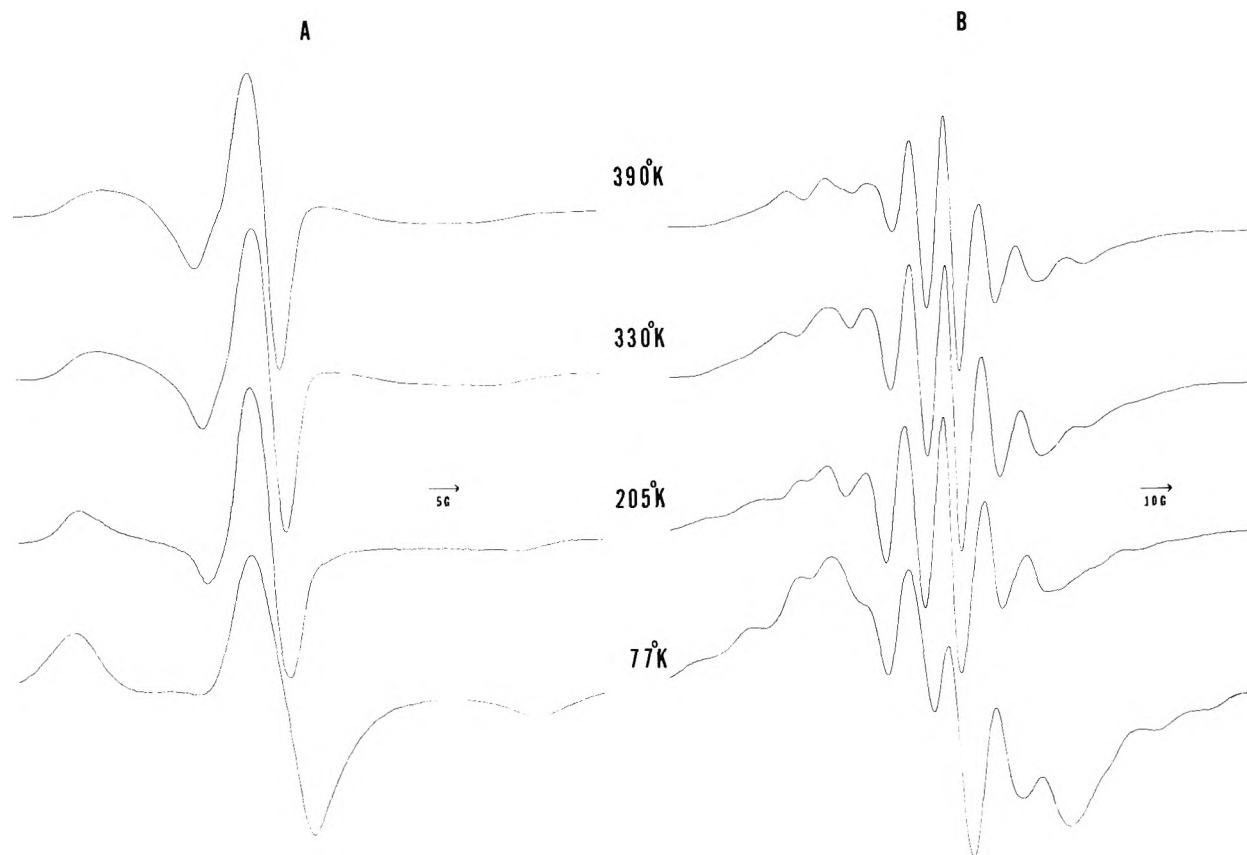


Figure 4. Variable-temperature epr spectra of surface DTBN: (A) type I spectrum on silica; (B) type II spectrum on silica-alumina.

alumina is reversible. Storage in Dry Ice overnight restored the type I spectrum ($\sim 90\%$ type I), and the type II could be reobtained by heating. No loss of signal occurred over a cycle. Water vapor completely displaced DTBN from surface aluminum sites without decomposition.

Y Zeolite. Since the crystalline lattice of decationated zeolites may be damaged by exposure to water vapor, some samples were given the standard calcination and rehydration pretreatment (S samples) and others were untreated (NS samples) before activation. S samples were only studied after activation at 500° and displayed no epr signals before addition of DTBN. NS samples were prepared with $T_A = 110, 330,$ and 500° and in all cases had a background spectrum with a fairly weak multiplet near $g = 2$.

For both types of samples considerable decomposition occurred upon addition of DTBN, and from 2×10^{16} to 1×10^{17} molecules of DTBN/mg were required to observe a broad type I epr signal. Brief equilibration at 50° typically decreased the signal to 25% and after prolonged heating the signal completely disappeared.

Nitroxides are not observed to coordinate to Al^{3+} on the sodium form of Y zeolites.¹¹ However, after addition of DTBN and brief equilibration at 50° , S samples of the decationated Y zeolites gave quite broadened type II signals; through the use of second-derivative detection the parallel hfs constant could be measured (Table I). A_N is similar to that of Al^{3+} on silica-alumina. Addition of water vapor displaced the DTBN from coordination to Al^{3+} , giving a slightly broadened type I signal with $\sim 50\%$ decomposition. Pumping at room temperature sharpened the signal. The value of A_N is considerably larger than that observed for the DTBN hydrogen bonded on the other surfaces.

DTBN addition to NS samples gave only very poorly resolved type I spectra. Heating degraded the signal and no type II signal was observed. On a sample with $T_A = 110^\circ$, the signal disappeared within 5 days at room temperature. Addition of water to an NS sample with $T_A = 500^\circ$ produced no change in signal.

13X Zeolite. Only one S sample ($T_A = 500^\circ$) and one NS sample ($T_A = 300^\circ$) were examined. In both cases, only type I quite broadened signals were observed. Warming under vacuum destroyed the paramagnetic centers.

Motional Effects. The spectra of surface DTBN at $77^\circ K$ (Figure 1) are associated with molecules rigidly immobilized with respect to the surface. For DTBN on silica we have verified this fact by observing that the spectrum is unchanged at $4.2^\circ K$. However at temperatures above $77^\circ K$, the nitroxide exhibits a hindered rotation both when surface hydrogen bonded (silica) and when complexed to surface aluminum ions (silica-alumina). These temperature dependences have been studied from 77 to above $400^\circ K$. In both cases, progressive decrease in observed A_N with temperature and other changes in the spectra are characteristic of increasing nitroxide mobility (Figure 4).²² However, even at $400^\circ K$ the rotation is still relatively slow. At the higher temperatures, the low-field peak(s) begins (begin) to merge with the center region and the high field peak(s) becomes (become) very broad so uncertainties in A_N increase. Second-derivative epr detection was used to permit more accurate determination of the position of these extrema. For aluminum-coordinated DTBN, A_{Al} does not appreciably change from its low-temperature limit (16.4 G) while B_{Al} decreases from 14.2 to 11.5 G over the total range of observation.

For a slowly tumbling nitroxide the separation of the extremal features in the epr spectrum decreases from the value $2A_N$ in a rigid matrix. If $2A_N(\tau)$ is an observed separation, the correlation time for rotation, τ , can be related to the ratio $\sigma = A_N(\tau)/A_N$.^{23,24} In particular, Freed and co-workers²⁴ found that for isotropic rotation $\tau = a(1 - \sigma)^b$, where the values of a and b depend on the rotational model employed. Although the motion of an adsorbed radical is unlikely to be isotropic, nevertheless σ is still a useful motional parameter.^{25,26}

Figure 5 is a plot of $\ln(1 - \sigma)$ vs. T^{-1} for surface H-bonded and aluminum-bonded DTBN. The rotational behaviors in these two cases are similar but clearly not identical. The solid lines are the result of least-squares fit to the linear relationship

$$\ln(1 - \sigma) = cT^{-1} + d \quad (1)$$

and the resulting parameters are given in the figure legend. Using Freed's equation, the existence of such linear behavior over large temperature ranges is consistent with a motional process for which the rotational correlation time is governed by a single activation energy

$$\tau = a(1 - \sigma)^b = \tau_0 e^{\Delta/RT}$$

where, from substitution in eq 1, $\Delta = Rbc$ is the energy of activation for rotation and $\tau_0 = ae^{bd}$ is the correlation time at "infinite" temperature. If, for illustrative purposes, we choose the values for isotropic Brownian diffusion $a = 0.54$ nsec and $b = -1.36$,²⁴ we obtain for surface H-bonded DTBN, $\Delta^I \approx 1.9$ kcal/mol, $\tau_0^I \approx 0.3$ nsec, and for surface Al-coordinated DTBN, $\Delta^{II} \approx 1.0$ kcal/mol, $\tau_0^{II} \approx 1.0$ nsec. Thus, for the two types of coordination we find the activation energies Δ and preexponential terms τ_0 are different. Alternatively the nature of the motional processes themselves may differ.

The unusually low values of Δ reflect the very weak temperature dependence of DTBN tumbling, while the large values of τ_0 show that the process being observed could not achieve solution-like motional behavior even at "infinite" temperature. For the H-bonded radical, the linear relationship is not observed for $T \lesssim 140^\circ\text{K}$ ($\sigma \sim 0.99$). The rigid-lattice limit is being reached and motion has become so slow that $\sigma \rightarrow 1$ and $\log(1 - \sigma)$ can no longer be reliably calculated. For aluminum coordination the low-temperature limit is not approached until an even lower temperature ($\lesssim 110^\circ\text{K}$) is reached.

Discussion

Hydrogen bonding of DTBN can be seen on all surfaces studied. The H-bonded complex on silica activated at any temperature is chemically stable under vacuum at all temperatures below 600° . Indeed, a sample with DTBN on silica sealed off under vacuum and kept at room temperature for months showed no decrease in signal. The H-bonded complex forms on alumina activated at low temperature and is also stable. In contrast, at low T_A , the silica-alumina surface is quite active in radical decomposition but somewhat less so at high T_A . In all these cases, the radical is also stable upon exposure to air and/or water vapor. The radical is unstable, however, on zeolites activated at any temperature.

The heat of adsorption for a molecule is typically 2-3 times its heat of vaporization plus a contribution of several kcal/mol if hydrogen bonding occurs.²⁷ Since ΔH_{vap} for DTBN is ~ 11 kcal/mol¹⁸ it is then less surprising to observe the tenacity with which DTBN clings to these surfac-

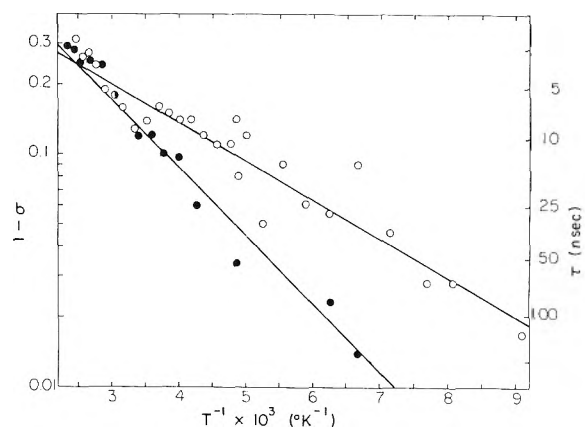


Figure 5. Plot of $\ln(1 - \sigma)$ vs. inverse temperature for surface DTBN: (●) type I spectrum on silica; (○) type II spectrum on silica-alumina. Solid lines are from least-squares fitting to eq 1; $c = -697^\circ\text{K}$, $d = 0.40$ for type I; $c = -380^\circ\text{K}$, $d = -0.46$ for type II.

es, only prolonged evacuation at 600° producing significant desorption.

All the surface hydroxyls have electron-pair acceptor strengths (ΔA_N) similar to that of phenol, with the exception of Y zeolite, for which ΔA_N is even slightly greater than that of $\text{C}_6\text{F}_5\text{OH}$ ($\Delta A_N = 5.7$ G).¹³ The temperature of catalyst activation has no effect on the value of A_N for any type I spectrum. Infrared studies have also found the hydroxyls on silica and silica-alumina to be alike.²⁸ For alumina, however, five slightly different types of aluminols could be observed.²⁹ Since our epr results do not resolve different types of aluminols, it appears that the type I spectrum for alumina may represent a distribution of hydroxyl groups of slightly varying strengths. DTBN that is H bonded with zeolite surfaces is considerably less stable chemically.

As a second kind of surface interaction, a nitroxide can act as a Lewis base and coordinate to a surface aluminum ion. The existence of these complexes is indicated by well-resolved aluminum hfs and an even larger electron-withdrawing strength (ΔA_N) than that for the H-bonded DTBN. Coordination with surface aluminum has been detected in all aluminum-containing catalysts. The poisoning experiments with CO_2 suggest a connection of such sites with catalytic reactions. Observation of appreciable numbers of Al^{3+} sites generally requires high activation temperature, but on silica-alumina some are observed even with $T_A = 125^\circ$. On zeolite surfaces no significant interaction with such sites are observed for $T_A < 500^\circ$ in agreement with previous ir studies.³⁰ The initial formation of surface aluminum complexes on alumina is accompanied by some nitroxide decomposition, but the remaining radicals are subsequently quite stable. DTBN will continue to decompose on silica-alumina, and zeolites are even more reactive.

The electron-withdrawing strength (ΔA_N)³¹ of surface aluminum ions is sensitive to the nature of the catalyst. For all surfaces, ΔA_N is substantially less than that for the AlCl_3 complex (Table I). The Al^{3+} ions and Y zeolite and silica-alumina are similar, with ΔA_N values comparable to that of TiCl_4 ($\Delta A_N = 11.1$ G).¹³ The smaller ΔA_N for alumina is even less than for $\text{Al}(i\text{-Bu})_3$ ($\Delta A_N = 9.2$ G).¹³

The variation in the aluminum hfs further demonstrates slight differences in bonding between DTBN and the surface aluminum ions of different catalyst. Table I exhibits a roughly parallel trend in the spin-Hamiltonian parameters

in the several DTBN-aluminum complexes. We see that as electron-withdrawing strength (ΔA_N) increases, so does the aluminum isotropic hfs (a_{Al}), while T_{Al} , which is a measure of the π -spin density on aluminum, decreases. Thus, the π -bonding ability of a surface aluminum progressively changes as its σ -electron-withdrawing strength increases.

A similar ordering of Lewis acid properties is observed in ir studies of adsorbed pyridine,^{4,30} in contrast with studies of complexed carbonyl compounds³² which exhibit a weaker rather than stronger interaction with $AlCl_3$.

We have interpreted the enhanced decomposition of the nitroxide on silica-alumina at low T_A and the even greater decomposition seen on decationated zeolites as the result of reaction with strong Brønsted acid sites. This is consistent with previous observations which show that DTBN can be decomposed by Brønsted acids and further that the $AlCl_3$ complex is more stable than the protonated nitroxide.³³ Some Brønsted sites are expected to remain at higher T_A and these may be responsible for the residual decomposition observed.

At low T_A no decomposition is seen on alumina and only slight initial decomposition is seen at high T_A . This would suggest that few strong Brønsted sites exist on alumina. Ir studies of adsorbed pyridine also indicate the existence of Brønsted acid sites on silica-alumina and zeolites but their absence on alumina.^{5,32,34} It is interesting to note that rehydration of the complex on alumina or silica-alumina displaces DTBN from surface aluminum complexation but gives no appreciable decomposition.

This study shows that transfer of DTBN from an H bond with a surface silanol to coordination with Al^{3+} is accompanied by an enthalpy change of about +5 kcal/mol. If a surface aluminum ion is coordinatively unsaturated in the absence of adsorbate, the observed ΔH could be simply interpreted as the enthalpy difference between the two complexes. It has been proposed, however, that surface aluminum ions are in fact weakly coordinated to adjacent hydroxyl groups.³ In this case, ΔH would include a positive contribution from breaking this bond upon formation of a DTBN-aluminum ion complex.

The fact that an Al^{3+} ion has a greater electron-pair acceptor strength (ΔA_N) but higher enthalpy than a surface hydroxyl may merely reflect a specific property of the hindered Lewis base employed. Nevertheless, it is interesting to speculate that a surface site which can strongly perturb an adsorbed species as indicated by a large electron-pair acceptor strength yet exhibit a low tendency toward stable coordinate bonding might be responsible for catalytic activity.

Acknowledgment. We are deeply indebted to Professor Robert L. Burwell, Jr., for many enlightening discussions. This work was supported by DA-ARO-D Grant No. 31-124 and by the donors of the Petroleum Research Fund, administered by the American Chemical Society.

References and Notes

- (1) G. A. Somorjai, "Principles of Surface Chemistry," Prentice-Hall, Englewood Cliffs, N. J., 1972.

- (2) M. L. Hair, "Infrared Spectroscopy in Surface Chemistry," Marcel Dekker, New York, N. Y., 1967.
- (3) J. J. Fripiat, A. Leonard, and J. B. Uytterhoeven, *J. Phys. Chem.*, **69**, 3274 (1965).
- (4) E. P. Parry, *J. Catal.*, **2**, 371 (1963).
- (5) M. R. Basila and T. R. Kantner, *J. Phys. Chem.*, **71**, 467 (1967).
- (6) W. K. Hall, H. P. Leftin, F. J. Cheselke, and D. E. O'Reilly, *J. Catal.*, **2**, 506 (1963).
- (7) J. H. Lunsford, *Advan. Catal.*, **22**, 265 (1972).
- (8) (a) P. H. Kasai and R. J. Bishop, *J. Amer. Chem. Soc.*, **94**, 5560 (1972); (b) B. Hoffman and N. Nelson, *J. Chem. Phys.*, **50**, 2598 (1969).
- (9) J. H. Lunsford, *Catal. Rev.*, **8**, 135 (1973).
- (10) (a) A. T. T. Oei and J. L. Garnett, *J. Catal.*, **19**, 176 (1970); (b) T. Komatsu and A. Lund, *J. Phys. Chem.*, **76**, 1727 (1972); (c) G. M. Muha, *ibid.*, **74**, 787 (1970).
- (11) (a) V. I. Evreinov, V. B. Golubev, and E. V. Lunina, *Russ. J. Phys. Chem.*, **47**, 118 (1973); (b) V. I. Evreinov, E. V. Lunina, and V. B. Golubev, *ibid.*, **47**, 578 (1973).
- (12) G. P. Lozos and B. M. Hoffman, *J. Phys. Chem.*, **78**, 200 (1974).
- (13) (a) A. H. Cohen and B. M. Hoffman, *Inorg. Chem.*, **13**, 1484 (1974); (b) A. H. Cohen, Ph.D. Thesis, Northwestern University, Evanston, Ill., 1974.
- (14) (a) C. L. Thomas, *Ind. Eng. Chem.*, **41**, 2564 (1949); (b) M. W. Tamele, *Discuss. Faraday Soc.*, **No. 8**, 270 (1950); (c) T. H. Milliken, G. H. Mills, and A. G. Oblad, *ibid.*, **No. 8**, 279 (1950); (d) V. C. F. Holm, G. C. Bailey, and A. Clark, *J. Phys. Chem.*, **63**, 129 (1959).
- (15) (a) T. B. Eames and B. M. Hoffman, *J. Amer. Chem. Soc.*, **93**, 3141 (1971); (b) T. B. Eames and B. M. Hoffman, *ibid.*, **91**, 5168 (1969).
- (16) (a) A. H. Cohen and B. M. Hoffman, *J. Amer. Chem. Soc.*, **95**, 2061 (1973); (b) A. H. Cohen and B. M. Hoffman, *J. Phys. Chem.*, **78**, 1313 (1974).
- (17) G. A. Abakumov, V. D. Tikhonov, and G. A. Razuvaev, *Dokl. Akad. Nauk SSSR*, **187**, 571 (1969).
- (18) A. H. Cohen and G. P. Lozos, unpublished results.
- (19) (a) S. A. Goldman, G. V. Bruno, C. F. Polnaszek, and J. H. Freed, *J. Chem. Phys.*, **56**, 716 (1972); (b) R. J. Faber and G. K. Fraenkel, *ibid.*, **47**, 2462 (1967).
- (19c) Note Added in Proof. This program has been submitted to the Quantum Chemistry Program Exchange, Bloomington, Ind.
- (20) (a) L. J. Libertini and O. H. Griffith, *J. Chem. Phys.*, **53**, 1359 (1970); (b) O. H. Griffith, D. W. Cornell, and H. M. McConnell, *ibid.*, **43**, 2909 (1965).
- (21) (a) J. W. Hightower, *J. Catal.*, **8**, 298 (1967); (b) P. C. Saunders and J. W. Hightower, *Amer. Chem. Soc., Div. Petrol. Chem., Prepr.*, **15**, A79 (1970).
- (22) For example, see (a) P. Jost and O. H. Griffith, *Methods Pharmacol.*, **2**, 223 (1972); (b) R. G. Gordon and T. Messenger, "Electron Spin Relaxation in Liquids," L. T. Muus and P. W. Atkins, Ed., Plenum Press, New York, N. Y., 1972, p 341.
- (23) R. C. McCalley, E. J. Shimshick, and H. M. McConnell, *Chem. Phys. Lett.*, **13**, 115 (1972).
- (24) (a) J. H. Freed, B. V. Bruno, and C. F. Polnaszek, *J. Phys. Chem.*, **75**, 3385 (1971); (b) S. Goldman, G. V. Bruno, and J. H. Freed, *ibid.*, **76**, 1858 (1972).
- (25) The type I spectra can be compared with those of nitroxides undergoing either slow rotation in isotropic media²² or rapid uniaxial motion.²⁵ The overall shapes in Figure 4A are most similar to those of nitroxides in isotropic media and appear to rule out rapid rotation about any single axis. The decrease of A_N does show that the rotational motion has a finite component along direction(s) perpendicular to the $2p_z$ orbital on nitrogen; such motion would be expected for a σ -bonded nitroxide. Additional studies at 35 GHz and spectral simulations allowing for anisotropic slow rotation are required for a final characterization of these surface motions.
- (26) (a) G. B. Birrell, S. P. Van, and O. H. Griffith, *J. Amer. Chem. Soc.*, **95**, 2451 (1973); (b) G. B. Birrell, O. H. Griffith, and D. French, *ibid.*, **95**, 8171 (1973).
- (27) G. C. Bond, "Catalysis by Metals," Academic Press, New York, N. Y., 1962, p 52.
- (28) M. R. Basila, *J. Phys. Chem.*, **66**, 2223 (1962).
- (29) J. B. Peri, *J. Phys. Chem.*, **69**, 220 (1965).
- (30) J. W. Ward, *J. Catal.*, **9**, 225 (1967).
- (31) In ref 13, acceptor strengths were discussed in terms of the isotropic ^{14}N hfs (a_N). Since this is not a measurable quantity in surface studies, we here adopt this equivalent, alternate approach.
- (32) M. L. Hair and I. D. Chapman, *J. Phys. Chem.*, **69**, 3949 (1965).
- (33) (a) B. M. Hoffman and T. B. Eames, *J. Amer. Chem. Soc.*, **91**, 2169 (1969); (b) V. Malatesta and K. U. Ingold, *ibid.*, **95**, 6404 (1973).
- (34) (a) J. B. Uytterhoeven, L. G. Christner, and W. C. Hall, *J. Phys. Chem.*, **69**, 2117 (1965); (b) M. R. Basila and T. R. Kantner, *ibid.*, **70**, 1681 (1966).

Infrared Spectroscopic Studies of the Surface Bond of Carbon Dioxide on Uranium Oxides¹

Carlos Colmenares

Lawrence Livermore Laboratory, University of California, Livermore, California 94550 (Received January 24, 1974; Revised Manuscript Received June 24, 1974)

Publication costs assisted by the Lawrence Livermore Laboratory

Infrared spectra of chemisorbed and adsorbed CO₂ on uranium oxide films have been measured using transmission techniques. UO_{2.18±0.02} bands at 1540 and from 1370 to 1380 cm⁻¹ and shoulders at 1300 and 1600 cm⁻¹ were interpreted as produced by strongly chemisorbed carboxylate species, CO₂⁻. A broad band in the 3200–3600-cm⁻¹ region and a broad shoulder in the 620–710-cm⁻¹ region suggested the presence of physically adsorbed species. For UO_{2.00±0.05} a single band at 845 cm⁻¹ was observed after oxidation of the uranium films and also after exposure to CO₂. This band was interpreted to correspond to the optical phonon frequency for n-type stoichiometric, or slightly substoichiometric, uranium dioxide.

Introduction

Carbon dioxide is readily adsorbed on the surface of most oxidized metals. Then chemisorption, which results in the formation of various types of surface carbonates, occurs. Many experimental techniques, including transmission infrared spectroscopy,² have been used to study this phenomenon. There are numerous reports about the chemisorption of carbon dioxide on metal oxides based on investigations by infrared spectroscopy. The most recent is that of Grigorev³ on various oxides.

Uranium metal is usually coated with an oxide film which varies with the history and purity of the sample. Because this oxide film is a semiconductor that may exhibit either n- or p-type electrical characteristics and because uranium may be exposed to carbon dioxide atmospheres in reactors, it is of particular interest to attempt to elucidate the type of surface carbonates that will form when uranium oxides or oxidized metal samples are exposed to carbon dioxide.

Infrared Spectra and the Electrical Properties of Uranium Dioxides

Hyperstoichiometric uranium dioxide is a p-type extrinsic semiconductor up to a temperature of about 1100 K. The electrical conduction arises from positive holes resulting from deviations from stoichiometric composition.⁴ Work by Heikes and Johnston,⁵ Wolfe,⁶ Aronson, *et al.*,⁷ and Amelinckx⁸ has shown that the semiconductor band model is not adequate to explain the conduction in uranium dioxide; they have explained the conduction mechanism by the concept of hopping electrons, or holes, from one cation to a neighboring cation, *i.e.*, between U⁵⁺ and U⁴⁺. Stoichiometric or hyperstoichiometric uranium dioxide exhibits a "transmission window" between 3300 and 770 cm⁻¹.^{9–11} Above 3300 cm⁻¹ the energy transmitted decreases rapidly as the absorption edge is approached and as the oxygen-to-uranium ratio is increased⁹ from the stoichiometric value. Below 770 cm⁻¹ the energy transmitted also decreases rapidly as the U–O lattice vibration band (412 cm⁻¹) is approached.¹¹ The oxygen-to-uranium ratio also has a marked effect on this infrared-active vibration.

Stoichiometric or substoichiometric uranium oxide is an

n-type semiconductor that exhibits an optical phonon band at about 882 cm⁻¹.^{11,12} The "optical window" available in hyperstoichiometric uranium dioxide is severely narrowed. The maximum transmission is observed between 1000 and 1200 cm⁻¹; the transmission decreases gradually above 1200 cm⁻¹ and rapidly below 1000 cm⁻¹.

Experimental Section

A uranium film, approximately 400 Å thick, was sputtered onto both sides of five single-crystal KBr disks, 32 mm in diameter and 1 mm thick. The sputtering was done in a triode system with an argon pressure of 6.67×10^{-2} Pa. The disks were then placed in a cylindrical aluminum holder that had pump-out paths milled along its length. The loaded holder was placed into a specially designed stainless steel cell (Figure 1).

An identical reference cell that contained clear KBr disks was used in the optical measurements. Both cells were subjected to the same treatment during all experimental manipulations.

The spectrophotometer was operated in a double-beam mode with both sample and reference cells filled with CO₂ to the same pressure from a common manifold and maintained at the same constant temperature during fill. By this technique, we were able to cancel out all of the absorption bands caused by gaseous carbon dioxide and, therefore, to observe only those bands that arose from adsorbed or chemisorbed species of CO₂ on uranium dioxide films. Thus, the strong fundamental band of CO₂ at 2349 cm⁻¹ was completely canceled by double-beam operation.

In the cell, the holder was contained in the sample cavity of an oxygen-free hard copper block that had a heater and a thermocouple. The block was welded into a stainless steel flange, which could be sealed to the cell body by means of a copper gasket. The cell was designed to permit vacuum outgassing and oxidation of the samples *in situ*. Temperature was controlled to $\pm 0.01^\circ$.

View windows of KBr were sealed into two sides of the cell with Viton O rings. To prevent cracking of the windows as a result of thermal shock, the area near the windows was water cooled through copper coils soldered to the cell.

Infrared spectra of the samples were obtained with a

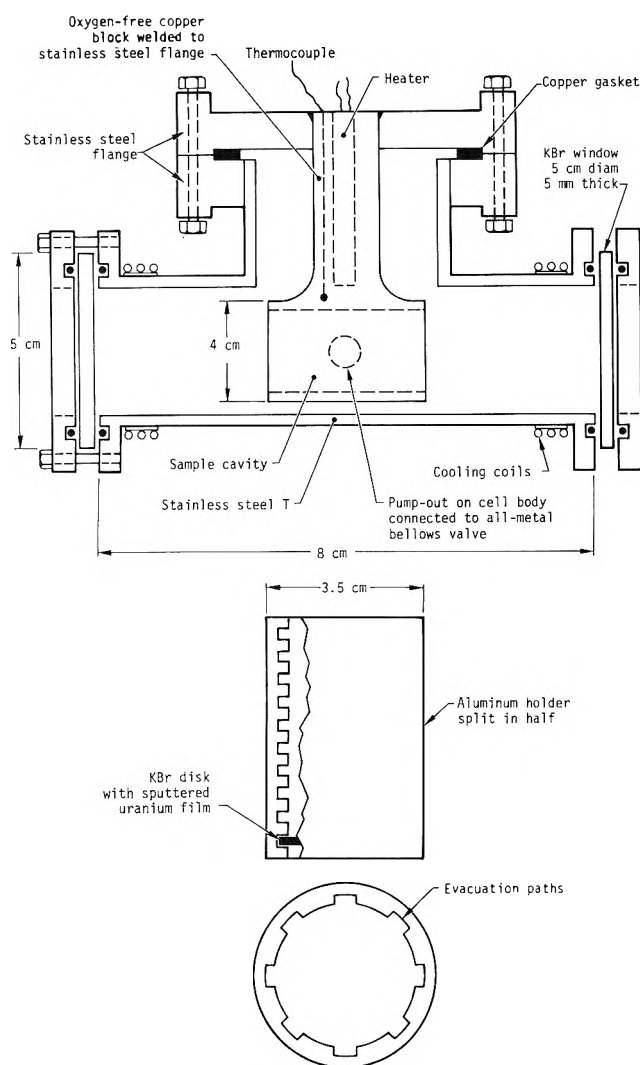


Figure 1. Bakeable infrared cell and sample holder.

Beckman IR-9 spectrophotometer¹³ in the range from 400 to 4000 cm^{-1} .

The films were first vacuum outgassed. Then, in an attempt to minimize oxidation of the films by water vapor during the outgassing, the temperature was raised to 350° over a period 33 hr. However, for the first set of films studied, the evacuation path between the films and the holder was not large enough for rapid outgassing; the uranium films oxidized to light brown, partially transparent uranium dioxide films before they could be subjected to the normal oxidization procedure. The films were subsequently treated with 51.59 kPa of carbon dioxide at 300° for 18 hr. Research grade CO_2 (minimum purity 99.995 vol %) was used. Carbon monoxide, oxygen, and hydrogen impurities were removed by repeatedly freezing the CO_2 at liquid nitrogen temperatures and pumping on the solid. The schedule of film exposure to CO_2 and the experimental conditions used are summarized in Table I. A second set of films was prepared and outgassed for 326 hr as the temperature was slowly raised from 25 to 380°. No noticeable oxidation took place. The films were oxidized with research grade oxygen and subsequently exposed to carbon dioxide, purified in the manner already described. The schedule of film exposure to O_2 and CO_2 and the experimental conditions used are summarized in Table II.

Stoichiometry of the UO_2 films was determined by X-ray diffraction of material scraped from the KBr disks. The UO_2 lines obtained by X-ray were broad and lattice parameters had to be determined on three low-angle lines. Values of $a_0 = 5.448$ and 5.468 ± 0.005 for a face-centered cubic lattice were obtained for the two sets of films studied. These values correspond to $\text{UO}_{2.18 \pm 0.02}$ and $\text{UO}_{2.00 \pm 0.05}$ after Lynds, *et al.*¹⁴

Results and Discussion

$\text{UO}_{2.18}$ Films. Bands arising from the CO_2 adsorption, chemisorption, or both, on $\text{UO}_{2.18 \pm 0.02}$ were observed at the following frequencies: a broad weak band from 3200 to 3600 cm^{-1} ; bands at 1540 and from 1370 to 1380 cm^{-1} , and shoulders at 1600 and 1300 cm^{-1} ; a broad weak shoulder from 620 to 710 cm^{-1} ; a very weak band at 845 cm^{-1} ; and a very weak shoulder between 1000 and 1100 cm^{-1} . A complete scan from 500 to 4000 cm^{-1} is shown in Figure 2, where the regions of interest are expanded by factors of 1 and 10.

Possible structures for chemisorbed CO_2 are shown in Figure 3. Structure 1 may be formed directly on the surfaces by chemisorption of CO_2 involving the transfer of an electron from the semiconductor $\text{UO}_{2.18}$. The structure is similar to the ionized salts of the carboxylic acids (formates)^{2b} and has typical bands in the 1350–1400- and 1560–1580- cm^{-1} regions. This structure does not give rise to any bands in the 1000- cm^{-1} region.

The carbonate, structure 2, displays a band at about 1440 cm^{-1} and three other bands below 900 cm^{-1} .^{2b} Again, there are no bands observed around 1000 cm^{-1} . The monodentate carbonate, structure 3, has bands at about the following frequencies: 1450, 1370, 1000, 850, and 600–750 cm^{-1} .

The bidentate carbonate, structure 4, may assume either of two forms. Structure 4a has bands at the following frequencies: 1630–1640, 1220, ~ 1070 cm^{-1} , and three bands below 800 cm^{-1} . Structure 4b has band assignments in the following regions: 1560–1580, 1320–1380, ~ 1070 , and several bands below 800 cm^{-1} . The most distinguishing feature between the carboxylate structure and the carbonate structures is the absence of a band at about 1070 cm^{-1} for carboxylate.

Because the observed experimental band between 1000 and 1100 cm^{-1} was weak and poorly defined and because two bands at 1370 and 1540 cm^{-1} were clearly defined, it appears that we may assign these two bands to the CO_2^- carboxylate structure based on the arguments cited above. Furthermore, since the $\text{UO}_{2.18}$ sample is a p-type semiconductor, significant coverage of this surface may only be attained by an electron-acceptor molecule¹⁵ such as the carboxylate or the carbonate ions. The latter has been ruled out because of the absence of bands at 1440 and below 900 cm^{-1} . It is possible that monodentate or bidentate structures are present in addition to the carboxylate because we recorded a very weak band at 845 cm^{-1} and a weak shoulder at about 1000 cm^{-1} (Figure 2).

The broad, weak band observed in the region from 3200 to 3600 cm^{-1} and the shoulder from 620 to 710 cm^{-1} may tentatively be assigned to physically adsorbed species of CO_2 . However, this assignment is rather uncertain because bands in this region may be caused by slight differences between the sample and reference cells as well by instrumental behavior caused by low energy in this region. The behavior in this region could be reproduced repeatedly simply

TABLE I: Experimental Sequence and Conditions for UO_{2.18} Films

Experimental step	Experimental condition		Length of time under given set of conditions, hr	Remarks
	Pressure, kPa	Temp, °C		
Outgassing of uranium film		23–350	33	Film oxidized during outgassing
Conditioning of film with CO ₂	51.6 (~38.7 after cooling cells)	300 (23)	18	Intended oxidation treatment; however, films oxidized during outgassing
CO ₂ exposure	38.7	23	140	Infrared spectra taken at different times
Cells quickly evacuated and refilled with fresh CO ₂	77.75	23	67	Infrared spectra taken at different times
Evacuation		23	~2	Infrared spectra recorded after evacuation
Evacuation		360	65	Infrared spectra recorded after evacuation
CO ₂ exposure	40.95	23	17	Infrared spectra recorded after evacuation

TABLE II: Experimental Sequence and Conditions for UO_{2.00} Films

Experimental step	Experimental condition		Length of time under given set of conditions, hr	Remarks
	Pressure, kPa	Temp, °C		
Outgassing		25–380	326	No noticeable oxidation took place
Oxidation	0.08	350	96	Pure oxygen used, films turned iridescent
	3.74	350	93	green during oxidation, infrared spectrum taken
Evacuation		350	2	Infrared spectrum taken
Evacuation		22.5	17	Infrared spectrum taken
CO ₂ exposure	1.62	22.5	1.5	Infrared spectrum taken
	1.62	250	2	Infrared spectrum taken
	1.62	22.5	24	Infrared spectrum taken
	65.83	22.5	2	Infrared spectrum taken
Evacuation		22.5		Infrared spectrum taken

by varying the carbon dioxide pressure over the films. One of the fundamental vibrations of gaseous CO₂ occurs at 667 cm⁻¹ and corresponds to the perpendicular bending mode of CO₂, while the bands in the region around 3600 result from combinations of the two fundamentals at 2349 and 667 cm⁻¹. We believe that the bands observed in the high- and low-frequency regions could belong to physically adsorbed species, because when a molecule becomes adsorbed it loses most, if not all, of its rotational movement but little of its vibrational modes. Thus, physically adsorbed molecules will usually give rise to bands in the same region as those observed in the gas phase.

The structures displaying bands at 1540 and 1370 are strongly chemisorbed. A partial removal of these structures was possible only after outgassing at 350° for 65 hr (Figure 4). Exposure of the films to CO₂ following outgassing restored the bands that were time dependent (Figure 4). There seemed to be little effect on these bands as the CO₂ pressure was raised. A slight blunting of the bands and some effect on the shoulders at 1600 and 1300 cm⁻¹ was observed.

The shoulder observed in the region from 600 to 700 cm⁻¹ developed very slowly with time at a pressure of 38.66 kPa. However, when the pressure was raised to 77.75

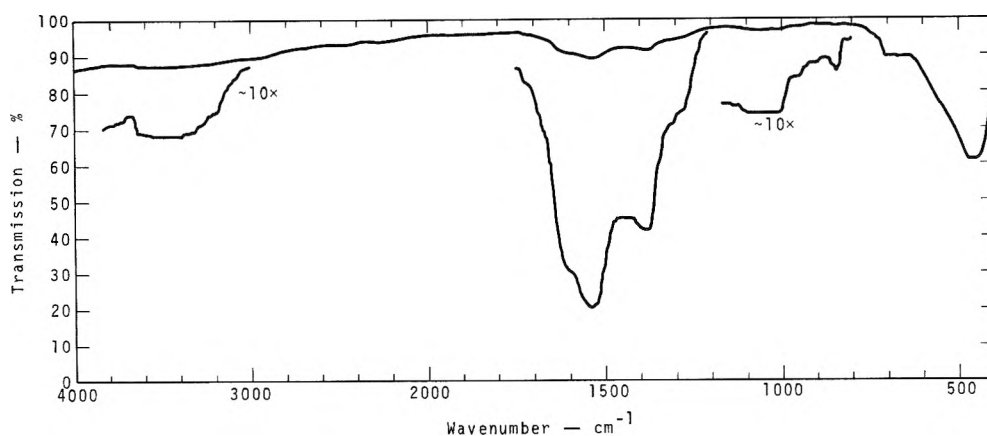


Figure 2. Adsorption of CO_2 on $\text{UO}_{2.18\pm 0.02}$. Complete scan from 400 to 4000 cm^{-1} . Regions of interest are expanded by a factor of 10. Note the excellent cancellation of gas-phase bands of CO_2 by the use of identical sample and reference cells. $P_{\text{CO}_2} = 77.75\text{ kPa}$ in both cells at 23° .

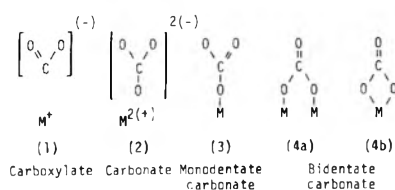


Figure 3. Possible structures for chemisorbed CO_2 .

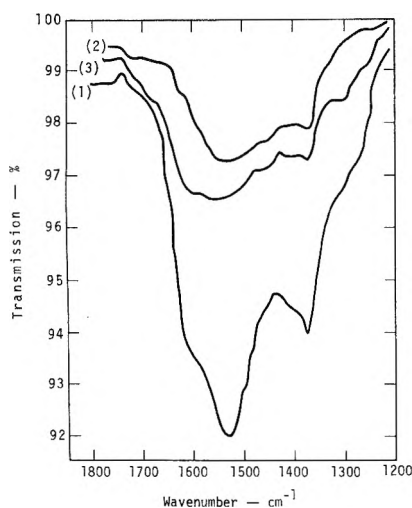


Figure 4. Adsorption of CO_2 on $\text{UO}_{2.18\pm 0.02}$. Spectra were taken under the following conditions: (1) 140 hr after treatment of films with CO_2 at 300° , $P_{\text{CO}_2} \sim 38.7\text{ kPa}$ at 23° ; (2) after evacuation and outgassing at 350° for 65 hr; and (3) 17 hr after filling with 40.95 kPa of CO_2 following step 2. All spectra are expanded by a factor of 10.

kPa it immediately sharpened and changed little with time, as it may be observed in Figure 5. This figure also shows that evacuation both at room temperature and at 350° produced a drastic change; subsequent exposure to CO_2 restored the shoulder immediately. There was very little change in the shoulder 17 hr later.

The broad band observed in the $3200\text{--}3600\text{-cm}^{-1}$ region decreased slowly with time and appeared to have shifted to higher frequencies (Figure 6). An increase in CO_2 pressure did not produce significant changes. Evacuation at room temperature resulted in a slight decrease in intensity, while outgassing at 350° for 65 hr completely removed the species. A partial restoration of this band was effected after CO_2 exposure following outgassing.

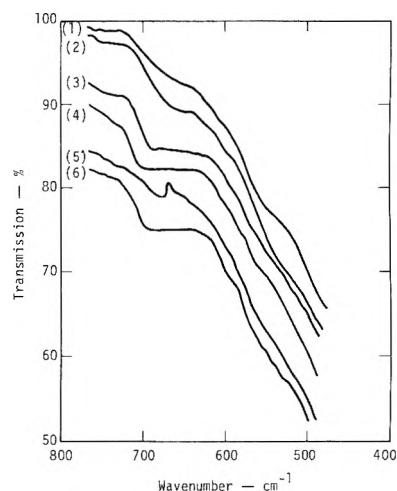


Figure 5. Adsorption of CO_2 on $\text{UO}_{2.18\pm 0.02}$. Spectra were taken under the following conditions: (1) 2 hr after treatment of films with CO_2 at 300° , $P_{\text{CO}_2} \sim 38.7\text{ kPa}$ at 23° ; (2) 72 hr after step 1, $P_{\text{CO}_2} \sim 38.7\text{ kPa}$ at 23° ; (3) immediately after quick pumpout of original CO_2 (38.7 kPa) and refill to 77.75 kPa at 23° ; (4) 36 hr after step 3, $P_{\text{CO}_2} = 77.75\text{ kPa}$ at 23° ; (5) after evacuation at 23° for 1 hr and at 350° for 65 hr; and (6) immediately after filling with 40.95 kPa CO_2 at 23° and also 17 hr later.

$\text{UO}_{2.0}$ Films. Our experimental results are shown in Figure 7. Spectrum no. 1 was taken after oxidation of the uranium films with oxygen. This spectrum remained unchanged after evacuation at 350° for 2 hr followed by evacuation at 22.5° for 17 hr. The significant feature of the spectrum is the band at about 845 cm^{-1} , which had not been observed in previously reported results with hypostoichiometric uranium dioxide. There are slight indications of bands at about 1150, 1380, and 1550 cm^{-1} . The addition of 1.62 kPa of CO_2 at 22.5° followed by a temperature increase to 250° for 2 hr did not produce any changes in the spectrum. An increase in CO_2 pressure to 65.83 kPa produced the changes in the spectrum shown in curve 2 of Figure 7. A shoulder appeared from 620 to 690 cm^{-1} and a very weak band appeared at 1340 cm^{-1} . The shoulder from 620 to 690 cm^{-1} was easily removed by evacuation at room temperature. The comments about possible differences between the sample and reference cells as well as about instrument behavior also apply to these weak bands.

It appears that what little CO_2 chemisorbed on the films was picked up during the outgassing and oxidation steps either from CO_2 outgassing and diffusing through the Viton

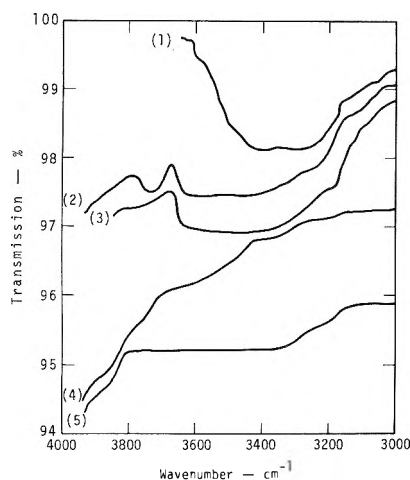


Figure 6. Adsorption of CO₂ on UO_{2.18±0.02}. Spectra were taken under the following conditions: (1) 140 hr after treatment of films with CO₂ at 300°, $P_{\text{CO}_2} \sim 38.7$ kPa at 23°; (2) 24 hr after quickly pumping out original CO₂ and refilling to 77.75 kPa at 23°; (3) 45 hr after step 2, $P_{\text{CO}_2} = 77.75$ kPa; (4) after evacuation and outgassing at 350° for 65 hr; and (5) 17 hr after filling with 40.95 kPa CO₂ at 23° following step 4.

O rings used to seal the cell windows or from trace amounts of CO₂ in the oxygen. The weak bands observed at 1380 and 1550 cm⁻¹ indicate the behavior. These are the areas where chemisorbed CO₂⁻ ions were observed on UO_{2.18}. Exposure of the films to low-pressure CO₂ both at room temperature and at elevated temperatures did not change these bands. However, at 65.83 kPa of CO₂ the shoulder that appeared from 620 to 690 cm⁻¹ had been observed previously and possibly assigned to physically adsorbed CO₂. The bands at 1150 and 1340 cm⁻¹ are too weak to attempt an assignment or sensible explanation. The intensity of the bands at 1380 and 1550 cm⁻¹ is only about one tenth of the intensity of the bands observed for CO₂ chemisorption of UO_{2.18}. This indicates that the CO₂ coverage on the surface was extremely small.

The band observed at 845 cm⁻¹ may be explained in terms of the electrical behavior of uranium oxide. Stoichiometric or slightly substoichiometric uranium dioxide is an n-type semiconductor,¹² whose conduction electrons at low temperatures (25 to 150°) are affected by the lattice to the extent that many of them remain in some sort of "self-trapped" state. The optical phonon frequency of these electrons may be calculated from Frohlich's relation

$$\nu = \left(\nu_0 \frac{\xi}{\xi_0} \right)^{1/2}$$

where ν = optical phonon frequency, cm⁻¹, ν_0 = reststrahlen frequency, ξ = electronic dielectric constant, and ξ_0 = static dielectric constant.

Iida¹² measured $\xi_0 = 36$ and $\xi = 165$ at room temperature for oxides varying in stoichiometry from UO_{1.994} to UO_{2.000}. Using a value of 412 cm⁻¹ for the reststrahlen frequency of UO_{2.00},¹¹ we estimate that the optical phonon frequency for n-type UO_{2.00} is about 882 cm⁻¹. This is in fairly good agreement with the experimentally observed value of 845 cm⁻¹, if we consider differences in materials and sample preparation between our work and the data from Iida¹² and Tsuboi,¹¹ as well as the behavior of this band with slight changes in stoichiometry.

We may conclude that our results are consistent with the behavior of an electron-acceptor molecule (CO₂) chemisorbed onto an n-type semiconductor of low mobility

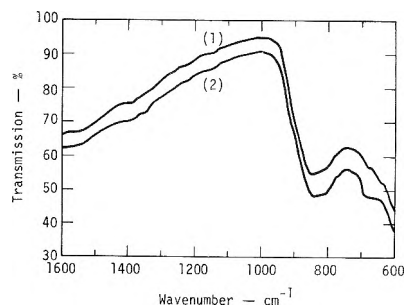


Figure 7. Adsorption of CO₂ on UO_{2.00±0.05}. (1) Spectra remain unchanged after each of the following operations: oxidation of uranium with pure oxygen (0.08 and 3.74 kPa) at 350°; evacuation at 350° for 2 hr; and CO₂ exposure at 1.62 kPa at both 22.5 and 250°. (2) Spectra after CO₂ pressure was increased to 65.83 kPa. Subsequent evacuation restored spectrum no. 1.

(UO_{2.00}). In this case, depletive chemisorption takes place and a potential barrier, which permits only a very low coverage of the surface (0.1%), is created.¹⁶

Summary and Conclusions

The infrared spectrum of adsorbed and chemisorbed species of CO₂ on uranium dioxide films was studied in the range from 400 to 4000 cm⁻¹.

The UO_{2.18} bands at 1540 and from 1370 to 1380 cm⁻¹ and the shoulders at 1300 and 1600 cm⁻¹ were interpreted to be produced by strongly chemisorbed carboxylate species, CO₂⁻. These species could be partially removed by outgassing at 350° for 65 hr. They could not be removed at room temperature. There was little CO₂ pressure effect on these bands. The possible existence of either a monodentate or a bidentate carbonate species was raised by the observation of a very weak band at 845 cm⁻¹ and a very weak shoulder in the 1000–1100-cm⁻¹ range. A broad band in the 3200–3600-cm⁻¹ region and a broad shoulder in the 620–710-cm⁻¹ region suggested the presence of physically adsorbed species. These bands were found to be both pressure and time dependent; it was possible to remove them completely by outgassing at 350° for 65 hr. Complete restoration of the 620–710-cm⁻¹ shoulder was obtained by subsequent CO₂ exposure; however, only partial restoration of the 3200–3600-cm⁻¹ band occurred.

A single strong band at 845 cm⁻¹ was observed after oxidation of the uranium films with pure oxygen to produce UO_{2.00}. We failed in an attempt to remove the band by evacuating the cell for 2 hr at 350°. Subsequent pump-out at room temperature for 24 hr did not produce any changes in the spectrum. The exposure of the films to CO₂ at a pressure of 1.62 kPa both at room temperature and at 250° did not produce any significant changes in the spectrum. An increase in the pressure to 65.83 kPa produced a shoulder in the 620–700-cm⁻¹ region, which had been previously reported and tentatively assigned to physically adsorbed species of carbon dioxide. The band at 845 cm⁻¹ has been interpreted to correspond to the optical phonon frequency for n-type stoichiometric, or slightly substoichiometric, uranium dioxide. This experimental value compares well with a value of 882 cm⁻¹ reported by Iida¹² for n-type UO_{1.994} to UO_{2.000}. We have concluded that the absence of CO₂ chemisorption on this sample is consistent with the behavior of an electron-acceptor molecule on an n-type semiconductor surface, where an electrical depletion layer, which prevents any significant coverage of the surface, is created.

References and Notes

- (1) Work performed under the auspices of the U. S. Atomic Energy Commission.
- (2) (a) L. H. Little, "Infrared Spectra of Adsorbed Species," Academic Press, New York, N. Y., 1966; (b) M. L. Hair, "Infrared Spectroscopy in Surface Chemistry," Marcel Dekker, New York, N. Y., 1967.
- (3) Ya. M. Grigorev, *Russ. J. Phys. Chem.*, **46**, 2, 186 (1972).
- (4) International Atomic Energy Agency, Vienna, Technical Report Series No. 39., 1965.
- (5) R. R. Heikes and W. D. Johnston, *J. Chem. Phys.*, **26**, 582 (1957).
- (6) R. A. Wolfe, Westinghouse Electric Corp., Bettis Atomic Power Laboratory, Pittsburgh, Pa., Report No. WAPD-270, 1963.
- (7) S. Aronson, J. E. Rulli, and B. E. Schaner, *J. Chem. Phys.*, **35**, 1382 (1961).
- (8) S. Amelinckx, Centre d' Etude de l' Energie Nucleaire, MOL, Belgium, Report No. EUR-1414e, 1965.
- (9) J. L. Bates, *Nucl. Sci. Eng.*, **21**, 21 (1965).
- (10) R. M. Berman, Westinghouse Electric Corp., Bettis Atomic Power Laboratory, Pittsburgh, Pa., Report No. WAPD-316, 1967.
- (11) M. Tsuboi, M. Terada, and T. Shimanouchi, *J. Chem. Phys.*, **36**, 1301 (1962).
- (12) S. Iida, *Jap. J. Appl. Phys.*, **4**, 823 (1965).
- (13) Reference to a company or product name does not imply approval or recommendation of the product by the University of California or the U. S. Atomic Energy Commission to the exclusion of others that may be suitable.
- (14) L. Lynds, W. A. Young, J. S. Mohl, and G. G. Libowitz, *Advan. Chem. Ser.*, **No. 39** (1963).
- (15) F. F. Vol'keshtein, "The Electronic Theory of Catalysis on Semiconductors," Pergamon Press, New York, N. Y., 1963.
- (16) D. O. Hayward and B. M. W. Trapnell, "Chemisorption," 2nd ed, Butterworths, Washington, D. C., 1964.

Absolute Quantum Yields of ${}^2E_g \rightarrow {}^4A_{2g}$ Luminescence in $K_3(\text{Co,Cr})(\text{CN})_6$ Powders¹

Francesco Castelli and Leslie S. Forster*

Department of Chemistry, University of Arizona, Tucson, Arizona 85721 (Received February 21, 1974)

The absolute quantum yields of $\text{Cr}(\text{CN})_6^{3-} \text{ } {}^2E_g \rightarrow {}^4A_{2g}$ luminescence have been measured for $K_3(\text{Co,Cr})(\text{CN})_6$ powders of varying concentration. Evidence for energy transfer from $\text{Co}(\text{CN})_6^{3-}$ to $\text{Cr}(\text{CN})_6^{3-}$ has been obtained. Surface defects quench the powder luminescence. After correction for the intermolecular energy transfer and surface quenching, the intramolecular luminescence yield is close to unity at low Cr^{3+} concentrations, indicating an intersystem crossing (${}^4T_{2g} \leftrightarrow {}^2E_g$) yield $\alpha^2 0.8 \leq \Phi_{2E} \leq 1$.

Introduction

Considerable interest has been evidenced in the photochemical properties of $\text{Cr}(\text{CN})_6^{3-}$. Studies in fluid systems have been focussed on the identification of the photoreactive state^{2a} and on the evaluation of the efficiency (Φ_{2E}) for the nonradiative ${}^4T_{2g} \leftrightarrow {}^2E_g$ (Figure 1) intersystem crossing transition.^{2b} The importance of this complex lies in the failure of $\text{Cr}(\text{CN})_6^{3-}$ to fit into the photochemical pattern apparently followed by other Cr^{3+} complexes, *viz.*, the photoaquation yield increases with Dq .³ An understanding of the anomalous case may provide a basis for rationalizing the more general behavior.

In addition to the impetus generated by the concern with the photochemical behavior of $\text{Cr}(\text{CN})_6^{3-}$, studies of this species in the solid state have been prompted by an interest in intermolecular energy transfer. For this purpose stoichiometric,⁴ *e.g.*, $\text{Cr}(\text{urea})_6^{3+} \cdot \text{Cr}(\text{CN})_6^{3-}$, and nonstoichiometric,⁵ *e.g.*, $K_3(\text{Co,Cr})(\text{CN})_6$, mixed crystals have been employed.

Our attention was drawn to $K_3(\text{Co,Cr})(\text{CN})_6$ systems in connection with an evaluation of absolute quantum yields (Φ_P) of powders containing Cr^{3+} complexes.⁶ In contrast to the independence of Φ_P with excitation wavelength, as in the case of $\text{NaMg}(\text{Al,Cr})(\text{C}_2\text{O}_4)_3 \cdot 9\text{H}_2\text{O}$ powders, an apparent wavelength variation was observed for $K_3(\text{Co,Cr})(\text{CN})_6$ powders. Since the absorption of the $K_3\text{Co}(\text{CN})_6$ host is important in this instance, a somewhat more involved procedure is required for the determination of Φ_P . We have now evaluated the absolute Φ_P of $K_3(\text{Co,Cr})(\text{CN})_6$ powders as a

function of Cr^{3+} concentration with the aim of answering the following questions. (1) Is excitation energy transfer from $\text{Co}(\text{CN})_6^{3-}$ to $\text{Cr}(\text{CN})_6^{3-}$ important? (2) What is the intersystem crossing efficiency (${}^4T_{2g} \leftrightarrow {}^2E_g$) in $\text{Cr}(\text{CN})_6^{3-}$? (3) Is Φ_P concentration dependent? In addition to these specific points, a more general purpose of this work is to validate the powder technique for absolute Φ_P measurements in systems where the host absorption is large.

Experimental Section

Apparatus. The apparatus used for the measurement of quantum yields consisted of a PEK 100-W Hg lamp, and a Bausch & Lomb (6.6-nm band width) monochromator for excitation. Light intensities reflected and emitted from the sample and from the MgO reference were measured by a photodiode. For more details on the apparatus and a discussion of the method used see ref 6. For the excitation and reflectance spectra, the radiation from a 75-W Xe lamp, passed through a Bausch & Lomb monochromator with 1.65-nm band width, was used as the source. This source was calibrated with a Rhodamine B solution quantum counter.⁷ The same exciting light band width was used for both excitation and reflectance of spectra. The detection system consisted of a 0.25-m Jarrell-Ash monochromator (3.3 nm/mm dispersion) and a Centronic photomultiplier (Q4283SA, red extended S-20 response). The photomultiplier output was dc amplified and recorded. In the reflectance spectral measurements no slits (10-mm aperture) were used on the Jarrell-Ash monochromator, *i.e.*, the band

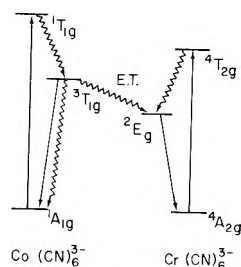


Figure 1. Energy levels of $\text{Co}(\text{CN})_6^{3-}$ and $\text{Cr}(\text{CN})_6^{3-}$.

width of the detection system was larger than that of the excitation source. The excitation spectra were monitored at 826 nm. The linearity of the detection system was confirmed with calibrated filters.

Pulsed measurements were performed with a N_2 pulsed laser (AVCO C-950) for 337 nm and N_2 laser pumped PBD and BBOT dye lasers for 366 and 436 nm, respectively, for excitation. The pulse widths were 10 nsec or less. The dye lasers were operated in the transverse configuration with line widths of ~ 3 nm. A sample holder, with 2-mm deep parallel recesses on both sides, similar to that used for the steady-state measurements was used. This holder was mounted rigidly, and by 180° rotation it was possible to quickly interchange two different samples in precisely the same position. In measuring C (see text) a pure $\text{K}_3\text{Co}(\text{CN})_6$ sample in one side of the holder was used as a reference in order to check the constancy of the excitation intensity. The emission from the sample was focussed through 5 cm of a saturated $\text{K}_2\text{Cr}_2\text{O}_7$ solution onto the slit of the Jarrell-Ash monochromator. The slits used were typically 5 mm although 2-mm slits were used for the rise time measurement. The light was detected by a C-31034 RCA photomultiplier with a 1 k Ω load resistance. The output of the photomultiplier was fed to the probe of a Tektronix 7904 oscilloscope with a 7A11 amplifier. The response time of the detection system was less than 0.1 μsec .

For time-resolved spectra the output of the photomultiplier was fed into the 50- Ω input of a PAR Model 60 boxcar integrator.

The angle between the excitation and emission was 45° and the excitation was normal to the powder surface.

Except as indicated, all the measurements were performed at room temperature.

Powder Sample Preparation. Recrystallized $\text{K}_3\text{Cr}(\text{CN})_6$ and $\text{K}_3\text{Co}(\text{CN})_6$ were dissolved in water in the desired mole ratios and reprecipitated in tetrahydrofuran as described in ref 5. The powders obtained were passed through screens and ~ 45 μm powders were used for the measurements.

Single crystals were grown by evaporation from aqueous solutions. The Cr^{3+} concentration was determined by dissolving the crystals and measuring the absorbance of the resulting solutions.

$\text{K}_3\text{Cr}(\text{CN})_6$ was electronic grade from City Chemical Corp. $\text{K}_3\text{Co}(\text{CN})_6$ was from Alfa Inorganics. PBD and BBOT dyes were from Calbiochem.

Results

Energy Transfer, $\text{Co}(\text{CN})_6^{3-} \rightsquigarrow \text{Cr}(\text{CN})_6^{3-}$. A comparison of the emission spectra of $\text{K}_3\text{Co}(\text{CN})_6$ and $\text{K}_3(\text{Co,Cr})(\text{CN})_6$ indicates that the emission at 700 nm arises, in both systems, from the ${}^3\text{T}_{1g} \rightarrow {}^1\text{A}_{1g}$ transition of the $\text{Co}(\text{CN})_6^{3-}$ moiety. On the contrary, the 826-nm emission of 5% $\text{K}_3(\text{Co,Cr})(\text{CN})_6$ excited at 337 nm contains con-

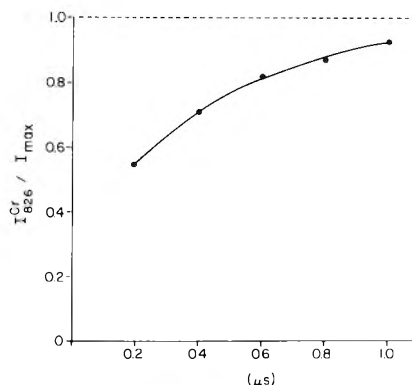


Figure 2. Rise time of ${}^2\text{E}_g \rightarrow {}^4\text{A}_{2g}$ Cr^{3+} emission in 5% $\text{K}_3(\text{Co,Cr})(\text{CN})_6$ (337-nm excitation).

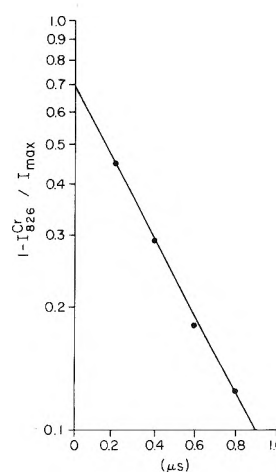


Figure 3. Evaluation of the rise time from data in Figure 2.

tributions from both the ${}^3\text{T}_{1g} \rightarrow {}^1\text{A}_{1g}$ $\text{Co}(\text{CN})_6^{3-}$ and the ${}^2\text{E}_g \rightarrow {}^4\text{A}_{2g}$ $\text{Cr}(\text{CN})_6^{3-}$ transitions.⁵ Since the ${}^3\text{T}_{1g}$ state in $\text{Co}(\text{CN})_6^{3-}$ has a much shorter lifetime (~ 5 μsec) than the $\text{Cr}(\text{CN})_6^{3-}$ ${}^2\text{E}_g$ state (~ 60 msec), energy transfer from $\text{Co}(\text{CN})_6^{3-}$ to $\text{Cr}(\text{CN})_6^{3-}$ will be evidenced by a rise time in the ${}^2\text{E}_g \rightarrow {}^4\text{A}_{2g}$ emission intensity that corresponds to the ${}^3\text{T}_{1g}$ lifetime.

Due to the overlapping ${}^3\text{T}_{1g} \rightarrow {}^1\text{A}_{1g}$ and ${}^2\text{E}_g \rightarrow {}^4\text{A}_{2g}$ emissions, the direct observation of the rise time is not possible. However, the contribution of the $\text{Co}(\text{CN})_6^{3-}$ emission can be subtracted from the total emission at 826 nm and the time course of the ${}^2\text{E}_g \rightarrow {}^4\text{A}_{2g}$ emission determined. The correction for the ${}^3\text{T}_{1g} \rightarrow {}^1\text{A}_{1g}$ emission was made in the following manner. For $\text{K}_3\text{Co}(\text{CN})_6$, the ratio of the ${}^3\text{T}_{1g} \rightarrow {}^1\text{A}_{1g}$ intensities (k) at 826 and 700 nm is dependent of time after pulsed excitation. By monitoring the decay of 5% $\text{K}_3(\text{Co,Cr})(\text{CN})_6$ at both 700 and 826 nm, the Cr^{3+} emission can be calculated from the expression, $I_{826}^{\text{Cr}}(t) = I_{826}^{\text{Co+Cr}}(t) - kI_{700}(t)$, where $I_{826}^{\text{Co+Cr}}(t)$ and $I_{700}(t)$ are the measured decays at the indicated wavelengths. Cr^{3+} emission is negligible at 700 nm. The computed $I_{826}^{\text{Cr}}(t)$ clearly exhibits the delay in reaching the maximum value that is characteristic of energy transfer (Figure 2).

At 337-nm excitation, Cr^{3+} is excited directly by absorption into ${}^4\text{T}_{2g}$ (I_d) and indirectly by energy transfer from Co^{3+} (I_l). On the time scale indicated in Figures 2 and 3, the ${}^2\text{E}_g$ decay is negligible and the signal intensity (I_{max}) remains constant after the Co^{3+} emission has decayed. If γ is the fraction of the Cr^{3+} emission induced by energy

transfer, then $I_t = \gamma(1 - e^{-t/\tau})I_{\max}$ and $I_d = (1 - \gamma)I_{\max}$, where the rise time, τ , is the "effective" lifetime of the donor. Since $I_{826\text{Cr}} = I_t + I_d = (1 - \gamma e^{-t/\tau})I_{\max}$ a plot of $\log(1 - I_{826\text{Cr}}/I_{\max})$ vs. t , should yield τ . A good exponential fit is obtained with $\tau = 0.5 \mu\text{sec}$. Extrapolation to $t = 0$ leads to $\gamma = 0.70$ (Figure 3).

The 0.5- μsec risetime is much smaller than the "normal" 5.0- μsec ${}^3\text{T}_{1g}$ lifetime of $\text{K}_3\text{Co}(\text{CN})_6$. In $\text{K}_3(\text{Co,Cr})(\text{CN})_6$, the ${}^3\text{T}_{1g}$ decay is nonexponential. As the Cr^{3+} concentration increases, the 5- μsec component decreases; it is quite small at the 10% level and undetectable in the 15% samples. Up to 5%, the ${}^3\text{T}_{1g}$ decay can be well described by a double exponential with 5.0 and 0.5 μsec components, but at higher Cr^{3+} levels a 3.2- μsec component grows in importance and replaces the 5.0- μsec decay. Nonetheless, the 0.5- μsec component persists up to 15% Cr^{3+} . The 0.5- μsec ${}^3\text{T}_{1g}$ decay is thus associated with the 0.5- μsec ${}^2\text{E}_g \rightarrow {}^4\text{A}_{2g}$ rise time.

In view of the possible involvement of surface defects (*vide infra*), it is noteworthy that nonexponential ${}^3\text{T}_{1g}$ decay is also observed in single crystals of 5% $\text{K}_3(\text{Co,Cr})(\text{CN})_6$ at room and low temperatures.

Time-resolved spectra were also recorded using 337- and 366-nm excitation for pure $\text{K}_3\text{Co}(\text{CN})_6$ and 5% $\text{K}_3(\text{Co,Cr})(\text{CN})_6$ powders. In general, these spectra are the sum of the emission spectra of $\text{Co}(\text{CN})_6^{3-}$ and $\text{Cr}(\text{CN})_6^{3-}$, the relative contributions changing with time. With excitation at 337 nm the short-time (100 nsec after the excitation pulse) emission spectra for the two powders are very similar and the $\text{Cr}(\text{CN})_6^{3-}$ emission is barely visible. The absolute intensity of this latter signal increases with time in the microsecond range due to energy transfer from $\text{Co}(\text{CN})_6^{3-}$. On the other hand, at 366-nm excitation the $\text{Cr}(\text{CN})_6^{3-}$ emission intensity does not change appreciably in the same time range indicating that at this excitation wavelength most of the $\text{Cr}(\text{CN})_6^{3-}$ emission comes from direct absorption and that the ${}^4\text{T}_{2g} \rightsquigarrow {}^2\text{E}_g$ intersystem-crossing process is much faster than 100 nsec.

Additional support for the energy transfer hypothesis can also be obtained from steady-state measurements. The corrected excitation spectrum (826-nm emission) and absorption spectrum (from reflectance data) obtained from the same powder samples are presented in Figure 4.

The ratio of the absorption at 370 nm, where Cr^{3+} absorption dominates, to that at 310 nm, where Co^{3+} is the principal absorber, is not very different for the 5 and 15% powders. However, the relative intensity of ${}^2\text{E}_g \rightarrow {}^4\text{A}_{2g}$ emission excited at 310 nm compared to 370 nm increases with the Cr^{3+} concentration. The same pattern is also obtained with the 1 and 10% powders. Since the increased Cr^{3+} emission is not due to increased Cr^{3+} absorption, it can only originate in an energy transfer from $\text{Co}(\text{CN})_6^{3-}$ to $\text{Cr}(\text{CN})_6^{3-}$. The efficiency of the energy transfer increases with Cr^{3+} concentration, since the likelihood that an acceptor will be close to an excited donor increases with acceptor concentration.

On energetic grounds, ${}^1\text{T}_{1g}$ can transfer to either ${}^4\text{T}_{2g}$ or ${}^2\text{E}_g$, but only ${}^2\text{E}_g$ can be excited by ${}^3\text{T}_{1g}$. The quenching of the $\text{Co}(\text{CN})_6^{3-}$ ${}^3\text{T}_{1g} \rightarrow {}^1\text{A}_{1g}$ emission, coupled with the concomitant rise of the $\text{Cr}(\text{CN})_6^{3-}$ ${}^2\text{E}_g \rightarrow {}^4\text{A}_{2g}$ emission, clearly demonstrates the importance of the energy transfer process ${}^3\text{T}_{1g} + {}^4\text{A}_{2g} \rightarrow {}^1\text{A}_{1g} + {}^2\text{E}_g$. In the following discussion energy transfer from ${}^1\text{T}_{1g}$ will be ignored and the ${}^1\text{T}_{1g} \rightsquigarrow {}^3\text{T}_{1g}$ intersystem crossing efficiency in $\text{Co}(\text{CN})_6^{3-}$ will be assumed to be unity. We will show later that the results support this assumption.

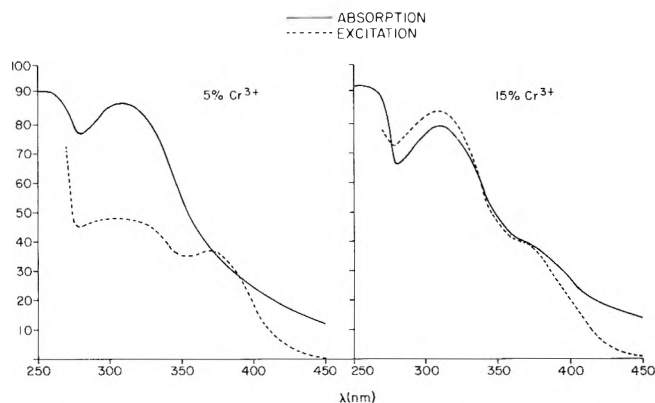


Figure 4. Per cent absorption and relative excitation spectra of $\text{K}_3(\text{Co,Cr})(\text{CN})_6$. The excitation spectra were determined by monitoring the emission at 826 nm.

Absolute Quantum Yields of ${}^2\text{E}_g \rightarrow {}^4\text{A}_{2g}$ Luminescence. We have demonstrated the applicability of the powder method for the determination of the luminescence yields of ruby and $\text{NaMg}(\text{Al,Cr})(\text{C}_2\text{O}_4)_3 \cdot 9\text{H}_2\text{O}$.⁶ The basic equation employed was

$$\Phi_P = \left(\frac{\text{quanta emitted}}{\text{quanta absorbed}} \right) \frac{D}{C} = \frac{D}{C} \phi_P \quad (1)$$

where D and C are the correction factors for reabsorption of the emission and absorption of excitation by the host, respectively. Φ_P refers to excitation into ${}^4\text{T}_2$ followed by emission from ${}^2\text{E}$. The overlap between the ${}^2\text{E} \leftrightarrow {}^4\text{A}_2$ emission and absorption for the above Cr^{3+} species is significant and D was as large as 1.45. On the contrary, C , as estimated by the Kubelka-Munk functions,⁸ was within 3% of unity because of the small host absorption. In the $\text{K}_3(\text{Co,Cr})(\text{CN})_6$ powders, the converse situation obtains. The overlap between the $\text{Cr}(\text{CN})_6^{3-}$ absorption and emission spectra is small and the reabsorption correction, D , never deviates from unity by more than 10% in $\text{K}_3(\text{Co,Cr})(\text{CN})_6$ powders.

The Kubelka-Munk theory is now unsatisfactory for the evaluation of C due to the large host absorption.⁸ Furthermore, the absorption varies from one powder preparation to another of the same concentration, even in pure $\text{K}_3\text{Co}(\text{CN})_6$. In spite of this variation, ϕ_P is quite reproducible ($\pm 5\%$), but application of the Kubelka-Munk theory requires that the host absorption be constant. Not only must a different procedure be devised for the evaluation of C , but a correction must be made for the Cr^{3+} emission produced by energy transfer from Co^{3+} if the intramolecular quantum efficiency, Φ_P , is to be computed. Equation 1, as modified to correct for energy transfer to ${}^2\text{E}$, is

$$\Phi_P = \phi_P D \Phi_{2E} / [\alpha(1 - C) + C \Phi_{2E}] \quad (1')$$

where α is the fraction of light absorbed by Co^{3+} that is transferred to the ${}^2\text{E}$ state of Cr^{3+} and is independent of excitation wavelength.

Estimation of α . This quantity is evaluated by plotting the decay curves of $\text{K}_3\text{Co}(\text{CN})_6$ ($\text{Cr} = 0$) and $\text{K}_3(\text{Co,Cr})(\text{CN})_6$ powders for emission monitored at 700 nm (Co^{3+} emission). If the $t = 0$ intensities are normalized to compensate for differences in ${}^1\text{T}_{1g} \leftarrow {}^1\text{A}_{1g}$ absorption, the areas are proportional to the total number of ${}^3\text{T}_{1g} \rightarrow {}^1\text{A}_{1g}$ quanta emitted (Figure 5) and α can be computed from the expression

TABLE I

Cr ³⁺ concn, %	α	337 nm				366 nm			
		$\phi_P D$	C	Φ_P^a	Φ_P/β^a	$\phi_P D$	C	Φ_P^a	Φ_P/β^a
1	0.06	0.06	0	1.0	1.0	0.22	0.19	0.92	0.92
5	0.28	0.24	0.10	0.68	0.92	0.47	0.55	0.70	0.93
10	0.57	0.21	0.13	0.34	0.55	0.26	0.75	0.29	0.48
15	0.65	0.16	0.17	0.23	0.42	0.16	0.80	0.17	0.37

^a Computed for $\Phi_{2E} = 1$.

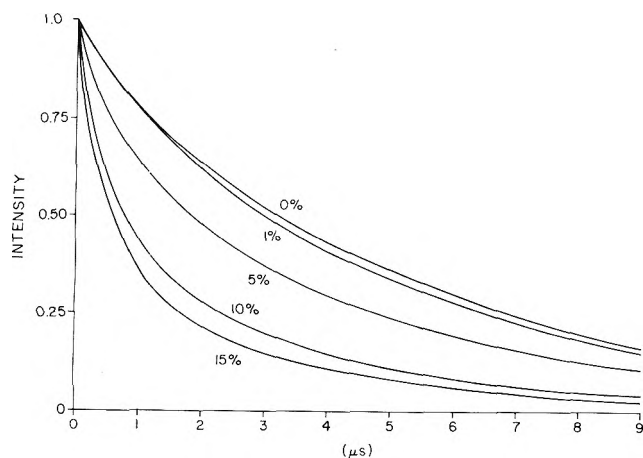


Figure 5. ${}^3T_{1g} \rightarrow {}^1A_{1g}$ $\text{Co}(\text{CN})_6^{3-}$ decays from $K_3(\text{Co,Cr})(\text{CN})_6$ powders. All curves arbitrarily normalized to 1.0 at $t = 0$ (337-nm excitation).

$$\alpha = (A_{C_{Cr=0}} - A_{C_{Cr}}) / A_{C_{Cr=0}} \quad (2)$$

where $A = \int_0^\infty I dt$. In using eq 2 to calculate α , we assume that ${}^3T_{1g} \rightarrow {}^1A_{1g}$ quenching is due solely to energy transfer and ${}^1T_{1g} \rightarrow {}^3T_{1g}$ has unit efficiency. These assumptions are necessary because only the ${}^3T_{1g}$ state quenching is monitored by the measurements. The radiative rate constant for this transition is unaffected by changes in the Cr^{3+} concentration as is shown by the near constancy of $I_{700}(0)$ (cf. next section). The α values are included in Table I.

Determination of C . The $t = 0$ intensities of the 700-nm emission are proportional to the light absorbed by $\text{Co}(\text{CN})_6^{3-}$. The fraction of the absorption due to $\text{Cr}(\text{CN})_6^{3-}$ is then

$$C = 1 - \frac{[I_{700}(0)]_{Cr}}{[I_{700}(0)]_{Cr=0}} \frac{a_{Cr=0}}{a_{Cr}} \quad (3)$$

where $a_{Cr=0}$ and a_{Cr} are the fractions of incident light absorbed by the $K_3\text{Co}(\text{CN})_6$ and $K_3(\text{Co,Cr})(\text{CN})_6$ powders (Figure 4) and the I 's are the corresponding ${}^3T_{1g} \rightarrow {}^1A_{1g}$ $t = 0$ $\text{Co}(\text{CN})_6^{3-}$ emissions at 700 nm. The variation of $I_{700}(0)$ at 337 nm is less than 15% in the 0–15% Cr^{3+} range.

The values of C computed from eq 3 for both 337- and 366-nm excitation are listed in Table I for $K_3(\text{Co,Cr})(\text{CN})_6$ samples of varying Cr^{3+} concentration. Implicit in eq 3 is the condition that the host absorption is due mainly to $\text{Co}(\text{CN})_6^{3-}$ centers, a situation likely to obtain at 337 and 366 nm where the $\text{Co}(\text{CN})_6^{3-}$ molecular absorption is high compared to the nonspecific absorption of the powder. The reabsorption at 700 nm is negligible in all samples.

Computation of Φ_P . It was convenient to measure ϕ_P at the emission wavelengths of the Hg lamp (366, 404, and 436 nm). The reabsorption corrections, D , were computed as described in ref 6 and the relevant quantities are listed in Table I. Each Φ_P represents the average of at least three determinations with different samples. Except for the 1% powders where C and α are small and errors as large as 15% are possible, the Φ_P values are reliable to 5%. In Table II the effect of Φ_{2E} on Φ_P computed from eq 1' is illustrated. The value of ϕ_P at 337 nm was obtained by a comparison of the 826-nm excitation (E) and absorption (a) spectra of a given sample at 337 and 366 nm (Figure 4). In all cases the ${}^3T_{1g} \rightarrow {}^1A_{1g}$ $\text{Co}(\text{CN})_6^{3-}$ emission was negligible at 826 nm and the expression employed was

$$\phi_P^{337} = \phi_P^{366} \frac{E_{337} a_{366}}{E_{366} a_{337}}$$

Since $1.0 < D < 1.1$ at 366 nm, $D \approx 1$ at 337 nm where the penetration depth is less. The Φ_P values for 337 nm are also collected in Tables I and II.

Surface Luminescence. The 2E_g decay from single crystals of $K_3(\text{Co,Cr})(\text{CN})_6$ is accurately exponential up to 25% Cr^{3+} .⁹ In 1% powders the emission decay is likewise exponential, but as the Cr^{3+} concentration increases, a fast ${}^2E_g \rightarrow {}^4A_{2g}$ component is observed (Figure 6). The absence of the fast component in single crystals suggests an origin in the powder surface. In the steady-state measurements the yield from the surface centers will be less than 1% of the bulk emission, but the absorption by the surface sites will decrease Φ_P . If all the properties, except the lifetime, are the same for the surface and bulk species, the $t = 0$ intensities of the fast and slow components will be measures of the light absorbed by the two types of centers. The correction factors, β , are calculated from

$$\beta = I_s^{826}(0) / [I_s^{826}(0) + I_f^{826}(0)]$$

where $I_f^{826}(0)$ and $I_s^{826}(0)$ are the $t = 0$ intensities for the fast and slow components of ${}^2E_g \rightarrow {}^4A_{2g}$. The corrected quantum yields, Φ_P/β , are included in Tables I and II and β decreases with the Cr^{3+} concentration.

Although β is almost the same at 337 and 366 nm, it becomes smaller at longer wavelengths and other faster components appear in the decay curves of $\geq 5\%$ powders. For the 1% powder and for crystals with Cr^{3+} concentration as high as 5%, the decay remains exponential (the lifetimes of crystals with higher Cr^{3+} concentrations were not measured). At excitation wavelengths of 404 and 436 nm the values of Φ_P calculated from eq 1 (C determined by the Kubelka-Munk function) are 0.50 and 0.11 respectively, for the 5% powder. The decrease, from $\Phi_P = 0.7$ found at 337- and 366-nm excitation, is probably due to the decrease of β

TABLE II

Cr ³⁺ concn, %	Φ_P^{337}			Φ_P^{366}			Φ_P^{337}/β			Φ_P^{366}/β		
	Φ_{2E}	1	0.8	0.5	1	0.8	0.5	1	0.8	0.5	1	0.8
1	1.0	0.8	0.50	0.92	0.88	0.77	1.0	0.80	0.50	0.92	0.88	0.77
5	0.68	0.58	0.40	0.70	0.66	0.59	0.92	0.78	0.54	0.93	0.88	0.78
10	0.34	0.28	0.19	0.29	0.28	0.25	0.55	0.45	0.30	0.48	0.46	0.41
15	0.23	0.19	0.13	0.17	0.17	0.15	0.42	0.35	0.23	0.37	0.36	0.33

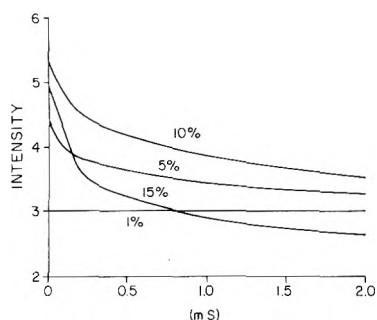


Figure 6. ${}^2E_g \rightarrow {}^4A_{2g}$ Cr(CN)₆³⁻ decays from K₃(Co,Cr)(CN)₆ powders (337-nm excitation).

at longer wavelengths. In the case of 404- and 436-nm excitation, it is more reasonable to use the Kubelka-Munk function in order to calculate C because of the smaller absorption of Co(CN)₆³⁻ for $\geq 5\%$ K₃(Co,Cr)(CN)₆ powders; for these powders C was ~ 0.93 . At 404- and 436-nm excitation, increasing the concentration of Cr³⁺ from 5% also led to a large decrease in Φ_P . For these excitations it was not possible to calculate the correction factor β , but it decreases at the longer wavelengths.

The possibility that surface defects affect Φ_P by absorbing part of the incident light is supported by the 77°K measurements. While Φ_P at 366 nm, a wavelength close to the absorption maximum, did not change with temperature, lowering the temperature to 77°K led to a large decrease in Φ_P at longer wavelengths. For the 5% K₃(Co,Cr)(CN)₆ powder, the values of Φ_P are 0.16 and 0.016 at 404 and 436 nm, respectively. Moreover, these values change with time when irradiated, becoming as large as 0.7 at 404 nm and 0.22 at 436 nm for the 5% powder. In the emission spectrum new bands appeared in the 750–800-nm range upon irradiation, their relative intensities depending on the excitation wavelength. These phenomena, which are reversible with temperature, were found for all the powders. However they were absent in single crystal samples.

Discussion

Energy Transfer. Although Kirk, *et al.*,⁵ did not completely exclude Co³⁺ \leftrightarrow Cr³⁺ energy transfer, they did not believe that energy transfer was responsible for a major portion of the Cr(CN)₆³⁻ ${}^2E_g \rightarrow {}^4A_{2g}$ emission. However, the observation of the 0.5- μ sec rise time for a significant part of the ${}^2E_g \rightarrow {}^4A_{2g}$ emission clearly implicates energy transfer as an important source of Cr³⁺ luminescence in the mixed crystals when the ${}^1T_{1g} \leftarrow {}^1A_{1g}$ Co³⁺ band is the principal absorber. As discussed below, we attribute the 0.5- μ sec component in the Co³⁺ ${}^3T_{1g}$ decay to Co³⁺ with one nearest neighbor site occupied by Cr³⁺. Thus, the bulk of

the Cr³⁺ emission excited by energy transfer should exhibit a 0.5 μ sec rise time.

As described above, the fraction of Cr³⁺ emission due to energy transfer was calculated from Figures 2 and 3 as 0.7 for 5% K₃(Co,Cr)(CN)₆. γ can also be calculated from the equation

$$\gamma = \alpha(1 - C)/[\alpha(1 - C) + C\Phi_{2E}] \quad (4)$$

In deriving eq 4 we have again assumed that the ${}^1T_{1g} \leftrightarrow {}^3T_{1g}$ intersystem crossing efficiency is equal to unity. At 337-nm excitation γ , as obtained from eq 4 and the data in Table I, is 0.72 if $\Phi_{2E} = 1$ and 0.83 if $\Phi_{2E} = 0.5$.

Analysis of the ${}^3T_{1g} \rightarrow {}^1A_{1g}$ Co(CN)₆³⁻ decays as a function of Cr³⁺ concentration provides insight into the distance dependence of the energy transfer. The single exponential decay ($\tau = 5.0 \mu$ sec) observed in pure K₃Co(CN)₆ becomes increasingly nonexponential as the Cr³⁺ concentration is increased. The intensity of the 5.0- μ sec component diminishes and the 3.2- μ sec component grows. In addition to the slow components, a fast (0.5 μ sec) decay is observed in the mixed crystals. As the Cr³⁺ concentration is increased further, additional components are observed, but the 0.5- μ sec component is still evident up to 15% Cr³⁺.

K₃Co(CN)₆ is polytypic and crystallizes in either orthorhombic or monoclinic lattices.¹⁰ The differences between the Co–Co distances in both lattices are small and for our purposes can be ignored. Each Co has six nearest neighbors with Co–Co distances of approximately 7 Å. The second nearest neighbors at 8.5 Å are separated by an intervening K⁺ ion, but there are two Co sites at 9.2 Å without any intervening K⁺. In the mixed crystals, Cr³⁺ occupies the Co³⁺ sites substitutionally. If the six 7-Å sites are all occupied by Co³⁺, the ${}^3T_{1g}$ lifetime is 5.0 μ sec. We ascribe the 0.5- μ sec lifetime to Co³⁺ with a single Cr³⁺ at 7 Å. Multiple occupancy of 7-Å sites then reduces τ to a still smaller value. The fraction of the more distant sites occupied by Cr³⁺ increases rapidly with Cr³⁺ concentration and the less efficient transfer to these more distant Cr³⁺ will merely serve to reduce the 5.0- μ sec component to $\sim 3.2 \mu$ sec.

The likelihood that all six 7-Å sites surrounding an excited Co³⁺ are occupied by Co³⁺ is $(X_{Co})^6$ (X_{Co} is the Co/(Co + Cr) atom ratio). If this analysis is correct, the fraction of the $t = 0$ emission associated with the long-lived emission (either 5.0 or 3.2 μ sec) should also be $(X_{Co})^6$. The agreement demonstrated in Table III is better than might be expected.

Intersystem Crossing Efficiency in Cr(CN)₆³⁻ (Φ_{2E}). Although the 2E_g lifetime of K₃(Co,Cr)(CN)₆ decreases somewhat as the temperature is increased from 77°K to room temperature, it has been found that this increase is caused by a change in the radiative ${}^2E_g \rightarrow {}^4A_{2g}$ rate.¹¹ Once the molecule reaches 2E_g , it radiates. Consequently $\Phi_P = \Phi_{2E}$.

The quantum efficiency of the radiationless ${}^4T_{2g} \leftrightarrow {}^2E_g$

TABLE III

Cr ³⁺ concn, %	Ratio between the slow component and the total Co emission at $t = 0^a$	(X_{Co}) ⁶
1	0.94	0.94
5	0.70	0.74
10	0.46	0.53
15	0.37	0.38
25	0.19	0.18

^a The ratio was calculated by extrapolating the exponential tail of the decay back to $t = 0$. Because the tail of the emission decay is nonexponential in the 10% $K_3(\text{Co,Cr})(\text{CN})_6$ powder, the value for this sample is the least reliable.

process in $\text{Cr}(\text{CN})_6^{3-}$ has been variously estimated as 0.15 and ≤ 0.5 .^{2b,12} The small Φ_{2E} in $K_3(\text{Co,Cr})(\text{CN})_6$ was based on a comparison of the single crystal absorption and excitation spectra.¹¹ This measurement was apparently erroneous since we have repeated the excitation spectrum of this system and found that $0.5 \leq \Phi_{2E} \leq 1.0$. An upper limit of Φ_{2E} (0.5) was obtained from the measurements of the benzil sensitized luminescence of $\text{Cr}(\text{CN})_6^{3-}$ in a fluid solution at -113° .¹² However, the data upon which this value was based scatter considerably and $\Phi_{2E} = 1$ is consistent with the measurements. This leaves the comparison of the direct and $\text{Ru}(\text{Bipy})_3^{2+}$ sensitized luminescence at room temperature in dimethylformamide $\Phi_{2E} \leq 0.5$, as the strongest basis for the belief that $\Phi_{2E} < 1$.^{2b} The evidence to support $\Phi_{2E} \approx 1$ is as follows. (1) For the 1% $K_3(\text{Co,Cr})(\text{CN})_6$ powder, where $\beta = 1$, Φ_P 's are equal (within 10%) for both 337- and 366-nm excitation. If $\Phi_{2E} = 0.5$, the wavelength independence disappears. (2) For the 5% powder, Φ_P is the same at 337 and 366 nm only if $\Phi_{2E} \geq 0.8$ and then $\Phi_P/\beta \approx 1$. The invariance of Φ_P/β to excitation wavelength and concentration (up to 5% Cr^{3+}) supports the conclusion that $0.8 \leq \Phi_{2E} \leq 1$. (3) In spite of very different values of C , Φ_P/β are the same for the 10 and 15% powders at 337 and 366 nm if $\Phi_{2E} \approx 0.8$. (4) The agreement between γ computed from eq 4 and directly from the rise time obtains only if $\Phi_{2E} \geq 0.8$. Equation 4 also depends upon the assumption that ${}^1T_{1g} \rightsquigarrow {}^3T_{1g}$ is unity. (5) At 404 nm $\Phi_P = 0.5$ for the 5% powders. At 366 nm $\beta = 0.75$. We have not quantitatively determined β at 404 nm, but this quantity definitely decreases at the longer wavelengths. These results again support the belief that $0.8 \leq \Phi_{2E} \leq 1$.

To summarize, two assumptions, *viz.*, (i) all $\text{Co}^{3+} {}^3T_{1g}$ quenching is due to energy transfer, and (ii) ${}^1T_{1g} \rightsquigarrow {}^3T_{1g}$ has unit efficiency, and one parameter (Φ_{2E}) are employed in the calculation of Φ_P by eq 1' which involves the computation of C and α by eq 2 and 3, respectively. When $\Phi_{2E} \geq 0.8$, Φ_P/β is the same with 337- and 366-nm excitation at all Cr^{3+} concentrations, but better agreement is obtained for the 5% powder when $\Phi_{2E} = 1$. Concordance between the Φ_P/β value for the 5% powders at 404-nm excitation, a quantity that does not depend upon assumptions i and ii, and the Φ_P/β values calculated from eq 1' provides further evidence for the validity of the assumptions.

It is possible that there is a real difference between Φ_{2E} in the solid state and in solution.^{2b} Photosolvation has been reported to take place in the ${}^4T_{2g}$ state,^{2a} but the quantum yield of this process is only 0.1. Perhaps this value is not the yield of the primary reaction and $\text{Cr}(\text{CN})_6^{3-}$ is reformed after a dissociative process, thus reducing Φ_{2E} at room temperature.

In any case, the ${}^4T_{2g}$ lifetime is < 1 nsec because we have found that the rise time of the 2E_g emission is < 1 nsec in aqueous solution at room temperature. A previously reported 50- μsec emission in a glassy solution¹³ is not fluorescence.¹⁴

The concentration dependence of Φ_P and Φ_P/β in the powders may be illusory. Although the close equality of Φ_P at 337 and 366 nm for 10 and 15% powders indicates that the intersystem crossing efficiency is nearly unity, the values of Φ_P/β are sensibly smaller than unity. It is possible that at these high concentrations some of the light absorbed does not lead to detectable luminescence from surface defects even in the pulsed measurement. Different emission spectra and/or radiative rate constants for the defects could lead to an overestimation of β . The 2E_g decay is exponential in crystals of $\leq 25\%$ $K_3(\text{Co,Cr})(\text{CN})_6$.⁹ In powders we find that defects began to contribute as the Cr^{3+} concentration is increased from 1 to 5%. Concentration quenching is observed in $\text{NaMg}(\text{Al,Cr})(\text{C}_2\text{O}_4)_3 \cdot 9\text{H}_2\text{O}$ powders, although at much higher concentrations.⁶

Conclusions

The powder method can be used for the determination of absolute luminescence yields when host absorption and/or energy transfer is significant, if the host and guest luminescence spectra do not completely overlap and if the host emission decays can be monitored. Considerable care must be employed to validate the several assumptions that are made. The method described would be inapplicable in the absence of host luminescence.

On the basis of the luminescence yields, the intersystem crossing efficiencies of both $\text{Cr}(\text{CN})_6^{3-}$ and $\text{Co}(\text{CN})_6^{3-}$ appear to approach unity. Concentration quenching of the ${}^2E_g \rightarrow {}^4A_{2g}$ luminescence is small below the 15% Cr^{3+} level.

Surface defects play an important role in the luminescence of powdered $K_3(\text{Co,Cr})(\text{CN})_6$ samples.

References and Notes

- (1) Supported by the National Science Foundation.
- (2) (a) H. F. Wasgestian, *J. Phys. Chem.*, **76**, 1947 (1972); (b) N. Sabbatini, M. A. Scandola, and V. Balzani, *ibid.*, **78**, 541 (1974).
- (3) A. Chiang and A. W. Adamson, *J. Phys. Chem.*, **72**, 3827 (1968).
- (4) H. Gausmann and H. L. Schläfer, *J. Chem. Phys.*, **48**, 4056 (1968).
- (5) A. D. Kirk, A. Ludi, and H. L. Schläfer, *Ber. Bunsenges. Phys. Chem.*, **73**, 669 (1969).
- (6) F. Castelli and L. S. Forster, *J. Luminescence*, **8**, 252 (1974).
- (7) W. H. Melhuish, *J. Opt. Soc. Amer.*, **52**, 1256 (1962).
- (8) G. Kortüm, "Reflectance Spectroscopy," Springer-Verlag, New York, N. Y., 1969.
- (9) H. U. Zander, Dissertation, Frankfurt am Main, 1969 (quoted in ref 5).
- (10) J. A. Kohn and W. D. Townes, *Acta Crystallogr.*, **14**, 617 (1961).
- (11) F. D. Camassei and L. S. Forster, *J. Chem. Phys.*, **50**, 2603 (1969).
- (12) D. J. Binet, E. L. Goldberg, and L. S. Forster, *J. Phys. Chem.*, **72**, 3017 (1968).
- (13) S. N. Chen and G. B. Porter, *J. Amer. Chem. Soc.*, **92**, 2189 (1970).
- (14) F. Castelli and L. S. Forster, *J. Amer. Chem. Soc.*, **95**, 7223 (1973).

Solvent and Temperature Effects in the Photoionization of Tetramethyl-*p*-phenylenediamine¹

Richard A. Holroyd* and Robert L. Russell

Chemistry Department, Brookhaven National Laboratory, Upton, New York 11973 (Received March 27, 1974)

Publication costs assisted by Brookhaven National Laboratory

Single-photon ionization quantum yields are reported for tetramethyl-*p*-phenylenediamine (TMPD) as a function of wavelength and temperature in various dielectric liquids. At 23° the maximum quantum yield is observed at short wavelengths and is 0.07 in tetramethylsilane, less in cyclopentane, 2,2,4-trimethylpentane, and 2,2-dimethylbutane, and $\sim 10^{-5}$ in *n*-alkanes (C₄-C₁₄). In the *n*-alkanes there is a marked temperature effect on the quantum yield. For branched hydrocarbons the effect of temperature is less pronounced. The variation in yields with temperature is accounted for by the Onsager equation; this suggests that $\phi(\text{ion pairs})$ is close to unity and that electrons and cations separate characteristic distances in each liquid. These distances range from 31 Å in *n*-hexane to 106 Å in tetramethylsilane. Wavelengths for ionization onsets depend on the energy of the excess electron (V_0) in the solvent and are used to evaluate this quantity for 18 different liquids. The results also suggest that V_0 shifts toward more positive values at lower temperatures.

Introduction

TMPD is readily converted to Wurster's blue (TMPD⁺) on exposure to ultraviolet light. The two-photon mechanism of this photoionization is well known. More recently single-photon ionization of TMPD has been demonstrated in both polar^{2,3} and nonpolar liquids.^{4,5} In nonpolar solvents the onset of one-photon ionization occurs at different wavelengths dependent on the solvent.^{4,6} The magnitude of such shifts in ionization is correlated with the energy of the excess electron (V_0).^{6,7} One purpose of this study is to measure V_0 for several different liquids. This quantity is important to theoretical descriptions of the excess electron state and also appears to be related to the mobility of the electron in these liquids.^{8,9}

Another purpose is to obtain a better understanding of the mechanism of photoionization of TMPD. In this respect we have studied the effect of variation of solvent, temperature, wavelength, and light intensity. The process of ionization in a liquid can be divided into two stages: the first is the creation of an ion pair and the second the separation of the charges. The probability that the ions will separate (ϕ_{escape}) and contribute to an observed current is given by eq 1, where ϵ and k are the dielectric and

$$\phi_{\text{escape}} = e^{-e^2 / \epsilon k r T} \quad (1)$$

Boltzmann constants and r is the initial ion-pair separation distance.¹⁰ Thus a study of the yield of photoionization *vs.* temperature provides direct information about the initial separation distance.

Experimental Section

Chemicals. All hydrocarbons used were Phillips Research Grade with the exception of 2,2,4,4-tetramethylpentane (99%) obtained from Chemical Samples Co., 2,3-dimethylbutene-2 from Aldrich Chemical Co., and 2,2,5-trimethylhexane and 2,3,4-trimethylpentane which were Phillips Pure grade. Tetramethylsilane (TMS) was nmr grade obtained from Peninsular ChemResearch. All liquids were first dried on a column of silica gel which was previously

activated at 400° for 24 hr. The *N,N,N',N'*-tetramethyl-*p*-phenylenediamine (TMPD) was supplied by C. Capellos; the sample was resublimed, but no difference in results was observed between the original and the resublimed TMPD. For the actinometry measurements the following chemicals were used without further purification: potassium ferrioxalate (supplied by R. Weston of this laboratory) and *o*-phenanthroline monohydrate (certified ACS, Fisher Scientific).

Apparatus. The initial experiments were done with a cell (no. 1) which consisted of a 2.5 cm diameter cylindrical quartz tube having a flat quartz plate window to admit the light. Parallel aluminum electrodes, 1 cm wide by 2 cm high, were mounted perpendicular to the window and were attached to tungsten rods sealed into the quartz cylinder. The electrodes were separated by 0.5 cm and came to within 3 mm of the window. The cell (no. 2) used for the temperature control study is shown in Figure 1. Most of the work was performed with electrodes mounted about 8 mm away from the window. When quantum yields were measured for liquids yielding high currents, a set of electrodes, within about 2 mm from the window, was used to minimize current losses.

Light from a 450-W xenon arc was focused on the entrance slit of a high-intensity Bausch & Lomb monochromator. For the majority of the experiments the monochromator entrance and exit slits were 2.5 and 1.55 mm, respectively, corresponding to a band pass width of 11.5 nm. In some experiments the slit widths were reduced. The emerging beam was filtered to remove scattered light of shorter wavelengths and was focused to form an image of the exit slit between the electrodes in the cell. A flat quartz plate, between the cell and condensing lens, placed at a 45° angle to the light beam reflected about 10% of the light into an EMI-9558 QC photomultiplier tube to monitor light intensity. Current measurements were made at fields of 2 kV/cm. Currents from the cell and from the PM tube were measured with Keithley micro-microammeters.

For temperature control the cell shown in Figure 1 was placed inside a quartz dewar which had two flat quartz

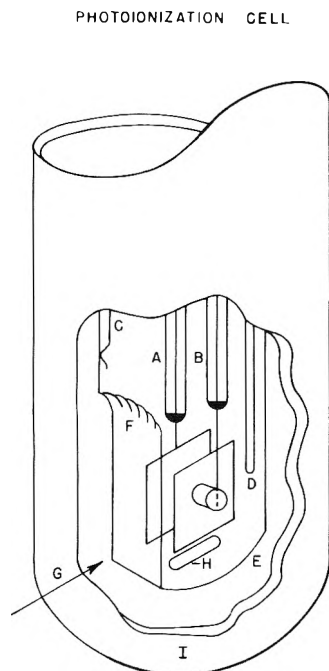


Figure 1. Temperature controlled photoionization cell (cell 2): (A) current measuring electrode, (B) high-voltage electrode, (C) ground wire to tin oxide coating, (D) thermocouple well, (E) tin oxide coated quartz cell, (F) flat quartz window, (G) light beam, (H) glass encased magnetic stirrer, (I) quartz dewar flask.

windows to allow the light to enter. A stream of nitrogen gas cooled to -196° passed through a vacuum jacketed flow tube into the dewar. A heater in the flow tube, controlled by a Varian 4540 variable temperature controller, brought the nitrogen gas to the desired temperature. The temperature of the liquid in the cell was measured with an iron-constantan thermocouple.

Experimental Procedure. For solvents which are liquid at room temperature, 50 μ M solutions of TMPD were prepared and poured into the photoionization cell. For solvents which are gases at 23° , 50 λ of a 5×10^{-3} M stock solution of TMPD was pipetted into the cell and the solvent evaporated by a stream of flowing nitrogen. After cooling the cell to $\leq -70^{\circ}$ it was evacuated and the gas allowed to condense into it until it held approximately 50 ml of liquid. During the condensing process the solution was stirred magnetically.

Starting at some wavelength where there was nearly a zero photocurrent, the wavelength was decreased in 5-nm intervals down to 200 nm. The following Corning filters were used to minimize stray light of shorter wavelength: No. 7-54 between 280 and 250 nm, and No. 9-54 between 250 and 235 nm. Below 235 nm no filter was used. Scattered light of long wavelengths was measured by inserting a Pyrex filter in the light beam. As shown in the Results section the photocurrent increases very rapidly below a certain wavelength. At wavelengths longer than this a small but finite current is always observed with voltage applied. For the *n*-alkanes this current, as measured at 255 m μ , was typically 0.03 pA and was due primarily to the background conductivity of the liquid. This was taken as the "dark" current (DC) and was subtracted from the observed currents. For liquids such as TMS which show conductivity to longer wavelengths the dark current was taken at 295 m μ and was somewhat higher (~ 0.2 pA) but still 10^6 times less than the current observed at shorter wavelengths. The ob-

served currents were converted to a relative quantum yield (RQY) via eq 2 where PMR is the photomultiplier re-

$$\text{RQY} = [(i - \text{DC}) / (I - I_{s1})] (\text{PMR} / \%T) (1/F) \quad (2)$$

sponse, %*T* the per cent of light transmitted through the quartz windows of the cell or cell plus the dewar, *I* the photomultiplier reading, *I*_{s1} the photomultiplier reading for scattered light, and *F* the fraction of incident light absorbed by the TMPD as defined by eq 3 where *A*_{soln} is the

$$F = \left[\frac{\text{OD}_{\text{soln}} - \text{OD}_{\text{solvent}}}{\text{OD}_{\text{soln}}} \right] A_{\text{soln}} \quad (3)$$

fraction of the incident light absorbed by the solution.

Actinometry. The potassium ferrioxalate actinometer^{11,12} was used to determine the incident light intensity in the temperature-controlled cell. The primary actinometry measurements were made at 23° and 255 nm, using exit slit widths between 0.5 and 2.50. Measurements were also made at 275 and 215 nm. The potassium ferrioxalate solutions were stirred continuously by a magnetically driven stirrer and continuously bubbled with nitrogen gas during the photolysis. All manipulations involving actinometer solutions were carried out in the presence of red light.

The yield of Fe²⁺ o-phenanthroline was determined from the optical density at 510 nm assuming the extinction coefficient¹³ to be 1.1×10^4 M⁻¹ cm⁻¹. A check on this value was made by preparing known solutions of ferrous sulfate plus o-phenanthroline. The concentrations of these solutions determined from the optical density agreed to 5% with the calculated concentration based on weight. The average incident light intensity for normal operating conditions based on five determinations was 9.4×10^{13} quanta/sec at 255 nm, and 35×10^{13} quanta/sec at 275 nm. The intensity at 215 nm was 2.2×10^{13} quanta/sec on the assumption that the quantum yield ($\phi = 1.25$) is the same as at 255 nm; however, photomultiplier tube readings at the two wavelengths indicated the intensity at 215 nm was 1.1×10^{13} . The quantum yield of Fe²⁺ at wavelengths less than 254 nm has not been reported and it is possible that it is greater than 1.25. We therefore used the measured light intensity at 255 nm, normalized by PM tube readings to calculate quantum yields at any given wavelength. Since the quantum yield of electrons, ϕ_e , is equal to $6.24 \times 10^{18} (i - \text{DC}) / I_a$ and since *I*_a (the light absorbed) is *F* (*I*₀)₂₅₅ then from eq 2 we obtain

$$\phi_e = 6.24 \times 10^6 (\text{RQY}) (\%T / \text{PMR})_{255} (I - I_{s1})_{255} / (I_0)_{255} \quad (4)$$

Here (*I*₀)₂₅₅ is the incident light intensity in quanta/sec measured at 255 nm.

Voltage and Intensity Dependence of the Photocurrent. For light intensities which gave currents of less than 1 nA, the current rose rapidly below 1.5 kV/cm, while above 1.5 kV/cm the current was linearly dependent on the field strength. There are two effects that changes in the field have on the current. *Volume* recombination of free ions depends on the concentration and predominates at very low fields. As the field increases more and more ions drift to the electrodes, this accounts for the rapid rise in observed current. At higher fields the current rises less rapidly, here recombination is less important. The current would reach a plateau except that with increasing field, the number of ions escaping *geminate* recombination increases. The fraction of ions that escape is given to first order by¹⁰

TABLE I: Measured and Calculated Slope to Intercept Ratios of Current-Voltage Plots

Solvent	λ , nm	Slits, mm	T , °K	Current at $E = 2$ kV, nA	Slope/intercept, cm/V $\times 10^4$	
					Exptl	Calcd ^a
<i>n</i> -Hexane	225	1.6	297	0.06	0.62	0.58
<i>n</i> -Pentane	220	1.6	232	0.01	1.8	0.93
	223	0.5	297	0.03	0.70	0.60
<i>n</i> -Butane	215	1.6	275	0.06	0.89	0.71
2,2,4-Trimethylpentane	225	1.6	294	5.4	~2.8	0.58
	225	0.5	294	0.91	1.3	0.58
	225	0.5	294	0.10	0.56	0.58
Tetramethylsilane	230	0.5	296	12.3	~5.0	0.60
	230	0.1	296	0.97	1.5	0.60
	230	0.05	296	0.51	0.51	0.60

^a Slope/intercept = $e^3/2\epsilon k^2 T^2$.

TABLE II: Solvent Shifts and Values of V_0

Solvent	$I(S)$, eV	$-P_0$, eV	V_0 , eV			a , Å
			This work ^a	Ref 8	Ref 18	
<i>n</i> -Tetradecane	4.93	1.48	0.21			3.03
<i>n</i> -Decane ^a	4.94	1.44	(0.18)			2.66
<i>n</i> -Octane ^a	4.92	1.41	(0.13)			2.44
<i>n</i> -Hexane	4.99	1.31	0.10	0.04	0.0	2.19
Methylcyclohexane ^a	4.82	1.46	(0.08)			2.22
Cyclohexane	4.74	1.47	0.01			1.92
<i>n</i> -Pentane	4.89	1.32	0.01	-0.01	0.04	2.03
3-Methylpentane ^a	4.84	1.37	(0.01)		0.0	2.16
2,3,4-Trimethylpentane	4.73	1.42	-0.05			2.38
2,2,5-Trimethylhexane	4.68	1.42	-0.10			2.50
1,3-Dimethyladamantane	4.37	1.53	-0.30			
2,2,4-Trimethylpentane	4.66	1.37	-0.17	-0.18	-0.14	2.36
Cyclopentane	4.61	1.38	-0.21	-0.28	-0.17	1.87
2,3-Dimethylbutene-2	4.51	1.44	-0.25			2.07
2,2-Dimethylbutane	4.62	1.32	-0.26			2.11
2,2,4,4-Tetramethylpentane	4.44	1.43	-0.33			2.41
Neopentane	4.52	1.30	(-0.38)	-0.43	-0.35	1.96
Tetramethylsilane	4.34	1.27	-0.59	-0.62	-0.55	2.01

^a Values in parentheses were obtained by recalculation of data in ref 6.

$$P(E) = e^{-e^2/\epsilon k r T} (1 + e^3 E / 2\epsilon k^2 T^2) \quad (5)$$

Equation 5 predicts a linear dependence of the escape probability on the electric field. Since the quantum yield, ϕ_e , is proportional to $P(E)$, ϕ_e should also increase linearly with the field. From eq 2 and 4 it also follows that if a sample is being exposed to a constant light intensity at a single wavelength, ϕ_e is proportional to the observed photocurrent. At higher fields an absolute value for the ratio of slope to intercept, namely, $e^3/2\epsilon k^2 T^2$, is predicted from (5) for the plots of current *vs.* field. Comparison of our measured and calculated slope to intercept values is shown in Table I. In general if the current, at a field of 2 kV/cm, is less than 1 nA reasonable agreement between measured and calculated values is observed. For light intensities which produce a current greater than 1 nA at 2 kV/cm, the slope to intercept

ratios indicate that volume recombination of the ions is relatively important. For most of the experiments reported here, quantum yields were determined under conditions where recombination was minimal. The only exceptions are cyclopentane and 2,2-dimethylbutane; in these cases the quantum yields are probably somewhat higher than reported since higher light intensities were used.

Results

Ionization Onsets. Figure 2 is a semilog plot of the relative ionization yield (RQY) *vs.* photon energy for TMPD in several solvents at 24°. These results were obtained in cell 1. The onset of photocurrent is at a different wavelength for each solvent. Above onset the current rises rapidly with increasing photon energy. The increase is a factor of ~30 for each 0.1 eV at photon energies near onset. The current

TABLE III: Maximum Quantum Yield of Ionization vs. Temperature^a

Solvent	Temp, °K	Exptl $\phi_e(\text{max})$, $\times 10^4$	r , Å	b , Å ^b
<i>n</i> -Hexane	335	1.2	30	19
	297	0.52	30	18
	251	0.15	30	18
	204	0.022	31	17
	193	0.0089	30	16
	175	0.0024	30	16
<i>n</i> -Pentane	297	2.6	37	23
	270	1.5	37	23
	260	1.1	37	23
	229	0.38	36	22
<i>n</i> -Butane	271	0.43	33	20
	239	0.15	33	20
	224	0.069	33	19
	199	0.024	33	18
Tetramethylsilane	295	613.0	106	91
	273	520.0	106	90
	260	443.0	104	87
	227	328.0	104	87
	185	194.0	106	86
Propane	222	1.3 (7.6)	48	(40)
	211	1.1 (5.9)	49	(40)
	197	0.67 (3.9)	49	(40)
	179	0.40 (2.2)	50	(39)
2,2,4-Trimethylpentane	295	36.0 (111)	51	(48)
	277	29.0 (90)	52	(48)
	261	24.0 (70)	52	(47)
	223	13.0 (36)	54	(46)
	196	6.0 (19)	54	(45)
2,2-Dimethylbutane	295	45.0 (89)	55	(47)
	223	14.0 (29)	56	(45)
	189	6.6 (13)	57	(44)
	177	4.3 (8.8)	57	(43)
Cyclopentane	296	22.0 (221)	46	(58)
	256	14.0 (138)	48	(57)
	206	6.1 (59)	51	(55)
	187	3.7 (38)	52	(54)

^a Quantities in parentheses are derived quantities (see text). ^b Value of b parameter for an assumed gaussian distribution of ion-pair separation distances.

levels off at different values for each solvent. In general the maximum quantum yield is higher for the compounds of more symmetrical structure and lowest for the *n*-alkanes. Most of the curves terminate at $h\nu = 5.5$ eV because we were interested primarily in the threshold portion in the early stages of this work.

Values of V_0 were calculated from ionization onsets $I(S)$, defined as the photon energy at which the RQY equals a certain minimal value. (Since the curves are roughly parallel near threshold, the magnitude of this value is arbitrary.) The value of V_0 for any liquid is given by eq 6, where the

$$V_0 = I(S) - IP - P_+ \quad (6)$$

gas-phase ionization potential (IP) is taken as 6.2 eV¹⁴ and P_+ is the polarization energy of the positive ion assumed to be given by $P_+ = -A(\epsilon - 1)/\epsilon$.^{15a} In order to provide a point of reference, an average value of $A = 2.89$ was calculated from measured values of $I(S)$ for five solvents: *n*-pentane,

cyclopentane, 2,2,4-trimethylpentane, neopentane, and TMS, for which V_0 was known.⁸ This allowed calculation of the parameter P_+ for other liquids and thus values of V_0 were obtained. The observed values of $I(S)$ along with the derived V_0 's are given in Table II for all solvents investigated at 23°.

The observation of shifts in photoionization onsets is not unique to TMPD. A brief study of perylene as a solute was also made; in this case onsets were at shorter wavelengths compared to TMPD. However, the shifts relative to a standard solvent, in this case cyclohexane, gave the following approximate values of V_0 : for 2,2-dimethylbutane, -0.3; for 2,2,4-trimethylpentane, -0.2; and for tetramethylsilane, -0.6, consistent with the TMPD results.

Temperature Effects. Figure 3 shows the temperature effect on the complete photoionization curves for tetramethylsilane and *n*-hexane. In general the lower the temperature, the lower the observed current at all wavelengths. The effect is small for tetramethylsilane and much larger

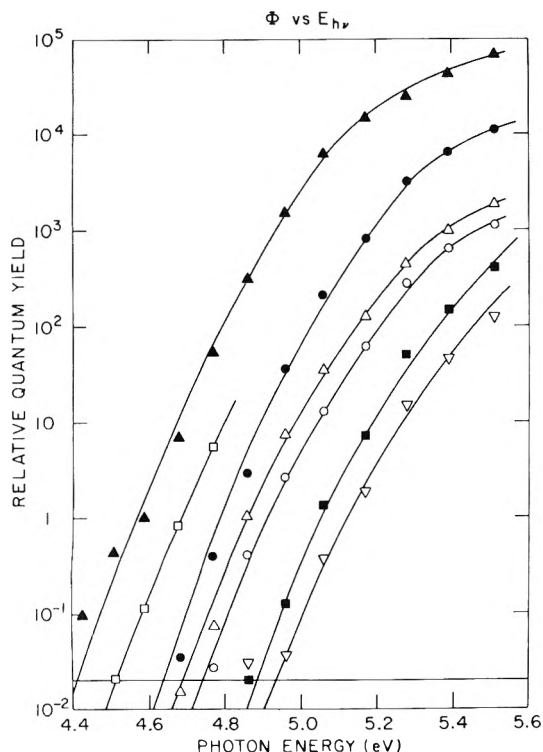


Figure 2. Relative quantum yield (photocurrent normalized to constant absorbed light intensity) vs. photon energy ($T = 23^\circ$): (▲) 2,2,4,4-tetramethylpentane, (□) tetramethylethylene, (●) 2,2,5-trimethylhexane, (Δ) 2,3,4-trimethylpentane, (○) cyclohexane, (■) n-pentane, (▽) *n*-tetradecane.

for *n*-hexane where the maximum quantum yield decreased from 5×10^{-5} at 23° to 2.4×10^{-7} at -98° . The results for the effect of temperature on the ionization quantum yields for eight solvents are given in Table III.

For highly branched compounds, such as 2,2,4,4-tetramethylpentane and 2,2,5-trimethylhexane, observed currents were very high near the maximum (see Figure 2). At these high currents volume recombination was significant and it was necessary to reduce the light intensity to obtain true quantum yields. This was accomplished by closing the slits on the monochromator. Decreasing the light intensity increases the quantum yield observed at the maximum while changing the yield near threshold only slightly. This is illustrated in Table IV where a change in exit slit width from 1.55 to 0.1 raised the yield near the maximum by a factor of 3 for TMS. The yields reported by Jarnagin⁵ are slightly lower than ours for TMS but in good agreement for *n*-hexane. Some of the results reported in Table III were obtained at high intensities and high currents; thus for the last four compounds a corrected quantum yield which takes this effect into account is given in parentheses in column 3.^{15b}

To evaluate V_0 from the data at temperatures other than 23° , the effect of temperature on the escape probability of ion pairs (see eq 1) must be considered. To account for this, ionization curves such as in Figure 3 were translated vertically so that all maxima were at the same current. This in effect is the same as dividing the quantum yield by the escape probability so that the curves represent only ion pair formation yields. Values of $I(S)$ and V_0 were then calculated in the usual way. As shown in Table V, $I(S)$ increases slightly with decreasing temperature. For hexane $I(S)$ increases by ~ 0.2 eV with a 160° drop in temperature; for

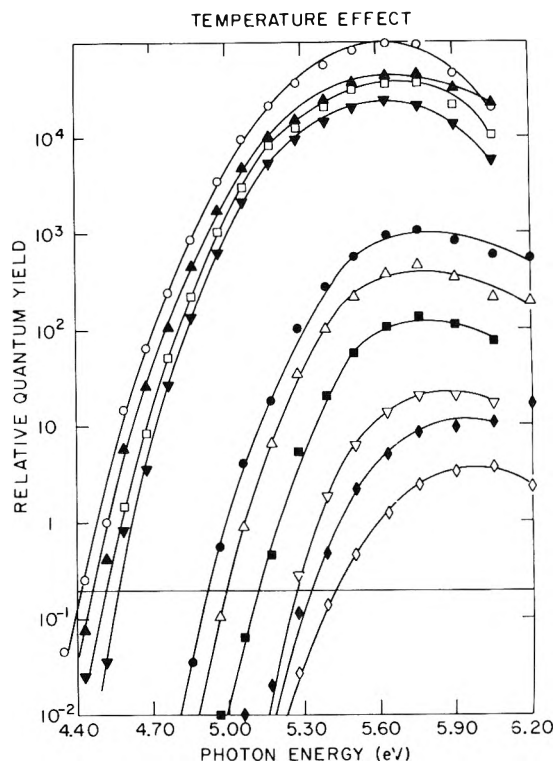


Figure 3. Relative quantum yield vs. photon energy at various temperatures (in $^\circ\text{K}$): tetramethylsilane (○) 297° , (▲) 251° , (□) 201° , (▼) 185° ; *n*-hexane (●) 335° , (Δ) 297° , (■) 251° , (▽) 204° , (◆) 193° , (◇) 175° .

TMS the change is ~ 0.1 eV in 110° . However, $I(S)$ also is assumed to reflect changes in P_+ which should change with temperature because of the change in dielectric constant. If this is included then V_0 becomes more positive by ~ 0.4 for *n*-hexane and ~ 0.3 for TMS.

Discussion

In this study TMPD is photoionized monophotonically by exciting in the second absorption band centered at 265 nm. The nature of the solvent does not change the absorption band,⁴ but does play a major role in determining ion yields. This suggests that the initially formed higher excited singlet mixes with a semiionized¹⁶ or Rydberg-like⁷ state in which the electron is in direct contact with solvent molecules. This state must be short lived and depending on its energy either internally converts to the ground state or forms an ion pair. In the latter case the electron retains some residual kinetic energy and separates a distance r from the positive ion. The probability of this ionization process ($\phi_{\text{ion pair}}$) depends both on the solvent and the excitation energy.¹⁷ In all cases r is less than the coulombic escape distance and only a fraction (this probability is given by eq 5) of the initial ion pairs will separate sufficiently to contribute to the current. Thus the total electron yield is given by the product of $\phi_{\text{ion pair}}$ times the escape probability, $P(E)$.

$$\phi_e = \phi_{\text{ion pair}} P(E) \quad (7)$$

On combining eq 7 with 5 we obtain

$$\phi_e / (1 + e^3 E / 2 \epsilon k^2 T^2) = \phi_{\text{ion pair}} (e^{-e^2 / \epsilon r k T}) \quad (8)$$

At short wavelengths, where $\phi_{\text{ion pair}}$ has reached its maximum, a plot of the log of the left-hand side of eq 8 vs.

TABLE IV: Quantum Yield of Photoionization vs. Photon Energy and Monochromator Slit Widths

Solvent	Photon energy, eV	ϕ_e for monochromator exit slit width of			Ref 5
		1.55 mm	0.10 mm	0.05 mm	
TMS	4.77	9.8×10^{-5}	1.1×10^{-4}	6.0×10^{-5}	2.3×10^{-5}
	4.96	8.4×10^{-4}	1.2×10^{-3}	1.5×10^{-3}	3.3×10^{-4}
	5.17	3.9×10^{-3}	9.7×10^{-3}	9.7×10^{-3}	3.0×10^{-3}
	5.39	8.4×10^{-3}	3.3×10^{-2}	5.3×10^{-2}	1.0×10^{-2}
	5.64	1.7×10^{-2}	6.0×10^{-2}	6.3×10^{-2}	
	5.77	2.2×10^{-2}	6.4×10^{-2}	7.2×10^{-2}	
	5.90	2.2×10^{-2}	5.2×10^{-2}	7.1×10^{-2}	
<i>n</i> -C ₆	5.06	1.6×10^{-7}			8.0×10^{-8}
	5.28	3.9×10^{-6}			2.0×10^{-6}
	5.64	4.2×10^{-5}			3.2×10^{-5}
	5.77	5.3×10^{-5}			
	5.90	4.1×10^{-5}			4.0×10^{-5}

TABLE V: Effect of Temperature on V_0

Solvent	T , °K	$I(S)$, eV	$-P_e$, eV	V_0 , eV	
				Exptl	Calcd ^a
<i>n</i> -Hexane	335	4.95	1.26	0.01	0.01
	298	4.99	1.31	0.10	(0.10)
	251	5.06	1.36	0.22	0.22
	204	5.13	1.41	0.34	0.37
	193	5.15	1.42	0.37	0.41
	175	5.16	1.44	0.40	0.47
<i>n</i> -Pentane	297	4.95	1.27	0.02	(0.02)
	270	5.01	1.31	0.12	0.09
	260	5.02	1.32	0.14	0.11
	229	5.04	1.36	0.20	0.18
<i>n</i> -Butane	271	5.04	1.28	0.12	(0.12)
	239	5.10	1.33	0.23	0.23
	224	5.12	1.35	0.27	0.28
Propane	199	5.17	1.38	0.35	0.36
	222	4.95	1.18	-0.07	(-0.07)
	211	4.99	1.20	-0.01	-0.05
	197	5.03	1.23	0.06	-0.02
2,2,4-Trimethylpentane	179	5.05	1.26	0.11	0.04
	296	4.66	1.37	-0.17	(-0.17)
	191	4.80	1.48	0.08	0.02
Cyclopentane	296	4.61	1.38	-0.21	(-0.21)
	256	4.67	1.41	-0.12	-0.13
	206	4.74	1.46	0.00	-0.01
	187	4.76	1.47	0.03	0.05
2,2-Dimethylbutane	295	4.60	1.32	-0.28	(-0.26)
	223	4.76	1.42	-0.02	-0.14
	189	4.83	1.46	0.09	-0.06
	177	4.85	1.47	0.12	-0.03
Tetramethylsilane	297	4.35	1.27	-0.58	(-0.59)
	251	4.37	1.34	-0.49	-0.57
	201	4.45	1.41	-0.34	-0.54
	185	4.47	1.43	-0.30	-0.52

^a Calculated from Wigner-Seitz parameters. See text.

$(\epsilon T)^{-1}$ should be linear, with the slope equal to e^2/kr . Figure 4 shows plots of the maximum yield vs. $1/\epsilon T$ in the various liquids. Good straight lines are obtained. Quite differ-

ent slopes are observed for the various liquids indicating separation distances are different in each liquid. The values of r derived from the slopes vary from 31 Å for *n*-

TABLE VI: Ranges of Low-Energy Electrons

Solvent	Separation distance (r), Å		
	From slopes in Figure 4		
	a	b	Ref 18 ^c
Tetramethylsilane	106	(207) ^d	207
2,2,4-Trimethylpentane	63	95	120
Cyclopentane	73	117	102
2,2-Dimethylbutane	63	99	
Propane	60	82	
<i>n</i> -Pentane	34	41	47
<i>n</i> -Butane	31	37	
<i>n</i> -Hexane	31	35	54

^a $\phi_{\text{ion pair}}$ is assumed independent of temperature. ^b $\phi_{\text{ion pair}} = e^{-\Delta E/RT}$ assumed with $\Delta E = 870$ cal. ^c Values obtained by fitting data in ref 18 to a single range. ^d Assumed value from ref 18.

hexane to 106 Å for TMS (Table VI, column 2). Here it is assumed that $\phi_{\text{ion pair}}$ is independent of temperature.

With r evaluated we can calculate the escape yield $P(E)$ to compare with the experimental electron quantum yield and estimate $\phi_{\text{ion pair}}(\text{max})$. For *n*-hexane and TMS calculated values of $P(E)$ are 6.3×10^{-5} and 5.6×10^{-2} , respectively, at 23° for the separation distances given in Table VI. The observed quantum yields are 5.2×10^{-5} and 6.1×10^{-2} , respectively. The near agreement of these two sets of numbers allows us to conclude that at the maximum in the current *vs.* photon energy curves the quantum yield of ion pair formation is approximately unity ($\phi_{\text{ion pair}} \approx 1$).

This conclusion provides an alternative method of evaluating r from the data. If we begin with the assumption that the maximum ion pair yield is unity, then r can be evaluated directly from the quantum yields for each temperature with eq 8. The values so obtained are summarized in Table III (column 4). For most liquids this method leads to the same r value at all temperatures; further the average values of r are in excellent agreement with the values of r obtained from the slopes in Figure 4 for *n*-hexane, *n*-pentane, *n*-butane, and TMS. For the other four liquids the values of r obtained from the quantum yield data are lower than from the slope method. As explained in the Results section, in these liquids the quantum yields are expected to be low because recombination was not entirely eliminated.

The interpretation in terms of a single separation distance, r , gives excellent agreement both with the temperature dependence and the absolute magnitude of quantum yields; in the case of *n*-hexane, for example, ϕ_e varies from 2.4×10^{-7} to 1.2×10^{-4} in a 160° temperature range and this is accounted for if $r = 31$ Å. The postulation of a single separation distance is perhaps physically unrealistic. However, there is some support for the idea. First, in photoionization the electron may have a specific kinetic energy and may therefore travel a specific distance depending on the rate of energy loss. Second, low-energy electrons appear to travel large distances before undergoing scattering events in which there is a large change in momentum.¹⁸

An earlier photoelectric study¹⁸ indicated ranges of low-energy electrons somewhat larger than those reported here. If larger values of r are assumed then the temperature effect on the escape probability (P) is less. Consequently, in

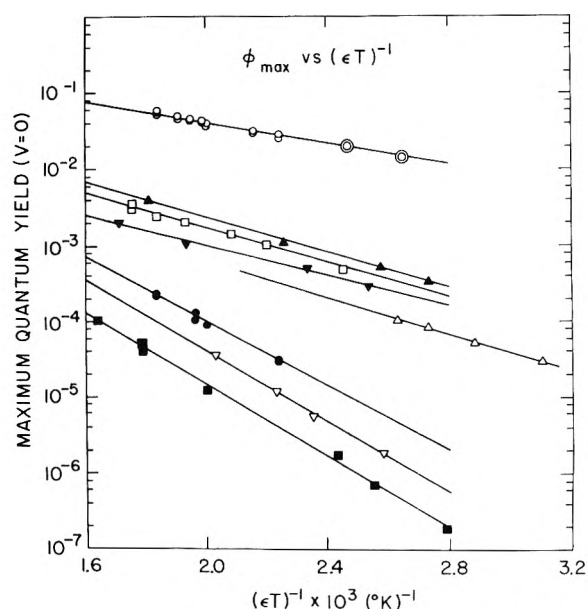


Figure 4. Maximum quantum yield of electrons (at $E = 0$), *vs.* (ϵT) , $\phi_{\text{electrons}}/(1 + e^3 E/2\epsilon k^2 T^2)$: (○) TMS, (▲) 2,2-dimethylbutane, (□) 2,2,4-trimethylpentane, (▼) cyclopentane, (Δ) propane, (●) *n*-pentane, (▽) *n*-butane, (■) *n*-hexane.

order to account for the slopes in Figure 4, $\phi_{\text{ion pair}}$ would have to be temperature dependent. This introduces additional parameters and the slopes in Figure 4 would then be attributed to two terms: the Onsager term (P) and the activation energy of $\phi_{\text{ion pair}}$. Any such activation energy must be small and an upper limit for this is provided by the TMS data where the quantum yield changes only a factor of 3 over the temperature range studied. To estimate the magnitude of this we assumed a value of $r = 207$ Å for TMS,¹⁸ from which E_a is computed to be 0.87 kcal/mol for $\phi_{\text{ion pair}}$. If this value is assumed to apply in the other liquids, new values of the separation distance can be calculated. The results of this calculation are shown in Table VI, column 3. For the *n*-alkanes the ranges are only slightly increased over the former values (from $r = 34$ to 41 Å for *n*-pentane); whereas for 2,2,4-trimethylpentane, cyclopentane, and 2,2-dimethylbutane this results in a 50% increase in r . These new values are upper limits allowed by the present results which are more in accord with the photoelectric results.

Although the possibility of a temperature dependence for $\phi_{\text{ion pair}}$ leads to some ambiguity, we can conclude that at room temperature $\phi_{\text{ion pair}}$ is between 0.2 and 1.0¹⁹ and the electron ranges are less than found by the photoelectric work for *n*-alkanes and less or equal to the photoelectric values for the other hydrocarbons.

Ionization Onsets and V_0 . The photoionization technique has been used to determine values of V_0 at 23° for 16 alkanes, 1 alkene, and TMS. For the normal alkanes V_0 increases with chain length and is +0.18 for *n*-decane and +0.21 for *n*-tetradecane, the highest value yet observed. For the branched hydrocarbons V_0 is lower and this applies also to the branched alkene. The lowest value reported is for TMS for which V_0 is -0.59 eV. It has been noted^{8,9} that the electron mobility decreases as V_0 increases and this relationship, which is approximately $\mu = A \exp(-BV_0)$, is borne out by the present results. Of particular interest are the high values of V_0 near +0.2 for which we anticipate mobility values of the order of 10^{-2} .

Ionization onsets appear to shift to higher photon energies as the temperature is lowered. The magnitude of this shift is ~ 0.15 eV per 100° . Because the dielectric constant increases, P^+ also increases with decreasing temperature and consequently our derived V_0 values increase ~ 0.3 eV over a 100° temperature decrease.²⁰

Butane and propane were investigated only at temperature below 0° . The data in Table V show that the V_0 values for butane are very similar to the values found for pentane and hexane at corresponding temperatures. V_0 values for propane, however, are significantly lower than those for the other *n*-alkanes. This difference is reflected in the electron mobility which is about the same in butane and pentane but much larger in propane (μ_e in propane is 11 times μ_e in butane at 238°).²¹

It has been pointed out that V_0 should become more positive with increasing density or decreasing temperature for methanol and ethanol.²² This conclusion was reached from considerations of the excess electron in terms of the semi-continuum model.²³ Since our results tend to confirm this suggestion we have applied this model to our results. The effect of temperature on V_0 would be mitigated largely in terms of the density changes.²⁴ The method of calculation which employs the Springett, Jortner, and Cohen²³ model has been described.^{25,26} The results at 20° are used to first evaluate the kinetic energy term T , where $V_0 = T + U_p$ and U_p is the polarization energy term. Then the hard core radius a is calculated from T . Values of these radii are given in the final column of Table II.²⁷ The process is then reversed to evaluate V_0 at other temperatures (*i.e.*, densities). The calculations indicate both T and U_p increase in magnitude with decreasing temperature. The change in the T term is greater than the change in U_p which results in an increase in V_0 as the temperature is lowered. There is very good agreement between theory and experiment in all cases except for TMS, where the calculated change in V_0 with temperature is less than 0.1 eV and the observed change is 0.28 eV which is comparable to, although smaller than, that observed in the other liquids.

Acknowledgments. The authors wish to express their ap-

preciation to Drs. A. O. Allen and H. A. Schwarz for their advice and assistance during the course of this work.

References and Notes

- (1) Research performed under the auspices of the U. S. Atomic Energy Commission.
- (2) T. Imura, N. Yamamoto, H. Tsubomura, and K. Kawabe, *Bull. Chem. Soc. Jap.*, **44**, 3185 (1971).
- (3) J. T. Richards and J. K. Thomas, *Trans. Faraday Soc.*, **66**, 621 (1970).
- (4) S. S. Takeda, N. E. Houser, and R. C. Jarnagin, *J. Chem. Phys.*, **54**, 3195 (1971).
- (5) R. C. Jarnagin, *Accounts Chem. Res.*, **4**, 42 (1971).
- (6) R. A. Holroyd, *J. Chem. Phys.*, **57**, 3007 (1972).
- (7) Y. Nakato, M. Ozaki, and H. Tsubomura, *J. Phys. Chem.*, **76**, 2105 (1972). The solute in this case was tetrakis(dimethylamino)ethylene.
- (8) R. A. Holroyd and M. Allen, *J. Chem. Phys.*, **54**, 5014 (1971).
- (9) N. R. Kestner and J. Jortner, *J. Chem. Phys.*, **59**, 26 (1973).
- (10) L. Onsager, *Phys. Rev.*, **54**, 554 (1938).
- (11) C. G. Hatchard and C. A. Parker, *Proc. Roy. Soc., Ser. A*, **235**, 518 (1956).
- (12) J. H. Baxendale and N. K. Bridge, *J. Phys. Chem.*, **59**, 783 (1955).
- (13) J. G. Calvert and J. N. Pitts, Jr., "Photochemistry," Wiley, New York, N. Y., 1967, p 785.
- (14) Y. Nakato, M. Ozaki, A. Egawa, and H. Tsubomura, *Chem. Phys. Lett.*, **9**, 615 (1971).
- (15) (a) M. Born, *Z. Phys.*, **1**, 45 (1920). (b) The correct quantum yields were arrived at by first determining the ion separation distance r from temperature plots of electron yields; then a quantum yield was calculated from this r value using eq 5.
- (16) M. Ottolenghi, *Chem. Phys. Lett.*, **12**, 339 (1971).
- (17) The exact form of the threshold function is not considered here. We attribute the shape of the current vs. wavelength curves to the role of thermal population of vibrational levels of ground state TMPD as given by the appropriate Boltzmann factors.
- (18) R. A. Holroyd, B. K. Dietrich, and H. A. Schwarz, *J. Phys. Chem.*, **76**, 3794 (1972).
- (19) It should be noted that fluorescence, which is a competing process at long wavelength, is of less importance (see ref 4) at the high photon energies to which these yields apply.
- (20) Since ionization thresholds become sharper as the temperature is lowered and since we have assumed that the shape of the photoionization curve does not change with temperature, our observed changes of V_0 with temperature must be regarded as upper limits. Preliminary measurements on TMS in this laboratory utilizing the photoelectric work function technique support an increasing V_0 with decreasing temperature but the increase is only approximately +0.1 eV over a 100° temperature range.
- (21) M. G. Robinson and G. R. Freeman, *Can. J. Chem.*, **52**, 440 (1974).
- (22) D. F. Feng, K. Fueki, and L. Kevan, *J. Chem. Phys.*, **57**, 1253 (1972); *J. Phys. Chem.*, **78**, 393 (1974).
- (23) B. E. Springett, J. Jortner, and M. H. Cohen, *J. Chem. Phys.*, **48**, 2720 (1968).
- (24) L. Kevan and H. T. Davis, private communications.
- (25) K. Fueki, D-F. Feng, and L. Kevan, *Chem. Phys. Lett.*, **13**, 616 (1972).
- (26) K. Fueki, *Can. J. Chem.*, **50**, 3379 (1972).
- (27) The values of a correlate well with the van der Waals radii for each compound as has been pointed out (H. T. Davis and L. D. Schmidt, *Can. J. Chem.*, **51**, 3443 (1973)).

Electron Spin Resonance of Palladium(I). IV. Mixed-Ligand Complexes of Palladium(I)

Michihiro Nakamura* and Shizuo Fujiwara

Department of Chemistry, Faculty of Science, The University of Tokyo, Hongo, Tokyo 113, Japan (Received December 13, 1973; Revised Manuscript Received June 21, 1974)

Publication costs assisted by the Kuraray Co. Ltd.

Esr spectra were obtained for mixed-ligand complexes of palladium(I), which were formed in frozen solutions of the complexes of palladium(II) by γ irradiation. The g values for $\text{Pd}^I \text{Cl}_{4-n} \text{L}_n$ ($n = 0-4$ for L = ammonia, ethylamine, n -butylamine, NO_2^- , and SCN^- ; $n = 0-2$ for L = di- n -butylamine and tri- n -butylamine), $\text{Pd}^I (\text{C}_2\text{O}_4)\text{L}_2$ (L = ammonia, NO_2^- , and SCN^-), and $\text{Pd}^I (\text{OCOCH}_3)_m \text{L}_n$ ($n = 0-4$ for L = n -butylamine; $n = 0-3$ for L = pyridine) were determined. Two spectra observed for frozen solutions of diacetato- or dipropionatopalladium(II) in toluene were attributed to monomeric and trimeric species.

Introduction

Palladium(II) complexes in solutions have been identified mainly by means of uv or optical spectroscopy. However absorption bands for palladium(II) complexes are usually broad. Therefore if more than two kinds of complexes are contained in a solution, it is difficult to separate each of their absorption bands. In the preceding articles,¹⁻³ it has been shown that palladium(II) ions in a variety of complexes are reduced by γ irradiation to form the complexes of palladium(I), which can be observed by means of esr spectroscopy. In addition, it was found that the ligands in original palladium(II) complexes are kept unchanged in reduced complexes. This technique is applicable to a variety of metal ions, and esr spectra for Co(II),⁴ Pb(III),⁵ Zn(I), Cd(I), Hg(I),⁶ and Ni(I)⁷ have been reported.

In the present work, this technique was applied to identify the mixed-ligand complexes of palladium(II) formed in a variety of solutions.

Experimental Section

Lithium chloropalladate, potassium chloropalladate, and potassium bis(oxalato)palladium(II) trihydrate were prepared by standard methods. Diacetato-, dipropionato-, and dibenzoatopalladium(II) were prepared and recrystallized according to the method described in literature.⁸ Ligand compounds such as lithium chloride, potassium thiocyanate, potassium nitrite, ethylamine, n -butylamine, di- n -butylamine, tri- n -butylamine, ammonia, and pyridine were supplied by Wako Pure Chemicals Co. and used without further purification. Ethanol (99.5%), toluene, a mixture of ethylene glycol (EG) and water (2:1 by volume), and a mixture of glacial acetic acid (HOAc) and ethanol (3:7 by volume) were used as solvents which provide glassy matrices on freezing.

The solutions containing palladium(II) complexes and ligand compounds were kept at room temperature for 24 hr. Then the solutions were degassed in esr sample tubes, frozen by putting the sample tubes into a liquid nitrogen dewar vessel, and given at 77°K a γ -ray dosage of 1×10^6 R from a cobalt-60 source with the dose rate of 5×10^4 R/hr. After irradiation, the sample tubes were transferred from above-mentioned dewar vessel into another dewar vessel made for esr measurements as quickly as possible.

The esr spectra were recorded at 77°K on a JEOL 3BS X-band spectrometer by using 100-kHz modulation with

the modulation width of 5 G. The doublet signal of hydrogen atoms, which were produced by irradiation in the quartz tube, was used as the standard of swept magnetic field.

Results and Discussion

1. *Li₂PdCl₄ in EtOH.* γ -Irradiated ethanol matrix containing lithium chloropalladate (50 mM) gives the esr spectrum shown in Figure 1a. In this figure a set of signals with $g_{\parallel} = 2.577$ and $g_{\perp} = 2.069$ is observed. The g_{\perp} component of this signal is split into 13 poorly resolved lines, a part of which are hidden in the strong signals of radicals formed in the matrix. These 13 lines with a splitting of 1.5×10^{-3} cm⁻¹ can be attributed to the superhyperfine interaction between the electron and the four equivalent chlorine nuclei ($I = \frac{3}{2}$ for ³⁵Cl and ³⁷Cl). This signal is reasonably attributed to $[\text{PdCl}_4]^{3-}$.

In addition to this signal, weak signals with $g_{\parallel} = 2.242$, 2.273, and 2.79 are observed in this figure. The relative intensities of the signals with $g_{\parallel} = 2.273$ and 2.79 increase as the concentration of lithium chloride increases as shown in Figure 1b. The signal with $g_{\parallel} = 2.273$ is enhanced also by the increase of the concentration of lithium chloropalladate as shown in Figure 1c.

The values of g_{\parallel} for the complexes of palladium(I) of the PdCl_4 or PdO_4 type are usually in the range from 2.48 to 2.62.³ In addition, mixed-ligand complexes of the $\text{PdCl}_{4-n}\text{O}_n$ type are supposed to have similar g_{\parallel} values. Therefore it is difficult to assign the above three signals to usual mixed-ligand complexes such as $[\text{PdCl}_{4-n}(\text{EtOH})_n]^{n-3}$. In other words, the g_{\parallel} value 2.79 is too large and 2.242 and 2.273 are too small to be assigned to these mixed-ligand complexes. It is supposed that these signals are due to somewhat unusual complexes. These signals can be observed also when n -propyl or n -amyl alcohol is used instead of ethanol. However these signals do not appear when EG-H₂O is used as a solvent.

2. *Pd^ICl_{4-n}L_n.* When potassium thiocyanate is added to an ethanol solution of lithium chloropalladate (5 mM), resultant esr spectra change as shown in Figure 2. As the concentration of potassium thiocyanate increases from 5 to 50 mM, the signals with $g_{\parallel} = 2.360$, 2.278, 2.213, and 2.190 appear one after another, and these signals can be attributed to $[\text{PdCl}_{4-n}(\text{SCN})_n]^{3-}$ with $n = 1, 2, 3$, and 4, respectively. The last signal has already been reported.³ In these com-

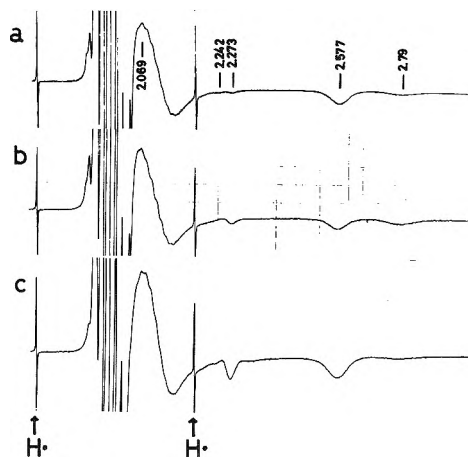


Figure 1. ESR spectra for γ -irradiated ethanol matrices containing 50 mM Li_2PdCl_4 (a), 50 mM Li_2PdCl_4 + 500 mM LiCl (b), and 500 mM Li_2PdCl_4 (c).

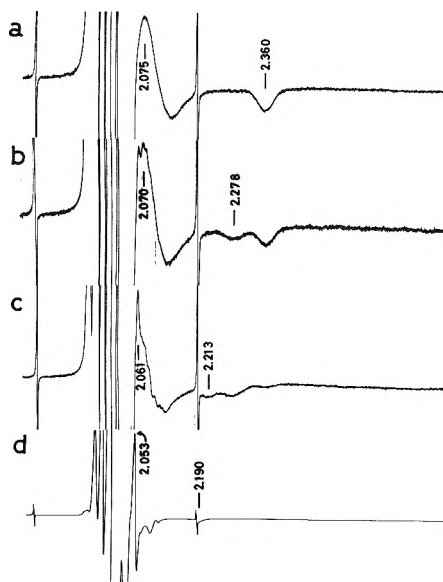


Figure 2. ESR spectra for γ -irradiated ethanol matrices containing 5 mM Li_2PdCl_4 and (a) 5, (b) 10, (c) 15, and (d) 50 mM KSCN .

plexes, it is supposed that thiocyanate ion coordinates to palladium ion by its sulfur atom and not by its nitrogen atom, since superhyperfine signals due to the nitrogen atom cannot be observed in Figure 2.

In a similar way, esr spectra for $\text{Pd}^{\text{II}}\text{Cl}_{n-4}\text{L}_n$ with $\text{L} = n$ -butylamine and ethylamine in ethanol and $\text{L} = \text{ammonia}$ and nitrite ion in $\text{EG-H}_2\text{O}$ were obtained for $n = 1-4$, and their esr parameters are given in Table I. The esr spectra for $[\text{PdCl}_{4-n}((n\text{-Bu})\text{am})_n]^{n-3}$ (am = amine) are shown in Figure 3.

When di- or tri- n -butylamine is added to an ethanol solution of lithium chloropalladate, esr spectra for $[\text{PdCl}_3(\text{am})]^{2-}$ and $[\text{PdCl}_2(\text{am})_2]^-$ can be observed. However esr spectra for $[\text{PdCl}(\text{am})_3]$ and $[\text{Pd}(\text{am})_4]^+$ could not be observed even when excess of amine was used. This indicates that more than three molecules of these amines can hardly coordinate to a palladium(II) ion, probably due to an interligand steric repulsion. This in turn suggests that $\text{PdCl}_2((n\text{-Bu})_2\text{am})_2$ and $\text{PdCl}_2((n\text{-Bu})_3\text{am})_2$ have a trans configuration.

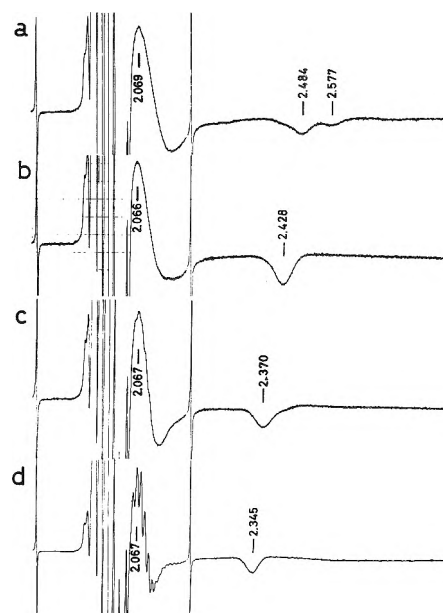


Figure 3. ESR spectra for γ -irradiated ethanol matrices containing 50 mM Li_2PdCl_4 and (a) 50, (b) 100, (c) 150, and (d) 200 mM n -butylamine.

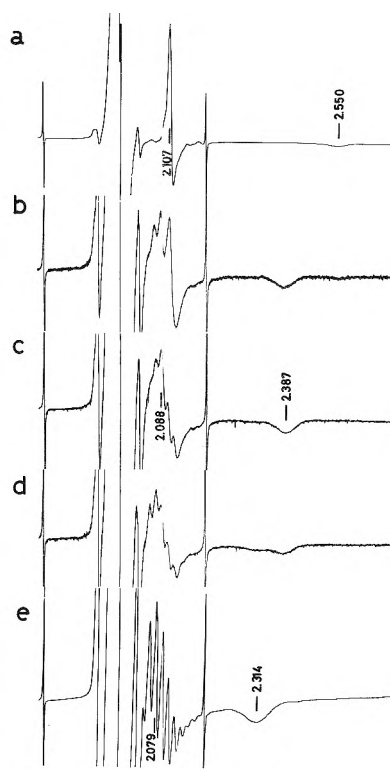


Figure 4. ESR spectra for γ -irradiated $\text{EG-H}_2\text{O}$ matrices containing 5 mM $\text{K}_2\text{Pd}(\text{C}_2\text{O}_4)_2$ and (a) 0, (b) 5, (c) 10, (d) 15, and (e) 20 mM KNO_2 .

3. $\text{Pd}^{\text{II}}(\text{C}_2\text{O}_4)_2\text{L}_2$. A γ -irradiated $\text{EG-H}_2\text{O}$ matrix containing potassium bis(oxalato)palladium(II) (5 mM) gives an esr spectrum with $g_{\parallel} = 2.550$ and $g_{\perp} = 2.107$ as shown in Figure 4a. This spectrum is attributed to $[\text{Pd}(\text{C}_2\text{O}_4)_2]^{3-}$.³ On adding potassium nitrite to this solution, a set of new signals with $g_{\parallel} = 2.387$ and $g_{\perp} = 2.088$ appears as shown in Figure 4c. The g_{\perp} component of this signal is split into five lines with a splitting of $2 \times 10^{-3} \text{ cm}^{-1}$. This indicates that

TABLE I: g Values for Mixed-Ligand Complexes of Palladium(I)

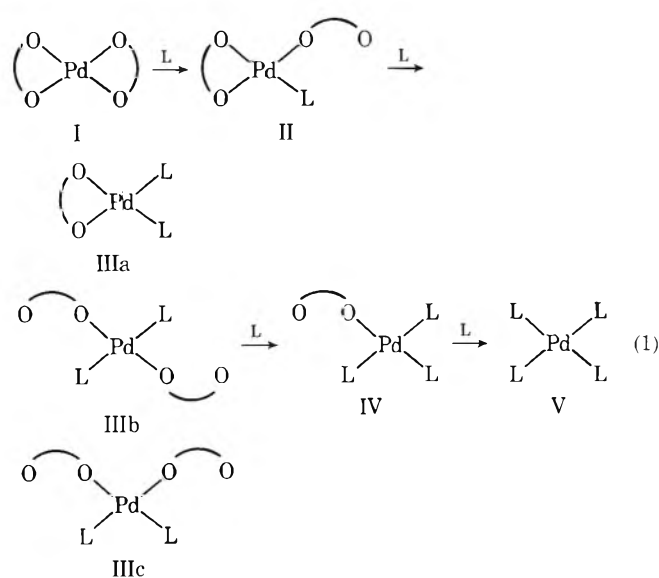
No. of ligand		g_{\parallel}	g_{\perp}	Host lattice	Solutes
Cl ⁻ , EtNH ₂					
4	0	2.577	2.069	EtOH	Li ₂ PdCl ₄ + LiCl
3	1	2.491	2.071		
2	2	2.433	2.072		
1	3	2.382	2.069		
0	4	2.351	2.068		
Cl ⁻ , <i>n</i> -BuNH ₂					
3	1	2.484	2.069	EtOH	Li ₂ PdCl ₄ + <i>n</i> -BuNH ₂
2	2	2.428	2.066		
1	3	2.370	2.067		
0	4	2.345	2.067		
Cl ⁻ , (<i>n</i> -Bu) ₂ NH					
3	1	2.495	2.072	EtOH	Li ₂ PdCl ₄ + (<i>n</i> -Bu) ₂ NH
2	2	2.431	2.069		
Cl ⁻ , (<i>n</i> -Bu) ₃ N					
3	1	2.485	2.073	EtOH	Li ₂ PdCl ₄ + (<i>n</i> -Bu) ₃ N
2	2	2.429	2.070		
Cl ⁻ , NH ₃					
3	1	2.485	2.071	EG-H ₂ O	K ₂ PdCl ₄ + NH ₃
2	2	2.436	2.065		
1	3	2.385	2.064		
0	4	2.344	2.065		
Cl ⁻ , NO ₂ ⁻					
3	1	2.432	2.068	EG-H ₂ O	K ₂ PdCl ₄ + KNO ₂
2	2	2.357	2.070		
1	3	2.340	2.070		
0	4	2.314	2.079		
Cl ⁻ , SCN ⁻					
3	1	2.360	2.075	EtOH	Li ₂ PdCl ₄ + KSCN
2	2	2.278	2.070		
1	3	2.213	2.061		
0	4	2.190	2.053		
C ₂ O ₄ ²⁻ , NH ₃					
2	0	2.550	2.108	EG-H ₂ O	K ₂ [Pd(C ₂ O ₄) ₂]
1	2	2.448	2.080		
C ₂ O ₄ ²⁻ , NO ₂ ⁻					
1	2	2.387	2.088	EG-H ₂ O	K ₂ [Pd(C ₂ O ₄) ₂] + KNO ₂
C ₂ O ₄ ²⁻ , SCN ⁻					
1	2	2.345	2.073	EG-H ₂ O	K ₂ [Pd(C ₂ O ₄) ₂] + KSCN
OAc ⁻ , <i>n</i> -BuNH ₂					
2	0	2.617	2.105	Toluene	Pd(OAc) ₂
2	1	2.520	2.091		
2	2	2.448	2.073		
1	3	2.384	2.074		
0	4	2.342	2.074		
OAc ⁻ , py					
2	1	2.500	2.100	Toluene	Pd(OAc) ₂ + py
2	2	2.431	2.080		
1	3	2.363	2.078		

this signal is due to the complex in which a palladium ion is coordinated by two equivalent nitrogen atoms ($I = 1$ for ¹⁴N). On further addition of potassium nitrite the signal with $g_{\parallel} = 2.314$, $g_{\perp} = 2.079$, and $|A_{\perp}(\text{N})| = 2.0 \times 10^{-3} \text{ cm}^{-1}$ (nine lines) appears (Figure 4e). This signal has been attributed to $[\text{Pd}(\text{NO}_2)_4]^{3-}$.³ No other signals could not be

observed when the concentration of potassium nitrite was changed from 5 to 50 mM as shown in Figure 4a-e. This indicates that only one kind of mixed-ligand complex of the PdN₂O₂ type is abundant enough to be detectable in these solutions.

Ligand substitution of bis(oxalato)palladium(II) ions is

supposed to proceed through the reactions shown in eq 1.



Experimental results show that a mixed-ligand complex such as II or IV in eq 1 is not stable in this case. This suggests that the oxalato ion cannot coordinate to the palladium(II) ion as a unidentate ligand, but only as a bidentate ligand. This in turn suggests that the PdN_2O_2 type complex observed above is not IIIb or IIIc, but IIIa. In mixed-ligand complexes II, IIIa, IIIb, IIIc, and IV, only IIIa is the complex which does not contain unidentate oxalate ion.

When ammonia or potassium thiocyanate is used instead of potassium nitrite, similar results are obtained, and the g values for $[\text{Pd}(\text{C}_2\text{O}_4)(\text{NH}_3)_2]^-$ and $[\text{Pd}(\text{C}_2\text{O}_4)(\text{SCN})_2]^{3-}$ are given in Table I. In $[\text{Pd}(\text{C}_2\text{O}_4)(\text{SCN})_2]^{3-}$, thiocyanate ions are supposed to coordinate to a palladium ion by their sulfur atoms, since superhyperfine signals due to nitrogen atoms cannot be observed, as in the case of $[\text{PdCl}_{4-n}(\text{SCN})_n]^{3-}$.

4. $\text{Pd}(\text{OCOR})_2$. It has been reported that diacetato- and dipropionatopalladium(II) in benzene are trimeric at 37° (osmometric method) and monomeric at 80° (ebullioscopic method).⁹ However, all attempts to observe each of the spectra for monomer and trimer by infrared, ultraviolet, and nmr spectroscopy have not succeeded.

Figure 5a is the esr spectrum for a γ -irradiated toluene matrix containing 25 mM diacetatopalladium(II). In this figure, two sets of signals can be observed: the stronger signal with $g_{\parallel} = 2.588$ and the weaker one with $g_{\parallel} = 2.618$. The g_{\perp} components are superposed at $g_{\perp} = 2.104$. When the concentration of diacetatopalladium(II) is increased to 100 mM, the signal with $g_{\parallel} = 2.618$ becomes very weak, as shown in Figure 5b. A similar result is obtained for dipropionatopalladium(II) in toluene. In this case two signals with $g_{\parallel} = 2.626$ and 2.595 are observed, with g_{\perp} components superposed at $g_{\perp} = 2.107$. The signal with $g_{\parallel} = 2.625$ becomes weak as the concentration of dipropionatopalladium(II) becomes large.

These results suggest that the signal with the larger g_{\parallel} is attributed to the monomer ion $[\text{Pd}(\text{OCOR})_2]^-$ and that with the smaller g_{\parallel} to the trimer ion $(\text{Pd}(\text{OCOR})_2)_3^-$, where $\text{R} = \text{CH}_3$ or C_2H_5 . It is supposed that an unpaired electron in $(\text{Pd}(\text{OCOR})_2)_3^-$ is not delocalized over the whole trimeric molecule but is localized on a PdO_4 unit. If the unpaired

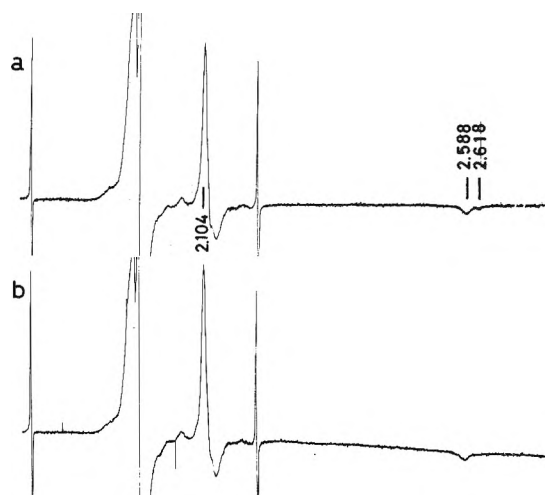


Figure 5. ESR spectra for γ -irradiated toluene matrices containing (a) 25 and (b) 100 mM diacetatopalladium(II).

electron is delocalized, the g values for the trimer ion will be largely different from those of the monomer ion.

A γ -irradiated toluene matrix containing dibenzoatopalladium(II) gives only a set of signals with $g_{\parallel} = 2.579$ and $g_{\perp} = 2.102$. It has been reported that benzoate is trimeric at 37° and remains trimeric at 80° in benzene, and even at 132° in chlorobenzene.⁹ Therefore the above signal is reasonably attributed to a trimer ion, $(\text{Pd}(\text{OCOC}_6\text{H}_5)_2)_3^-$. A γ -irradiated AcOH-EtOH matrix containing diacetatopalladium(II) gives only a set of signals with $g_{\parallel} = 2.613$ and $g_{\perp} = 2.104$. This signal is assigned to a monomer ion, since it has been reported that diacetatopalladium(II) in acetic acid is monomeric.¹⁰

From these results it is concluded that the g_{\parallel} values for monomer ions are in the range from 2.61 to 2.63 and those for trimer ions from 2.58 to 2.60. As far as we know, this is the first observation of each of the monomer and trimer of dicarboxylatopalladium(II) by a spectroscopic method.

5. $[\text{Pd}(\text{OCOCH}_3)_m\text{L}_n]^{1-m}$. When n -butylamine is added to the solution of diacetatopalladium(II) (50 mM) in toluene, the signals shown in Figure 5a disappear and the signals with $g_{\parallel} = 2.520$, 2.448, 2.384, and 2.342 appear one after another. The last signal agrees with that for $[\text{Pd}(n\text{-Bu})\text{am}]_4^+$. The other signals are attributed to mixed-ligand complexes. Since the acetate bridge in trimeric diacetatopalladium(II) can be easily cleaved by amine,⁹ these mixed-ligand complexes are supposed to be monomeric.

Ligand substitution of diacetatopalladium(II) is also supposed to proceed through the reactions shown in eq 1, where in this case L is n -butylamine and O-O is the acetate ion. From dipole moment measurements, it has been supposed that among three PdN_2O_2 type complexes, IIIa, IIIb, and IIIc, only IIIb is stable in benzene,⁹ and this might be also true in toluene. Therefore the signals with $g_{\parallel} = 2.520$, 2.448, and 2.384 are assigned to the complexes corresponding to II, IIIb, and IV, respectively.

In a similar way, the g values for the mixed-ligand complexes $[\text{Pd}(\text{OCOCH}_3)_m(\text{py})_n]^{1-m}$ with $n = 1-3$ were determined by adding pyridine to the solution of diacetatopalladium(II) in toluene. The g values for these complexes are given in Table I. In this case the signal due to $[\text{Pd}(\text{py})_4]^+$ could not be detected even when a mixture of pyridine and toluene (1:1 by volume) is used as solvent.

References and Notes

* To whom correspondence should be addressed at the Central Research Laboratories, Kuraray Co. Ltd., Kurashiki, Okayama 710, Japan.

- (1) S. Fujiwara and M. Nakamura, *J. Chem. Phys.*, **52**, 6299 (1970).
- (2) S. Fujiwara and M. Nakamura, *J. Chem. Phys.*, **54**, 3378 (1971).
- (3) M. Nakamura and S. Fujiwara, *J. Coord. Chem.*, **1**, 221 (1971).
- (4) S. Fujiwara, T. Watanabe, and H. Tadano, *J. Coord. Chem.*, **1**, 195 (1971).
- (5) J. Isoya, H. Ishizuka, A. Yamasaki, and S. Fujiwara, *Chem. Lett.*, 397 (1971).
- (6) J. Isoya and S. Fujiwara, *Bull. Chem. Soc. Jap.*, **45**, 2182 (1972).
- (7) C. Amano and S. Fujiwara, *Bull. Chem. Soc. Jap.*, **46**, 1379 (1973).
- (8) T. A. Stephenson, S. M. Morehouse, A. P. Powell, J. P. Heffer, and G. Wilkinson, *J. Chem. Soc.*, 3632 (1965).
- (9) S. M. Morehouse, A. P. Powell, J. P. Heffer, T. A. Stephenson, and G. Wilkinson, *Chem. Ind. (London)*, 544 (1964).
- (10) M. Tamura and T. Yasui, *Kogyo Kagaku Zasshi*, **71**, 1855 (1968).

Oxygen-17 Anisotropic Dipolar Interaction in the Carbonyl Group of Semiquinones

E. Melamud and Brian L. Silver*

Chemistry Department, Technion—Israel Institute of Technology, Haifa, Israel (Received April 25, 1974)

The esr spectrum of ^{17}O -labeled chloranil and chloranilic acid anion radicals has been observed in frozen solutions. The measured ^{17}O hyperfine splittings depend strongly on the cation. With quarternary ammonium ions the values of ρ_{O} derived from the anisotropic dipolar interaction are in good agreement with those derived from the solution value of a_{O} , by use of the equation $|a_{\text{O}}| = |41|\rho_{\text{O}}$. With K^+ or Na^+ ions the observed splittings in frozen solution imply very different values of ρ_{O} from those estimated from solution spectra, indicating the formation of ion pairs.

Introduction

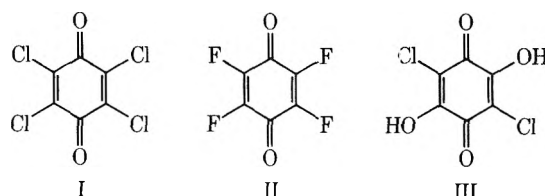
Radicals containing the carbonyl group are of considerable chemical and biological importance. In particular the semiquinones and semidiones have been the subject of intensive theoretical and experimental study for many years.¹ The proton splittings in semiquinones were among the first hyperfine interactions to attract the attention of chemists, and subsequently hyperfine interactions due to ^{19}F ,² ^{13}C ,³ ^{17}O ,⁴ and other nuclei have been observed. The distribution of spin densities in these molecules and their correlation with isotropic hyperfine splittings have provided a continuing challenge to the theoretician. Spin densities have been calculated by methods ranging from simple Hückel to SCF configuration interaction. σ - π polarization parameters for ^{13}C and ^{17}O have also been estimated by numerous authors.³⁻⁵ All these studies suffer from the drawback that they are indirect and there were no independent measurements of spin densities available against which to check those calculated theoretically or estimated semiempirically from isotropic splittings. Ideally the anisotropic ^{13}C and ^{17}O tensors should be studied since they provided a far more direct and convincing estimate of π -spin densities. Such studies have not been reported since it is not easy to prepare magnetically dilute single crystals of semiquinones. However, in favorable circumstances anisotropic dipolar tensors can be determined from the esr spectra of powder samples and oxygen-17 is relatively favorable for this kind of study since the hyperfine interaction is often large.

In the present communication we report the observation of anisotropic ^{17}O splittings for a *p*- and an *o*-semibenzoquinone in frozen solution. The purpose of obtaining these data was twofold: (i) to allow a more reliable estimate of the spin density on the carbonyl oxygen than has hitherto been available and (ii) to determine whether the data fit

the equation $a_{\text{O}} = -41\rho_{\text{O}}$. This equation has been found to account well for all previously reported isotropic ^{17}O splittings in π radicals, where ρ_{O} was measured from the anisotropic hyperfine interaction.⁶

Experimental Section

Chloranil (2,3,5,6-tetrachloro-1,4-benzoquinone) (I) and tetrabutylammonium iodide, both of puriss grade, were obtained from Fluka AG. Fluoranil (II) (tetrafluoro-*p*-benzoquinone) was a Pierce Chemical product. Both chloranilic acid (2,5-dichloro-3,6-dihydroxy-*p*-benzoquinone) (III)



and tetramethylammonium hydroxide, 10% in water, were obtained from Eastman Organic. Purified sodium dithionite ($\text{Na}_2\text{S}_2\text{O}_4$) was obtained from Baker Chemical Co. ^{17}O -enriched water (up to 40 atom %) was obtained from Yeda, Rehovot, Israel. ^{17}O -labeled quinones were prepared by exchange with H_2^{17}O as described previously.⁴ Semiquinone radicals were produced by two methods: reduction of quinones with iodide ion in acetone and reduction with dithionite ion in basic aqueous solution. Spectra were recorded at the X band on a Varian V-4502 esr spectrometer with 100-kc modulation, equipped with a variable-temperature accessory.

Description of Spectra

The radicals referred to in the following discussion are

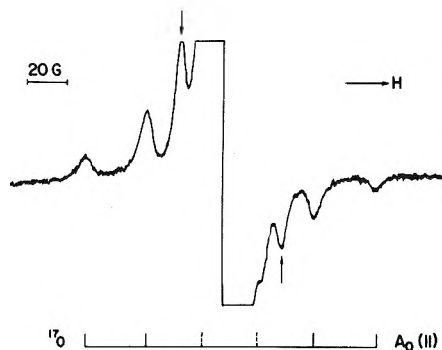


Figure 1. Esr spectrum of the chloranilic acid anion radical (containing 20 atom % ¹⁷O) in a frozen solution of 5 N NaOH at -30°. The two lines indicated by arrows are $m_1 = \pm 5/2$ satellites associated with $A_0(\perp)$.

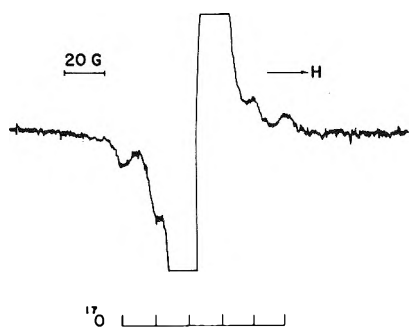


Figure 2. Esr spectrum of the ¹⁷O-labeled chloranilic acid anion radical (containing 40 atom % ¹⁷O) in a frozen solution of 10% (CH₃)₄NOH at -30°.

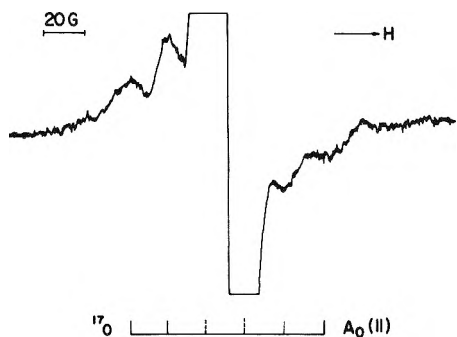


Figure 3. Esr spectrum of the chloranil anion radical (containing 40 atom % ¹⁷O) in a frozen KI-acetone solution at -100°.

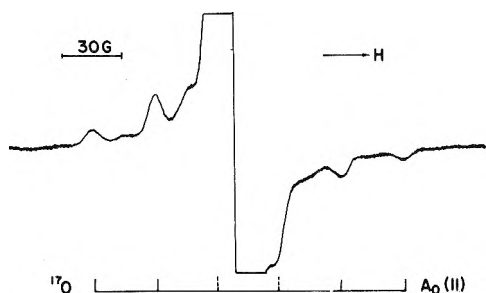


Figure 4. Esr spectrum of the chloranil anion radical (containing 40 atom % ¹⁷O) in a frozen (t-Bu)₄NI-acetone solution at -100°. The stick diagram indicates the ¹⁷O satellites due to singly labeled molecules.

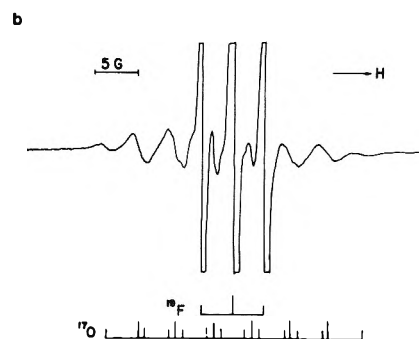
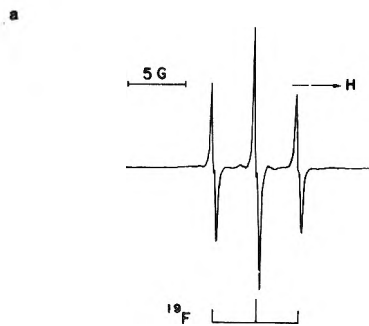
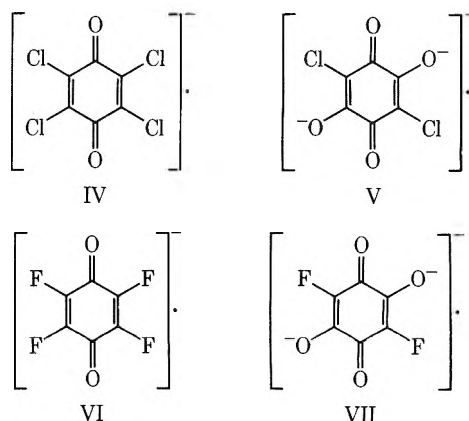


Figure 5. (a) Esr spectrum of the fluoranilic acid anion radical in a solution of 5 N NaOH at room temperature. (b) Esr spectrum of the fluoranilic acid anion radical (containing 20 atom % ¹⁷O) in a solution of 5 N NaOH at room temperature.



Figure 6. Esr spectrum of a solution of fluoranil in 1 N NaOH containing sodium dithionite, at room temperature.

IV-VII. The hyperfine couplings observed are listed in Table I and esr spectra are given in Figures 1-6.



Solution Spectra. The solution esr spectrum obtained from chloranil using dilute NaOH and dithionite, or I⁻ in acetone (line 1, Table I), is the same as that previously obtained^{2,4} by electrolysis, identifying the radical as the chloranil anion (IV). On the other hand the solution spectrum obtained on dithionite reduction of chloranil in strong base gave solution spectra with ¹⁷O and ¹³C splittings typical

TABLE I: Observed Hyperfine Coupling (in Gauss)

Quinone	Method	Radical	$-a_O$	$-A_O(\parallel)$	$-2B_O$	$ a_{C_1} $	$ a_{C_2} $	$ a_F $	$ a_X $	Figure no. of spectrum
Chloranil	NaOH (0.1 N) + dithionite	IV	8.5			4.8	2.8			1
Chloranil	NaOH (KOH)(1 N, 5 N) + dithionite	V	4.6	30	25.4	7.9	2.7			2
Chloranil	$(CH_3)_4NOH$ (10%) + dithionite	V	4.7	16.6	11.9	7.9	2.5			3
Chloranil	Acetone + KI	IV	8.5	19	10.5					4
Chloranil	Acetone + (<i>t</i> -Bu) ₄ NI	IV	8.5	32	23.5					
Chloranilic acid	Acetone + (<i>t</i> -Bu) ₄ NI	V				7.9	2.7			
Fluoranil	NaOH (1 N) + dithionite	VI						3.8 (quintet)		
Fluoranil	NaOH (0.01 N)	VII	4.6			7.7	2.5	3.7 (triplet)	0.3	5
Fluoranil	NaOH (5 N) + dithionite	?						0.9 (quintet)	0.3	6
Fluoranil	NaOH 1 N + dithionite									

(line 2, Table I) of the chloranilic acid anion (V) which has been observed both here and previously.^{2,4} It appears that in strong base two chlorine atoms are replaced by hydroxyl groups. To provide supporting evidence for this reaction we carried out some experiments on fluoraril-¹⁷O, which has the advantage that fluorine splittings are readily seen and allow the number of fluorine atoms in the radical to be determined directly. In dilute base fluoranil gave the spectrum (line 7, Table I) previously found⁷ for the fluoranil anion radical (VI), a quintet with $|a_F| = 3.8$ G. In 5 N NaOH in the presence of dithionite a 1:2:1 spectrum is observed (line 8, Table I) with $|a_F| = 3.75$, $|a_O| = 4.6$, $|a_{C_1}| = 7.7$, and $|a_{C_2}| = 2.5$ G, indicating the presence of only two fluorines. The splittings observed in 5 N NaOH are close to those reported² for 1,4-difluoro-3,5-dioxobenzosemiquinone (VII) in 0.5 N NaOH, *viz.*, $|a_F| = 3.85$, $|a_O| = 4.75$, and two ¹³C splittings of 2.55 and 8.02 G. By analogy with the assignment of the two ¹³C splittings in the chloranilic acid trianion,⁸ carbon atoms C₁ and C₂ are assigned to the fluorine-bonded and carbonyl carbons, respectively. In our spectra a small additional doublet splitting of ~0.3 G is observed, the origin of which is not clear. Although not relevant to this work, the spectra observed (line 9, Table I, Figure 6) for fluoranil in 1 N aqueous NaOH solution may be of chemical interest. The 1:4:6:4:1 quintet with a splitting of 0.9 G indicates the presence of four spin 1/2 nuclei but the authentic fluoranil anion radical gives $|a_F| = 3.8$ G and we have no suggestion as to the structure of the radical observed here. It is of relevance to the observations reported above that in alkaline solution quinones with a free quinoid position react at room temperature to form a hydroxy adduct and subsequently a hydroxysemibenzoquinone radical.⁹ If aromatic hydrogens can be readily replaced, it is not surprising that halogen atoms can also be lost.

Frozen-Solution Spectra. Chloranil Anion Radical. The chloranil anion radical (IV), enriched in ¹⁷O (~40 atom %), was prepared in acetone solution by the addition of both KI and (*t*-Bu)₄NI. The solutions were frozen and the esr spectra examined at -100° (Figures 3 and 4; lines 4 and 5, Table I). The solution containing KI shows satellites which can be assigned to ¹⁷O, with a measured splitting of $|19|$ G. The ¹⁷O hyperfine tensor in the semiquinone can be predicted to have roughly axial symmetry with the direction associated with the largest principal hyperfine value $A_O(\parallel)$ being parallel to the axis of the $p\pi$ orbitals. From the standard treatment of random spectra it follows that the observed splittings can be assigned to $A_O(\parallel)$.

The solution containing (*t*-Bu)₄NI has a better signal to noise ratio and shows, in addition to strong ¹⁷O satellites (corresponding to the stick diagram in Figure 4), weaker satellites. These are located halfway between the stronger satellites which indicates that they arise from radicals doubly labeled with ¹⁷O. Since the quinone contains ~40 atom % ¹⁷O, the ratio of singly to doubly labeled molecules is 4:1. The doubly labeled satellites have relative intensities of 1:2:3:4:5:6:5:4:3:2:1 and thus the outer satellites are difficult to observe. If the anisotropic hyperfine tensor is assumed to be axial and the value of a_O in solution, -8.5 G, is assumed to apply in the frozen solution, then the value of $A_O(\perp)$ can be estimated at ~3.3 g. Thus the extreme ($m_I = \pm 5/2$) satellites associated with $A_O(\perp)$ are expected to have a separation of ~16 G and would fall under the main peak due to the unlabeled molecules.

Chloranilic Acid Trianion Radical (V). The trianion enriched in ¹⁷O (20 atom %) was prepared by dithionite re-

TABLE II: Oxygen Spin Densities in Chloranil and Chloranilic Acid Anion Radicals

Radical	Method of prepn	ρ_O from $2B_O$	ρ_O from a_O
Chloranil anion	(<i>t</i> -Bu) ₄ NI in acetone	0.228	0.207
Chloranil anion	KI in acetone	0.102	0.207
Chloranilic acid anion	(CH ₃) ₄ NOH + dithionite	0.116	0.115
Chloranilic acid anion	KOH or NaOH + dithionite	0.247	0.112

duction in NaOH, 1 and 5 *N*, and in 10% (CH₃)₄NOH. The solutions were frozen and the esr spectra studied at -30° (Figures 1 and 2; lines 3 and 6, Table I). The frozen sodium hydroxide solution showed well-resolved peaks, four of which can be assigned to the $m_I = \pm\frac{3}{2}$ and $m_I = \pm\frac{5}{2}$ satellites associated with $A_O(\parallel)$. If the solution values of a_O , -4.6 G, is used and the anisotropic dipolar tensor assumed to be axial, the predicted value of $|A_O(\perp)|$ is ~8.1 G, leading to a separation of ~40 G between the $m_I = \pm\frac{5}{2}$ satellites associated with $A_O(\perp)$. As may be seen in Figure 1 there are two unassigned peaks with a separation of 50 G. These are assigned to $A_O(\perp)$, which is thus deduced to have a value of 10 G. The appearance of only one set of satellites apart from those associated with $A_O(\parallel)$ indicates either that the assumption of axiality is valid or that there is a marked deviation from axiality and that a further set of satellites is buried under the main peak. The frozen (CH₃)₄NOH solution shows somewhat less well-resolved ¹⁷O satellites, which are once again assigned to $A_O(\parallel)$. The value of $|A_O(\perp)|$ estimated as for previous spectra is ~1.3 G, and thus satellites associated with $A_O(\perp)$ are expected to fall within the main peak of the spectrum.

In the above discussion we have taken A_O to be negative, which has been demonstrated experimentally for *p*-benzosemiquinone¹⁰ and on the basis of theoretical studies⁴ is expected to be true for other π radicals.

Discussion

The ¹⁷O couplings listed in Table I can be used to derive spin densities in two quite different ways. The solid spectra, together with values of a_O from solution, can be used to derive the magnitude of $2B_O$, the anisotropic contribution to the ¹⁷O splitting when the field is perpendicular to the plane of the radical. Taking the value of 2β as -103 G¹¹ the spin density on the oxygen atom can then be estimated by putting $\rho_O = 2B_O/103$. This procedure neglects the very small contribution to $2B_O$ from spin on the neighboring carbon atom. Alternatively values for ρ_O can be estimated from the solution spectra by using the equation $a_O = 41\rho_O$, which has been proposed to hold for ¹⁷O splittings in π radicals.⁶ The results are shown in Table II.

The spin densities estimated by both methods agree well for chloranil anion and chloranilic acid trianion prepared using quarternary ammonium compounds. The previously calculated values of 0.2244 and 0.2031 obtained by the HMO and McLachlan SCF methods respectively⁴ for chloranil agree quite well with the present results. The corresponding theoretical values for chloranilic acid anion are 0.1515 and 0.1243, from which it appears that the HMO method overestimates ρ_O . While it is not possible to generalize from our results, it is known that *o*-semiquinones present difficulties in regard to the calculation of proton splittings, since they appear to require different Hückel parameters from *p*-semiquinones.

In a previous paper it was shown that for π radicals in which values of ρ_O can be deduced from anisotropic couplings, the equation $a_O = -41\rho_O$ is valid to a high degree of accuracy.⁶ At the time there were two important groups for which anisotropic ¹⁷O couplings were not available, *viz.*, the carbonyl group and the peroxy group. The results of the present paper concern the carbonyl group and an account of a single-crystal study of tetralin peroxy radical is in the press.¹² Regarding the carbonyl group, the results in Table II for the uncomplexed chloranil anion and chloranilic acid trianion show that the values of ρ_O calculated from the equation $a_O = -41\rho_O$ agree very well with those estimated from the anisotropic ¹⁷O couplings. The results for the peroxy group are also extremely satisfactory. For the two oxygen atoms, taking the values of 18.0 and 24.0 G for a_O (see ref 6) and the values of $2B_O$ as 60 and 88 G,¹² it follows that the values of ρ_O calculated from the anisotropic coupling are 0.41 and 0.62, compared to the values of 0.44 and 0.59 calculated from the equation $a_O = -41\rho_O$. Thus there is now overwhelming evidence for the applicability of the latter equation. The fact that the value of ρ_O for uncomplexed chloranilic acid, derived from the equation $a_O = -41\rho_O$, agrees with that derived from $2B_O$ indicates that the σ - π parameters of the *o*-semiquinones are effectively the same as those of the *p*-semiquinones.

Ion Pairing. From Table I it can be seen that in solutions prepared using potassium or sodium compounds the values of $A_O(\parallel)$ observed in the solid for chloranil anion are far smaller and for chloranilic acid anion far larger than those found when quarternary ammonium compounds are used. From Table II it can be seen that for the solutions containing K⁺ the spin densities derived from $2B_O$ are entirely different from those derived from a_O .

It is known from much previous work that the carbonyl group is very strongly complexed in solution by alkali metal ions in solvents of comparatively low dielectric constant.¹³ Acetone and water are too polar to allow observable effects on the esr spectrum in solution due to complexing of singly charged cations, but there may well be ion-pair formation on freezing. The results indicate that the large ions (CH₃)₄N⁺ and (*t*-Bu)₄N⁺ are not significantly complexed, since the spin densities derived from the solid spectra are close to those deduced from the solution spectra. It is not possible to predict the effect of ion pairing on spin distribution unless the site of complexation is known. That large changes could occur on complexation of cations at oxygen is suggested by the work of Sullivan, *et al.*, on the hydroquinone cation radical¹⁴ for which $|a_O| = 7.83$ G in CH₃NO₂, compared to the value of 9.46 G for the *p*-benzosemiquinone radical in DMSO. A similar case is that of the nitroxyl group for which protonation results in an increase in a_N from 15 to 22 G.¹⁵ Taking a_N to be approximately proportional to ρ_N , the change in a_N implies an increase of ~50% in ρ_N . Since $\rho_N \approx \rho_O = 0.5$ in the nitroxyl group,¹⁶

this implies a decrease of $\sim 50\%$ in ρ_O . Thus the large decrease in ρ_O for the chloranil anion in the solid suggests that the K^+ ion may be complexed at the carbonyl oxygens. Since only one type of ^{17}O splitting is seen in the spectrum, it must be assumed that K^+ complexes at both oxygens. The increase in ρ_O for the chloranilic acid anion in the presence of K^+ in the solid cannot be accounted for by such a mechanism and we have no explanation of this phenomenon.

Conclusion

The oxygen spin densities in an *o*- and *p*-benzosemiquinone have been decided directly from the anisotropic ^{17}O coupling. The values agree very well with those estimated from the solution spectra using the relationship $a_O = -41\rho_O$ and provide additional support for this simple relationship between a_O and ρ_O .

The results for frozen solutions containing K^+ or Na^+ ions serve as a general warning that even if ion pairing shows no observable effects in solution it can seriously affect spin density distribution in the solid.

If, as we contend, spin densities in semiquinones can be confidently estimated from observed isotropic ^{17}O splittings in solution, this fact has direct relevance to the question of σ - π polarization parameters for ^{13}C in the carbonyl group. The spin density in semiquinones can now be estimated at the oxygen atoms and at the carbon atoms bonded to protons. In many cases the only remaining carbon atoms are the carbonyl carbons, the spin on which can now

often be determined more reliably than heretofore. Such data can provide a firmer basis for the determination of the Q matrix for carbonyl ^{13}C .

References and Notes

- (1) (a) G. A. Russell in "Radical Ions," E. T. Kaiser and L. Kevan, Ed., Interscience, New York, N. Y., Chapter 3; (b) G. Vincow, *ibid.*, Chapter 4.
- (2) W. E. Geiger and W. M. Gulick, *J. Amer. Chem. Soc.*, **91**, 4657 (1969).
- (3) M. Broze and Z. Luz, *J. Chem. Phys.*, **51**, 749 (1969).
- (4) M. Broze and Z. Luz, *J. Chem. Phys.*, **51**, 738 (1969); M. Broze, Z. Luz, and B. L. Silver, *ibid.*, **48**, 4891 (1967).
- (5) R. Poupko, B. L. Silver, and M. Rubinstein, *J. Amer. Chem. Soc.*, **92**, 4512 (1970).
- (6) E. Melamud and B. L. Silver, *J. Phys. Chem.*, **77**, 896 (1973). In Table II of this reference the values of $|\Sigma a_O|$ for $(CH_3)_2COO^0$ and $C_6H_5(CH_3)_2COO^0$ should both be changed from 38.2 to 42.0 G, since there was an error in the original measurements. The revised values of a_O are 18.0 and 24.0 G; J. R. Morton, private communication; J. A. Howard, *Can. J. Chem.*, **50**, 1981 (1972). This change results in even better agreement than previously with the prediction that for the compounds in the table, $|\Sigma a_O| = 41 G$.
- (7) J. W. Eastman, G. M. Andros, and M. Calvin, *Nature (London)*, **193**, 1067 (1962).
- (8) M. Broze and Z. Luz, *J. Phys. Chem.*, **71**, 3690 (1967).
- (9) J. A. Pedersen, *J. Chem. Soc., Perkin Trans. 2*, **4**, 424 (1973).
- (10) B. L. Silver, Z. Luz, and C. Eden, *J. Chem. Phys.*, **44**, 4258 (1966).
- (11) P. B. Ayscough, "Electron Spin Resonance in Chemistry," Methuen, London, 1967, Appendix III. The symbol 2β denotes the anisotropic dipolar contribution from unpaired spin in a p orbital when the external magnetic field is along the axis of the orbital.
- (12) E. Melamud, S. Schlick, and B. L. Silver, *J. Magn. Resonance*, in press.
- (13) N. Hirota in "Radical Ions," E. T. Kaiser and L. Kevan, Ed., Interscience, New York, N. Y., 1968, Chapter 2.
- (14) P. D. Sullivan, J. R. Bolton, and W. E. Geiger, Jr., *J. Amer. Chem. Soc.*, **92**, 4176 (1970).
- (15) A. H. Cohen and B. M. Hoffman, *J. Amer. Chem. Soc.*, **95**, 2061 (1973).
- (16) H. Hayat and B. L. Silver, *J. Phys. Chem.*, **77**, 72 (1973).

A Theoretical Interpretation of the Rotational Barrier in Benzophenone Ketyl

Fernando Bernardi, Maurizio Guerra,

Laboratorio del C.N.R. dei Composti del Carbonio Contenenti Eteroatomi e loro Applicazioni, Ozzano Emilia, Bologna, Italy

and Gian Franco Pedulli*

Istituto di Chimica Organica, Viale Risorgimento 4, 40136 Bologna, Italy (Received February 19, 1974)

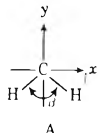
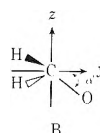
Publication costs assisted by Laboratorio del C.N.R. di Ozzano Emilia

The equilibrium geometry and the mode of rotation of benzophenone ketyl have been investigated within the INDO framework. In order to test the reliability of INDO predictions on this type of molecules, a detailed comparison of INDO and *ab-initio* MO calculations has been carried out on the formaldehyde ketyl with satisfactory results. The optimum geometry of benzophenone ketyl is discussed with relation to that of the parent neutral molecule. The computed energy barrier to rotation of 7.5 kcal compares favorably with the experimental value of 6.35 kcal. The calculated hyperfine splitting constants in both formaldehyde and benzophenone ketyls are also briefly discussed.

Introduction

The determination by electron resonance spectroscopy of rotational barriers in some radical anions of mono-¹ and diaryl^{2,3} ketones (ketyls) has been the subject of recent investigations. Ketyls containing the phenyl ring have re-

ceived more attention because of their stability and ability to be produced by a variety of methods from the corresponding ketones. By analyzing the line width variations with temperature of the esr spectrum of benzophenone ketyl Takeshita and Hirota² determined the rates of rotation of the aromatic rings and the corresponding activation

TABLE I: Optimum Geometrical Parameters and Inversion Barriers of Formaldehyde Ketyl Computed at INDO (A) and *ab-initio* (B) Levels



	Pyramidal		Planar	
α	34.8	0	27	0
β	107.4	120	113	113
r_{CH}	1.143	1.132	1.09	1.08
r_{CO}	1.302	1.305	1.306	1.317
Inversion barrier, kcal	4.71		0.54	

energy as 4.65 kcal mol⁻¹; a more accurate kinetic investigation on the same radical, recently made in this laboratory,³ provided a value of 6.35 kcal mol⁻¹ for the energy barrier to rotation.

Because of the intrinsic interest in this molecule and since many other diaryl ketyls are expected to behave similarly to benzophenone ketyl, it seemed worthwhile to examine this radical theoretically as far as the equilibrium geometry and the mode of rotation are concerned. Moreover since approximate MO calculations are reported in the literature for the parent ketone,⁴ it should be also interesting to compare the results for the ketyl with the corresponding neutral molecule and to examine how the presence of the additional electron modifies the equilibrium geometry and the rotational energy barrier.

Results and Discussion

Because of the molecular complexity of benzophenone ketyl, a theoretical investigation of this radical by means of *ab initio* calculations seems hardly practical. A more suitable way to study this problem is to work within the INDO⁵ framework, considering that we are dealing with an open shell system. However, some doubt could be cast on the reliability of the INDO approximate SCF method, when used for predicting equilibrium geometries and rotational energy barriers. In fact, in neutral benzophenone, the same CNDO/2 method gave results which are in complete disagreement with experimental evidence, as the energy minimum was found for a geometry with the two phenyl rings perpendicular to the plane of the carbonyl carbon atom.⁴

Before attempting to perform any calculations on benzophenone ketyl and in order to test the reliability of the INDO predictions on this type of radical, we have carried out a detailed comparison of INDO and *ab-initio* computations on the simplest ketyl, the formaldehyde radical anion.

Formaldehyde Ketyl. The most stable geometry of this radical has been determined by optimizing all the geometrical parameters with the procedure described in ref 6. The *ab-initio* approach used here is the unrestricted Hartree-Fock treatment⁷ and the computational programs were those of the Gaussian 70 series.⁸ All the calculations were performed by using the extended basis set 4-31 G.⁹

The optimum geometries are reported in Table I together with those calculated using the INDO method. Both treatments predict a pyramidal structure at the carbonyl carbon atom. The numerical values of the angle α between the plane containing the CH₂ group and the C-O bond

computed at the semiempirical and *ab-initio* levels are in good agreement (35 and 27°, respectively). Since the anomalous magnitude of the ¹⁷O and ¹³C hyperfine splitting constants in aliphatic ketyls have been explained in terms of the nonplanarity of the carbonyl carbon,¹⁰ our results give further support to this interpretation.

Also the optimized values of the other geometrical parameters computed with the two methods are in substantial agreement, and are consistent with the data given in a recent paper concerning a semiempirical investigation of aliphatic ketyls.¹¹

Our calculations predict also that the C-O bond length should increase, with respect to the neutral molecule, from the value of 1.22–1.23 Å experimentally found¹² in formaldehyde to the value of 1.30–1.31 Å computed for the corresponding ketyl. Although geometrical data on this type of radical are not available, the latter value favorably compares with the bond lengths determined in the excited states ¹A₂ and ³A₂ (1.32 and 1.31 Å, respectively) of formaldehyde,¹³ as it should be reasonably expected. Since these two states are pyramidal with out-of-plane angles of 20 and 35°, their structural similarity with the formaldehyde ketyl is also confirmed by the computed nonplanarity of this radical and may be justified in terms of the orbital occupancy in the three systems. In fact, in each case there is the same occupancy of the bonding π HOMO (double) and of the antibonding π LUMO (single), while the "oxygen" nonbonding orbital is singly occupied in the two excited states of formaldehyde and doubly occupied in the ketyl. The different occupancy of the nonbonding orbital should not have a significant effect on the molecular geometry, while, compared with the ground state of formaldehyde, population of the π LUMO, which is antibonding in character, results in an increase of the C-O bond length and a nonplanarity at the C center.

In Figure 1 is shown the potential energy curve for the motion of the oxygen atom out of the CH₂ plane, computed at the *ab-initio* level. The resulting inversion barrier (0.54 kcal) is smaller than that calculated within the INDO framework (4.7 kcal), suggesting that in such cases the INDO method tends to overestimate the height of this barrier.

The conclusion that may be drawn from these findings is that both methods give consistent results and reasonable equilibrium geometries for formaldehyde ketyl. This gives us more confidence in using the INDO method for a similar optimization of benzophenone ketyl.

Benzophenone Ketyl. The INDO calculations have been

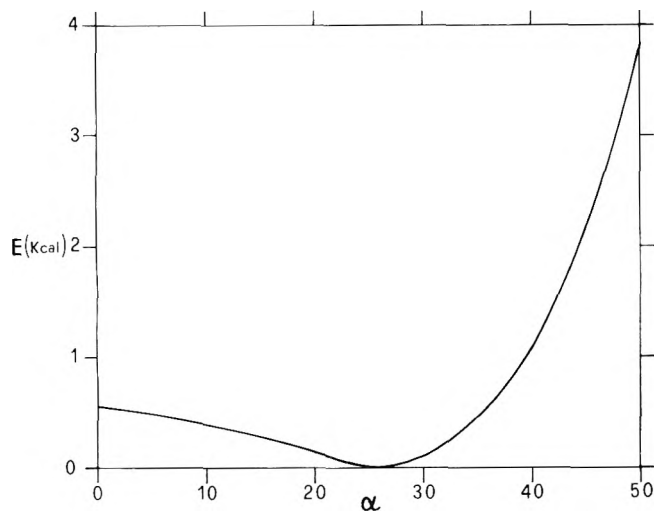


Figure 1. Potential energy curve for the motion of the oxygen atom out of the CH_2 plane in formaldehyde ketyl.

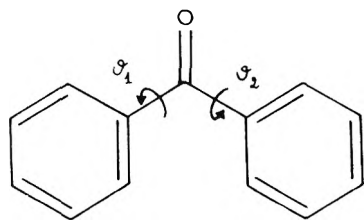


Figure 2. The conrotatory mode of rotation has been defined with both ϑ_1 and ϑ_2 positive according to the indicated direction of rotation.

performed on this radical starting from the geometrical parameters found on the parent benzophenone by X-ray studies:¹⁴ C–O, 1.23 Å; C'(phenyl)–C(carbonyl), 1.49 Å; angle C'CC'', 122°; the geometry of benzene has been assumed for the phenyl rings. At first we studied the conrotatory twisting of the two phenyls away from the plane of the carbonyl carbon atom (see Figure 2). Both rings were assumed to be twisted at the same angle ϑ . The potential energy curve, plotted in Figure 3, shows a minimum for the conformation having the two phenyls rotated by 22°. Since, however, in the formaldehyde ketyl the C–O bond distance was computed to be larger than in the parent neutral molecule, the calculations were repeated by varying this distance together with the C–C' and C–C'' bond lengths. In fact, the energy minimum was found by shortening the latter bonds to 1.445 Å and by increasing the C–O bond distance to 1.33 Å, a value almost identical with that calculated for formaldehyde ketyl; the rotation angle ϑ is only slightly modified to 23°. The last degree of freedom of the ground state we studied was the out-of-plane motion of the carbonyl oxygen. However, even very small deviations from planarity produce an increase of the potential energy; we must then conclude that, contrary to that calculated for formaldehyde ketyl, the out-of-plane angle for benzophenone ketyl is zero. This is not completely unexpected as a pyramidal configuration at the carbonyl carbon would greatly prevent the conjugation between phenyls and the carbonyl group. It is noteworthy that our calculations predict a reduction of both the twisting angle ϑ of the phenyls and the C–C' bond length accompanied by an increase of the C–O distance, with respect to benzophenone. This effect may be explained in terms of the occupancy, by the extra electron, of the π LUMO, which has a

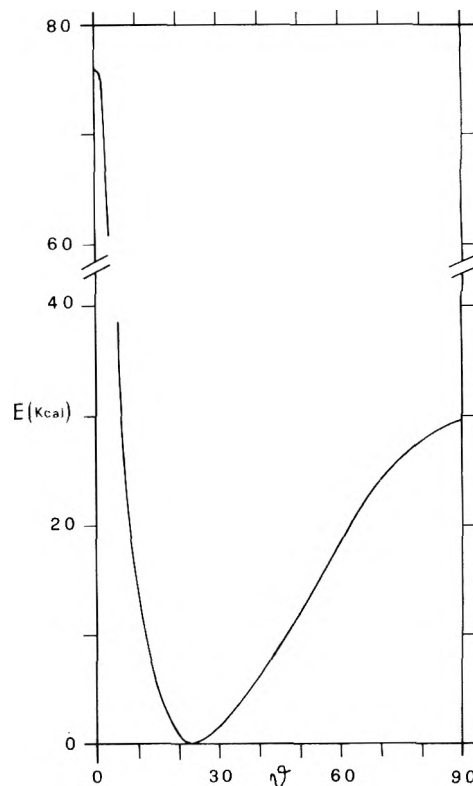


Figure 3. INDO potential energy curve for the conrotatory twisting of phenyl rings in benzophenone ketyl.

strong bonding character between the C and C' carbon atoms and an antibonding character in the C–O region, and is also in accord with the geometry predicted by extended Hückel MO calculations for the (n, π^*) excited state of benzophenone.⁴

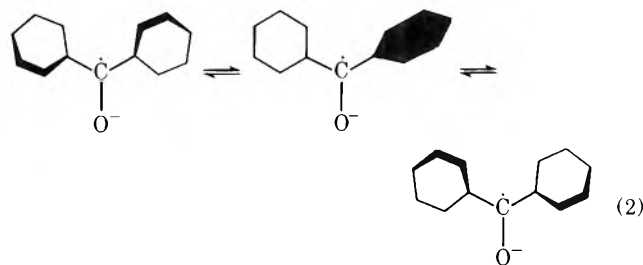
We have examined the mechanism of rotation of the phenyl rings to gain insight into the structure of the transition state and to determine the theoretical height of the rotational barrier. As discussed by Hoffmann and Swenson⁴ for the parent benzophenone, we can consider three possible mechanisms of interconversion which will lead to transition states which have (a) a planar conformation, (b) the two phenyls rotated by 90°, or (c) one phenyl coplanar with the carbonyl group and the other perpendicular. As shown in Figure 3 the first two mechanisms are characterized by energy barriers of 76 and 30 kcal, respectively, which are exceedingly large with respect to the experimental value of 6.35 kcal. Moreover they may be discarded on the basis of the experimental findings,³ since the first mechanism would imply a lack of line width alternation in the esr spectrum because no modulation of hyperfine splittings will occur, and the second should originate a different line broadening because of the simultaneous interconversion of the ortho and meta proton splittings in both rings. The third mechanism seems, therefore, the most reasonable one and the corresponding most probable transition state seems to be the conformation with $\vartheta_1 = 0^\circ$, $\vartheta_2 = 90^\circ$. In order to verify this we have evaluated the corresponding force constants. To this purpose we have computed the energies of several conformations varying both ϑ_1 and ϑ_2 by $\pm 5^\circ$ around the point $\vartheta_1 = 0^\circ$, $\vartheta_2 = 90^\circ$. First the energy corresponding to the latter conformation has been optimized with respect to the C–O, C–C', and C–C'' bond distances; the computed optimum values are 1.33, 1.42, and 1.47 Å, respectively, where the latter quantity refers to the

ring perpendicular to the carbonyl group. Then, keeping these values for the geometrical parameters fixed we have computed the energies of the other conformations and from these values we have evaluated the force constants according to

$$f_{JK} = \partial^2 E / \partial J \partial K \quad (1)$$

where the second derivative of the total energy E is taken with respect to the rotational coordinates. The force constants in the ϑ_1, ϑ_2 reference system were then transformed into the normal coordinate system, in which the force constant matrix f is diagonal. The latter values are 0.2868 and -0.1573 mdyn \AA for the two rotational degrees of freedom, showing that the conformation at $\vartheta_1 = 0^\circ, \vartheta_2 = 90^\circ$ actually is the transition state. Examination of the normal coordinates shows that passage through the transition state occurs almost exclusively by the rotation of the phenyl ring which is perpendicular to the plane of the carbonyl group. The calculated energy barrier to rotation is 7.5 kcal, in excellent agreement with the experimental value of 6.35 kcal. Also in this case the planar configuration at the carbonyl carbon is favored with respect to pyramidal structures, although the potential energy curve is more flat than in the ground state.

The rotational process in benzophenone ketyl may then be simplified as shown in eq 2, where the conversion from



one enantiomer into the other proceeds through a disrotatory twisting of the two phenyl rings.

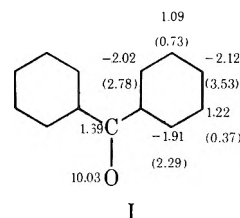
When comparing the heights of the rotational barrier calculated in benzophenone and in corresponding ketyl, a much larger value is found for the latter (7.5 vs. 1.2 kcal⁴). Although no experimental value of this barrier is known for benzophenone, the increase of the energy barrier to rotation in ketyls with respect to ketones seems to be a real effect, common to the entire class of aromatic carbonyl derivatives. This is confirmed by the activation energy values for rotation found in benzaldehyde¹⁶ (≈ 6.8 kcal) and in the benzaldehyde radical anion¹ (>10 –12 kcal). This effect should be attributed to the increased double bond character between the carbonyl and phenyl groups, which also induce a flattening of the radical as discussed before.

Hyperfine Splitting Constants. Since the gaussian basis set used in the *ab-initio* calculations gives unrealistic absolute values for the hyperfine splitting constants,¹⁷ only the INDO results will be given.

In formaldehyde ketyl the experimental proton splitting constant is 14.34 G;¹⁸ since the relative sign of this constant is unknown, the INDO calculations give the same agreement both for the minimum energy pyramidal configuration (15.8 G) and for the planar structure (-13.9 G). The computed ¹⁷O splitting is practically independent of the structure as it takes the values of 6.8 and 7.9 G in the two configurations. Although in formaldehyde ketyl no experimental determination of this constant has been made, the discrepancy with the oxygen splitting measured in aliphatic

ketyls is significant as, for example, in hexamethylacetone ketyl a_o is -11.1 G.¹⁹ Of course the agreement would be much better if the experimental oxygen splitting had a positive sign, but this seems most unlikely. On the other hand, the ¹³C hyperfine splitting constant is strongly dependent on the configuration at the carbon atom, calculated to be 105.7 and 26.5 G in the pyramidal and planar structures. In hexamethylacetone ketyl a_c is 52.7 G and in other aliphatic ketyls it ranges between 45 and 50 G.¹¹ The comparison with the calculated coupling constants is discouraging for both structures, however, the experimental value of 50 G clearly favors the pyramidal configuration as the calculated 26.5-G splitting can be considered an upper limit for the planar structure.

In benzophenone ketyl the INDO calculations reproduce satisfactorily the experimental² (in parentheses) proton splitting constants as shown in I. It may then be of some in-



terest to compare the assignment of the nonequivalent splittings at the ortho and meta positions predicted by the INDO method with that made by Takeshita and Hirota² using the McLachlan method. To account for the asymmetry induced in the phenyl ring by the presence of the carbonyl group, they modified the Coulomb integral of the carbon adjacent to the oxygen atom.

Both ortho and meta protons were calculated to have larger splittings when they are trans to the carbonyl oxygen. The INDO calculations give the reverse assignment for the meta splittings, but the same assignment at the ortho positions. The latter result gives further support to a series of recent papers^{3,20} dealing with the conformational analysis of thiophen-containing ketyl radicals, where the spatial structures were assigned to the observed isomers from the differences in the coupling constants and g factors, on the assumption that smaller spin densities are expected at nuclei adjacent to the negative carbonyl oxygen because of strong electrostatic interaction.

Acknowledgments. We thank Dr. M. Camaggi for providing us with a CDC version of the INDO program. We also acknowledge useful discussions concerning the computation of force constants with Mr. H. Bernhard Schlegel.

References and Notes

- (1) W. Kaminski and K. Möbius, *J. Magn. Resonance*, **5**, 182 (1971).
- (2) T. Takeshita and N. Hirota, *J. Chem. Phys.*, **51**, 2146 (1969).
- (3) M. Guerra, G. F. Pedulli, M. Tiecco, and G. Martelli, *J. Chem. Soc., Perkin Trans. 2*, 562 (1974).
- (4) R. Hoffmann and J. R. Swenson, *J. Phys. Chem.*, **74**, 415 (1970).
- (5) J. A. Pople, D. L. Beveridge, and P. A. Dobosh, *J. Amer. Chem. Soc.*, **90**, 4201 (1968).
- (6) M. D. Newton, W. A. Lathan, W. J. Hehre, and J. A. Pople, *J. Chem. Phys.*, **52**, 4064 (1970).
- (7) J. A. Pople and R. K. Nesbet, *J. Chem. Phys.*, **22**, 571 (1954).
- (8) W. J. Hehre, W. A. Lathan, R. Ditchfield, M. D. Newton, and J. A. Pople, Quantum Chemistry Program Exchange, Indiana University, Bloomington, Ind.
- (9) R. Ditchfield, W. J. Hehre, and J. A. Pople, *J. Chem. Phys.*, **54**, 724 (1971).
- (10) E. T. Strom, *J. Phys. Chem.*, **72**, 4715 (1968).
- (11) G. R. Underwood, *Mol. Phys.*, **22**, 729 (1971).
- (12) L. E. Sutton, *Chem. Soc., Spec. Publ.*, No. 11 (1958).

- (13) G. W. Robinson and V. E. Di Giorgio, *Can. J. Chem.*, **36**, 31 (1958); *J. Chem. Phys.*, **31**, 1678 (1959); V. A. Job, V. Sethuraman, and K. K. Innes, *J. Mol. Spectrosc.*, **30**, 365 (1969).
- (14) E. B. Fleischer, N. Sung, and S. Hawkinson, *J. Phys. Chem.*, **72**, 4311 (1968).
- (15) When considering the two rings rotated by different angles around the minimum, the calculated energies are always higher than that corresponding to the constrained conformation at 22°.
- (16) F. A. L. Anet and M. Ahmad, *J. Amer. Chem. Soc.*, **86**, 119 (1964); H. G. Silver and J. L. Wood, *Trans. Faraday Soc.*, **60**, 5 (1964); F. A. Miller, W. G. Fatley, and R. E. Witkowski, *Spectrochim. Acta, Part A*, **23**, 891 (1967).
- (17) This failure is probably due to the inadequacy of the 4-31G basis set near the nucleus. See, for example, H. Konishi and K. Morokuma, *J. Amer. Chem. Soc.*, **94**, 5604 (1972), and references therein.
- (18) K. Eiben and R. W. Fessenden, *J. Phys. Chem.*, **75**, 1186 (1971).
- (19) G. A. Russell and G. R. Underwood, *J. Phys. Chem.*, **72**, 1074 (1968).
- (20) A. Hudson and J. W. E. Lewis, *Tetrahedron*, 4413 (1970); L. Lunazzi, G. F. Pedulli, M. Tiecco, C. A. Veracini, and C. Vincenzi, *J. Chem. Soc., Perkin Trans. 2*, 751 (1972).

Thermal Electron Transfer Reactions in Polar Solvents

Neil R. Kestner,* Jean Logan,

Department of Chemistry, Louisiana State University, Baton Rouge, Louisiana 70803

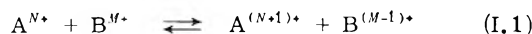
and Joshua Jortner

Department of Chemistry, Tel-Aviv University, Tel-Aviv, Israel (Received December 10, 1973; Revised Manuscript Received June 6, 1974)

A quantum mechanical theory of electron transfer reactions is developed using the techniques employed in solid-state and radiationless transition theory. This theory allows one to incorporate the effects of both the long-range polaron modes of the liquid and the short-range specific hydration modes around the ions. Typical calculations suggest that the resulting temperature dependence of the activation energy may be observed experimentally in some cases.

I. Introduction

The experimental progress in the kinetic studies of ionic oxidation-reduction reactions in polar liquids



(where A and B are ionic species) has coincided with the development of numerous theories of thermal electron transfer processes.¹⁻³ From the point of view of the chemist such outer-sphere electron transfer processes in a polar solvent exhibit the following unique features. (a) The chemical reaction does not involve the rupture of chemical bonds. (b) As the chemical process proceeds *via* charge exchange between well-separated ions the pertinent nuclear configurations of the system consists of a huge number (of the order of Avogadro's number) of nuclear coordinates involving the molecules in the first coordination layers and those of all the polar molecules in the bulk. Thus a proper semi-classical or quantum mechanical description of this chemical process has to consider a "supermolecule" consisting of the two ions and the solvent. (c) The interaction inducing the charge transfer process (or in the chemists language the weak electronic interaction in the "activated complex") can result in nonadiabatic chemical reactions, in analogy to unimolecular decomposition processes of some triatomic molecules which involve a change in the electronic state.

An important contribution to the understanding of homogeneous and electrochemical electron transfer processes was provided by the extensive theoretical studies of Marcus,^{2,4} which involves the following ingredients. (a) A classical general approach based on absolute reaction rate theory was adopted. (b) The nuclear motion was assumed

to be classical. (c) Nonequilibrium dielectric polarization theory was developed to account for the contribution of the rotational (permanent) polarization of the solvent outside the first coordination layer to the reaction coordinate. The bulk was handled as a continuous dielectric medium. (d) The contribution of configurational changes in the first coordination layer to the reaction coordinate was handled classically. (e) All electron transfer reactions were assumed to be adiabatic, although his use of κ allowed for nonadiabatic situations to be considered.

From the point of view of a theoretical chemist outer-sphere electron transfer reactions should be amenable to a fairly complete quantum mechanical description, which should rest on the following general picture. (a) The chemical reaction can be envisaged in terms of a change in the electronic state of the total system which involves the two ions embedded in the polar liquid. (b) The transition between states has to be properly formulated to account for the coupled electronic and nuclear motion of the total system. (c) The total Hamiltonian of the system is partitioned into a zero-order Hamiltonian and a (weak) perturbation term. Within the framework of the Born-Oppenheimer approximation the initial and the final zero-order states of the total system can be conveniently chosen to constitute dense manifolds of vibronic levels, as each of these states involves a superposition of the polar modes of the solvent (which form a continuum analogous to the optical modes of a solid). Provided that the eigenstates of the zero-order Hamiltonian constitute a "reasonable" description of the physical system, the electron transfer reaction can be described in terms of a relaxation process. The zero-order vibronic state corresponding to the initial electronic configu-

ration is nonstationary but is coupled to a continuum of final states, and thus ensuring a reversible decay process.

These general features of the quantum mechanical description of thermal electron transfer processes bear a close resemblance to the theoretical description of a wide class of molecular relaxation processes such as nonradiative intramolecular relaxation processes in large molecules in the statistical limit, radiationless decomposition processes such as predissociation and autoionization in electronically excited states, and unimolecular decomposition processes. Finally and perhaps most important the theoretical description of electron transfer reactions is completely analogous to the study of radiationless process such as thermal ionization of impurity centers and thermal electron capture in semiconductors which were studied by Kubo, Toyozawa, Lax, and others.⁵ This theory of multiphonon processes in solids is directly applicable to electron transfer reactions in polar solvents. A major contribution to the quantum mechanical theory of electron transfer processes in solution was provided by Levich⁶ and his school⁷ which began with the following assumptions. (a) The reaction rate is expressed in terms of the thermally averaged quantum mechanical transition probability between the vibronic levels of the total system. (b) The ions with their first coordination layers are regarded as rigid "metallic" spheres. Configurational changes in the first solvation layer are neglected.⁸ (c) The bulk of the solvent is considered as a continuous dielectric. (d) The harmonic approximation was applied for the orientational vibrational polarization modes of the medium. (e) The normal polar modes of the medium are recast in terms of the Fourier components of the total energy of the polarization field, as is common in polaron theory. The equilibrium values of the medium coordinates were recast in terms of the derivatives of the potential energy with respect to these medium coordinates. (f) As common in polaron theory the frequencies of the medium polar modes were approximated by a single frequency. The effect of dispersion was also subsequently studied.^{9,10} (g) For a weak electron exchange perturbation the transition probability for electron transfer can be expressed within the framework of first-order time-dependent perturbation theory in terms of Fermi's golden rule. This approach provides the basis for the study of nonadiabatic electron transfer reactions. (h) Adiabatic electron transfer reactions were handled on the basis of a semiclassical treatment in terms of the Landau-Zener theory.

A complete quantum mechanical theory of electron transfer reactions will be of considerable interest because of the following reasons. (a) The quantum mechanical rate expressions do not invoke the classical concept of the activated complex. (b) A general formulation of adiabatic and nonadiabatic chemical reactions should be found without introducing semiclassical theories. (c) The nature of quantum effects on electron transfer reactions, in particular the temperature dependence of the activation energy, can be elucidated.

A partial resolution of these questions was provided by the work of Levich and Dogonadze.⁶ Concerning points a and c above it was demonstrated that for nonadiabatic reactions in the low-temperature limit the electron transfer process corresponds to nuclear tunnelling between zero-order states, while in the high-temperature limit the major contribution to the transition probability and to the rate constant originates from the vicinity of the crossing of the potential surfaces. This general feature is common to all

nonadiabatic unimolecular and solid-state processes. However the Levich theory cannot reproduce many interesting real life situations as the configurational changes in the first coordination layer were disregarded. Further theoretical work in this field is therefore required. The work of Dogonadze⁹ has been in this direction also.

In this paper we pursue the formal analogy between electron transfer reactions and nonradiative relaxation processes in molecular and solid-state physics. The main goals and accomplishments of the present study can be summarized as follows.

(a) The transition probability for electron transfer, which involves a weighted density of states function (*i.e.*, the density of states weighted by different interstate coupling terms for each state), was handled by the mathematical methods previously applied for the Mössbauer effect, multiphonon processes in solids and in large molecules, and the optical line shapes in solids. Indeed, transition probabilities for both radiative and nonradiative processes can be recast in terms of a generalized line shape function, and the nonradiative decay probability can be expressed in terms of the line shape function at zero frequency. The transition probability is expressed in terms of a Fourier transform of a generating function. These techniques were applied to electron transfer processes and enabled us to handle a system characterized by many vibrational modes, while the original work of Levich and Dogonadze⁶ was limited to a quantum mechanical expression for a single-frequency model, and subsequent work utilizes semiclassical approximation for a high-frequency mode.

(b) Numerical techniques based on the steepest descent method and expansion methods of the generating function were introduced to derive general expressions for the electron transfer probability in the high-temperature limit, while in the low-temperature case series expansion of the generating function lead to explicit expressions for the transition probability. Schmidt¹¹ has also considered these techniques for this application.

(c) The nature of the medium polar modes was reinvestigated. On the basis of polaron theory we were able to derive explicit expressions for the displacement of each normal polar mode, thus providing a slight extension of Levich's continuum model. Configurational changes in the first coordination layer were estimated from experimental spectroscopic and structural data.

(d) We were thus able to derive general quantum mechanical expressions for the nonadiabatic electron transfer transition probability including both the medium modes and the configurational changes in the first coordination layer. Other efforts have recently been made in this area by Dogonadze, Ulstrup, and Kharkats,¹² Schmidt,¹³ and Schmickler and Vielstich.¹⁴

(e) In view of the high frequency of the ligands in the first coordination layer interesting quantum effects on the rate constant are predicted for systems characterized by large local configurational changes.

Let us first recall the general features of the electron transfer problem, where an electron is exchanged between a pair of solvated ions. The initial state of the system consists of a pair of ions ($A^{N+} + B^{M+}$) while the final state involves the A species in its reduced state and the B species in its oxidized state, *i.e.* ($A^{(N+1)+} + B^{(M-1)+}$). In the present model the two ions interact strongly with their first coordination layers and exert long-range electrostatic interactions on the bulk of the solvent outside the first coordi-

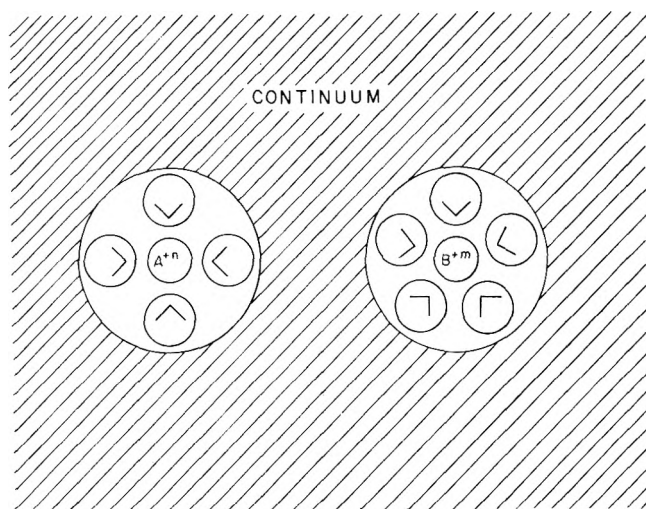


Figure 1. General model of electron transfer reactions. The medium outside the first coordination layer is treated as a continuum. The first solvation sheath is characterized by a totally symmetric vibration.

nation layers (Figure 1). The role of solvent exchange in the first coordination layer is neglected and one considers two supermolecules each consisting of an ion with its first coordination layer embedded in the polar solvent. The long-range interactions between the ionic charge distribution and the solvent outside the first coordination layers bear a close analogy to the problem of the motion of a small polaron in polar crystals.¹⁵

It is worthwhile to consider the Hamiltonian for this system and the corresponding equation of motion. A reconsideration of this problem is of interest because of the following reasons. (a) The Hamiltonian for the electron transfer problem between the two centers A and B cannot be separated into the simple form $H_A + H_B + V_{AB}$ (where H_A and H_B are the Hamiltonians for the two centers and V_{AB} corresponds to the coupling term) as is the case for energy transfer between atomic or molecular pairs.¹⁶ (b) The Hamiltonian for the electron transfer problem can be conveniently dissected to yield two different zero-order basis sets, corresponding to localization of the electron on center A or on center B, respectively. Either one of these two electronic basis sets is adequate from the formal point of view, and some care must be exerted to avoid overcomplete expansions. (c) These two electronic basis sets are nonorthogonal, and the nonorthogonality problem has to be incorporated in the time-dependent formalism. This problem resembles exchange perturbation theories of intermolecular forces, where elaborate schemes must be employed. Since we are interested in a time-dependent problem we cannot adopt these theories and an alternative approach has to be developed.

The total Hamiltonian for the system can be written as consisting of the following contributions

$$\mathcal{H} = T_E + T_N + H_a + H_b + V_{ab} + V_{ea} + V_{eb} + H_s + H_c + V_{int}^s + V_{int}^c \quad (I.2)$$

where the indices a and b refer to the two ionic centers A and B, respectively, e labels a single electron which is being transferred while s and c label the bulk of the solvent and to the first coordination layers. T_e is the kinetic energy of the transferred electron, T_N corresponds to the sum of the nuclear kinetic energy operators for the whole system (con-

taining the contributions of the two ions, T_N^a and T_N^b , the first coordination layers T_N^c , and the solvent T_N^s)

$$T_N = T_N^a + T_N^b + T_N^c + T_N^s \quad (I.3)$$

H_a and H_b correspond to the electronic Hamiltonians (the electronic Hamiltonians contain the relevant electronic kinetic energy contributions) of the bare reduced ions $A^{(N+1)}$ and B^{M+} , respectively, while V_{ea} and V_{eb} correspond to the interaction potential between the electron and these bare reduced ions. V_{ab} is the nuclear repulsion potential between the reduced ions. H_s and H_c represent the electronic Hamiltonians of the solvent and of the first coordination layers, respectively.

Finally V_{int}^s and V_{int}^c are the electrostatic interaction terms of the total ionic and electron charge distribution with the solvent (s) and with the first coordination layers (c), respectively. We have presented this cumbersome notation and definitions as a very recent treatment of this problem failed to include all the pertinent terms (such as V_{int}^s) in the Hamiltonian.

The details of the time-dependent quantum mechanical treatment of the system specified by the Hamiltonian (I.2) are outlined in Appendix A. The electronic states at fixed nuclear configuration, \mathbf{Q} , are characterized in terms of the eigenfunctions $\{\Psi_{ai}(\mathbf{r}, \mathbf{Q})\}$ for the total system ($A^{N+} + B^{M+}$) and by $\{\Psi_{bj}(\mathbf{r}, \mathbf{Q})\}$ for ($A^{(N+1)+} + B^{(M-1)+}$), obtained from eq A.2. The indices i and j refer to all ground and excited electronic states of the systems. The corresponding eigenvalues $E_{ai}(\mathbf{Q})$ and $E_{bj}(\mathbf{Q})$ correspond to the potential energy surfaces of the pairs ($A^{N+} + B^{M+}$) and ($A^{(N+1)+} + B^{(M-1)+}$) in various electronic states, respectively. The time-dependent wave function of the system can be expanded either in terms of a single basis set $\{\Psi_{ai}\}$ or $\{\Psi_{bj}\}$ (e.g., (A.3)) or alternatively in terms of both sets. The physically plausible expansion (A.4) results in a coupled set of equations (eq A.11) for the expansion coefficients. Equation A.11 involves a complicated complete expansion (including continuum states). To simplify the treatment two assumptions are introduced.

(A) A two electronic level system is considered, including only the lowest states $\Psi_a = \Psi_{a0}$ and $\Psi_b = \Psi_{b0}$ which are characterized by the adiabatic surfaces $E_a(Q)$ and $E_b(Q)$, respectively. This simplifying assumption may be justified as the basis of perturbation arguments as the off-diagonal terms are usually negligibly small (for the case of weak overlap) relative to the electronic excitation energies. This assumption is common in solid-state theory where configuration interaction effects are disregarded.

(B) The contribution of the Born-Oppenheimer operator L , eq A.6, is disregarded. This assumption is fully justified⁶ for electron transfer between ordinary ions where $\langle V_{e\alpha} \rangle / \langle L \rangle \sim M/m$. In the case of reduction reactions involving the solvated electron the $\langle L \rangle$ term may be important in view of the strong dependence of the electron wave function on the nuclear coordinates. Thus for a two electronic level system we have the simple expansion $\Psi(r, Q, T) = X_a(Q, t)\Psi_a(r, Q) + X_b(Q, t)\Psi_b(r, Q)$ where the expansion coefficients are obtained from the coupled equations (A.12). At this stage one defines zero-order vibrational wave functions $X_{av}(\mathbf{Q})$ and $X_{bv}(\mathbf{Q})$, satisfying the eigenvalue equations (A.13). The zero-order vibronic states of the two system

$$\begin{aligned} |av\rangle &\equiv \Psi_a X_{av}^0(\mathbf{Q}) \\ |bv\rangle &\equiv \Psi_b X_{bv}^0(\mathbf{Q}) \end{aligned} \quad (I.4)$$

are characterized by the energies E_{av}^0 , and E_{bv}^0 , respectively. To obtain the equations of motion and the transition probabilities we have followed the techniques introduced by Holstein¹⁵ in the study of the small polaron (eq A.14 and A.15). Application of second-order perturbation theory to eq A.15 the decay probability W_{av} of a zero-order vibronic level $|av\rangle \equiv \Psi_a X_{av}^0$ to the manifold $\{|bw\rangle\} = \{\Psi_b X_{bv}^0\}$ results in the familiar Fermi golden rule where the coupling matrix element of

$$V_{av,bw} = (X_{av}^0 | \langle \Psi_a | V_{eb} + S_{ab}^{-1} \langle \Psi_b | V_{eb} | \Psi_a \rangle | \Psi_b \rangle | X_{bv}^0 \rangle \quad (\text{I. 5})$$

the generalized exchange operator and () refers to integration over nuclear coordinates.

$$W_{av} = \frac{2\pi}{\hbar} \sum_w |V_{av,bw}|^2 \delta(E_{av}^0 - E_{bv}^0) \quad (\text{I. 6})$$

The generalized exchange perturbation term $V_{av,bw}$ (I.6) induces transitions between two different vibronic manifolds corresponding to electronic ground states. If we would have incorporated electronically excited states, refraining from accepting assumption A, the exchange operator will act in a dual role. (a) It will induce transitions between different centers, resulting in electron transfer involving electronically excited states. (b) It will force transitions between different electronic states on the same center, in analogy with the role of the nonadiabatic operator which is conventionally allowed for nonradiative relaxation of excited states of molecules and of solvated ions. This is a nice example for the effect of an external field on nonradiative electronic relaxation processes. These externally induced electronic relaxations of excited ionic states can explain the effects of self-quenching of the fluorescence yield of rare earth ions in solution.

Adopting the language of molecular relaxation theory the width, Γ_{av} , of each "initially prepared" zero-order state $|av\rangle$ is related to W_{av} (eq I.5) by

$$\Gamma_{av} = \hbar W_{av} \quad (\text{I. 7})$$

The present model (see Figure 1) implies that the zero-order states $|av\rangle$ are metastable. A sufficient validity condition for the irreversible decay of each of these states into the manifold $\{|bw\rangle\}$ is that either the states in the density of the accepting (final) states is exceedingly large, so that the spacing between adjacent levels $\delta E_b = |E_b^0(w+1) - E_{bv}^0|$ is small satisfying the conditions

$$\Gamma_{av} \gg \delta E_b \quad (\text{I. 8})$$

whereupon the width Γ_{av} spans a large number of levels. Alternatively one may require that the total width γ_{bv} of each of the accepting states $|bv\rangle$ is large relative to their spacing

$$\delta E_b \ll \gamma_{bv} \quad (\text{I. 9})$$

The total width γ_{bv} consists of a nonradiative electron transfer contribution $|bv\rangle \rightarrow \{|av\rangle\}$ better than (*i.e.*, the back reaction), Γ_{bv} , and most important, vibrational relaxation in the $\{|bv\rangle\}$ manifold. As we consider here a dense polar liquid coupling to the medium will result in medium induced vibrational relaxation characterized by a width $\tilde{\gamma}_{bv}$ within the manifold $\{|bv\rangle\}$, so that $\gamma_{bv} = \tilde{\gamma}_{bv} + \Gamma_{bv}$. Provided that either of eq I.8 and I.9 (or both) will be satisfied, the manifold $\{|bv\rangle\}$ constitutes an effective continuum for the relaxation process. In a polar liquid we expect that the coupling between the polar modes is always sufficient to

ensure at least effective vibrational relaxation process so that (I.9) is satisfied. In many cases of interest we also believe that the dense dual spacing condition (I.8) for the polar modes holds. We thus conclude that in any case the manifold $\{|bv\rangle\}$ provides an effective dissipative continuum for the electron transfer process.

It is important to notice at this point that the decay probability of an "initial" zero-order state $|av\rangle$ can be expressed by the first-order perturbation expression (II.19) only when it is justified to consider the decay of a single resonance. We thus invoke the basic assumption that the spacing between the resonances $\{|av\rangle\}$ considerably exceeds their widths. Denoting by $\delta E_a = |E_{av} - E_{a(v+1)}|$ the energy spacing between the adjacent order states $|av\rangle$ and $|a(v+1)\rangle$ we imply that

$$\Gamma_{av} \ll \delta E_a \quad (\text{I. 10})$$

We note in passing that condition (I.10) does not violate the irreversibility requirement, as it is sufficient that only relation (I.9) is valid.

Thus, when interference effects between resonances can be disregarded, the decay pattern of each zero-order state is exponential and being characterized by reciprocal decay time (I.5). The applicability of restriction (I.10) will imply that the thermally averaged rate constant will involve a preexponential factor which involves the interstate coupling matrix element $|V_{av,bw}|$. This physical situation is often referred to in chemical kinetics as a nonadiabatic transition.

Up to this point we have been concerned with the decay of an initially prepared isolated resonance, without referring to the "preparation" of the decaying states. Two trivial further assumptions are introduced at this point.

(D) Thermal vibrational excitation (and relaxation) rates in the initial manifold $\{|av\rangle\}$ considerably exceed the nonradiative decay probabilities whereupon

$$\Gamma_{av}/\hbar \ll t_v^{-1} \quad (\text{I. 11})$$

where t_v is the vibrational relaxation time.

(E) The width of exact resonance is considerably less than the thermal energy $k_B T$, in the temperature range of interest

$$\Gamma_{ai} \ll k_B T \quad (\text{I. 12})$$

Thus all the mixed ($\{|av\rangle + \{|bw\rangle\}$) states in a single resonance are equally thermally populated.

The thermally averaged nonadiabatic electron transfer probability from the initial manifold $|av\rangle$ to the final manifold $\{|bw\rangle\}$ is now

$$W_a = \frac{1}{Z} \sum_v \exp(-\beta E_{av}^0) W_{av} \quad (\text{I. 13})$$

where

$$Z = \sum_v \exp(-\beta E_{av}^0) \quad (\text{I. 13a})$$

and

$$\beta = (k_B T)^{-1}$$

In the theory of unimolecular nonadiabatic reactions the "high-pressure" rate constant is identified with W_a , eq II.24. In the present case the zero-order states $\{|av\rangle\}$ and $\{|bw\rangle\}$ which can be obtained from eq A.13 are very complicated. To simplify the problem further we utilize Levich's approach.⁶

(F) We calculate the electron transfer probability at a

fixed relative separation of the ions. This implies neglecting the contribution $T_N^a + T_N^b$ in eq I.3 and consequently also in eq A.13. The zero-order energies E_{av}^0 and E_{bw}^0 are then calculated at a fixed nuclear separation R_{ab} between the two solvated ions. The transition probability (I.5) is a function of R_{ab} , i.e., $W_a \equiv W_a(R_{ab})$. The bimolecular rate constant k is expressed in terms of the volume integral of the probability $f(R_{ab})$ for finding the ions at a distance R_{ab} , whereupon

$$k = \int d^3R_{ab} f(R_{ab}) W_a(R_{ab}) \quad (\text{I.14})$$

In the limit of a dilute ionic solution one can approximate each ion with its coordination sphere by a hard-core radius $R = R_i + 2r_s$ (see Figure 2) so that for outer-sphere reactions

$$f(r) = 0 \quad r < R$$

$$f(r) = \exp[-\beta u(r)] \quad r > R \quad (\text{I.15})$$

with $u(r)$ being the interionic interaction potential

$$u(r) = nm e^2 / R D_{eff} \quad (\text{I.16})$$

This concludes an outline of the theory of nonadiabatic outer-sphere electron transfer reactions. This lengthy exposition leads to the original results of Levich. We believe, however, that the present treatment is more systematic than previously attempted. In particular, our expressions are general, being applicable for the interesting case of configurational changes in the first solvation layer.

II. Formal Expressions for the Electron Transfer Probability

In order to evaluate the nonradiative electron transfer probability (I.5) and its thermal average (I.13) we require explicit expressions for the energies $E_a(Q)$ and $E_b(Q)$ which correspond to the adiabatic potential surfaces and the total energies of these states E_{av}^0 and E_{bw}^0 (at fixed R_{ab}). To reduce the formal results into a useful and tractable theoretical expression we introduce the following approximations.

(G) The harmonic approximation is invoked for the potential energy surfaces $E_a(Q)$ and $E_b(Q)$. These are multidimensional potentials which are determined by the nuclear coordinates $\mathbf{Q} = \{Q_i\}$ of the first coordination layers and of all the solvent molecules outside them are expanded around the equilibrium configurations $Q^{0(a)} \equiv \{Q_i^{0(a)}\}$ and $Q^{0(b)} \equiv \{Q_i^{0(b)}\}$ in the initial and in the final states.

$$E_a(\mathbf{Q}) = \frac{1}{2} \sum_{ij} \alpha_{ij} (Q_i - Q_i^{0(a)}) (Q_j - Q_j^{0(a)}) + E(\mathbf{Q}^{0(a)}) \quad (\text{II.1})$$

$$E_b(\mathbf{Q}) = \frac{1}{2} \sum_{ij} \beta_{ij} (Q_i - Q_i^{0(b)}) (Q_j - Q_j^{0(b)}) + E_b(\mathbf{Q}^{0(b)}) \quad (\text{II.2})$$

where α_{ij} and β_{ij} are the second derivatives of $E_a(\mathbf{Q})$ and of $E_b(\mathbf{Q})$ with respect to Q_i and Q_j , respectively.

(H) We introduce a further simplifying assumption that the normal modes and their frequencies (corresponding to the two first solvation layers and to the medium) are the same in the two states, except for displacements in the origins of the normal coordinates. This assumption can be relaxed as one can account formally for frequency changes and for the change in the direction of the principal axis of the normal coordinates between the two electronic states. The resulting equations are very cumbersome, and in view

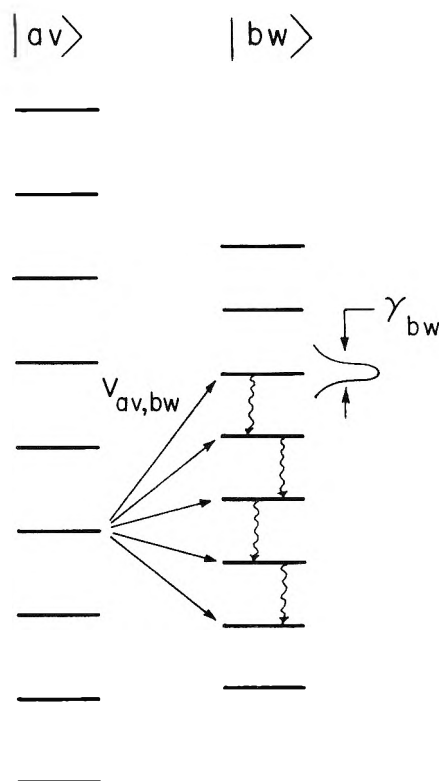


Figure 2. Typical energy level diagram for radiationless transitions or electron transfer reactions. The coupling matrix elements and the width of the accepting states are also indicated.

of our present ignorance of the "molecular" parameters involved we shall use the simple version of the multiphonon relaxation theory which rests on the present approximation.

The normal modes of the system in both states are characterized by the frequencies $\{\omega_j\}$ and by the effective masses $\{M_j\}$. It will be convenient to define reduced normal coordinates q_j normalizing the displacements from origin $\{Q_j - Q_j^{0(a)}\}$ for one state in terms of the zero energy mean square displacements $\langle Q_j^2 \rangle = (\hbar/m_j \omega_j)^{-1/2}$ so that

$$q_j = (Q_j - Q_j^{0(a)}) \left(\frac{M_j \omega_j}{\hbar} \right)^{1/2} \quad (\text{II.3})$$

Finally the reduced displacements between the origins of the two potential surfaces are given by

$$\Delta_j = \left(\frac{M_j \omega_j}{\hbar} \right)^{1/2} (Q_j^{0(a)} - Q_j^{0(b)}) \quad (\text{II.4})$$

The two potential surfaces (see Figure 3) are expressed in the final form

$$E_a(Q) = \frac{1}{2} \sum_j \hbar \omega_j q_j^2 \quad (\text{II.5})$$

$$E_b(Q) = \frac{1}{2} \sum_j \hbar \omega_j (q_j - \Delta_j)^2 + \Delta E = E_a(Q) - \sum_j \hbar \omega_j q_j \Delta_j + \frac{1}{2} \sum_j \hbar \omega_j \Delta_j^2 + \Delta E \quad (\text{II.6})$$

The energy gap between the minima of the two potential surfaces (see Figure 3) is

$$\Delta E = E_a(\mathbf{Q}^{0(a)}) - E_b(\mathbf{Q}^{0(b)}) \quad (\text{II.7})$$

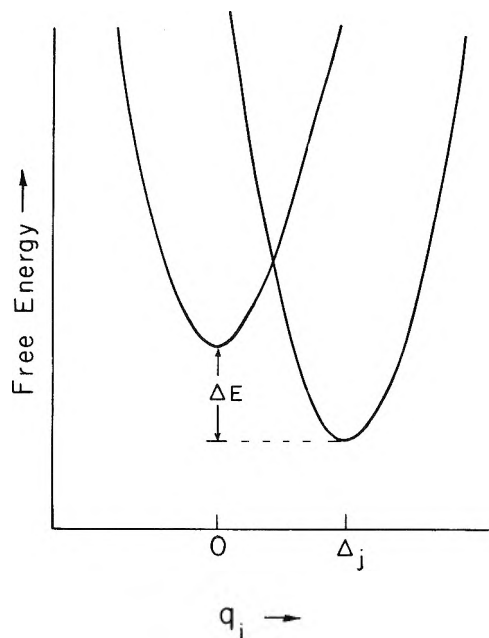


Figure 3. A general diagram for the change in a medium coordinate, q_j , between two states. A quadratic energy dependence is assumed.

The energy term in eq II.6

$$E_M = \frac{1}{2} \sum_j \hbar \omega_j \Delta_j^2 \quad (\text{II. 8})$$

corresponds to the shift of the vertical energy difference between the two potential surfaces at $Q^{0(a)}$ from ΔE . In molecular spectroscopy E_M corresponds to half the Stokes shift.

Finally the quantized energy states E_{av}^0 and E_{bw}^0 can be specified in terms of the two sets of vibrational quantum numbers $v \equiv \{v_j\}$ and $w \equiv \{w_j\}$, so that

$$E_{av}^0 = \sum_j \left(v_j + \frac{1}{2} \right) \hbar \omega_j + E_a(Q^{0(a)}) \quad (\text{II. 9})$$

$$E_{bw}^0 = \sum_j \left(w_j + \frac{1}{2} \right) \hbar \omega_j + E_b(Q^{0(b)})$$

The evaluation of the electron transfer transition probability (I.13) is reduced to the calculation of the nonradiative relaxation rates between two harmonic potential surfaces. A further assumption will greatly simplify matters.

(I) The electronic matrix element in (I.6) is weakly dependent on the nuclear coordinates, so that within the "Condon approximation" the interstate coupling matrix element is recast as a product of an electronic matrix element and a vibrational overlap term

$$V_{av,bw} \approx v(\chi_{av}^0 | \chi_{bw}^0) \quad (\text{II. 10})$$

where

$$v = \langle \Psi_a | V_{eb} + S_{ab}^{-1} \langle \Psi_b | V_{eb} | \Psi_a \rangle | \Psi_b \rangle \quad (\text{II. 11})$$

calculated at $Q^{0(a)}$. This approximation is not valid for nonradiative processes induced by the nuclear momentum operator L , however, for the present case it is perfectly acceptable.

Our problem thus reduces to the calculation of a multiphonon type relaxation rate induced by a coupling b which is independent of changes in nuclear coordinates. The non-

radiative decay probability (I.5) of a single level corresponds to a weighted density of states function where each delta function is the formal expression for the density of states $\rho(E_{av}^0) = \sum_w \delta(E_{av}^0 - E_{bw}^0)$ of the manifold E_{bw}^0 at the energy E_{av}^0 modified by the vibrational overlap term $(\chi_{av}^0 / \chi_{bw}^0)$. A closed form for (I.5) with (II.10) can be obtained by the Feynman operator techniques and subsequently inserted into (I.13). Alternatively the thermally averaged probability (I.13) can be directly evaluated by the generating functions method. As these techniques have been widely utilized for nonradiative decay processes in solids and molecules we shall just quote the final result.^{5,17} The electron transfer probability (I.13) is expressed in terms of a Fourier integral

$$W_a = \frac{|v|^2}{\hbar^2} \int_{-\infty}^{\infty} f(t) \exp[-i\Delta E t / \hbar] dt \quad (\text{II. 12})$$

where the Fourier transform of the nonradiative decay probability is

$$f(t) = \exp[-G] \exp[G_+(t) + G_-(t)] \quad (\text{II. 13})$$

where the auxiliary functions in eq II.13 are

$$G_+(t) = \frac{1}{2} \sum_j \Delta_j^2 (\bar{n}_j + 1) \exp(i\omega_j t) \quad (\text{II. 14})$$

$$G_-(t) = \frac{1}{2} \sum_j \Delta_j^2 \bar{n}_j \exp(-i\omega_j t)$$

\bar{n}_j corresponds to the number of excited vibrations at the frequency in thermal equilibrium

$$\bar{n}_j = [\exp(\beta \hbar \omega_j) - 1]^{-1} \quad (\text{II. 15})$$

Finally the dimensionless quantity

$$G = G_+(0) + G_-(0) = \frac{1}{2} \sum_j \Delta_j^2 (2\bar{n}_j + 1) \quad (\text{II. 16})$$

is referred in solid-state physics as the electron-phonon coupling strength. A very rough estimate of G is obtained replacing all the frequencies by an average frequency $\langle \omega \rangle$, which as shown in section III is unjustified for our system. In this case from eq II.11 and II.8 we have

$$G \sim (E_M / \hbar \langle \omega \rangle) \coth(\beta \hbar \langle \omega \rangle) \quad (\text{II. 17})$$

Two physical situations were distinguished. (a) The weak coupling situation $G < 1$ which is realized at low temperature ($\hbar \langle \omega \rangle \gg k_B T$) and when $E_M < \hbar \langle \omega \rangle$. (b) The strong coupling limit $G \gg 1$ which is realized at high temperatures ($\hbar \langle \omega \rangle \ll k_B T$) and/or when $E_M \gg \hbar \langle \omega \rangle$.

Molecular electronic relaxation processes usually correspond to the weak coupling situation, while the corresponding multiphonon processes in solids at high temperatures correspond to the strong coupling limit, which was also applied to Levich⁶ for electron transfer processes. We shall now demonstrate that when configurational changes in the first coordination layer are incorporated the electron transfer probability has to be handled in a more complicated manner.

The calculation of the electron transfer probability reduces to the evaluation of the integral (II.12)–(II.16). Integrals of the form

$$I = \int_{-\infty}^{\infty} \exp[-A(t)] dt \quad (\text{II. 18})$$

where the integrand is a highly oscillatory function can be approximated by the saddle point method.¹⁷ The saddle point is taken at t_0 where

$$[\partial A(t)/\partial t]_{t_0} = 0 \quad (\text{II. 19})$$

so that the Taylor series expansion

$$A(t) = A(t_0) + \frac{1}{2}(\partial^2 A/\partial t^2)_t(t - t_0) \quad (\text{II. 19a})$$

is utilized in (II.19) to yield

$$I \simeq [2\pi/(\partial^2 A/\partial t^2)]_{t_0}^{1/2} \exp[-A(t_0')] \quad (\text{II. 20})$$

When the integral (II.12)–(II.16) is handled by this method the saddle point in the complex t plane is obtained from the relation

$$-\Delta E + \sum_i \hbar\omega_i \Delta_i^2 (\bar{n}_i + 1) \exp(i\omega_i t) - \frac{1}{2} \sum_i \hbar\omega_i \Delta_i^2 \bar{n}_i \exp(-i\omega_i t) = 0 \quad (\text{II. 21})$$

In the high-temperature case when

$$\hbar\omega_i \ll k_b T \quad (\text{II. 22})$$

for all i , $G \gg 1$ corresponding to the strong coupling situation. Under these conditions one can expand the right-hand side of the saddle point eq II.21 in a power series in t

$$-\Delta E + E_M + i\hbar D^2 t - \frac{3}{16} \sum_i \hbar\omega_i^3 \Delta_i^2 t^2 + \dots = 0 \quad (\text{II. 23})$$

where we have defined

$$D^2 = \frac{1}{2} \sum_i \omega_i^2 \Delta_i^2 (2\bar{M}_i + 1) \quad (\text{II. 24})$$

and E_M is given by (II.8). Retaining the linear term in t

$$it_0 = -(\Delta E - E_M)/\hbar D^2 \quad (\text{II. 25})$$

whereupon eq II.12 takes the familiar form

$$W = \frac{v^2}{\hbar} \left(\frac{2\pi}{\hbar^2 D^2} \right)^{1/2} \exp \frac{(\Delta E - E_M)^2}{2D^2 \hbar^2} \quad (\text{II. 26})$$

Equation II.26 has been widely utilized in the electron transfer theory of Levich.⁶ It is interesting to note that we can easily obtain a formal relation between this quantum mechanical result and conventional reaction rate theory. The points of intersection of the two harmonic potential hypersurfaces are obtained from the relation $E_a(\mathbf{Q}) = E_b(\mathbf{Q})$. The intersection point of minimum energy, E_A , measured relative to the origin, $E_a(\mathbf{Q}^{0(a)})$, satisfies the relation

$$E_A = (\Delta E - E_M)^2/4E_M \quad (\text{II. 27})$$

Thus eq II.26 can be reduced to the form

$$W = v^2 \left(\frac{\pi}{\hbar^2 E_M k_B T^*} \right)^{1/2} \exp[-E_A/k_B T^*] \quad (\text{II. 28})$$

where the effective temperature is defined by

$$k_B T^* = \hbar^2 D^2/2E_M \quad (\text{II. 29})$$

In the high-temperature limit (II.22) $T^* \rightarrow T$ and the transition probability in the strong coupling limit

$$W = v^2 (\pi/\hbar^2 E_M k_B T)^{1/2} \exp[-\beta E_A] \quad (\text{II. 28a})$$

assumes the conventional form of an activated rate equation. This result has been obtained without invoking the concept of the activated complex.

It is important at this point to establish the validity condition for eq II.26, which implies that the term $0(t^2)$ in (II.23) is negligible, so that

$$iD^2 t_0 \gg \frac{3}{16} \hbar \sum_i \omega_i^3 \Delta_i^2 t_0^2 \quad (\text{II. 30})$$

which from eq II.24 and II.25 implies that

$$\hbar \left[\sum_i \Delta_i^2 \omega_i^2 (2\bar{n}_i + 1) \right]^2 \gg |\Delta E - E_M| \sum_i \Delta_i^2 \omega_i^3 \quad (\text{II. 31})$$

Obviously the validity condition (II.31) is satisfied (for reasonable values of Δ_i) only at high temperature. To demonstrate this point consider single frequency whereupon this condition is simply

$$(2\bar{n} + 1) \gg |\Delta E - E_M|/E_M \quad (\text{II. 27a})$$

and for symmetric electron transfer processes when $\Delta E = 0$ we require that $\bar{n} \gg 1$. In general, for physically realistic model of electron transfer, when the role of the first coordination layer is incorporated relation II.31 does not hold and consequently eq II.26 has to be modified.

III. A Semimolecular Model for Electron Transfer

We adopt a simplified model, which has been popular in the studies of ionic solvation and in classical formulation of electron transfer processes. The first coordination layers of the two ions are treated in terms of a molecular model accounting for the totally symmetric vibrations of the nearest solvent molecules. The contribution of the first coordination layer in the initial $A^{N+} + B^{M+}$ and in the final $A^{(N+1)+} + B^{(M-1)+}$ state to the potential surface is specified in terms of the four equilibrium configurations $r^0(A^{N+})$, $r^0(B^{M+})$, $r^0(A^{(N+1)+})$, and $r^0(B^{(M-1)+})$. These equilibrium configurations are obtained from the ionic radii r_i , so that $r^0 = r_i + r_s$ where r_s is the radius of the solvent molecule. Utilizing the simple model of displaced identical potential surfaces we take the vibrational frequencies of the first coordination layer of the A or of the B ionic species to be equal in both valence states, so that $\omega_A = \omega(A^{N+}) = \omega(A^{(N+1)+})$ and $\omega_B = \omega(B^{M+}) = \omega(B^{(M-1)+})$. The available experimental data (Table I) indicate that this approximation is not too bad.

Finally we can define reduced displacement coordinates for the first coordination layer

$$q_A = (M_A \omega_A / \hbar)^{1/2} (r(A^{N+}) - r^0(A^{N+})) \quad (\text{III. 1})$$

$$q_B = (M_B \omega_B / \hbar)^{1/2} (r(B^{M+}) - r^0(B^{M+}))$$

and the two displacements

$$\Delta_A = (M_A \omega_A / \hbar)^{1/2} (r^0(A^{(N+1)+}) - r^0(A^{N+})) \quad (\text{III. 2})$$

$$\Delta_B = (M_B \omega_B / \hbar)^{1/2} (r^0(B^{(M-1)+}) - r^0(B^{M+}))$$

in terms of the reduced masses M_A and M_B of the ions with the first coordination layer. The contributions of the first coordination layers to the potential energy surfaces (II.5) and (II.6) are

$$f_a(q_A, q_B) = \frac{1}{2} \hbar \omega_A q_A^2 + \frac{1}{2} \hbar \omega_B q_B^2 \quad (\text{III. 3})$$

$$f_b(q_A, q_B) = f_a(q_A, q_B) - \hbar \omega_A q_A \Delta_A - \hbar \omega_B q_B \Delta_B + E_M^C$$

TABLE I: Totally Symmetric Vibrations of Coordination Layers and Approximate Radii

Ion	$\hbar\omega$, cm ⁻¹	Comments	r , Å ^d
Cr ³⁺ -H ₂ O	490	Aqueous solution ^a and Cr(H ₂ O) ₆ Cl ₃ in crystal ^b	0.65
Cr ²⁺ -H ₂ O			0.83
Mn ²⁺ -H ₂ O	395	Aqueous solution ^a and Mn(H ₂ O) ₆ SiF ₆ in crystal ^b	
Fe ²⁺ -H ₂ O	389	Aqueous solution ^a and Fe(H ₂ O) ₆ SiF ₆ in crystal ^b	0.83
Fe ³⁺ -H ₂ O			0.67
Ni ²⁺ -H ₂ O	405	Aqueous solution ^a and Ni(H ₂ O) ₆ SiF ₆ in crystal ^b	
Cu ²⁺ -H ₂ O	440	Aqueous solution ^a	
Hg ²⁺ -H ₂ O	362	Aqueous solution ^a	
Zn ²⁺ -H ₂ O	385-400 or 369	Zn(H ₂ O) ₆ in crystal ^a	
Ni ²⁺ -D ₂ O	389	Ni(D ₂ O) ₆ SiF ₆ in crystal ^b	
Co ²⁺ -H ₂ O			0.83
Co ³⁺ -H ₂ O			0.67
V ²⁺ -H ₂ O			0.82
V ³⁺ -H ₂ O			0.65
Cr ²⁺ -H ₂ O			0.83
Cr ³⁺ -H ₂ O			0.65
Eu ²⁺ -H ₂ O			1.18
Eu ³⁺ -H ₂ O			0.99

^a Data compiled by D. E. Irish in "Ionic Interactions," Vol. II, S. Petrucci, Ed., Academic Press, New York, 1971. ^b I. Nakagawa and T. Shimanouchi, *Spectrochim. Acta*, 20, 429 (1964). ^c R. E. Hester and R. H. Plane, *Inorg. Chem.*, 3, 513 (1964); 768, 769 (1964). ^d Taken from E. Sacher and K. S. Laidler in "Modern Aspects of Electrochemistry," Vol. 3, J. O'M Bockris and B. E. Conway, Ed., Butterworths, Washington, D.C., 1964.

where we defined

$$E_M^C = \frac{1}{2}(\hbar\omega_A \Delta_A^2 + \hbar\omega_B \Delta_B^2) \quad (\text{III. 4})$$

The medium outside the first coordination layers will be handled as a continuum dielectric as originally proposed by Levich⁶ who was the first to apply polaron theory to this problem. The vibrational modes of the outer medium are approximated by a single mean vibrational frequency, ω_0 , which was estimated from the dielectric loss measurements as $\omega_0 \sim 1$ cm⁻¹. This approach has been common in polaron theory. The polar modes are specified in terms of the set of coordinates $\{Q_\kappa\}$ and reduced masses $\{M_\kappa\}$, which provide the equivalent of lattice optical modes for a polar liquid. The equilibrium configurations of the medium modes are affected by the charge distribution which is different in the initial and in the final state. The equilibrium configurations are $\{Q_\kappa^{0(a)}\}$ and $\{Q_\kappa^{0(b)}\}$ in the initial and final states. The reduced coordinates and displacements of the outer medium are

$$q_\kappa = (\hbar/M_\kappa\omega_0)^{1/2}(Q_\kappa - Q_\kappa^{0(a)}) \quad (\text{III. 5})$$

$$\Delta_\kappa = (\hbar/M_\kappa\omega_0)^{1/2}[Q_\kappa^{0(a)} - Q_\kappa^{0(b)}] \quad (\text{III. 6})$$

so that the contribution of the polar modes to the potential surfaces are

$$g_a(Q_\kappa) = \hbar\omega_0 \sum_\kappa q_\kappa^2 \quad (\text{III. 7})$$

$$g_b(Q_\kappa) = \hbar\omega_0 \sum_\kappa q_\kappa^2 - \hbar\omega_0 \sum_\kappa q_\kappa \Delta_\kappa + E_M^S \quad (\text{III. 8})$$

where the solvent induced Stokes shift is

$$E_M^S = \frac{1}{2}\hbar\omega_0\omega \sum_\kappa \Delta_\kappa^2 \quad (\text{III. 9})$$

Applying polaron theory (see Appendix) we get Levich's result for the contribution of the external medium

$$\begin{aligned} E_M^S = & \frac{Ce^2}{2} \iint d^3x d^3x' \{[\rho^a(\mathbf{x} - \mathbf{x}_0) - \rho^b(\mathbf{x} - \mathbf{x}_0)] \times \\ & [\rho^a(\mathbf{x}' - \mathbf{x}_0) - \rho^b(\mathbf{x}' - \mathbf{x}_0)]\} / |\mathbf{x} - \mathbf{x}'| = \\ & \frac{Ce^2}{8\pi} \int d^3\mathbf{x} (\mathbf{D}^a - \mathbf{D}^b)^2 \quad (\text{III. 10}) \end{aligned}$$

where ρ^a and ρ^b are the charge densities in the initial and in the final state, respectively, while \mathbf{D}^a and \mathbf{D}^b represent the electric displacement vectors in the initial and in the final states, and

$$C = \bar{D}_0^{-1} - D_s^{-1} \quad (\text{III. 10a})$$

The total potential surfaces for this simplified model take the form

$$\begin{aligned} E_a(\mathbf{Q}) &= f_a(q_A, q_B) + g_a(q_\kappa) \\ E_b(\mathbf{Q}) &= f_b(q_A, q_B) + g_b(q_\kappa) - \Delta E \quad (\text{III. 11}) \end{aligned}$$

The quantum mechanical treatment of the electron transfer probability is now more complicated than previously considered in view of the appearance of the contributions of the first coordination layers. These local frequencies of the solvent molecules are rather high $\omega_A \sim \omega_B \sim 300$ – 400 cm⁻¹ for hydrated ion (see Table I). The high-temperature approximation (II.22) does not hold for the local modes, which under ordinary circumstances at room temperature are "frozen." The frequency of the polar modes is expected to be low $\omega_0 \approx 1$ cm⁻¹ so that for these modes the high-temperature approximation (II.22) is valid. Thus the Levich equation (II.26 or II.28) is valid only for systems where the configurational changes in the first solvation layers are negligible, i.e., $\Delta_A \approx \Delta_B = 0$. On the other hand, for many outer-sphere electron transfer reactions the theory has to be modified (see also ref 12).

From the foregoing discussion we conclude that for many processes of interest we have to consider the local modes of the first coordination layer $\omega_A \approx \omega_B \equiv \omega_C$ in the low-temperature approximation while the medium modes have to be handled in the high-temperature limit, i.e., $\bar{n}_\kappa = (\beta\hbar\omega_\kappa)^{-1}$ for all κ . To derive a general expression for the electron transfer probability we separate the local (c) and the medium (s) modes in the vibrational wave function in eq I.4 so that

$$\begin{aligned} \chi_{av}^0 &= \chi_{av_c}^c(q_A, q_B) \chi_{av_s}^s(q_\kappa) \\ \chi_{bv}^0 &= \chi_{bv_c}^c(q_A, q_B) \chi_{bv_s}^s(q_\kappa) \quad (\text{III. 12}) \end{aligned}$$

which are characterized by the vibrational energies

$$\begin{aligned} E_{av}^0 &= E_{ac} + E_{av} = [(v_A + 1/2) + \\ & (v_B + 1/2)]\hbar\omega_c + 1/2 \sum_\kappa (v_\kappa + 1/2)\hbar\omega_0 \\ E_{bv}^0 &= E_{bc} + E_{bv} = [(w_A + 1/2) + \\ & (w_B + 1/2)]\hbar\omega_c + 1/2 \sum_\kappa (w_\kappa + 1/2)\hbar\omega_0 \quad (\text{III. 13}) \end{aligned}$$

The electron transfer probability (I.13) is

$$W_a = \frac{2\pi |v|^2}{\hbar Z_c Z_s} \sum_{0\kappa} \sum_{0\kappa} \sum_{bc} \sum_{bs} \exp[-\beta(\epsilon_{ac} + \epsilon_{as})] (\chi_{av_c} | \chi_{bw_u})^2 (\chi_{bv_s} | \chi_{bw_s})^2 \delta(\epsilon_{ac} + \epsilon_{as} - \epsilon_{bc} - \epsilon_{bs} + \Delta E) \quad (\text{III. 14})$$

can be recast in terms of a convolution

$$W_a = \frac{2\pi |v|^2}{\hbar} \int_0^\infty dE F_c(\epsilon) F_s(\Delta E - \epsilon) \quad (\text{III. 15})$$

where we have defined two auxiliary functions

$$F_c(\epsilon) = \frac{1}{Z_c} \sum_{ac} \sum_{bc} \exp(-\beta\epsilon_{ac}) (\chi_{av_s} | \chi_{bw_c})^2 \delta(\epsilon_{ac} - \epsilon_{bc} + E)$$

$$F_s(\Delta E - \epsilon) = \frac{1}{Z_s} \sum_{as} \sum_{bs} \exp(-\beta\epsilon_{as}) \times (\chi_{av_s} | \chi_{bw_s})^2 \delta(\epsilon_{as} - \epsilon_{bs} + \Delta E - \epsilon) \quad (\text{III. 16})$$

We have thus separated the transition probability into the contribution of the external medium and the first coordination layer. The functions F_c and F_m represent generalized transition probabilities (at the energy) and can be regarded as generalized line shape functions. The line shape function for the low-frequency medium modes can be handled in terms of the high-temperature approximation (II.26) so that

$$F_s(\Delta E - \epsilon) = \left(\frac{1}{4\pi E_M^s k_B T} \right)^{1/2} \exp[(\Delta E - E_M^s - \epsilon)/2D_s^2 \hbar^2] \quad (\text{III. 17})$$

where the equivalent expression to eq II.24 is

$$\hbar^2 D_s^2 = \frac{1}{2} \hbar \omega_0 \sum_{\kappa} \coth \frac{\beta \hbar \omega_0}{2} = 2E_M^s / \beta \quad (\text{III. 18})$$

The line shape function for the first coordination layer can be represented formally as

$$F_0(E) = \exp[-(\Delta_c^2/2)(2n_c + 1)] \int dt \exp(i\epsilon t/\hbar) \times \exp\left[\frac{\Delta_c^2}{2}(n_c + 1) \exp(i\omega_c t) + \frac{\Delta_c^2}{2} n_c \exp(-i\omega_c t)\right] \quad (\text{III. 19})$$

where $\Delta_c^2 = \Delta_A^2 + \Delta_B^2$ and $n_c = [\exp(\beta \hbar \omega_c) - 1]^{-1}$. Expansion of the exponential in the integral results in

$$F_c(E) = \exp[-(\Delta_c^2/2)(2n_c + 1)] \times \sum_{k=0}^{\infty} \sum_{l=0}^{\infty} \frac{1}{l! k!} \left(\frac{\Delta_c^2}{2}\right)^{k+l} (n_c + 1)^l n_c^k \delta(E - \hbar \omega_c + k \hbar \omega_c) \quad (\text{III. 20})$$

Combining eq III.17 and III.20 we finally obtain

$$W_a = \frac{2\pi |v|^2}{\hbar} \left(\frac{1}{4\pi E_M^s k_B T} \right)^{1/2} \sum_{k=0}^{\infty} \sum_{k=0}^{\infty} \exp[-\beta \times (\Delta E - E_M^s - (1 - k)\hbar \omega_c)^2 / 4E_M^s] \frac{1}{l! k!} \times \exp[-(\Delta_c^2/2)(2n_c + 1)] (\Delta_c^2/2)^{k+l} (n_c + 1)^l n_c^k \quad (\text{III. 21})$$

This is a tractable quantum mechanical expression where Δ_c and $\hbar \omega_c$ are obtained from experiment while E_M^s is evaluated from strongly coupled polaron theory (Appendix B) via eq II.9.

IV. Quantum Mechanics of the First Coordination Layer

In order to evaluate the transition probability we need to express the results in a more compact notation. Introducing the expression for the occupation number of the coordination layer photons each of energy and

$$n_c = e^{-\beta \hbar \omega_c} (1 - e^{-\beta \hbar \omega_c})^{-1} \quad (\text{IV. 1})$$

$$n_c + 1 = (1 - e^{-\beta \hbar \omega_c})^{-1} \quad (\text{IV. 2})$$

we have

$$\frac{W}{|V|^2} = \exp\left[-\frac{\Delta_c^2 \coth(\hbar \omega_c \beta/2)}{2}\right] \left(\frac{\pi}{4\hbar^2 E_M^s k_B T}\right)^{1/2} \times \sum_{l=0}^{\infty} \sum_{k=0}^{\infty} \exp[-\beta(\Delta E - E_M^s(1 - k)\hbar \omega_c)^2 / 4E_M^s] \times \frac{1}{l! k!} \left(\frac{\Delta_c^2 e^{-\beta \hbar \omega_c / 2}}{2(e^{\beta \hbar \omega_c / 2} - e^{-\beta \hbar \omega_c / 2})}\right)^{l+k} e^{l\beta \hbar \omega_c} \quad (\text{IV. 3})$$

This result can be simplified by using Bessel functions of imaginary arguments, I , as has been shown by many authors^{5,18,19}

$$\left(\frac{4\hbar^2 E_M^s k_B T}{\pi}\right) \frac{W}{|V|^2} = \sum_{m=-\infty}^{\infty} \exp[-z_p \cosh(\beta \hbar \omega_c / 2) + m \hbar \omega_c \beta / 2] \times \exp[-(\Delta E - E_M^s - m \hbar \omega_c)^2 / 4E_M^s k_B T] I_m(z_p) \quad (\text{IV. 4})$$

where $z_p = (\Delta_c^2/2) \text{csch}(\beta \hbar \omega_c / 2)$ and $I_m(z_p) = I_{|m|}(z_p)$ with

$$I_m(z_p) = \left(z_p/2\right)^m \sum_{k=0}^{\infty} \frac{(z_p^2/2)^k}{k! (m+k)!} \quad (\text{IV. 5})$$

Several limiting forms of this result are of interest. At very low temperatures or low values of Δ_c , z_p is very small and for such arguments²⁰

$$I_m(z_p) \xrightarrow{z_p \rightarrow 0} (z_p/2)^m / m! \quad (\text{IV. 6})$$

so that

$$\left(\frac{4\hbar^2 E_M^s k_B T}{\pi}\right)^{1/2} \frac{W}{|V|^2} \xrightarrow{z_p \rightarrow 0} e^{-\Delta_c^2/2} \times \sum_{m=-\infty}^{\infty} \exp[-(\Delta E - E_M^s - m \hbar \omega_c)^2 / 4E_M^s k_B T] \times \exp[-(m + |m|)\hbar \omega_c \beta / 2] \left(\frac{\Delta_c^2}{2}\right)^{|m|} \frac{1}{|m|!} \quad (\text{IV. 7})$$

an expression obtained by Levich, *et al.*^{18,19} in another context. This is the same type of expression usually found for a weak coupling case in radiationless transitions. At these low temperatures (but still high for the polaron modes) only $m = 0$ contributes since $\hbar \omega_c \beta$ is large. Thus the right-hand side of the equation reduces to

$$e^{-\Delta_c^2/2} \exp[-(\Delta E - E_M^s)^2 / 4E_M^s k_B T] \quad (\text{IV. 8})$$

corresponding to an activation energy for this part of the expression E_A' of

$$E_A' = k_B T^2 \frac{\partial \ln(WT^{1/2})}{\partial T} = (\Delta E - E_M^s)^2 / 4E_M^s \quad (\text{IV.9})$$

For very large z_p , *i.e.*, high temperatures, another limiting expression can be derived. The simplest derivation begins with the basic equation (III.19) and making the strong coupling approximations as in section II but now for the vibrations in the first coordination layer, *i.e.*, we expand the exponentials in (III.19) and obtain

$$F_c(\epsilon) = \int dt \exp\left[-\frac{it}{\hbar}[-(\epsilon + E_c) - \frac{t^2}{2}D_c^2]\right] \quad (\text{IV.10})$$

where

$$D_c^2 = (\Delta_c^2/2)^2 \omega_c^2 (2n_c + 1) \quad (\text{IV.11})$$

and

$$E_c = \hbar\omega_c \Delta_c^2/2 \quad (\text{IV.12})$$

This leads to a total rate proportional to

$$\int_0^\infty d\epsilon \exp\left[-\frac{(\Delta E - E_M^s - \epsilon)^2}{4E_M^s k_B T} - \frac{(\epsilon + E_c)^2}{2D_c^2 \hbar^2}\right] \quad (\text{IV.13})$$

This can be integrated to yield

$$\begin{aligned} (\text{constant}) \exp\left[-\frac{(\Delta E - E_M^s)^2}{4E_M^s k_B T} - \frac{E_c^2}{\Psi E_c k_B T} + \frac{[E_M^s E_c - (\Delta E - E_M^s) E_c^2]^2}{2E_M^s E_c (E_M^s + E_c)}\right] \end{aligned} \quad (\text{IV.14})$$

which simplifies to

$$(\text{constant}) \exp\left[-\frac{(\Delta E - E_M^s - E_c)^2}{4(E_M^s + E_c) k_B T}\right] \quad (\text{IV.15})$$

or

$$E_A' = + \frac{(\Delta E - E_M^s - E_c)^2}{4(E_M^s + E_c)} \quad (\text{IV.16})$$

The limiting cases quoted are not useful for most applications as they represent temperature regions not usually studied for typical systems. The low-temperature limit is only applicable if there is only a very slight reorganization of the coordination layer as in the case of strongly bound complexes, *e.g.*, ferro- and ferricyanides, or if extremely low temperatures, way below the medium freezing point. The high-temperature limit is also unlikely in practice since for typical hydration cases it would involve temperatures of 500–1000°.

We can easily evaluate the entire expression, eq IV.3, by a straightforward computer program and extract from it the rates or values of E_A' for typical ranges of the parameters. In Tables III and IV we have tabulated the results for $E_M^s = 2$ eV, and for typical values of $\hbar\omega_c$, ΔE , and $\Delta_c^2/2$. Typically $\hbar\omega_c$ is about 400 cm^{-1} (see Table I) for hydration of ions and much higher when stable complexes are involved. $\Delta_c^2/2$ can be around 10 when major reorganization of hydration layers occurs but is much smaller for strongly bonded complexes.

Before commenting on these results it is useful to present a derivation of a reasonable approximate formula

TABLE II: Activation Energies, E_A' (°K)^a

Temp, T	$\Delta_c^2/2 = 5$	$\Delta_c^2/2 = 5$	$\Delta_c^2/2 = 15$
	$\hbar\omega_c = 400$	$\hbar\omega_c = 600$	$\hbar\omega_c = 400$
	cm^{-1}	cm^{-1}	cm^{-1}
50	5808.6	5800.7	5825.7
100	5941.1	5852.6	6224.1
150	6115.9	6009.4	6749.6
200	6240.6	6190.0	7123.9
250	6320.3	6342.2	7363.2
300	6371.9	6457.8	7517.1
350	6405.7	6543.2	7619.4
400	6429.7	6606.8	7691.8
450	6446.8	6655.1	7743.3
500	6459.9	6692.0	7780.5
600	6475.2	6743.1	7831.6
1000	6497.3	6825.2	7914.5
∞	6518.8	6878.8	7956.3

^a $E_M^s = 2$ eV, $\Delta E = 0$.

which is an accurate representation of the computer results.

Expanding eq IV.4 we can rewrite the right-hand side as

$$\exp[-z_p \cosh(\beta \hbar\omega_c/2)] \exp\left[-\frac{(\Delta E - E_M^s)^2 \beta}{4E_M^s}\right] \times \sum_{m=-\infty}^{\infty} \exp(-\alpha m^2) \exp(\gamma m) I_m(z_p) \quad (\text{IV.17})$$

where

$$\alpha = (\hbar\omega_c)^2 / 4E_M^s k_B T$$

and

$$\gamma = \Delta E \hbar\omega_c / E_M^s k_B T \quad (\text{IV.18})$$

For usual hydration parameters $\hbar\omega_c < kT$ and $\hbar\omega_c \ll E_M^s$ so that α is small ($\sim 3.9/T$) and $e^{-\alpha m^2} \sim 1$. Using this and the following identity

$$e^{z/2(t+1/t)} = \sum_{m=-\infty}^{\infty} t^m I_m(z) \quad (\text{IV.19})$$

we can simplify the results to

$$\begin{aligned} \frac{W}{(V)^2} \left(\frac{\hbar^2 E_M^s}{\beta \pi}\right)^{1/2} = \exp\left[-z_p \cosh \beta \hbar\omega_c/2 - \cosh\left(\frac{\Delta E \hbar\omega_c \beta}{E_M^s 2}\right)\right] \times \exp\left[-\frac{\beta}{4E_M^s}(\Delta E - E_M^s)^2\right] \end{aligned} \quad (\text{IV.20})$$

or

$$\begin{aligned} = \exp\left[-\frac{\Delta_c^2}{2}(\coth x - \text{csch } x \cosh(x\Delta E/E_M^s))\right] \times \exp[-(\beta/4E_M^s)(\Delta E - E_M^s)^2] \end{aligned} \quad (\text{IV.21})$$

where $x = \hbar\omega_c/2kT$. This leads to an effective activation energy E_{AA}' of

TABLE III: Activation Energies, E_A' ($^{\circ}\text{K}$)^a

Temp, T	$\Delta_c^2/2 = 5$ $\hbar\omega_c = 400 \text{ cm}^{-1}$	$\Delta_c^2/2 = 5$ $\hbar\omega_c = 600 \text{ cm}^{-1}$	$\Delta_c^2/2 = 15$ $\hbar\omega_c = 400 \text{ cm}^{-1}$	$\Delta_c^2/2 = 1.0$ $\hbar\omega_c = 2100 \text{ cm}^{-1}$	$\Delta_c^2/2 = 10$ $\hbar\omega_c = 400 \text{ cm}^{-1}$
50	5808.6	5800.7	5825.7	5800.0	5817.1
100	5941.1	5852.6	6224.1	5800.0	6082.5
150	6115.9	6009.4	6749.6	5800.1	6432.5
200	6240.6	6190.0	7123.9	5801.0	6682.0
250	6320.3	6342.2	7363.2	5805.2	6841.4
300	6371.9	6457.8	7517.1	5814.9	6944.2
350	6405.7	6543.2	7619.4	5831.3	7012.3
400	6429.7	6606.8	7691.8	5854.8	7060.7
450	6446.8	6655.1	7743.3	5883.5	7094.5
500	6459.9	6692.0	7780.5	5915.9	7119.8
600	6475.2	6743.1	7831.6	5985.7	7153.1
1000	6497.3	6825.2	7914.5	6218.8	7109.2
∞	6518.8	6878.8	7956.3	6554.8	7237.5

^a $E_m^s = 2 \text{ eV}$, $\Delta E = 0$.TABLE IV: Activation Energies, E_A' (kcal/mol)^a

Temp (T), $^{\circ}\text{K}$	$\Delta E = 0$		$\Delta E = 1 \text{ eV}$		$\Delta E = -1 \text{ eV}$	
	Numerical result ^b	Approximate formula ^c	Numerical result ^b	Approximate formula ^c	Numerical result ^b	Approximate formula ^c
50	11.546	11.547	2.9566	2.9636		26.02
100	11.810	11.818	3.2302	3.2483	26.28	26.31
150	12.157	12.168	3.4757	3.4880	26.53	26.55
200	12.405	12.416	3.6389	3.6402	26.70	26.70
250	12.564	12.573	3.7414	3.7334	26.80	26.79
300	12.666	12.674	3.8068	3.7923	26.87	26.85
350	12.733	12.742	3.8508	3.8311	26.91	26.89
400	12.781	12.788	3.8810	3.8577	26.94	26.92
450	12.958	12.822	3.9030	3.8767	26.90	26.94
500	12.841	12.846	3.9176	3.8906	26.98	26.95
600	12.871	12.879	3.9398	3.9093	27.00	26.97
1000	12.915	12.929	3.9764	3.9375	27.04	27.00
∞	12.958 ^d	12.958 ^e	3.9933 ^d	3.9496 ^e	27.05 ^d	27.01 ^e

^a $E_m^s = 2 \text{ eV}$, $\Delta_c^2/2 = 5$, $\hbar\omega_c = 400 \text{ cm}^{-1}$. ^b From eq IV.3. ^c From eq IV.20. ^d Asymptotic limit from eq IV.16. ^e Asymptotic limit from eq IV.23.

$$E_{AA}' = \frac{(\Delta E - E_m^s)^2}{4E_m^s} + \left(\frac{\Delta_c^2}{2}\right)\left(\frac{\hbar\omega_c}{2}\right) \text{csch } x \times$$

$$\left[-\text{csch } x + \cosh\left(\frac{\Delta E}{E_m^s} x\right) \coth x - \frac{\Delta E}{E_m^s} \sinh\left(\frac{\Delta E x}{E_m^s}\right) \right] \quad (\text{IV.22})$$

This approximate formula goes to the proper low-temperature limit but has a small error at high temperatures. Its high-temperature limit is

$$E_{AA}'(T \rightarrow \infty) = \frac{E_m^s + E_c}{4} - \frac{\Delta E}{2} + \frac{(\Delta E)^2}{4E_m^s} \left(1 - \frac{E_c}{E_m^s}\right) \quad (\text{IV.23})$$

vs. the exact result of eq IV.16 which can be written as

$$E_A'(T \rightarrow \infty) = \frac{E_m^s + E_c}{4} - \frac{\Delta E}{2} + \frac{(\Delta E)^2}{4(E_m^s + E_c)} \quad (\text{IV.24})$$

In both cases $E_c = (\Delta_c^2/2)\hbar\omega_c$ represents the shift in the zero-point energy of the primary solution layers. The two results are correct through the first order of (E_c/E_m^s) and since this is usually small (<0.25) the error involved in using is also small, *i.e.*

$$\sim [(\Delta E)^2/4E_m^s](E_c/E_m^s)^2 \quad (\text{IV.25})$$

The results of this approximate formula are also tabulated in Table IV for comparison.

In Figure 4 we also plot the activation energies determined from the exact formula for various values of $\Delta_c^2/2$ and $\hbar\omega_c$ for $\Delta E = 0$ and $E_m^s = 2 \text{ eV}$.

In order to evaluate these expressions for actual ions we need to evaluate E_m^s (eq III.10). This can be given in terms of D_i the initial electric displacement and D_f the final dis-

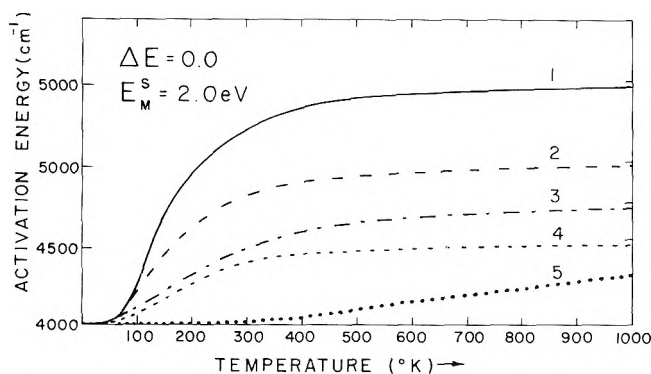


Figure 4. Typical results for the change in the effective activation energy with temperature for various values of the parameters. The parameters are curve 1, $\hbar\omega_c$ 400 cm^{-1} , $\Delta_c^2/2$ 15; curve 2, $\hbar\omega_c$ 400 cm^{-1} , $\Delta_c^2/2$ 10; curve 3, $\hbar\omega_c$ 600 cm^{-1} , $\Delta_c^2/2$ 5; curve 4, $\hbar\omega_c$ 400 cm^{-1} , $\Delta_c^2/2$ 5; curve 5, $\hbar\omega_c$ 2100 cm^{-1} , $\Delta_c^2/2$ 1. The horizontal lines to the right represent the asymptotic limits of these curves.

placement. If we initially have an ion with charge $+m$ on center A and an ion with charge $+n$ on center B with sizes a_m and b_n leading to ions of charges $m+1$ with size a_{m+1} , and charges $n-1$ with size b_{n-1} , on centers A and B, respectively, and if we further adopt Marcus' method of evaluating the terms using the concepts of metallized ions we have

$$\begin{aligned} D_i &= D_{ma} + D_{mb} \\ D_f &= D_{(m+1)a} + D_{(n-1)b} \end{aligned} \quad (\text{IV. 26})$$

where, for example

$$\begin{aligned} D_{ma} &= \begin{cases} 0 & r < a_m \\ m e \vec{r} / r^3 & r > a_m \end{cases} \\ D_{(m+1)a} &= \begin{cases} 0 & r < a_{m+1} \\ (m+1) e \vec{r} / r^3 & r > a_{m+1} \end{cases} \\ \text{and} \\ D_{mb} &= \begin{cases} 0 & |\vec{r} - \vec{r}_{ab}| < b_m \\ m e (\vec{r} - \vec{r}_{ab}) / |\vec{r} - \vec{r}_{ab}|^3 & |\vec{r} - \vec{r}_{ab}| > b_m \end{cases} \end{aligned} \quad (\text{IV. 27})$$

It is important to note that because we consider separately the first coordination layer all ionic radii refer to those of hydrated ions.

Since $a_m > a_{m+1}$ and $b_n < b_{n-1}$ we have

$$E_M^S = C e^2 \left[\frac{(m+1)^2}{2a_{m+1}} + \frac{n^2}{2b_n} - \frac{n^2-1}{2b_{n-1}} - \frac{m(m+1)}{2a_m} - \frac{1}{R} \right] \quad (\text{IV. 28})$$

For an isotopic exchange reaction $m = n - 1$, thus $b_n = a_{m+1}$ and $b_{n-1} = a_m$ so that the results reduce to

$$E_M^S = C e^2 \left[\frac{n^2}{a_n} - \frac{n^2-1}{a_{n-1}} - \frac{1}{R} \right] \quad (\text{IV. 29})$$

When $a_n = a_{n-1} = r_a$ we obtain the simplified formula often quoted

$$E_M^S = C e^2 \left[\frac{1}{r_a} - \frac{1}{R} \right] \quad (\text{IV. 30})$$

Our approximate formula (eq IV.21) is predicated on the magnitude of α being small. To justify this we must consider the available experimental parameters which determine the important quantities. In this work we will consider only the totally symmetric vibration of the hydration layer, although in principle all modes could be considered. The difficulties in using the other modes is that there is no simple way to estimate the shift in these coordinates between various oxidation states of an ion. These shifts are probably smaller than the radial mode whose change we can relate to the size of the ion. In Table I we list the experimental results for the totally symmetric mode for the hydration layer as determined by the Raman spectrum of aqueous solutions or crystals containing hydrated ions. The other quantity needed is the radius of the ions in the various oxidation states. In our discussion we will use those values quoted in Table I.

Since many redox couples have similar vibrational energies we shall concentrate on but one typical reaction, namely, the Fe^{2+} - Fe^{3+} system assuming that it proceeds *via* a direct outer-sphere mechanism. We will assume that $\hbar\omega_c = 389 \text{ cm}^{-1}$ in both oxidation states. From the definition

$$\Delta_c = \left(\frac{M_c \omega_c}{\hbar} \right)^{1/2} \Delta R = 2.2 \quad (\text{IV. 31})$$

since M_c is the appropriate reduced mass $\mu = (18)(1.66 \times 10^{-24}) = 2.98 \times 10^{-23} \text{ g}$ and $\Delta r = 0.16 \text{ \AA}$. Thus $E_M^C = (\hbar\omega_c \Delta_c^2/2) = 0.117 \text{ eV} \times 2 = 0.233 \text{ eV}$

$$z_p = 2.42 \text{ csch } x \quad (\text{IV. 32})$$

and $x = (1.4388)(389)/2T = 280/T$. The factor of 2 is required since two ions are involved. The other quantity needed in our calculation is E_M^S , the medium reorganization energy. Since we consider the first coordination layer separately, this quantity can only include effects of the medium beyond the primary solvation layer. The size of our ions are therefore the ionic radius plus the thickness of the solvation layer which we take to be 2.76 \AA . Thus the ferrous ion has an effective size for the continuum medium contributions of $a_2 = 3.59 \text{ \AA}$ and the ferric ion $a_3 = 3.43 \text{ \AA}$. Using the formula derived for E_M^S

$$E_M^S = C e^2 \left(\frac{9}{a_3} - \frac{8}{a_2} - \frac{1}{R} \right) \quad (\text{IV. 33})$$

and substituting the values appropriate to the Fe^{3+} - Fe^{2+} couple we get

$$E_M^S = \left(3.13 - \frac{7.94}{R_{ab}} \right) \text{ eV} \quad (\text{IV. 34})$$

where R_{ab} is in \AA . For a transition region of $R \sim 7 \text{ \AA}$ we get $E_M^S = 2.0 \text{ eV}$ or less.

We now have all of the factors to investigate the approximate formula derived earlier. For the Fe^{2+} - Fe^{3+} couple we obtain

$$\alpha = x(\hbar\omega_c/E_M^S)/4 = \left(\frac{280}{T} \right) \left(\frac{0.0482}{4} \right) = \frac{3.87}{T} \quad (\text{IV. 35})$$

Thus at ordinary temperatures, α is quite small. If it is small enough our approximate formulas will be reasonable.

We have already seen that there is a good agreement between the approximate and the exact formulation for such a range of α .

We can give further evidence by comparing the formula for $\Delta E = 0$, *i.e.*

$$\sum_{m=-\infty}^{\infty} e^{-\alpha m^2} I_m(z_p) = G(\alpha, z_p) \exp(z_p) \quad (\text{IV.36})$$

where for small α we expect $G(\alpha) \sim 1$. In Table V we list the function calculated or typical values of the parameters. From these results we can see that the error involved is only a few per cent, certainly an acceptable approximation in a rate calculation. For a specific estimate of the error we can consider the $\text{Fe}^{2+}\text{-Fe}^{3+}$ couple at room temperature (300°K) where we find $x = 0.93$, $z_p = 2.02$, and $\alpha = 0.0113$ corresponding to $G(\alpha, z_p)$ of about 0.98. At lower temperatures or larger $\hbar\omega_c$, it is even closer to one.

V. Evaluation of the Rate Constant

The rate constant can be written (I.14)

$$k = \int_R^{\infty} d^3R_{ab} \exp[-\beta U(R_{ab})] W_a(R_{ab})$$

where $U(R_{ab})$ is defined in eq I.15 and R is the distance of closest approach of the ions.

We can either substitute the numerical values for $W_a(R_{ab})$ or use the approximate formula from (IV.21). Using the latter course of action we have

$$k = \frac{4\pi}{\hbar} \left(\frac{\pi}{4E_M^s k_B T} \right)^{1/2} \int_R^{\infty} \exp \left[-\frac{\Delta_c^2}{2} (\coth x - \text{csch } x \cosh(x\Delta E/E_M^s)) \right] \exp[-(\beta/4E_M^s)(\Delta E - E_M^s)^2] |v'(R_{ab})|^2 \exp[-\beta U(R_{ab})] R_{ab}^2 dR_{ab} \quad (\text{V.1})$$

where specifically

$$U_{ab} = mne^2/R_{ab} D_{\text{eff}} \quad (\text{V.2})$$

for the ions involved using an effective dielectric constant D_{eff} .

If we restrict our attention to the $\text{Fe}^{2+}\text{-Fe}^{3+}$ couple where $\Delta E = 0$ and

$$E_M^s = (9/Q_3 - 8/Q_2 - 1/R_{ab})(c\beta e^2/4) \quad (\text{V.3})$$

the formulas simplify greatly to yield

$$k = \frac{4\pi}{\hbar} \left(\frac{\pi}{4E_M^s k_B T} \right)^{1/2} \exp \left[-\frac{\Delta_c^2}{2} (\coth x - \text{csch } x) \right] \int_R^{\infty} e^{-\beta U(R_{ab}) - E_M^s/4kT} |v(R_{ab})|^2 R_{ab}^2 dR_{ab} \quad (\text{V.4})$$

In any case, to proceed further we need to evaluate the matrix element v . As has been pointed out in section II, this matrix is simply

$$v(R_{ab}) = \frac{1}{D_{\text{eff}}} \left\langle a \left| \frac{e^2}{\mathbf{r}_a - \mathbf{R}_{ab}} \right| b \right\rangle \quad (\text{V.5})$$

For the moment we shall consider v as a parameter although the value will be related to the orbital exponent of the d orbitals as

$$v(R_{ab}) = 2e^2\gamma \exp(-\gamma R_{ab})/D_{\text{eff}} \quad (\text{V.6})$$

TABLE V: Value of $G(\alpha, z_p)$ (Eq IV.36) for Typical Values of the Parameters

α	z_p	$G(\alpha, z_p)$
0.000	All values	1.0000
0.010	1.0	0.9902
	2.0	0.9807
	3.0	0.9714
	4.0	0.9624
	5.0	0.9537
0.020	1.0	0.9808
	2.0	0.9626
	3.0	0.9454
	4.0	0.9290
	5.0	0.9135
0.030	1.0	0.9717
	2.0	0.9456
	3.0	0.9215
	4.0	0.8991
	5.0	0.8782
0.040	1.0	0.9629
	2.0	0.9296
	3.0	0.8994
	4.0	0.8720
	5.0	0.8469
0.050	1.0	0.9544
	2.0	0.9144
	3.0	0.8790
	4.0	0.8473
	5.0	0.8188

We now consider only the R_{ab} dependent factors in the integral in eq V.4, *i.e.*, for $\text{Fe}^{2+}|\text{Fe}^{3+}$

$$\int_R^{\infty} \exp(6\beta e^2/R_{ab} D_{\text{eff}}) \exp[C\beta e^2/\Psi R_{ab}] \times \exp[-2\gamma R_{ab}] R_{ab}^2 dR_{ab} \quad (\text{V.7})$$

and assuming that D_{eff} is only weakly dependent on R_{ab} . Following Levich we shall approximate this integral by its value at the distance where the exponential is a minimum, *i.e.*, at the value of R_{ab} called R_m , such that

$$-\frac{\beta e^2}{R_{ab}} \left[\frac{6}{D_{\text{eff}}} - \frac{C}{4} \right] - 2\gamma R_{ab} \quad (\text{V.8})$$

is a minimum. If this number is less than R , R_m is taken to be R . The value of R_m is found by setting the derivative of (V.8) equal to zero

$$R_m = \left[\frac{e^2}{2\gamma k_B T} \left(\frac{6}{D_{\text{eff}}} - \frac{C}{4} \right) \right]^{1/2} \quad (\text{V.9})$$

for reasonable values of γ (*i.e.*, $1\text{-}5 \text{ \AA}^{-1}$) and $20 < D_{\text{eff}} < 40$, R_m is real but small, less than 5 \AA . As a reasonable estimate regardless of D_{eff} , we shall use $R = R_m$. The meaning of this is important. The rate constant increases with decreasing R and thus it is dominated by the interaction at the distance of closest approach. This is in contrast to the work of Levich⁶ who used an extremely unphysical value for γ , namely, about $(6/D_{\text{eff}}) \text{ \AA}^{-1}$, taking D_{eff} about 45. Although we expect γ to be modified from its value in a free atom, there is no theoretical justification for dividing it by

D_{eff} . Using $R = R_m$ we now obtain

$$k = \frac{4\pi}{\hbar} \left(\frac{\pi}{4E_M^s k_B T} \right)^{1/2} \exp \left[-\frac{\Delta_c^2}{2} (\coth x - \operatorname{csch} x) \right] x v^2 (R_{\text{ab}}) \exp \left[-\left(\frac{9}{a_3} - \frac{8}{a_2} - \frac{1}{R} \right) \times \left(\frac{C\beta e^2}{4} \right) \right] \exp[-6e^2\beta/RD_{\text{eff}}] \chi(R^3/3) \quad (\text{V.10})$$

or

$$k = A \exp(-V/kT) \quad (\text{V.11})$$

where

$$A = \frac{4\pi}{E} \left(\frac{\pi}{4E_M^s k_B T} \right)^{1/2} \left(\frac{R^3}{3} \right) v^2 (R_{\text{ab}}) \quad (\text{V.12})$$

and

$$V = \frac{k_B T \Delta_c^2}{2} (\coth x - \operatorname{csch} x) + \left(\frac{9}{a_3} + \frac{8}{a_2} \right) \times \left(\frac{C e^2}{4} \right) + \frac{e^2}{R} \left(\frac{6}{D_{\text{eff}}} - \frac{C}{4} \right) = \frac{k_B T \Delta_c^2}{2} (\coth x - \operatorname{csch} x) + \frac{E_M^s}{4} + \frac{6e^2}{RD_{\text{eff}}} \quad (\text{V.13})$$

As a check this expression goes to the proper high-temperature limit of

$$U(T \rightarrow \infty) = \frac{E_c}{4} + \frac{E_M^s}{4} + \frac{6e^2}{RD_{\text{eff}}} \quad (\text{V.14})$$

For the general case of $\Delta E \neq 0$ we can derive an equivalent expression if $R_m = R$. It is the same as (V.11) except that V becomes more complicated than in eq V.13, namely

$$V = \frac{k_B T \Delta_c^2}{2} [\coth x - \operatorname{csch} x \cosh(x\Delta E/E_M^s)] + (\Delta E - E_M^s)^2 / 4E_M^s + U(R) \quad (\text{V.15})$$

However at the temperatures involved in most experiments there will be a temperature-dependent contribution from the first coordination layer. For moderate temperatures we can expand the results about $x = 0$. It is more important to concentrate our attention on the activation energy E_A and not on V itself since

$$E_A = k_B T^2 \frac{\partial \ln k}{\partial T} = E_A' + k_B T^2 \frac{\partial \ln A}{\partial T} + k_B T^2 \frac{\partial}{\partial T} (\beta V) \quad (\text{V.16})$$

where E_A' is the numerical results derived in the last section or the approximate form E_{AA} (eq IV.24). We shall use the approximate form here in which case

$$E_A(T) = E_{AA} \frac{kT}{2} - kT^2 \frac{mne^2}{R} \frac{\partial}{\partial T} \left(\frac{1}{kTD_{\text{eff}}} \right) \quad (\text{V.17})$$

$$= E_{AA}' + U(R) - \frac{kT}{2} - \frac{Tmne^2}{RD_{\text{eff}}} \left(\frac{\partial D_{\text{eff}}}{\partial T} \right) \quad (\text{V.18})$$

An approximate result can be obtained for moderate temperatures by expanding E_{AA}' about $x = 0$

$$E_{AA}(T) = \frac{(\Delta E - E_M^s)^2}{4E_M^s} + \frac{E_c}{2} \left(\frac{1}{2} - \frac{y^2}{2} \right) + \frac{E_c x^2}{2} \left(-\frac{1}{8} + \frac{y^2}{4} - \frac{y^4}{8} \right) + \dots \quad (\text{V.19})$$

where $y = \Delta E/E_M^s$. Thus

$$E_A(T) = E_A(T \rightarrow \infty) - \frac{E_c x^2}{16} (1 - 2y^2 + y^4) + \frac{Tmne^2}{RD_{\text{eff}}^2} \left(\frac{\partial D_{\text{eff}}}{\partial T} \right) \quad \hbar\omega_c \ll kT \quad (\text{V.20})$$

At low temperatures the activation energy is known exactly from IV.9 so we can find

$$E_A(T) = E_A(T \rightarrow \infty) + \frac{(\Delta E - E_c)^2}{4E_M^s} - \frac{(\Delta E - E_M^s - E_c)^2}{4(E_M^s + E_c)} + \frac{Tmne^2}{RD_{\text{eff}}^2} \left(\frac{\partial D_{\text{eff}}}{\partial T} \right) \quad \hbar\omega_c \gg kT \quad (\text{V.21})$$

if $\Delta E = 0$ the results simplify to

$$E_A(T) = E_A(T \rightarrow \infty) - \frac{E_c}{16} \left(\frac{\hbar\omega_c}{2kT} \right)^2 + \frac{mne^2}{RD_{\text{eff}}^2} \left(\frac{\partial D_{\text{eff}}}{\partial T} \right) \quad \hbar\omega_c \ll kT$$

$$= E_A(T \rightarrow \infty) - E_c - \left[\frac{1}{4} - (2kT/\hbar\omega_c) \right] + \frac{mne^2}{RD_{\text{eff}}^2} T \left(\frac{\partial D_{\text{eff}}}{\partial T} \right) \quad \hbar\omega_c \gg kT \quad (\text{V.22})$$

As an example of the magnitudes of these quantities we will consider the $\text{Fe}^{2+}|\text{Fe}^{3+}$ couple. In this case $E_c = 0.23$ eV = 5.30 kcal/mol and thus at room temperature the activation energy differs from its asymptotic limit by about 0.30 kcal/mol, at low temperatures ($\sim 100^\circ\text{K}$) it differs by $E_c/4$ or about 1.3 kcal/mol. For typical examples see Figure 4.

It is important to realize that these high- and low-temperature limits are accessible to experimental verification. There is another low-temperature limit discussed by Levich⁶ corresponding to the low temperature relative to the polaron modes but such effects can only be observed at extremely low temperatures, probably below 10°K . In both cases the activation energy decreases due to the increased importance of tunneling at the lower temperatures.

For the $\text{Fe}^{2+}|\text{Fe}^{3+}$ couple the preexponential factor is (in cgs units)

$$3.16 \times 10^{18} \nu^2 \quad (\text{V.23})$$

If we use the best single Slater orbital exponent to represent the 3d wave function we should use 4.7 \AA^{-1} as calculated by Watson and quoted by Slater²¹ we obtain

$$\nu = 0.61 \times 10^{-24} / D_{\text{eff}} \quad (\text{V.24})$$

which leads to an extremely low value of A . The value of ν is extremely sensitive to the orbital exponent. Unfortunately, we do not know the exact value to use in this system since the integral depends on the tails of the wave functions and these are greatly affected by all sorts of medium effects: orthogonality, screening, etc. As a reference, in the accurate evaluation of exciton states, Katz, *et al.*,²² found that these integrals in the range of $7\text{--}8 \text{ \AA}$ were about 1 cm^{-1} for organic crystals. If we adopt such a value we find

$$\nu = 2 \times 10^{-16} \text{ ergs} \quad (\text{V. 25})$$

or $A = 1.25 \times 10^{-14} \text{ cm}^3/\text{sec molecule}$ or $0.75 \times 10^{+7} \text{ sec}^{-1} \text{ mol}^{-1}$.

Working backward that value of ν corresponds to about $\gamma = 0.9 \text{ \AA}^{-1}$ if $D_{\text{eff}} \sim 10$. This value is not unreasonable as in a very accurate nonrelativistic SCF calculation on iron, Clementi has one small 3d exponent of 1.45 \AA^{-1} , however, its coefficient is only 0.15 in the 3d orbital wave function. Until better ways are found to estimate this matrix element, our value of 1 cm^{-1} is a reasonable estimate. The actual activation energy for this couple at room temperature is $E_A = E_A(T \rightarrow \infty) - 0.30 \text{ kcal/mol}$ where $E_A(T \rightarrow \infty) = (12.87 + 285/D_{\text{eff}}) \text{ kcal/mol}$, neglecting $(\partial D_{\text{eff}}/\partial T)$.²³ These values are slightly larger than those of Levich due to our improved treatment of E_M^s and the contribution of the first coordination layer.

The effects calculated for the $\text{Fe}^{2+}|\text{Fe}^{3+}$ couple are small. However, in many systems these effects could be much larger. Stynes and Ibers²⁴ from X-ray studies of cobalt-amine complexes obtain a charge in radius of 0.178 \AA based on the Co(II)-N and Co(IV)-N distances. This leads to $\Delta_c^2/2 = 7.9$ which along with an A_{1g} vibration of 495 cm^{-1} ²⁵ leads to a somewhat larger effect. The activation would be expected to change by about 6.3% in going from 200 to 350°K. Much larger temperature dependences should be observed in more complicated cobalt ligands [$\text{Co}(\text{[14]dineN}_4)(\text{CH}_2)_2$].²⁶ In that case the Co-O distance can change by 0.54 \AA along one axis. This can lead to huge $\Delta_c^2/2$ values of about 58. Using a reasonable guess for the vibrational frequency of 300 cm^{-1} one expects the activation energy to vary by 17.3% from 200 to 350°K and even 3.1% from 300 to 350°K (using the approximate algebraic expression).

VI. Discussion

We were able to derive quantum mechanical expressions for nonadiabatic electron transfer reactions where the role of configurational changes in the first coordination layer was incorporated in the theory. The probability for the electron transfer process was recast in terms of a generalized line shape function including the contribution of both the high-frequency modes of the first coordination layers and the low frequencies of the external medium resulting in manageable expressions. The present formulation provides an extension of the classical approach of Marcus and Hush to include the role of the first coordination layer, and of the early quantum mechanical theory of Levich and Dogonadze^{6,11} who disregarded these effects. Recent efforts by Dogonadze^{9,10,12} and others^{11,13,14} have also begun to include these contributions but in a less formal way. It is gratifying that the conventional simple-minded concepts of the ionic solvation and of the structure of the solvated electron, separating the role of the first solvation layer and the polarizable medium outside it, can be incorporated into a quantum mechanical rate theory for outer-sphere electron transfer. The present treatment is analogous to electron relaxation in a large supermolecule. The pertinent information for the relevant displacements and frequencies in the first coordination layer is obtained from structural and spectroscopic data, while the other medium is represented as a continuum dielectric. Thus this approximation in Levich's approach which was recently criticized by Bockris²⁷ can be relaxed. It is important to note (see Appendix B) that the treatment of the outer medium in terms of polaron

theory does not imply treating its interaction with a loosely bound electron (*i.e.*, the transferred electron) as suggested by Bockris.²⁷ Rather, polaron theory is applied to account for the response of the polar medium to the influence of the charge distribution of the ionic species in the initial and the final states, thus accounting properly for the configurational charges in the external medium. The present treatment rests on the relation between the bimolecular rate constant and the nonradiative electron transfer probability which are related in terms of an integral of an approximate distribution fraction. Thus relative ionic motion is disregarded. Schmidt²⁸ in his early work had attempted to account for the role of relative ionic motion on electron transfer processes. Unfortunately, Schmidt's early formulation of the electron transfer problem is open to some serious criticism.²⁹ The Hamiltonian employed by him (eq 7 ref 28a) is inappropriate as it omits some crucial terms which involve the ion-solvent interaction. It is desirable to write the Hamiltonian in the Schrödinger representation as was done by us before proceeding to second quantization formation. In his formal treatment Schmidt disregards the reverse reactions in the derivation of eq 12 of ref 28a which is inconsistent with the general formalism. Finally, in the Fourier transform of the autocorrelation function^{28a} Schmidt assumes that the coefficients are time independent, which is not valid in general. In addition, there are some other technical details in Schmidt's work²⁸ regarding commutation relations which were not properly handled. Thus we believe that Schmidt's results²⁸ cannot be considered as a valid extension of the Levich's theory. We assert that the role of ionic diffusion is still open. It should be noted, however, that the approximation of electron transfer between stationary ions is consistent with the adiabatic approximation and as thus it is not expected that ionic diffusion will result in appreciable corrections for the rate constant for these activated processes.

The final form of our rate expressions are summarized by eq V.1, V.4, and V.10. It is important to note that the quantum mechanical expression utilizing a continuum model outside the first coordination layer yields free energy contributions for the external solvent bulk. We did not attempt to follow conventional chemical treatments separating the free energy and the enthalpy of activation but rather defined the activation energy *via* eq IV.9 and V.16. The activation energy at room temperature includes a 10–20% temperature-dependent corrections due to quantum effects of the first coordination layer in systems where $\hbar\omega_c \sim 400 \text{ cm}^{-1}$. The outer medium can always be handled classically, as in view of its low characteristic frequency, extremely low and physically inaccessible temperatures will be required to study quantum effects originating from the effect of these modes.

The preexponential factor for the nonadiabatic rate constant exhibits a strong dependence on the scaling parameter of the electronic wave function. Its value depends on the behavior of the electronic wave functions at large distances, which is very poorly given even by the best available Hartree-Fock approximations. Similar problems were encountered in theoretical studies on electron mobility and triplet exciton band structure in molecular crystals in which the excess electron and the triplet exciton band structures are determined by intramolecular electron exchange or electron transfer matrix elements. The choice of $\nu \sim 1 \text{ cm}^{-1}$ is reasonable as much lower values suggested by the Hartree-Fock calculations for Fe^{2+} will result in an un-

physically low value for the electron transfer probability. Under these circumstances condition III.22 will be satisfied and outer-sphere electron transfer reactions will be always nonadiabatic and exceedingly slow. Adiabatic electron transfer processes as advocated by Marcus require that $V_{av,bw} > k_B T$ so that interference effects are crucial.

Nonadiabatic processes will occur when interference effects are negligible. The usual semiclassical description of a nonadiabatic transition is provided by implying that the splitting of the zero-order potential surfaces at the intersection point is "small." Levich and Dogonadze^{6,19} have provided a complete semiclassical criterion for the applicability of the nonadiabatic limit. To the best of our knowledge a complete quantum mechanical formulation of the adiabatic case has not yet been provided. In this context, Mies and Krauss³⁰ have provided a simplified model (equal resonance spacings and widths) which exhibits the transition from the adiabatic to the nonadiabatic case. This formalism is not applicable for the present problem as the resonance widths cannot be taken as constant, but rapidly increasing toward the intersection of the potential surfaces. Our nonadiabatic theory incorporating quantum effects of the first coordination layer results in a transmission coefficient of $\kappa \sim 10^{-4}$, when the temperature coefficient of the dielectric constant is neglected.²³ Similarly by the same calculations many other outer-sphere electron transfer reactions would exhibit transmission coefficients of 10^{-3} to 10^{-4} and we would have to concur with Levich⁶ that these processes correspond to nonadiabatic reactions. This nonadiabatic pattern in ionic solution is similar to many nonradiative processes in solids such as thermal ionizations and thermal electron capture which are adequately described in terms of second-order perturbation theory and where comparison with experiment provides a legitimate basis for the validity of the nonadiabatic limit. The relevant parameters for thermal electron transfer in solution and for thermal electron capture or ionization in solids are quite similar, so we believe that nonadiabatic outer-sphere electron transfer processes in polar solvents are encountered in real life.

Acknowledgments. This work was begun by one of us (N. R. K.) while on sabbatical leave at Tel-Aviv University. We are grateful for the hospitality provided to us in Tel-Aviv. He also thanks the Graduate Council of Louisiana State University for a Summer Faculty Fellowship during which time the work was completed. We also are grateful for the significant comments made by Mr. S. Efrima and Professor M. Bixon of the University of Tel-Aviv Chemistry Department and critical comments by Professors N. Sutin, R. R. Dogonadze, and P. Schmidt. While this paper may not be in complete accord with their desires, their input has helped shape its final form.

Appendix, A. Quantum Mechanical Manipulation

In this appendix we provide the details of the quantum mechanical treatment of the wave function of the Hamiltonian (II.1) Let us first rewrite the Hamiltonian (I.2) in two alternative forms

$$\begin{aligned} \mathcal{H} &= H_{ea} + V_{eb} + T_n \\ &= H_{eb} + V_{ea} + T_n \end{aligned} \quad (\text{A.1})$$

where

$$\begin{aligned} H_{ea} &= T_e + V_{ea} + H_a + H_b + V_{ab} + \\ &\quad H_s + H_c + V_{int}^s + V_{int}^c \\ H_{eb} &= T_e + V_{eb} + H_a + H_b + V_{ab} + \\ &\quad H_s + H_c + V_{int}^s + V_{int}^c \end{aligned} \quad (\text{A.1a})$$

Following the conventional treatment applied for the separation of electronic and nuclear motion one can define two sets of electronic wave functions at fixed nuclear configurations.

$$\begin{aligned} H_{ea}\Psi_{ai}(\mathbf{r}, \mathbf{Q}) &= \epsilon_{ai}(\mathbf{Q})\Psi_{ai}(\mathbf{r}, \mathbf{Q}) \\ H_{eb}\Psi_{bj}(\mathbf{r}, \mathbf{Q}) &= \epsilon_{bj}(\mathbf{Q})\Psi_{bj}(\mathbf{r}, \mathbf{Q}) \end{aligned} \quad (\text{A.2})$$

where \mathbf{r} and \mathbf{Q} refer to all the electronic coordinates and to all the nuclear coordinates of the system, respectively. The complete orthonormal set $\{\Psi_{ai}\}$ represent all the electronic states of the total system with the excess electron localized on center A [i.e., the ground and excited states of the pair $(A^{N+} + B^{M+})$]. Each of these electronic states is characterized by the nuclear potential energy surface $\epsilon_{ai}(\mathbf{Q})$. Similarly the set $\{\Psi_{bj}\}$ characterized by the nuclear potential surfaces $\epsilon_{bj}(\mathbf{Q})$ describes the ground and the excited electronic states of the pair $(A^{(N+)+} + B^{(M-)+})$. From the mathematical point of view either of these two basis sets is adequate for the expansion of the total time-dependent wave function $\bar{\Psi}(\mathbf{r}, \mathbf{Q}, t)$ of the system

$$\bar{\Psi}(\mathbf{r}, \mathbf{Q}, t) = 2 \sum_i \chi_{ei}(\mathbf{Q}, t) \Psi_{ai} = 2 \sum_j \chi_{bj}(\mathbf{Q}, t) \Psi_{bj} \quad (\text{A.3})$$

where $2\chi_{ai}$ and $2\chi_{bj}$ are expansion coefficients. However, such an expansion is inadequate from the practical point of view as a large number of basis functions of type ai (including continuum states) will be required to describe the system with the extra electron on center b. One should follow chemical intuition by setting

$$\bar{\Psi}(\mathbf{r}, \mathbf{Q}, t) = \sum_{\alpha} \chi_{\alpha}(\mathbf{Q}, t) \Psi_{\alpha} \quad (\text{A.4})$$

where the index α spans both ai and bj . The time-dependent Schrödinger equation for the total system yields a coupled set of equations for the expansion coefficients χ_{α}

$$\begin{aligned} \sum_{\alpha} S\beta_{\alpha} \left[T_N + \epsilon_{\alpha}(\mathbf{Q}) - i\hbar \frac{\partial}{\partial t} \right] \chi_{\alpha}(\mathbf{Q}, t) = \\ - \sum_{\alpha} \langle \Psi_{\beta} | U_{e\alpha} | \Psi_{\alpha} \rangle \chi_{\alpha}(\mathbf{Q}, t) \sum_{\alpha} \langle \Psi_{\beta} | L | \Psi_{\alpha} \rangle \chi_{\alpha}(\mathbf{Q}, t) \end{aligned} \quad (\text{A.5})$$

where $\langle \rangle$ refers to integration over electronic coordinates. L is the Born-Oppenheimer breakdown operator

$$L\Psi_{\alpha} = 2 \frac{\partial \Psi_{\alpha}}{\partial \mathbf{Q}} \frac{\partial}{\partial \mathbf{Q}} + \frac{\partial^2 \Psi_{\alpha}}{\partial \mathbf{Q}^2} \quad (\text{A.6})$$

The electrostatic interaction is defined by

$$U_{e\alpha} = U_{eb} \text{ for } \alpha \in ai; U_{ea} \text{ for } \alpha \in bj \quad (\text{A.7})$$

δ is the electronic overlap matrix

$$\begin{aligned} \delta_{\alpha\beta} &= \langle \Psi_{\alpha} | \Psi_{\beta} \rangle = \\ &\begin{cases} \delta_{\alpha\beta}; & \alpha, \beta \in ai \text{ or } \alpha, \beta \in bj \\ S_{\alpha\beta}; & \alpha \in ai, \beta \in bj \text{ or } \alpha \in bj, \beta \in ai \end{cases} \end{aligned} \quad (\text{A.8})$$

Defining the inverse S^{-1} of the overlap matrix

$$\sum_{\alpha} S_{\gamma\alpha}^{-1} S_{\alpha\beta} = S_{\gamma\beta} \quad (\text{A.9})$$

eq A.7 can be recast in the form

$$\left[T_N + \epsilon_\gamma^{(\mathbf{Q})} - i\hbar \frac{\partial}{\partial t} \right] \chi_\gamma = - \sum_\alpha \sum_\beta S_{\gamma\beta}^{-1} [\langle \Psi_\beta | U_{e\alpha} | \Psi_\alpha \rangle + \langle \Psi_\beta | L | \Psi_\alpha \rangle] \chi_\alpha \quad (\text{A.10})$$

Regrouping the diagonal matrix elements from the right-hand side of eq A.10 we get

$$\left[T_N + \epsilon_\gamma^{(\mathbf{Q})} + \langle \Psi_\gamma | U_{e\gamma} | \Psi_\gamma \rangle + \sum_\beta S_{\gamma\beta}^{-1} \langle \Psi_\beta | U_{e\beta} + L | \Psi_\gamma \rangle - i\hbar \frac{\partial}{\partial t} \right] \chi_\gamma = - \left[\sum_{\alpha \neq \gamma} \langle \Psi_\gamma | U_{e\alpha} + L | \Psi_\alpha \rangle + \sum_{\alpha \neq \gamma} \sum_{\beta \neq \gamma} S_{\gamma\beta}^{-1} \langle \Psi_\beta | V_{e\alpha} + L | \Psi_\alpha \rangle \right] \chi_\alpha \quad (\text{A.11})$$

This coupled set of equations for the nuclear motion is general. For the sake of simplicity and relevance let us assume that Ψ_γ corresponds to one of the two ground state electronic wave functions $\Psi_{a0} \equiv \Psi_a$ or $\Psi_{b0} \equiv \Psi_b$. The first sum of the right-hand-side of eq 13 then involves direct coupling between the ground state γ with the ground electronic state on the other site and with excited electronic states on both sites. The second sum involves an overlap correction to the coupling between the lowest zero-order electronic states on the two sites and overlap exchange contributions of excited states. Restricting the treatment to a two electronic level system Ψ_a and Ψ_b , and neglecting the contribution of the nonadiabatic operator L eq A.11 now reduces to the following pair of equations

$$\left[T_N + \epsilon_a(\mathbf{Q}) + \langle \Psi_a | U_{eb} | \Psi_a \rangle + S_{ab}^{-1} \langle \Psi_b | V_{eb} | \Psi_a \rangle - i\hbar \frac{\partial}{\partial t} \right] \chi_a = [\langle \Psi_a | U_{eb} | \Psi_b \rangle + S_{ab}^{-1} \langle \Psi_b | U_{eb} | \Psi_b \rangle] \chi_b \quad (\text{A.12a})$$

[same as (A.12a) with b in place of a and vice versa] $\chi_b =$ [same as (A.12a) with b in place of a and vice versa] χ_a (A.12b)

Following conventional procedures and neglecting the terms on the right-hand side eq A.12 one obtains the eigenvalue equations for the (zero order) vibrational wave functions $\chi_{av}^{0(\mathbf{Q})}$ and $\chi_{bv}^{0(\mathbf{Q})}$ of the two electronic states

$$\left[T_N + \epsilon_a(\mathbf{Q}) + \langle \Psi_a | U_{eb} | \Psi_a \rangle + S_{ab}^{-1} \langle \Psi_b | U_{eb} | \Psi_a \rangle - E_{av}^0 \right] \chi_{av}^0 = 0$$

[same as above with b in place of a and a in place of b] $\chi_{bv}^0 = 0$ (A.13)

The energies E_{av}^0 and E_{bv}^0 represent the zero-order vibronic states $\Psi_a \chi_{av}^0$ and $\Psi_b \chi_{bv}^0$ corresponding to the ground electronic states of the systems ($A^{N+} + B^{M+}$) and ($A^{(N+1)+} + B^{(M-1)+}$), respectively. Again, each of the sets $\{\chi_{av}^0\}$ and $\{\chi_{bv}^0\}$ completely spans the nuclear space.

The general nuclear functions $\chi_a(\mathbf{Q})$ and $\chi_{bv}(\mathbf{Q})$ can be expanded in the complete zero-order basis sets

$$\chi_a(\mathbf{Q}, t) = \sum_v C_{av}(t) \chi_{av}^0(\mathbf{Q}) \exp\left[-\frac{i}{\hbar} E_{av}^0 t\right]$$

$$\chi_b(\mathbf{Q}, t) = \sum_w C_{bw}(t) \chi_{bw}^0(\mathbf{Q}) \exp\left[-\frac{i}{\hbar} E_{bw}^0 t\right] \quad (\text{A.14})$$

Utilizing eq A.14 we are immediately led to the equations of motion for the expansion coefficients

$$i\hbar \frac{\partial C_{av}}{\partial t} = - \sum_w C_{bw}(t) V_{av,bw} \exp\left[-\frac{i}{\hbar} (\epsilon_{bw}^0 - \epsilon_{av}^0) t\right] \quad (\text{A.15})$$

$$i\hbar \frac{\partial C_{bw}}{\partial t} = - \sum_v C_{av} V_{bw,av} \exp\left[-\frac{i}{\hbar} (E_{av}^0 - E_{bw}^0) t\right]$$

resulting in the conventional expressions for the transition probability in second order.

Appendix B. Origin Displacements for the Polar Medium by Model Polaron Theory

The nuclear Hamiltonians for the initial and final states

$$\mathcal{H}^a = T_N^c + T_N^s + f_a(Q_A, Q_B) + g_a(Q_{\mathcal{X}}) \quad (\text{B.1})$$

$$\mathcal{H}^b = T_N^c + T_N^s + f_b(Q_A, Q_B) + g_b(Q_{\mathcal{X}})$$

which will be separated into the contributions of the first coordination lever and the medium outside it

$$\mathcal{H}^{a,b} = H_c^{a,b} + H_s^{a,b} \quad (\text{B.2})$$

where the continuum Hamiltonian is

$$H_s^i = T_N^s + g_i(Q_{\mathcal{X}}) \quad i \equiv a, b \quad (\text{B.3})$$

The Hamiltonian (B.3) can be handled by using the formal results of polaron theory as suggested by Levich. We shall apply the formalism of Frohlich and Allcock for the strongly coupled polaron to drive the reduced displacements Δ_{κ} and show how our result reduces to that of Levich. The physical situation is essentially as follows: in the initial state of the continuum at \mathbf{x} is polarized by a charge distribution ($\mathbf{x} - \mathbf{x}_0$), where \mathbf{x}_0 is an arbitrary origin, while in the final state b the charge distribution is $\rho^b(\mathbf{x} - \mathbf{x}_0)$. The polar modes can be represented in terms of the Fourier components of the polarization field, the coordinate and conjugate momentum of the V component being q_v and P_{ea} , respectively. The formulation of the Hamiltonian is equivalent to the Hartree approach for the strongly coupled polaron except that the charge distributions $\rho^i(\mathbf{x} - \mathbf{x}_0)$ ($i = a, b$) are static. The strongly coupled polaron Hamiltonian is

$$H_s^i = \sum_v (p_v^2 + q_v^2) + \sum_v [i(\alpha_v^{i*} - \alpha_v^i) p_v - (\alpha_v^{i*} + \alpha_v^i) q_v] \quad (\text{B.4})$$

where the linear coupling coefficients are

$$\alpha_v^i = \left(\frac{4\pi\delta_p}{S} \right)^{1/2} (1/v) \int d^3x \exp(i\mathbf{v} \cdot \mathbf{x}) \rho(\mathbf{x} - \mathbf{x}_0) \quad (\text{B.5})$$

here the polaron coupling constant is

$$\delta_p = \frac{e^2}{C\hbar} \left(\frac{m}{2\hbar\omega_0} \right) \quad (\text{B.6})$$

while S is the reduced volume, Ω

$$S = (2m\omega_0/\hbar)^{3/2} \Omega \quad (\text{B.7})$$

and the polaron coupling term is

$$C = (D_0^{-1} - D_s^{-1}) \quad (\text{B.8})$$

As $\alpha_v^* = \alpha_{-v}$ and $\alpha_{-v}^* = \alpha_v$ one can define new field coordinates for $v > 0$

$$\begin{aligned}q_{1v} &= (1/\sqrt{2})(q_v + q_{-v}) \\ q_{2v} &= (1/\sqrt{2})(p_v - p_{-v}) \\ p_{1v} &= (1/\sqrt{2})(p_v + p_{-v}) \\ p_{2v} &= (1/\sqrt{2})(q_v - q_{-v})\end{aligned}\quad (\text{B. 9})$$

The Hamiltonian (A.4) takes the form

$$H_s^i = \sum_v (q_{1v}^2 + q_{2v}^2 + p_{1v}^2 - p_{2v}^2) - \sum_{v>0} [\sqrt{2}(\alpha_v^i + \alpha_{-v}^i)q_{1v} + \sqrt{2}(\alpha_v^i - \alpha_{-v}^i)q_{2v}] \quad (\text{B. 10})$$

Comparing (A.8) with a general harmonic Hamiltonian we notice that the displacements of the origins of the normal polar modes induced by the static charge distribution ρ^i (relative to the unperturbed medium) are

$$\begin{aligned}\Delta_{1v}^i &= (1/\sqrt{2})(\alpha_{-v}^i + \alpha_v^i) \\ \Delta_{2v}^i &= (1/\sqrt{2})(\alpha_v^i - \alpha_{-v}^i)\end{aligned}\quad (\text{B. 11})$$

which from eq A.5 are

$$\Delta_{1v}^i = \left(\frac{4\pi\delta\rho}{S}\right)^{1/2} \frac{1}{V} \int d^3\mathbf{x} \cos(\mathbf{v} \cdot \mathbf{x}) \rho^i(\mathbf{x} - \mathbf{x}_0) \quad (\text{B. 12})$$

$$\Delta_{2v}^i = \left(\frac{4\pi\delta\rho}{S}\right)^{1/2} \frac{1}{V} \int d^3\mathbf{x} \sin(\mathbf{v} \cdot \mathbf{x}) \rho^i(\mathbf{x} - \mathbf{x}_0)$$

both of these displacements are real.

The relative displacements between the two states a and b $\Delta_{3c} = \Delta^a - \Delta^b$ are from (B.11)

$$\Delta_{3c} = \Delta_{1v}^a - \Delta_{1v}^b \quad (\text{B. 13})$$

$$\Delta_{1v} = \Delta_{1v}^a - \Delta_{1v}^b \quad (\text{B. 14})$$

$$\Delta_{2v} = \Delta_{2v}^a - \Delta_{2v}^b$$

The relevant energy parameter E_M^S (eq II.8) is now

$$E_M^S = \frac{1}{2} \hbar w_0 \sum_v [(\Delta_{1v}^a - \Delta_{1v}^b)^2 + (\Delta_{2v}^a - \Delta_{2v}^b)^2] \quad (\text{B. 15})$$

Utilizing eq A.10 we get

$$E_M^S = \frac{\hbar w_0}{2} \left(\frac{4\pi\delta\rho}{S}\right) \left\{ \sum_v \frac{1}{v^2} \int d^3\mathbf{x} \cos(\mathbf{v} \cdot \mathbf{x}) [\rho^a(x - x_0) - \rho^b(x - x_0)]^2 + \sum_v \frac{1}{v^2} \int d^3\mathbf{x} \sin(\mathbf{v} \cdot \mathbf{x}) [\rho^a(x - x_0)\rho^b(\mathbf{x} - \mathbf{x}_0)]^2 \right\}$$

Performing the relevant integrations in (A.14) and using

$$\frac{1}{S} \Sigma = \frac{1}{(2\pi)^3} \int d^3\mathbf{x}$$

we get

$$\begin{aligned}E_M^S &= \frac{C e^2}{2} \iint d^3x d^3x' \{ [\rho^a(x - x_0) + \rho^b(x - x_0)] [\rho^a(x' - x_0) + \rho^b(x' - x_0)] / |x - x'| \} \\ &= \frac{C e^2}{2} \iint d^3x d^3x' \{ [\rho^a(x)\rho^a(x') + \rho^b(x)\rho^b(x') + 2\rho^a(x)\rho^b(x')] / |x - x'| \} \quad (\text{B. 16})\end{aligned}$$

This is our final result. Equation B.15 can be recast in terms of the displacement vectors \mathbf{D}^a and \mathbf{D}^b in the initial and final states. It is easy to show that

$$J = \iint d^3x d^3x' \frac{\rho^i(x - x_0)\rho^j(x' - x_0)}{|x - x'|} = \frac{1}{4\pi} \int \mathbf{D}^i \mathbf{D}^j d^3x \quad (\text{B. 17})$$

so that we get Levich's result

$$E_M^S = \frac{C e^2}{8\pi} \int (\mathbf{D}^a - \mathbf{D}^b)^2 d^3\mathbf{x}$$

We have exposed the derivation of the E_M^S term in considerable detail to demonstrate that the application of polaron theory to the present problem does not involve the conventional picture of one loosely bound electron (*i.e.*, the transferred electron) with the polar liquid, but rather the energy changes accompanying the response of the medium to the different static charge distributions in the initial and in the final states. Our final expression is, of course, equivalent to the results of many other researchers.

References and Notes

- (1) For a general review see W. L. Reynolds and R. W. Lumry, "Mechanisms of Electron Transfer," Ronald Press, New York, N. Y., 1966.
- (2) R. A. Marcus, *Annu. Rev. Phys. Chem.*, **15**, 155 (1964).
- (3) H. Halperin, *Quart. Rev., Chem. Soc.*, **15**, 207 (1972).
- (4) R. A. Marcus, *J. Chem. Phys.*, **24**, 966 (1956); **41**, 2624 (1964); **43**, 679 (1965); *J. Phys. Chem.*, **67**, 2889 (1963); *Discuss. Faraday Soc.*, **29**, 21 (1960); *Can. J. Chem.*, **37**, 55 (1959); *Trans. N. Y. Acad. Sci.*, **19**, 423 (1957).
- (5) (a) R. Kubo and Y. Toyozawa, *Progr. Theor. Phys. (Osaka)* **13**, 161 (1955); (b) M. Lax, *J. Chem. Phys.*, **20**, 1752 (1952); (c) R. C. O'Rourke, *Phys. Rev.*, **91**, 265 (1953); (d) K. Huang and A. Rhyss, *Proc. Phys. Soc., Ser. A*, **204**, 413 (1951).
- (6) For a review, see V. G. Levich, *Advan. Electrochem. Electrochem. Eng.*, **4**, 249 (1966).
- (7) For recent work, see R. R. Dogonadze and A. A. Kornyshev, *Phys. Status Solidi*, **53**, 439 (1972); R. R. Dogonadze, A. M. Kuznetsov, and M. A. Vorotyntsev, *ibid.*, **54**, 125 (1972).
- (8) Recently this restriction has been partially relaxed by the work of M. A. Vorotyntsev and A. M. Kuznetsov, *Vestn. Moskov. Univ., Ser. Phys.*, **2**, 146 (1970), in which the inner degrees of freedom of the ion are considered. Further elaborations and improvements of the "metallic spheres" idea are presented by W. R. Fawcett and Yu. I. Kharkats, *Electroanal. Interfacial Electrochem.*, **47**, 413 (1973).
- (9) See, for example, M. A. Vorotyntsev, R. R. Dogonadze, and A. M. Kuznetsov, *Dokl. Akad. Nauk SSSR*, **195**, 1135 (1970); R. R. Dogonadze and A. A. Kornyshev, *Phys. Status Solidi 1b*, **53**, 439 (1972); R. R. Dogonadze, A. M. Kuznetsov, and A. A. Chernenka, *Sov. Phys. Solid State*, **9**, 1578 (1967); R. R. Dogonadze, *Ber. Bunsenges. Phys. Chem.*, **75**, 628 (1971).
- (10) R. R. Dogonadze and A. A. Kornyshev, "Physicheskaya Khimiya Kinetika," Moscow, 1973. We are grateful to Professor Dogonadze for supplying us with this important reference.
- (11) P. P. Schmidt, *J. Chem. Soc., Faraday Trans. 2*, **68**, 7441 (1972).
- (12) R. R. Dogonadze, J. Ulstrup and Yu. I. Kharkats, *J. Chem. Soc., Faraday Trans. 2*, **68**, 744 (1972). This article is primarily based on inner-sphere electron transfer reactions.
- (13) P. P. Schmidt, *Aust. J. Chem.*, **23**, 1287 (1970).
- (14) W. Schmickler and W. Vielstich, *Electrochim. Acta*, **18**, 883 (1973).
- (15) Holstein, *Ann. Phys. N. Y.*, **8**, 325, 343 (1959).
- (16) D. L. Dexter, *J. Chem. Phys.*, **21**, 836 (1953).
- (17) (a) R. Engman and J. Jortner, *Mol. Phys.*, **18**, 145 (1970); (b) K. F. Freed and J. Jortner, *J. Chem. Phys.*, **52**, 6272 (1970).
- (18) R. R. Dogonadze, A. M. Kuznetsov, and V. G. Levich, *Electrochim. Acta*, **13**, 1025 (1968).
- (19) See, for example, V. G. Levich in "Physical Chemistry: An Advanced Treatise," Vol. 9B, H. Eyring, D. Henderson, and W. Jost, Ed., Academic Press, New York, N. Y., 1973, p 986.
- (20) M. Abramowitz and I. A. Stegun, "Handbook of Mathematical Functions," National Bureau of Standards, Washington, D. C., 1964. Chapter 9.
- (21) J. Slater, "Quantum Theory of Atomic Structure," McGraw-Hill, New York, N. Y., 1960, p 384.
- (22) J. Katz, S. I. Choi, S. A. Rice, and J. Jortner, *J. Chem. Phys.*, **39**, 1683 (1963).
- (23) The neglect of $(\partial D_{0i}/\partial T)$ may be a serious assumption but since we do

- not know the best D_{eff} to use, we know even less about its temperature derivative. We are grateful to Professor N. Sutin for pointing this out to us.
- (24) H. C. Stynes and J. A. Ibers, *Inorg. Chem.*, **10**, 2304 (1971).
 (25) R. E. Kester, *Coord. Chem. Rev.*, **2**, 319 (1967).
 (26) M. D. Glick, J. M. Kuszaj, and J. F. Endicott, *J. Amer. Chem. Soc.*, **95**, 5097 (1973).
 (27) J. O'M. Bockris and R. K. Sen, *Nature (London)*, 143 (1972). For other criticisms of the Bockris note see P. P. Schmidt and J. Ulstrup, *Nature (London), Phys. Sci.*, **245**, 126 (1973).
 (28) (a) P. P. Schmidt, *J. Chem. Phys.*, **56**, 2775 (1972); (b) *ibid.*, **57**, 3749 (1972); (c) *ibid.*, **77**, 488 (1972).
 (29) In private communication he has agreed to most of these objections of his early work. (P. Schmidt, private communication and paper in preparation.) His more recent work is not dependent on the first paper.
 (30) F. H. Mies and M. Krauss, *J. Chem. Phys.*, **45**, 4455 (1966).

Unimolecular Reactions and Energy Partitioning. Three- and Four-Centered Elimination Reactions of Chemically Activated 1,1,2-Trichloroethane- d_0 , - d_1 , and - d_2

K. C. Kim and D. W. Setser

Department of Chemistry, Kansas State University, Manhattan, Kansas 66506 (Received March 11, 1974)

The unimolecular three- and four-centered hydrogen chloride elimination reactions of chemically activated 1,1,2-trichloroethane- $1-d$, formed by the combination of CH_2Cl and CDCl_2 radicals, have been studied. Two other isomers, 1,1,2-trichloroethane- d_0 and - $2,2-d_2$, also were studied to confirm reaction mechanisms and to establish intermolecular isotope effects. Partitioning of vibrational energy to the dichlorolefin was characterized by observing the cis-trans unimolecular isomerization rate of 1,2-dichloroethene. Approximately 81% of the total available energy was retained as internal energy of the olefin from the $\alpha\alpha$ process; both the average energy and the energy distribution are consistent with statistical partitioning of the excess energy. The results are less definitive for the $\beta\alpha$ elimination reaction, but substantially less of the available energy was released to the olefin. The energy release data are consistent with the different potential energy changes for the two channels. Fitting the magnitude of the various experimental rate constants to RRKM calculations using optimized four- and three-centered transition-state models gave E_0 values of 59, 57, and 60 kcal mol $^{-1}$ for the $\beta\alpha$, $\alpha\beta$, and $\alpha\alpha$ processes, respectively, of the d_0 isomer. In addition to trichloroethane, chemically activated 1,2-dichloroethane and 1,1,2,2-tetrachloroethane also were generated and the half-quenching pressures were as follows: 1,1,2-trichloroethane- d_0 , - d_1 , and - d_2 , 17, 11, and 8.0 Torr, respectively; 1,2-dichloroethane, 18 Torr; 1,1,2,2-tetrachloroethane, 10 Torr.

Introduction

The four-centered HX elimination reactions of halogenated alkanes are well characterized with respect to thermal and chemically activated unimolecular rate constants.¹ Generalized models²⁻⁴ of the transition state match the experimental rate data including inter- and intramolecular isotope effects. Three-centered ($\alpha\alpha$) elimination (followed by rapid rearrangement of the carbene to an olefin) competes with four-centered ($\beta\alpha$) elimination if two halogens are located on the same carbon.⁵⁻⁷ We previously used the intramolecular competition between HF and DF elimination from CD_3CHF_2 to characterize the transition state model for $\alpha\alpha$ elimination.⁶ In the current work the elimination reactions of chemically activated 1,1,2-trichloroethane- d_0 , - $1-d$, and - $2,2-d_2$ are reported. An advantage of the 1,1,2-trichloroethane system is that the energy released to the dichloro olefins can be deduced from the cis-trans isomerization rates, if the elimination reactions give nonequilibrium cis:trans ratios of 1,2-dichloroethene.

The energy release pattern for a unimolecular reaction depends upon the excess energy, $\langle E \rangle - E_0$, and the characteristics of the potential energy surface on the product side of the barrier. Since RRKM theory appears to be ade-

quate for describing the rate constants for HX elimination,^{1-4,6-8} we will assume, subject to testing, that the energy distribution of the microcanonical ensemble of systems attaining the transition-state configuration is statistical. In contrast to this statistical distribution of the excess energy, the potential energy (*i.e.*, the threshold energy for the reverse reaction) will be released according to the characteristics of the potential surface and associated dynamics of motion in a manner analogous to direct bimolecular exchange reactions.⁹ Thus energy partitioning data supplement conventional rate data for unimolecular reactions and give some information about the potential surface on the product side of the barrier. The potential energy changes associated with the $\alpha\alpha$ and $\beta\alpha$ elimination reactions differ. The four-centered process releases ~ 30 kcal mol $^{-1}$ of excess energy plus ~ 50 kcal mol $^{-1}$ of potential energy after crossing the barrier configuration. The three-centered process releases about the same excess energy since the threshold energies, E_0 , are similar, but virtually no potential energy is released in passing from the HCl elimination barrier to the carbene (*i.e.* the activation energy for addition of $:\text{CClCH}_2\text{Cl}$ to HCl is not known, but must be small). However, a large intramolecular energy release accompanies the rearrangement of the carbene to the dichloroethene. Since

the excess energy is expected to be statistically (or nearly statistically) distributed to products for both channels and since all of the rearrangement energy is released to the olefin by the $\alpha\alpha$ channel, the internal energy of dichloroethene should be higher for the $\alpha\alpha$ channel than for the $\beta\alpha$ channel. Our conclusions, combined with HX infrared chemiluminescence¹⁰ data, and kinetic energy measurements of HX elimination from halogenated alkane ions¹¹ provide a fairly complete picture of energy disposal in HX elimination reactions.

The present investigation utilized Cl and H abstraction reactions by methylene from chloroform to generate methyl, monochloromethyl, dichloromethyl, and trichloromethyl radicals, which form a chemical activation system for 1,2-dichloroethane, 1,1,2-trichloroethane, 1,1,2,2-tetrachloroethane, 1,1,1-trichloroethane, and 1,1-dichloroethane with ~ 90 kcal mol⁻¹ of energy. Only the first three molecules were investigated thoroughly, although some qualitative information was obtained for the last two molecules. The rate constant data for 1,2-dichloroethane are in agreement with previously determined results^{2,12} and will not be emphasized. The present data for 1,1,2-trichloroethane and 1,1-dichloroethane are in general agreement with an earlier report¹³ from this laboratory; however, some of the detailed interpretations differ since the importance of the three-centered channel was not then recognized.

The overall scope of the present work thus includes (1) investigation of methylene reactions with chloroform, (2) determination of the rate constants for the unimolecular decomposition of the chemically activated 1,1,2-trichloroethane and 1,1,2,2-tetrachloroethane, (3) characterization of the competing $\alpha\alpha$, $\beta\alpha$, and $\alpha\beta$ elimination reactions of 1,1,2-trichloroethane, (4) measurement of the product energy partitioning through study of the *cis*-*trans* isomerization of 1,2-dichloroethylene, and (5) explanation of inter- and intramolecular isotope effects.

Experimental Section

The experiments consist of photolyzing mixtures of ketene and chloroform at room temperature followed by gas chromatographic product analysis. In many instances the components separated by gas chromatography were trapped from the He effluent and further analyzed by mass spectrometry. The reactants were kept in nearly constant proportions ($\text{CH}_2\text{CO}:\text{CHCl}_3 = 2:3$, $\text{CH}_2\text{CO}:\text{CDCl}_3 = 2:3$, and $\text{CD}_2\text{CO}:\text{CHCl}_3 = 1:3$). The large fraction of ketene was needed to obtain sufficient yields for mass spectral analysis of individual product components. The products from reaction of methylene with ketene did not interfere with study of the chemically activated molecules. In all cases about 2 cm³ of the gas mixture was measured and placed in Pyrex vessels ranging from 15 to 10,000 cm³ in size. Photolysis was done at room temperature with the unfiltered light of a GE AH-6 high-pressure mercury lamp which provides an effective wavelength in Pyrex vessels of 3200 ± 200 Å for dissociating ketene. Samples were photolyzed for 1–3 hr depending on the size of the vessel. Photolysis of chloroform in the absence of ketene yielded no products. The vapor pressure of chloroform provided an upper limit, ≤ 200 Torr, to the pressure.

Reagent grade chloroform, Malinckrodt Chemical Co., was purified by gas chromatography on the same column that was used for product analyses. Chloroform-*d*₁ was purchased from Stohler Isotope Chemicals Inc. Following gas chromatographic purification, the mass spectrum indi-

cated an isotopic purity of better than 99.5%. Ketene-*d*₂ was prepared by hot-wire pyrolysis of acetone-*d*₆. Ethylene, one of the major impurities, was partially removed by trap-to-trap distillation and finally eliminated by gas chromatography at 77°K on a 30-ft Fluoropak column. Ketene-*d*₀ was prepared by pyrolysis of acetic anhydride purified by trap to trap distillation. Analysis of the ketene-*d*₀ indicated that it was sufficiently pure so that further treatment was not necessary. Other reagent grade compounds, purchased from various sources, were used without purification for calibration of gas chromatographic retention times and mass spectral references.

The general method of analyzing the photolyzed sample was as follows. The condensable components of the photolyzed sample were recovered by pumping the products through a glass wool packed trap cooled to 77°K; these products were transferred into the inlet system and injected onto the gas chromatographic column. Some 11 components of interest were separated on a 7-ft Porapak T column (80–100 mesh). The gas chromatographic unit was a Perkin-Elmer Model 82C with a thermal conductivity detector. During the first 5 min, the column was operated isothermally at 60°, which was sufficient to elute the extreme light end of the photolyzed products. This was followed by programming for 10 min at 0.5° min⁻¹ and then 30 min at 1.0° min⁻¹. After *cis*-1,2-dichloroethylene was eluted, the programming rate was advanced to 2° min⁻¹ until the maximum preset temperature (175°) was reached. Most of the components were eluted within 2 hr, although 2.5 hr was required for elution of the last component, 1,1,2,2-tetrachloroethane. The order for elution was vinyl chloride, 1,1-dichloroethylene, *trans*-1,2-dichloroethylene, *cis*-1,2-dichloroethylene, chloroform, 1,2-dichloroethane, trichloroethylene, 1,1,2-trichloroethane, and 1,1,2,2-tetrachloroethane. Hydrocarbon products arising from the interaction of CH₂ with ketene were not studied. Quantitative calibrations (peak areas) were made from prepared mixtures containing the components of interest. The ratio of the thermal responses of other compounds to that of *trans*-1,2-dichloroethylene (chosen as the reference) was nearly unity if areas of the gc peaks were used.

For many of the experiments 1,1-, *trans*-1,2-, and *cis*-1,2-dichloroethylene were trapped from the effluent and analyzed for isotopic compositions by mass spectrometry. The cracking pattern of 1,1-, *trans*-1,2-, and *cis*-1,2-dichloroethylene-*d*₀ are almost identical; the only difference is the relative abundance of the ions, particularly the parent molecular ion, with respect to the most abundant (*m/e* 61) ion, CHCl-CH⁺. The molecular ion consists of three mass peaks, 96, 98, and 100, which are characteristic of two chlorine atoms with 32.7% naturally abundant ³⁷Cl. Monodeuterated analogs of the above compounds gave their molecular ion peaks at 97, 99, and 101; the dideuterated species gave *m/e* 98, 100, and 102. Thus for mixtures of *d*₀- and *d*₁- or *d*₁- and *d*₂-labeled compounds, the spectra do not overlap and relative peak heights can be directly correlated to the isotopic composition. The spectra were recorded on an EAI "Quad 250" mass spectrometer at 70-eV electron energy.

Results

Reaction Mechanisms for Formation of Activated Molecules. Singlet methylene abstracts Cl atoms and triplet methylene abstracts H atoms in reactions with chloromethanes.¹⁴ The radicals generated by H or Cl abstraction

TABLE I: Reaction Products from Methylene- d_0 with Chloroform- d_0 and - d_1 and Methylene- d_2 with Chloroform- d_0

Reaction systems				Radical combination products		
I	II	III	Reaction no.	I	II	III
$\text{CH}_2\text{CO} + \text{CDCl}_3$	$\text{CH}_2\text{CO} + \text{CHCl}_3$	$\text{CD}_2\text{CO} + \text{CHCl}_3$		I	II	III
CH_2Cl and CDCl_2^a	CH_2Cl and CHCl_2^a	CD_2Cl and CHCl_2^a	1 ^c	$\text{CH}_2\text{Cl}-\text{CDCl}_2$	$\text{CHCl}_2-\text{CH}_2\text{Cl}$	$\text{CHCl}_2-\text{CD}_2\text{Cl}$
			2 ^c	$\text{CH}_2\text{Cl}-\text{CH}_2\text{Cl}$	$\text{CH}_2\text{Cl}-\text{CH}_2\text{Cl}$	$\text{CD}_2\text{Cl}-\text{CD}_2\text{Cl}$
			3 ^c	$\text{CDCl}_2-\text{CDCl}_2$	$\text{CHCl}_2-\text{CHCl}_2$	$\text{CHCl}_2-\text{CHCl}_2$
			4 ^d	$\text{CH}_2\text{Cl}-\text{CCl}_3$	$\text{CH}_2\text{Cl}-\text{CCl}_3$	$\text{CD}_2\text{Cl}-\text{CCl}_3$
CH_2D and CCl_3^b	CH_3 and CCl_3^b	CD_2H and CCl_3^b	5 ^d	$\text{CH}_2\text{Cl}-\text{CH}_2\text{D}$	$\text{CH}_2\text{Cl}-\text{CH}_3$	$\text{CD}_2\text{Cl}-\text{CD}_2\text{H}$
			6 ^d	$\text{CDCl}_2-\text{CCl}_3$	$\text{CHCl}_2-\text{CCl}_3$	$\text{CHCl}_2-\text{CCl}_3$
			7 ^d	$\text{CDCl}_2-\text{CH}_2\text{D}$	$\text{CHCl}_2-\text{CH}_3$	$\text{CHCl}_2-\text{CD}_2\text{H}$
			8 ^c	$\text{CH}_2\text{D}-\text{CH}_2\text{D}$	CH_3-CH_3	$\text{CD}_2\text{H}-\text{CD}_2\text{H}$
			9 ^c	$\text{CCl}_3-\text{CCl}_3$	$\text{CCl}_3-\text{CCl}_3$	$\text{CCl}_3-\text{CCl}_3$
			10 ^c	$\text{CH}_2\text{D}-\text{CCl}_3$	CH_3-CCl_3	$\text{CD}_2\text{H}-\text{CCl}_3$

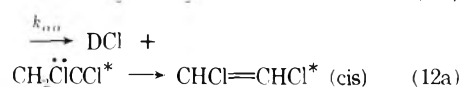
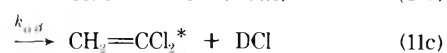
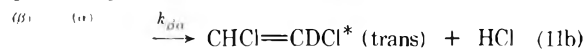
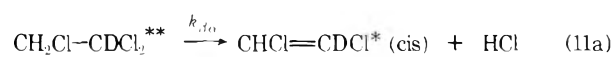
^a Abstraction products from reaction by singlet methylene. ^b Abstraction products from reaction by triplet methylene. ^c Radical combination products arising as a consequence of only singlet methylene reactions. ^d Radical combination products arising as a consequence of both singlet and triplet methylene reactions. ^e Since the concentration of singlet methylene exceeds that of triplet methylene, the yields of products which arise from combination of radicals derived only from triplet methylene are very low.

reactions of methylene- d_0 with chloroform- d_0 and - d_1 and methylene- d_2 with chloroform- d_0 and the resulting combination products are summarized in Table I. At high pressure, most of the compounds in Table I were found. However, products from reactions 1–3 were present in far greater quantity indicating that reaction of triplet CH_2 with chloroform is relatively unimportant, which is consistent with an estimate of ~70% singlet methylene under our conditions.^{14a} One complication is that some of the chemically activated molecules formed from reactions 4, 7, and 10 give the same decomposition products as those from steps 1–3. Although hydrogen abstraction reactions by CH_3 , CH_2Cl , CHCl_2 , etc. should be included to obtain total mass balance, products from these abstraction reactions were present in minor quantities relative to radical combination products. Although not explicitly studied, no evidence was found to support the previously suggested¹³ “disproportionation reactions” involving CHCl_2 . The previous gas chromatographic analysis scheme apparently was unsatisfactory and we retract the earlier suggestion.¹³

At pressures sufficiently high to quench the unimolecular elimination reactions, the product ratios in Table I should be constant and equal to the ratio of recombination rate constants. For the first three reactions the relationship $k_1 = \frac{1}{2}k_2 = \frac{1}{2}k_3$ would be expected. For the $\text{CH}_2\text{CO} + \text{CHCl}_3$ system, the ratio of 1,1,2-trichloroethane to 1,1,2,2-tetrachloroethane varied from 1.4 to 1.7. Accounting for the yield of 1,2-dichloroethane and its elimination product is complicated by the presence of 1,1-dichloroethane, which has a half-quenching pressure of $\sim 10^3$ Torr for formation of CH_2CHCl .¹³ If the vinyl chloride yield is ignored at the highest pressures (the half-quenching pressures of 1,2- $\text{C}_2\text{H}_4\text{Cl}_2$ is 18 Torr), the average ratios 1,2-dichloroethane:1,1,2-trichloroethane:1,1,2,2-tetrachloroethane are 1.0:1.5:1.1. These ratios thus support the general assignment of mechanism for formation of the activated molecules.

Unimolecular Rate Constants for $\text{CH}_2\text{ClCHCl}_2$, $\text{CH}_2\text{ClCDCl}_2$, and $\text{CD}_2\text{ClCHCl}_2$. The activated molecules have ~ 90 kcal mol^{-1} of energy and at reduced pressures unimolecular HCl elimination competes with collisional stabilization. The reactions will be defined for $\text{CH}_2\text{ClCDCl}_2$, which permits identification of all channels (see eq 11 and 12). The various channels will be labeled by specifying the site of the hydrogen atom by the first subscript of the rate constant. The carbon with two chlorines is

denoted by α . The three-centered elimination is followed



by rapid rearrangement of the carbene. The single asterisk is used to denote the possibility of retention of enough energy by the olefin for subsequent isomerization, hence, the use of the double asterisk on the trichloroethane. Collisional stabilization will be represented by the unit deactivation approximation



Although cascade deactivation with $\langle \Delta E \rangle = \sim 6 \pm 2$ kcal mol^{-1} probably is the better relaxation model,¹² minor corrections to the high-pressure rate constants for cascade effects can be made later. The product yield data are summarized in Figures 1 and 2 and Table II. Since gas chromatographic analysis separated *cis*- and *trans*-1,2-dichloroethene as well as 1,1-dichloroethene, mass spectrometric analysis of the dichloroethenes can give all channels of (11) and (12) for trichloroethane-1- d and trichloroethane-2,2- d_2 . Although both cases could have been examined in detail, efforts were focused on $\text{CH}_2\text{Cl}-\text{CDCl}_2$ and the results are presented in Table III.

Individual unimolecular rate constants are defined as $k_{ai} = k_M[M]D_i/S$ where i denotes the appropriate decomposition channel and S and D represent the concentrations of stabilized and decomposed products, respectively. $k_M[M]$, the collision frequency, is proportional to the pressure of the experiment and the rate constants are conveniently tabulated in pressure units and later converted to sec^{-1} . Decomposition plots giving 1,2-dichloroethylene are shown in Figure 1. Since there is no contribution to the decomposition product from any side reaction, the slopes in the high-pressure region ($D/S \lesssim 1.5$) give a reliable average high-pressure rate constant. Unfortunately the decomposition of 1,1,1-trichloroethane does contribute to the 1,1-di-

TABLE II: 1,1,2-Trichloroethane-1-d₁ and Dichloroethene Product Yields^a

Pressure, Torr	1,1-Dichloroethene	trans-1,2-Dichloroethene	cis-1,2-Dichloroethene	CH ₂ ClCDCl ₂	D/S	
					Total	CHClCHCl
0.2	5.4	12.5	15.4			
0.3	2.2	4.1	4.8			
0.7	6.1	7.0	8.4			
1.4	0.6	0.9	1.2			
1.8	0.9	2.3	3.1			
3.5	3.4	9.6	13.4	8.2	3.2	2.8
5.2	3.5	12.1	17.1	13.2	2.5	2.2
7.0	2.9	13.0	17.5	20.3	1.6	1.5
10.0	3.4	11.9	17.4	31.3	1.0	0.94
13.6	3.1	7.0	10.4	25.6	0.80	0.68
16.5	4.2	10.3	15.2	40.2	0.74	0.63
23.4	2.3	6.1	8.6	35.0	0.48	0.42
36.3	2.9	3.5	5.3	39.2	0.29	0.22
72.6	3.3	2.8	4.2	45.4	0.23	0.15
93.5	5.0	5.6	8.9	136.3	0.14	0.11
187.0	6.3	5.0	8.4	153.0	0.13	0.09

^a In units of 10⁻³ cm³ of gas at 25° and 1 atm pressure.

TABLE III: Analysis of 1,2-Dichloroethene from the CH₂Cl-CDCl₂ System

Pressure, Torr	Mass ratios ^a				[Cis]/[trans]			
	Trans (97/96)	Cis (97/96)	trans-Dichloroethene ^b		cis-Dichloroethene ^b		βα	
			C ₂ HDCl ₂	C ₂ H ₂ Cl ₂	C ₂ HDCl ₂	C ₂ H ₂ Cl ₂		αα
0.2	3.6	4.6	32.6	9.0	42.0	9.2	1.29	1.02
0.3	3.6	4.5	10.7	3.0	13.0	2.9	1.21	0.97
0.7	4.0	4.8	18.7	4.7	23.2	4.9	1.24	1.04
1.4	3.9	4.6	2.5	0.6	3.3	0.7	1.32	1.17
1.8	4.1	4.5	6.3	1.5	8.4	1.8	1.32	1.20
3.5	4.3	4.4	26.0	6.1	36.6	8.2	1.40	1.35
5.2	4.6	4.5	33.1	7.3	46.5	10.5	1.41	1.44
7.0	4.5	4.6	35.4	7.8	48.0	10.4	1.36	1.33
10.0	4.9	4.3	32.8	6.8	47.1	10.9	1.44	1.60
13.6	5.2	4.4	19.6	3.8	28.2	6.4	1.43	1.68
16.5	5.2	4.2	28.6	5.6	41.1	9.7	1.43	1.73
23.4	5.5	3.9	17.0	3.2	23.0	5.8	1.35	1.81
36.3	5.4	3.8	9.8	1.9	13.7	3.7	1.40	1.94
72.6	5.5	3.6	15.7	2.9	23.2	6.6	1.48	2.28
93.5	5.7	3.5	7.8	1.4	10.9	3.1	1.40	2.21
187.0	5.9	3.6	14.3	2.5	21.8	6.2	1.52	2.48

^a The mass spectral analyses give 97/96 = [cis-CHCl=CDCl]/[cis-CHCl=CHCl], 97/96 = [trans-CHCl=CDCl]/[trans-CHCl=CHCl]. ^b Yields in 10⁻³ cm³ of gas, obtained by combining the results of columns 2 and 3 with Table II.

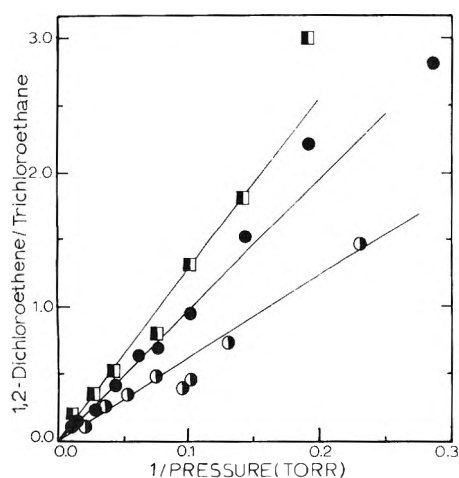


Figure 1. [cis- and trans-1,2-dichloroethene]/[1,1,2-trichloroethane] vs. reciprocal pressure for the d₀ (□), d₁ (●) and d₂ (○) systems. This plot includes only the αα and βα elimination channels. The slopes of the lines are the high pressure rate constants.

chloroethene product yield and a nonzero intercept was found for plots of 1,1-dichloroethene:1,1,2-trichloroethane vs. reciprocal pressure. The total decomposition product plots shown in Figure 2 have an insignificant (except for the CD₂Cl-CHCl₂ data) intercept and the total unimolecular rate constants were obtained from the slopes of this graph. Subtraction of the contribution from the 1,2-dichloroethene channels then gives $k_a(\alpha\beta)$. These ratios of $k_a(\alpha\beta)/[k_a(\alpha\alpha) + k_a(\beta\alpha)]$ were confirmed by point examination of the ratios of 1,1- and 1,2-dichloroethene product yields at low pressure. From the isotopic composition data of Table III, the ratio of the βα(C₂HDCl₂) to αα(C₂H₂Cl₂) channels was obtained and within experimental error the ratio was independent of pressure, as expected.⁶ Complete analysis for CD₂ClCHCl₂ was done for two experiments (3.3 and 9.6 Torr) and βα(C₂HDCl₂):αα(C₂D₂Cl₂) = 2.0. The reduced ratio is a consequence of the switch in the primary intramolecular isotope effect from the αα channel to the βα channel. The rate constants for the three isomers are summarized in Table IV. The $k_a(\alpha\beta)$ value for CD₂ClCHCl₂ is somewhat uncertain because of the exces-

TABLE IV: Experimental Rate Constants^a for 1,1,2-Trichloroethane-*d*₀, -*d*₁, and -*d*₂^c

Reaction channel	CH ₂ Cl-CHCl ₂		CH ₂ Cl-CDCl ₂		CD ₂ Cl-CHCl ₂	
	Torr	10 ⁸ sec ⁻¹	Torr	10 ⁸ sec ⁻¹	Torr	10 ⁸ sec ⁻¹
<i>k</i> _a (total)	17	2.1	11.4	1.39	8.0	0.95
<i>k</i> _a (αβ) (1,1-dichloroethene)	4.0	0.49	1.5	0.18	2.0 ^c	0.24
<i>k</i> _a (αα + βα) (1,2-dichloroethene)	13	1.6	9.9	1.2	6.0	0.71
<i>k</i> _a (αα)	(3.2) ^b	0.39	1.8	0.22	2.0 ^d	0.24
<i>k</i> _a (βα)	(9.8) ^b	1.2	8.1	0.99	4.0 ^d	0.48

^a The experimental rate constants in Torr units were converted to sec⁻¹ units using the collision diameters of 6.5 Å for trichloroethane, 4.5 Å for ketene, and 5.3 Å for CHCl₃. ^b Values in parentheses were estimated after allowing for isotope effects; see text. ^c Obtained from a weighted average of data in Figure 2 and the 1,1-dichloroethene to 1,2-dichloroethene yield ratio at low pressure. ^d Obtained from isotopic analysis of the 1,2-dichloroethylene products from two experiments. ^e The experimental rate constant for 1,1,2,2-tetrachloroethane was 10.5 Torr.

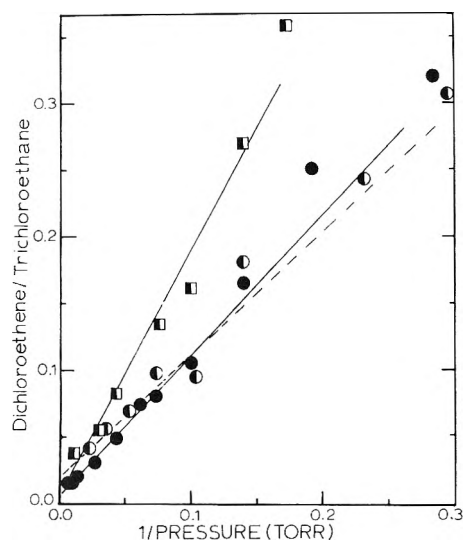


Figure 2. [1,1- and 1,2-dichloroethene]/[1,1,2-trichloroethane] vs. reciprocal pressure for the *d*₀ (□), *d*₁ (●), and *d*₂ (○) systems. This plot includes all elimination channels. The slopes of the lines give the high-pressure rate constants. The dotted line was used for trichloroethane-*d*₂ in order to call attention to the slightly higher intercept for this case. The data of this plot could be analyzed according to an equation similar to (I); however, within the experimental error of the data the resulting rate constants would be equal to just the slopes of the lines shown in this figure.

sive contribution to the 1,1-dichloroethene yield which seemed greater for this system than for the other two. The separation of the αα and βα channels for CH₂ClCHCl₂ was done by estimation of expected isotope effect; *vide infra*. As far as is known, the data for the CH₂Cl-CDCl₂ system are of high quality.

The variation with pressure of the overall cis:trans dichloroethane ratio, as well as that for the βα and αα channels, is a consequence of subsequent unimolecular reactions of the dichloroethene. The analysis of this isomerization is done in a later section.

Unimolecular Rate Constants for 1,1,2,2-Tetrachloroethane, 1,2-Dichloroethane, and 1,1-Dichloroethane: Tetrachloroethane was studied in the CH₂CO + CHCl₃ system; hence, the contributions from the αα and αβ channels to the total rate constant cannot be measured. The 1,1,1,2-tetrachloroethane molecule also is a product (see Table I) and, furthermore, its decomposition product is the same as from the symmetrical tetrachloroethane.



If the CH₂ClCCl₃ is formed in constant proportion, *R*, to CHCl₂-CHCl₂, the following expression describes the trichloroethene:1,1,2,2-tetrachloroethane ratio.

$$\frac{[\text{CHCl}=\text{CCl}_2]}{[\text{CHCl}_2-\text{CHCl}_2]} = \frac{k_a(14)}{P} + R \frac{k_a(15)}{P + k_a(15)} (1 + k_a(14)/P) \quad (I)$$

R is expected to be small because there is less H abstraction than Cl abstraction by methylene; therefore, the second term will be small. Since *k*_a(15) may be ~*k*_a(14), the intercept is not necessarily a measure of *R*. However, the data of Figure 3 show very little curvature which is evidence that *R* is small. If the second term in the above equation is neglected, a value of 10.5 Torr is obtained for *k*_a(14). This is about a factor of 2 lower than for 1,1,2-trichloroethane.

The decomposition of CH₂Cl-CH₂Cl can be studied in the CH₂CO + CDCl₃ and CH₂CO + CHCl₃ systems; however, CD₂Cl-CD₂Cl is obtained from CD₂CO + CHCl₃. Vinyl chloride and HCl (DCl) are the decomposition products. Although not a major product, 1,1-dichloroethane is formed and also decomposes to vinyl chloride. In the CH₂CO + CDCl₃ system, this contribution can be monitored because the CH₂D-CDCl₂ gives chloroethane-*d*₁ and -*d*₂ products, whereas, 1,2-C₂H₄Cl₂ gives only *d*₀ product. The rate constant for 1,1-dichloroethane previously¹³ was estimated as 1100 Torr. Thus, for the entire pressure region covered in this work, virtually complete decomposition would be expected. A single experiment at 23 Torr showed ~40% chloroethane-*d*₁ and -*d*₂, which supports both a lower yield and a larger rate constant for 1,1-dichloroethane-*d*₂ than for 1,2-dichloroethane-*d*₀, which is known to be 18 Torr.^{2,12} The ratios of [C₂H₃Cl]/[1,2-C₂H₄Cl₂] and [C₂D₃Cl]/[1,2-C₂D₄Cl₂] were measured and plotted vs. reciprocal pressure. Analysis of the data for the *d*₀ species, according to an equation similar to (16), gave *k*_a(1,2-C₂H₄Cl₂) = 18 Torr and *k*_a(1,1-C₂H₄Cl₂) > 350 Torr. The more limited data for 1,2-C₂D₄Cl₂ gave a kinetic isotope effect of ~3; these results for 1,2-dichloroethane-*d*₀ and -*d*₄ agree with more detailed studies.²

Isomerization of 1,2-Dichloroethene. In order to obtain cis-trans isomerization¹⁵ rate constants for the αα channel, Scheme I was employed for the data of Table III, which are displayed in Figure 4. Steady-state treatment for *trans*-CHCl=CHCl* (*t**) and *cis*-CHCl=CHCl* (*c**) gives

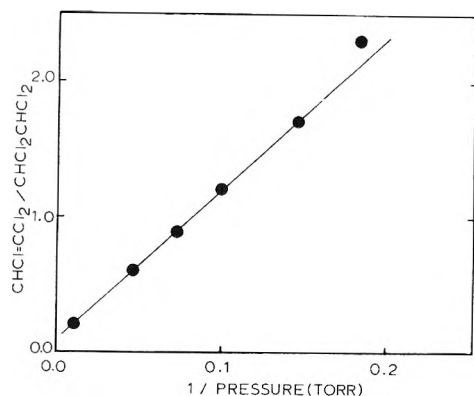


Figure 3. Decomposition-stabilization plot for 1,1,2,2-tetrachloroethane.

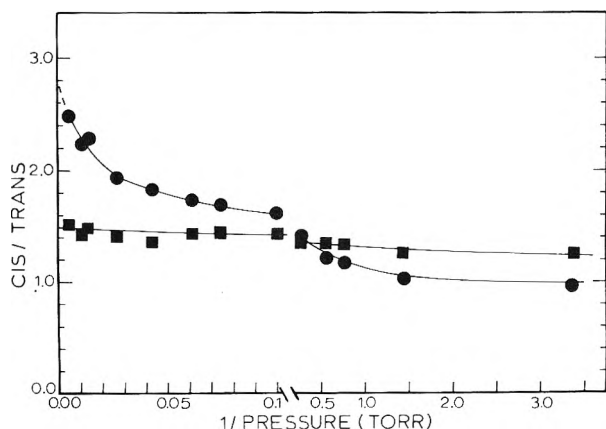


Figure 4. Plot of [cis-dichloroethene]/[trans-dichloroethene] vs. reciprocal pressure for $\text{CH}_2\text{Cl}-\text{CDCl}_2$: ●, $\alpha\alpha$ elimination ($\text{C}_2\text{H}_2\text{Cl}_2$); ■, $\beta\alpha$ elimination (C_2HDCl_2). An additional low-pressure point at $1/P = 5 \text{ Torr}^{-1}$ can be obtained from Table III.

$$[t^*] = \frac{[\text{CH}_2\text{ClCDCl}_2^{**}]\{(k_a(t))k_M[\text{M}] + (k_a(t))k_c + (k_a(c))k_c\}}{(k_M[\text{M}] + k_t)(k_M[\text{M}] + k_c) - k_c k_t} \quad (\text{II})$$

and

$$[c^*] = \frac{[\text{CH}_2\text{ClCDCl}_2^{**}]\{(k_a(c))k_M[\text{M}] + (k_a(c))k_c + (k_a(t))k_c\}}{(k_M[\text{M}] + k_t)(k_M[\text{M}] + k_c) - k_c k_t} \quad (\text{III})$$

The [cis]/[trans] ratio is related to the rate constants by

$$[\text{cis}] / [\text{trans}] = \frac{(k_a(c))k_M[\text{M}] + (k_a(c))k_t + (k_a(t))k_t}{(k_a(t))k_M[\text{M}] + (k_a(t))k_c + (k_a(c))k_c} \quad (\text{IV})$$

Since the ΔH_f° values of *cis*- and *trans*-dichloroethane¹⁶ favor *cis* by only $0.4 \text{ kcal mol}^{-1}$, the threshold¹⁵ energies (56 kcal mol^{-1}) for $\text{cis} \rightleftharpoons \text{trans}$ are nearly equal. The densities of states calculated from harmonic oscillator frequencies favor the *trans* isomer (a factor of ~ 1.5). The energy differences and the density ratio have opposite effects and for simplicity we set $k_c = k_t$. If the harmonic oscillator densities are reliable, the equilibrium ratio of $[c^*]/[t^*]$ may be less than unity. If so, this would indicate that a small fraction of the 1,2-dichloroethene molecules have less than 56

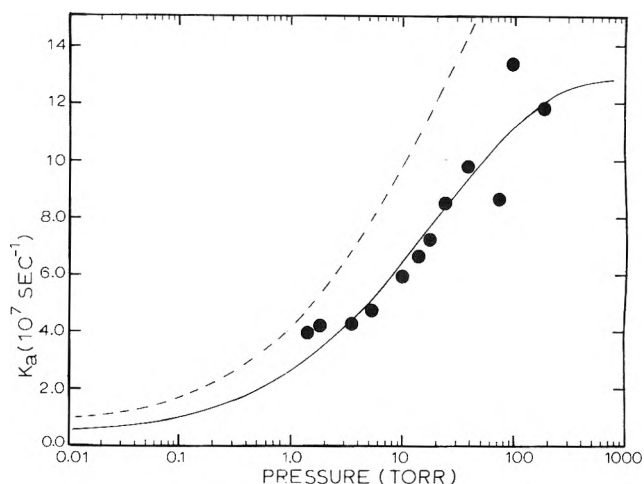
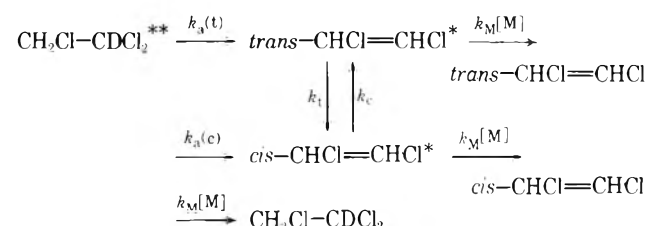


Figure 5. The experimental (●) and calculated *cis* \rightarrow *trans* isomerization rate constants for $\text{C}_2\text{H}_2\text{Cl}_2$ formed by $\alpha\alpha$ elimination from $\text{CH}_2\text{Cl}-\text{CDCl}_2$. The calculated results shown by --- are based on the rate constants and the statistical distribution ($\langle E \rangle = 66.7 \text{ kcal}$) shown in Figure 8. The calculated results shown by — are for the statistical distribution but with the whole distribution shifted to lower energy by 2 kcal mol^{-1} ($\langle E \rangle = 64.7 \text{ kcal}$).

Scheme I



kcal, because our experimental ratio was unity. At the high-pressure limit, $[\text{cis}]/[\text{trans}] = k_a(c)/k_a(t)$ and at the low pressure limit, the [cis]/[trans] ratio reduces to $k_c/k_t = 1$. Substitution of $k_a(c)/k_a(t) = 2.8$ and of k_c for k_t in the above equation yields

$$\frac{k_M[\text{M}](\text{[cis]}/[\text{trans}] - 2.8)}{3.8(1.0 - \text{[cis]}/[\text{trans}])} = k_c \quad (\text{V})$$

Collision diameters of 5.0 and 5.5 Å for the bath gas and olefin and the experimental [cis]/[trans] ratios give the rate constants (k_c) shown in Figure 5. There is fairly strong pressure dependence and the rate constants increase by about a factor of 3 over the pressure range examined. The experimental values at the high- and low-pressure limits are sensitive to the choices for $k_a(c)/k_a(t)$ and k_c/k_t ; however, the rate constants for the intermediate pressures are not subject to this restriction. The experimental rate constants of Figure 5 are used in a following section to deduce the energy distribution function of dichloroethene molecules.

Application of the same formulation to the *cis*- and *trans*-dichloroethene data from the $\beta\alpha$ elimination channel gives

$$\frac{k_M[\text{M}](\text{[cis]}/[\text{trans}] - 1.5)}{2.5(1.0 - \text{[cis]}/[\text{trans}])} = k_c \quad (\text{VI})$$

for a high-pressure limiting [cis]/[trans] ratio of 1.5. The [cis]/[trans] ratio neither attains unity at low pressure nor strongly favors *cis*-dichloroethene at high pressure. Appar-

ently only a fraction of the molecules are formed with energy greater than E_0 for isomerization. The result of this combination of factors is that the isomerization rate constants are not highly reliable. However the values of the rate constants k_c were $\sim(2-5) \times 10^6 \text{ sec}^{-1}$ for the pressure range of 1-10 Torr. The reduction of a factor of 10 in the magnitude of the rate constants, relative to the molecules formed by the $\alpha\alpha$ channel, indicates that significantly less energy is released to the olefin in the $\beta\alpha$ channel. However, the rate constants are not considered to be sufficiently reliable that their pressure dependence could be used to deduce an energy distribution function. For this reason the rate constants are not shown on a plot.

Discussion

The Three- and Four-Centered Elimination Channels for $\text{CH}_2\text{ClCDCl}_2$. The results establish that $\alpha\alpha$ and $\beta\alpha$ eliminations are competitive channels. Apparently such a competition can be expected whenever two Cl or two F (or probably two Br) atoms are attached to a primary carbon atom. The factor responsible for making the $\alpha\alpha$ channel competitive with $\beta\alpha$ channel is the lowering of the threshold energy for three-centered elimination which results from the enhanced thermodynamic stability of the halogen-substituted carbene relative to the hydrogenated carbene.⁶ Since subsequent hydrogen rearrangement is still exoergic for the halocarbene, the final product is the olefin. Recently a concerted elimination-rearrangement has been postulated to explain HCl elimination from $\text{CF}_3\text{CH}_2\text{Cl}$.^{17a} The total rate constant previously reported¹³ for $\text{CH}_2\text{ClCHCl}_2$ agrees well with the current measurements; however, the present data allow a much better assignment of the relative reaction channels. For $\text{CH}_2\text{ClCDCl}_2$ the ratio of $\alpha\alpha$ to $\beta\alpha$ elimination was 0.22; if the $\alpha\beta$ channel is included, the total ratio of three- to four-centered rates is 0.19. For $\text{CD}_2\text{ClCHCl}_2$ the ratio of $\alpha\alpha$ to $\beta\alpha$ products was 0.5; such an increase, relative to $\text{CHCl}_2\text{CDCl}_2$, is expected from the isotope effects. Based upon this isotope effect and upon calculations to be presented in the next section, the measured sum of $\alpha\alpha$ plus $\beta\alpha$ rate constants was partitioned (1:3) to the $\alpha\alpha$ and $\beta\alpha$ channels of $\text{CH}_2\text{ClCHCl}_2$ as shown in Table IV. Products from the $\alpha\beta$ and $\beta\alpha + \alpha\alpha$ channels were observed in a pyrolysis experiment^{17b} with $\text{CH}_2\text{ClCHCl}_2$; however, the $\alpha\alpha$ channel has not been identified by thermal activation. For this reason the critical energies were assigned from our chemical activation data.

The threshold energies were obtained by matching RRKM-calculated rate constants to the experimental values for all three molecules. The details of the calculations are summarized in the next section. Threshold energies of 60, 59, and 57 kcal mol⁻¹ for the $\alpha\alpha$, $\beta\alpha$, and $\alpha\beta$ channels of $\text{CH}_2\text{ClCHCl}_2$ are consistent with the data. As noted in footnote e of Table V, the $E_0(\alpha\alpha)$ could be raised 1 kcal mol⁻¹ to obtain even better agreement; however, the reliability of the E_0 values are only ± 2 kcal mol⁻¹ and this change is not particularly worthwhile. Thus the threshold energy for the $\alpha\alpha$ is 1-2 kcal mol⁻¹ higher than the directly competing ($\beta\alpha$) four-centered process. The threshold energy for the $\alpha\alpha$ process of CH_3CHF_2 was estimated to be 3 kcal mol⁻¹ higher than that for the $\beta\alpha$ elimination; the difference in the chloro and fluoro molecules is consistent with the enhanced ratio of $\alpha\alpha:\beta\alpha$ for $\text{CD}_2\text{ClCHCl}_2$ (0.76) relative to that for CD_3CHF_2 (0.22). Although calculations were not done for $\text{CHCl}_2\text{CHCl}_2$, the small reduction (factor of 2) in overall rate constant for tetrachloroethane relative

to 1,1,2-trichloroethane is consistent with threshold energies that are similar to trichloroethane.

The comparison of the calculated and experimental results imply that the threshold energy for $\alpha\beta$ elimination is ~ 2 kcal mol⁻¹ lower than for $\beta\alpha$ elimination. It should be noted that the calculated values for $k_{\alpha\beta}$ are lower (0.56) than for $k_{\beta\alpha}$, even for identical threshold energies (Figure 6). This characteristic of the model also is implied by the smaller calculated preexponential factor for the $\alpha\beta$ channel. Although the difference in the models did arise naturally, this effect, which contributes to the lower assignment of $E_0(\alpha\beta)$ relative to $E_0(\beta\alpha)$, may be overemphasized.¹ We would conclude, however, that $E_0(\alpha\beta) \lesssim E_0(\beta\alpha)$. The larger reaction path degeneracy for the $\beta\alpha$ channel relative to the $\alpha\beta$ channel should be noted (see Appendix) when comparing total rate constants.

Calculated Unimolecular Rate Constants and Isotope Effects. The rate constants in pressure units were converted to reciprocal seconds using Lennard-Jones collision diameters. It would be more realistic to include the $\Omega^{2,2}$ integral, which is a sizable factor for polar gases, in the collision diameter. This factor, however, would be offset by reducing the observed high-pressure cascade deactivation rate constants ($\langle \Delta E \rangle \approx 6$ kcal mol⁻¹ is expected¹² for CHCl_3 and CH_2CO bath gases) to unit deactivation values. The estimated uncertainty in the values of Table IV as unit deactivation rate constants could be $\pm 50\%$ (in addition to experimental error associated with individual measurements). For comparison with calculated results, Table V, the experimental rate constants were converted to unit reaction path degeneracy (see Appendix).

In order to calculate the RRKM unit deactivation rate constants, the specific rate constants, k_E , are averaged over the energy distribution function of formed molecules. An equation similar to that shown for $k_a(\alpha\beta)$ applies to each channel.

$$k_a(\alpha\beta) = k_M[M] \times \frac{\int_{E_{\min}}^{\infty} \frac{k_E(\alpha\beta)}{k_E(\alpha\beta) + k_E(\beta\alpha) + k_E(\alpha\alpha) + k_M[M]} f(E) dE}{\int_{E_{\min}}^{\infty} \frac{k_M[M]}{k_E(\alpha\beta) + k_E(\beta\alpha) + k_E(\alpha\alpha) + k_M[M]} f(E) dE} \quad (\text{VII})$$

Since the ratio of the specific rate constants is virtually constant over the relatively narrow distribution function for molecules formed by radical combination, any variation of the experimental rate constant with pressure will be less than the experimental error; therefore, only the limiting high-pressure form

$$k_a(\alpha\beta) = \int_{E_{\min}}^{\infty} k_E(\alpha\beta) f(E) dE / \int_{E_{\min}}^{\infty} f(E) dE \quad (\text{VIII})$$

will be used for the comparison with the experimental rate constants. This is not true for cis-trans isomerization results and in that case the pressure dependence of k_a is used to estimate $f(E)$. The introduction of cascade deactivation alters the formulation and can be especially important¹⁸ in the low-pressure region for multiple-channel systems; however, for relatively efficient bath gases this is not an important consideration.

The method for obtaining distribution functions of chemically activated molecules formed by radical combination is well known¹ and will not be discussed except to

TABLE V: Comparison of Calculated and Experimental Rate Constants^a

Molecule	Channel	Rate constants, 10 ⁷ sec ⁻¹		$E_0^{b,c}$ kcal mol ⁻¹	Preexponential factor, ^d 10 ¹³ sec ⁻¹
		Exptl ^a	Calcd ^b		
CH ₂ ClCHCl ₂	β (H) α (Cl)	4.5	4.3	58.8	0.63
	α (H) α (Cl) ^e	1.9	2.6	60.0	0.65
	α (H) β (Cl)	7.3	4.5	57.1	0.44
CH ₂ ClCDDCl ₂	β (H) α (Cl)	3.7	3.4	59.0	0.69
	α (D) α (Cl) ^e	1.1	1.5	61.0	0.72
	α (D) β (Cl)	2.7	2.7	58.0	0.45
CD ₂ ClCHCl ₂	β (D) α (Cl)	1.8	1.7	59.9	0.65
	α (H) α (Cl) ^e	1.2	1.7	59.8	0.67
	α (H) β (Cl)	3.6	2.8	56.9	0.41

^a All rate constants are for unit reaction path degeneracy. The experimental rate constants were converted to unit reaction path degeneracy basis using $\beta\alpha$ ($1/3$), $\alpha\alpha$ (2), and $\alpha\beta$ ($2/3$), as the degeneracy factors; see Appendix. ^b All calculated rate constants are the k_a^∞ values obtained from (VIII) with the CH₂Cl-CDCl₂ distribution function. Although $f(E)$ does change with deuterium substitution, ~ 0.5 kcal mol⁻¹ per deuterium, this effect is small relative to our experimental error. ^c Lowering the threshold energy by 1 kcal mol⁻¹ increases the calculated rate constant by a factor of 1.4. ^d The partition function form is $kT/h(I^\ddagger/I^*)^{1/2}(Q_v^\ddagger/Q_v^*)$ at 800°K for unit reaction path degeneracy. The calculated inertial ratios were between 1.1 and 0.95, and for simplicity, I^\ddagger/I^* was taken as 1.0 for all calculations. ^e The threshold energy for $\alpha\alpha$ elimination could be raised by ~ 1 kcal mol⁻¹ for better fit to the data. Since the experimental rate constant for the 1,2-dichloroethane channel for CH₂ClCHCl₂ was divided into the $\alpha\alpha$ and $\alpha\beta$ components by estimation of the isotope effects, the comparison of the experimental and calculated results should not be weighted heavily in this case.

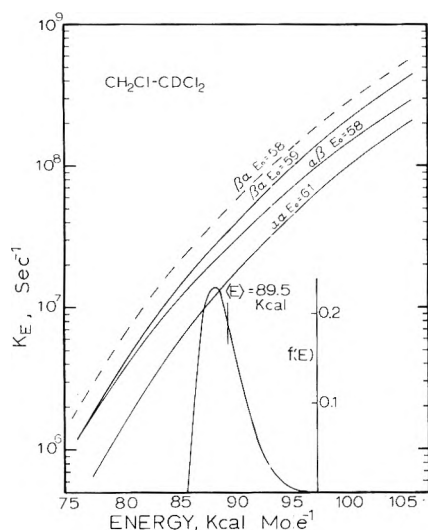


Figure 6. Specific rate constants for unit reaction path degeneracies and distribution function for 1,1,2-trichloroethane-d formed by radical combination at 300°K. The identification of the rate constants and channels is made in the figure; the $E_0 = 58$ kcal curve for $\beta\alpha$ elimination is shown to illustrate the effect of changing the critical energy by 1 kcal mol⁻¹.

identify the starting energy, E_{min} , which is the C-C bond energy at 0°K plus any activation energy for radical combination. To be consistent with previous work, the energy barrier for the radical combination was set at 1 kcal mol⁻¹. The $\Delta H_f^\circ(298\text{K})(\text{CH}_2\text{Cl}-\text{CHCl}_2)$ value¹⁶ of -34.0 kcal mol⁻¹ was used; this becomes -31.4 kcal mol⁻¹ at 0°K. The $\Delta H_f^\circ(0\text{K})$ values for CHCl₂ and CH₂Cl were taken as 24.6 and 28.8 kcal mol⁻¹, respectively.¹⁹ These were based upon $D^\circ(298\text{K})(\text{CHCl}_2-\text{H}) = 99$ and $D^\circ(298\text{K})(\text{CH}_2\text{Cl}-\text{H}) = 100.9$ kcal mol⁻¹. These values give $E_{\text{min}} = 85.8$ kcal mol⁻¹, which should be reliable to ± 2 kcal mol⁻¹. The distribution function was computed for combination of CH₂Cl and CDCl₂.

In order to compute values for k_E , threshold energies and the vibrational frequencies and moments of inertia of the molecules and transition states are needed. Threshold energies were assigned to match calculated and experimental k_a^∞ values for CH₂ClCDDCl₂, the other threshold ener-

gies follow from zero-point energy differences. Vibrational frequencies were obtained from the models described below.

The vibrational frequencies were assigned by selecting force constant fields for the molecules and the transition states. A similar treatment has been successfully used⁶ for CH₃CHF₂ and CD₃CHF₂. The first step was to estimate the approximate valence force constants by analogy with similar chloroalkanes; an iterative procedure then was used to refine the initial set of force constants to give the best fit to the observed 1,1,2-trichloroethane frequencies.²⁰ The method was based on King's iterative procedure and the actual computation was performed by Schachtschneider's "FPERT" computer program.²¹ It is not practical to include all interaction force constants for the entire molecule nor is it possible to assign them. However, off-diagonal elements that were available from analyses of other chloroalkanes were included. The force constants thus refined are given in Table VI. Consideration was given to only the asymmetric conformer. The two sets of observed frequencies²⁰ do not agree on the assignment in the C-H stretching and CCl₂ bending and rocking frequency regions. The calculated frequencies of the asymmetric conformer of CH₂Cl-CHCl₂ favored the lower values for the CCl₂ frequencies. Fundamental frequencies of CD₂ClCHCl₂ and CH₂ClCDDCl₂ were calculated from the assigned force constants; the frequencies are summarized in Table VII. Calculations for the $\beta\alpha$ transition state were based on trans geometry; a separate model was used for $\alpha\beta$ elimination. For each bond orders of 1.5, 0.9, 0.1, and 0.1 for the C-C, C-Cl, H-Cl, and H-C bonds, respectively, were used. Stretching force constants between these atoms were obtained from Johnston's relationship as previously described.² The C-C torsion force constant from the molecule was increased by a factor of 1.5 in accordance with a more rigid structure expected in the transition state. The reaction coordinate frequency was forced to be imaginary by setting $f_{ab} = (f_{af}f_b)^{1/2}$ for any two of the interaction force constants in the four-centered ring. We used the two breaking bonds C-H and C-Cl interacting with the C-C force constant, i.e., $f(\text{interaction}) = (f_{C-H}f_{C-C})^{1/2}$ and $f(\text{interaction}) = (f_{C-Cl}f_{C-C})^{1/2}$. The remaining force constants (stretching, bending, and in-

TABLE VI: Force Constants for Trichloroethane^a

$K_{C-Cl(1-3)}^b$	2.90	F_{CCH}^c	0.68
$K_{C-Cl(2-6,2-7)}^b$	3.05	F_{CCCl}^c	0.40
$K_{C-H(1-4,1-5)}^b$	4.71	F_{ClCCl}^c	0.25
$K_{C-H(2-8)}^b$	4.64	$F_{HCC-HCC}^d$	-0.015
K_{C-C}^b	4.52	$F_{HCC-C-H}^d$	0.11
$F_{HCC(3-1-5,3-1-4)}^c$	0.52	$F_{ClCCl-C-Cl}^d$	-0.057
$F_{HCC(7-2-8,6-2-8)}^c$	0.50	$F_{HCC-HCH}^d$	0.051
F_{HCH}^c	0.55	$F_{HCC-C-C}^d$	0.10
$F_{torsion}^c$	0.024	$F_{ClCC-C-C}^d$	-0.005

^a Refined by least-squares adjustments to reproduce the experimental frequencies for $CH_2Cl-CHCl_2$ to within 2%. The computer program was Schachtschneider's "FFERT."

^b Stretching force constants in units of $mdyn/\text{\AA}$. ^c Bending force constants in unit of $mdyn \text{\AA}/(\text{radian})^2$. ^d Stretch-bend interaction force constants in units of $mdyn/\text{radian}$.

TABLE VII: Calculated^a Frequencies^b of Trichloroethane- d_0 , $-d_1$, and $-d_2$

$CH_2Cl-CHCl_2$	$CH_2Cl-CDCl_2$	$CD_2Cl-CHCl_2$	Mode
3013	3013	2957	C-H or C-D str
2995	2995	2259	C-H or C-D str
2956	2198	2222	C-H or C-D str
1477	1472	1383	CH_2 or CD_2 def
1322	1324	1185	CH_2 or CD_2 def
1256	1238	1138	C-H or C-D bend
1215	1168	1019	C-H or C-D bend
1160	1048	888	CH_2 or CD_2 wag
1015	930	873	C-C str
910	788	845	$CHCl$ or $CDCl$ wag
822	697	752	C-Cl str
711	666	641	C-Cl str
666	638	610	C-Cl str
393	387	361	CCl_2 def
326	325	324	C-Cl bend
256	256	254	CCl_2 rock
191	189	181	CCl_2 rock
101	100	97	Torsional
10,392	9716	8995	Zero-point energy

^a Calculated for the asymmetric conformation, C_s symmetry. ^b These frequencies were grouped into sets of similar magnitude and represented by the geometric mean of the set with corresponding degeneracy for computation of densities of states.

interaction) were the same as for the 1,1,2-trichloroethane molecule. Normal-mode frequencies of the entire transition state were calculated by the Wilson's F-G matrix method. Normal modes in the low-frequency region are heavily mixed so that several force constants contribute to a particular normal mode. However, the torsional force constant mainly affects the ring puckering frequency. A summary of the grouped fundamental frequencies are given in Table VIII. A total of six frequencies arise from motions of the ring atoms: two symmetric ring deformations, two antisymmetric ring deformations, one ring puckering (out-of-plane bending), and the in-phase ring contraction and expansion mode ("ring breathing") which becomes the reaction coordinate. In our earlier treatments only the frequencies associated with the four bonds undergoing rearrangement were

TABLE VIII: Transition-State Models^{a,b}

System	Freq, cm^{-1}		
	$\beta\alpha$	$\alpha\alpha$	$\alpha\beta$
$CH_2Cl-CHCl_2$	2970 (2)	2988 (2)	2994 (2)
	1500 (3)	1500 (3)	1470 (3)
	1100 (3)	1210 (3)	1240 (3)
	711 (3)	973 (2)	822 (2)
	594 (2)	665 (2)	617 (3)
	344 (2)	374 (2)	340 (2)
	200 (2)	280 (2)	224 (2)
$CH_2Cl-CDCl_2$		140 (1)	
	2973 (1)	2988 (2)	2994 (2)
	2271 (1)	1418 (3)	1426 (3)
	1500 (3)	1209 (2)	1146 (3)
	993 (3)	960 (3)	800 (2)
	640 (5)	654 (2)	545 (3)
	302 (2)	365 (2)	339 (2)
$CD_2Cl-CHCl_2$	200 (2)	245 (2)	224 (2)
		140 (1)	
	2966 (1)	2220 (2)	2237 (2)
	2212 (1)	1370 (3)	1469 (2)
	1400 (2)	1075 (2)	1108 (2)
	1030 (4)	860 (2)	844 (4)
	631 (4)	613 (2)	589 (3)
370 (3)	385 (2)	322 (2)	
190 (2)	250 (2)	223 (2)	
	135 (1)		

^a Geometric mean of frequencies of similar magnitude.

^b The ratios of moments of inertia for the molecule and transition states were taken as unity for calculation of rate constants.

assigned by a force field, and the out-of-ring frequencies were obtained by analogy with other molecules. The ring puckering frequency was used as a semiadjustable parameter to obtain simultaneous fit to the thermal and chemical activation data. The major differences between the earlier treatment and the current method⁶ are (i) two interaction force constants were assigned to force an imaginary reaction coordinate frequency and this concept was incorporated in the general normal mode analyses of the transition state, (ii) the ring puckering frequency was calculated by assignment of a torsional force constant, and (iii) the out-of-ring frequencies were assigned from force constants rather than by analogy with other molecules. The range for the ring puckering frequencies for all four-centered models investigated was 180–200 cm^{-1} , which is considerably lower than the earlier results. The difference comes partly from the fact that 1,1,2-trichloroethane has low force constants for bending and torsional vibrations. However, the ring puckering frequency tends to be lower for the present method of assignment than for the earlier one, unless artificially high torsion force constants are used.

The approach just described also was used for the three-centered transition states. The bond length-bond order relations were used to define the geometry and force constants among C-Cl, C-H, and H-Cl; the bond orders were 0.8, 0.2, and 0.2, respectively. All other force constants for trichloroethane were retained. The reaction coordinate frequency was forced to be imaginary by setting $f(\text{interaction}) = (f_{CH/CCl})^{1/2}$. The frequencies are summarized in Table VIII.

The transition state models were used to calculate RRKM rate constants for the three reaction channels using harmonic oscillator sums and densities. After threshold energies for $CH_2ClCDCl_2$ are chosen, threshold energies for the other isotopically substituted reactions follow from

zero-point energy differences. The k_E values, with unit reaction path degeneracy, and $f(E)$ are shown in Figure 6 for $\text{CH}_2\text{ClCDCl}_2$. Although the average energy does change slightly with isotopic substitution, the effect² is small relative to our experimental error and $f(E)$ for $\text{CH}_2\text{Cl-CDCl}_2$ was used for all k_a^∞ calculations. The preexponential factors, k_a^∞ values, and threshold energies are summarized in Table V.

The main objective was to assign threshold energies for the $\alpha\alpha$, $\beta\alpha$, and $\alpha\beta$ channels and the general pattern of agreement between calculated and experimental k_a^∞ values for all three molecules is pleasing. The difference in threshold energies for the channels should be reliable, although the absolute values are less certain because of possible experimental error, uncertain collision cross sections, unreliable models of the transition states, and the use of harmonic oscillator sums and densities for k_a . Nevertheless, RRKM calculations from models based on the experimental preexponential factors consistently reproduce the experimental threshold energy.¹ The present method of selecting transition-state models is quite systematic; however, the force fields of the transition states are still arbitrary (the criteria were reasonableness of the force constants relative to the molecule and the magnitude of the resulting preexponential factors). An interesting aspect of the four-centered models is the looser transition state (larger preexponential factor) for the $\beta\alpha$ channel relative to the $\alpha\beta$ channel. Inspection of the frequencies shows that the two lowest frequencies for the $\beta\alpha$ channel are smaller than for the $\alpha\beta$ channel and, in addition, several other intermediate range frequencies are substantially lower. The lower torsional frequency of the 1,2-dichloroethene²² channel ($\beta\alpha$) relative to the 1,1-dichloroethene²² channel ($\alpha\beta$) is expected; however, the overall explanation involves complicated interactions of masses and force constants. We suspect that the difference has been exaggerated, but this would be an interesting point to test further.

Several intriguing isotope effects are portrayed in Table V. The *intermolecular* effects can be classified as secondary statistical effects, primary effects (the D atom is involved in the elimination), and combinations of both. One simplifying aspect of Table V is that all molecules were considered to have the same average energy. The calculated secondary statistical effect (E_0 unchanged) varies slightly from one case to another but in general $k_a^H/k_a^D = 1.3$. For both the three- and four-centered elimination $E_0^D - E_0^H \approx 1.0 \text{ kcal mol}^{-1}$, which introduces a factor of ~ 1.4 in favor of k_a^H ; this is augmented by a statistical effect arising from the lowered frequencies of the deuterium-substituted case which amounts to another factor of ~ 1.3 giving a total effect of ~ 1.7 for the primary effect. Several examples from Table V provide agreement with this general analysis: (i) the $\beta\alpha$ channels for trichloroethane- d_0 and - d_1 and the $\alpha\alpha$ and $\alpha\beta$ channels of the d_0 and d_2 compounds illustrate the secondary statistical effect; (ii) the $\alpha\alpha$ and $\alpha\beta$ channels of the d_0 and d_1 isomers illustrate the primary effect as does the $\beta\alpha$ channels of the d_1 and d_2 isomers. The $\beta\alpha$ channels of the d_0 and d_2 isomers illustrate the maximum expected isotope effect (1.7×1.3) which results from the combined E_0 difference and statistical effect for one D plus the statistical effect of the second D. The $\beta\alpha$ and $\alpha\alpha$ channels of d_1 vs. d_2 illustrate a cancellation of effects; *i.e.*, the deuterium would be expected to lower the rate constant of the d_2 isomer by a factor of 1.3; however, the atom being eliminated changes from D to H and the increase in E_0 cancels the

statistical effect and the rate constants for the d_2 isomer are hardly changed relative to the d_1 isomer. In fact, those for d_2 are slightly larger. Another way of explaining these two examples is that the isotope effect for d_1 is a primary effect and for d_2 it is a secondary effect, but with two deuteriums, and both effects give ~ 1.7 relative to the d_0 isomer. When extrapolating the intermolecular isotope effects summarized here to cases with several deuterium atoms, the change in the average energies of the formed molecule should be remembered.² This will tend to reduce the k_a^H/k_a^D ratio.

Since the statistical contribution, *i.e.*, the effect on the sums of states, is very similar for the deuterium either in ring or out of ring, the *intramolecular* primary isotope effect arises from the difference $E_0^H - E_0^D$. This is a factor of 1.4, and when this primary effect is switched from one channel to another, as for the $\beta\alpha$ and $\alpha\alpha$ comparisons of d_1 and d_2 , the effect is sizable. Both data and computations support this analysis.

The primary isotope effects provide further support for the necessity of a large $E_0^D - E_0^H$ difference. In the present procedure for developing models we reinvestigated the best bond order specifications of the C-H and H-Cl bonds of the transition state. Our former conclusion² regarding low bond orders for *both* bonds was reaffirmed. Our experience and derived views differ somewhat from those developed from a recent analysis²³ of isotopic effects for CH_3CF_3 and CD_3CF_3 .

Energy Partitioning by $\alpha\alpha$ and $\beta\alpha$ Elimination. The average energy of the trichloroethane molecules is 89.5 kcal mol⁻¹ and the elimination of HCl from 1,1,2-trichloroethane is 9.5 kcal endothermic; thus $\sim 30 \text{ kcal mol}^{-1}$ of excess energy and $\sim 50 \text{ kcal mol}^{-1}$ of potential energy are available for partitioning between HCl and the olefin. The experimental results showed that $\alpha\alpha$ elimination followed by H migration strongly favored the formation of *cis*-dichloroethene and that the olefin retained sufficient energy for isomerization. For the $\beta\alpha$ process, *cis*-dichloroethene was only slightly favored and, furthermore, only a fraction of the molecules were formed with energies greater than 56 kcal mol⁻¹, the threshold energy for *cis*-*trans* isomerization. The magnitude and pressure dependence of the experimental rate constants is used in the following section to assign average energies and energy distributions for the elimination reactions.

The analysis employs eq VII. The specific rate constants $k_c(E)$ were computed and the calculated rate constants were fitted to the experimental values by assigning $f(E)$. Calculation of $k_c(E)$ is straightforward since E_0 is known¹⁵ and the frequencies of *cis*-dichloroethene are well established.²² The transition-state model was the same as the molecule except that the torsional mode was taken as the reaction coordinate and the C-C stretch was lowered from 1587 to 990 cm⁻¹. The ratio of moments of inertia was 1.1 and the reaction path degeneracy was 2. The calculated thermal (800°K) preexponential factor (partition function form) was $1.97 \times 10^{13} \text{ sec}^{-1}$, which is in agreement with the experimental value.¹⁵

The ethylidene radical formed by photolytic processes has never been trapped. Thus H migration is fast, perhaps 10^{11} – 10^{12} sec^{-1} . Three general cases describing the thermochemistry associated with $\alpha\alpha$ elimination are shown in Figure 7. Case A corresponds to an appreciable energy minimum for $\text{CH}_2\text{ClCCl} + \text{DCl}$ with a threshold energy for rearrangement which is less than the threshold energy for addi-

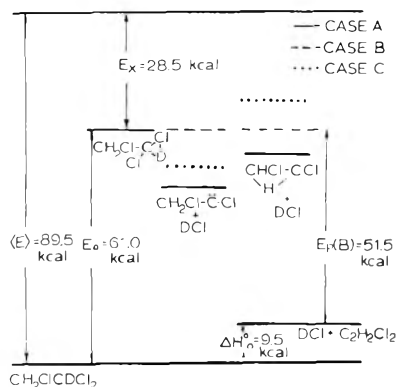


Figure 7. Energy diagram for α elimination from $\text{CH}_2\text{ClC(DCl)}_2$ followed by hydrogen migration to give dichloroethene. Cases A–C represent various assumptions about $\Delta H_f^\circ(\text{CH}_2\text{Cl}-\text{CCl})$ and the threshold energy for hydrogen migration. Note that the total potential energy change associated with H migration, E_0 (shown for case B), is released to dichloroethene. The threshold energy for *cis* \rightarrow *trans* isomerization is 56 kcal mol^{-1} .

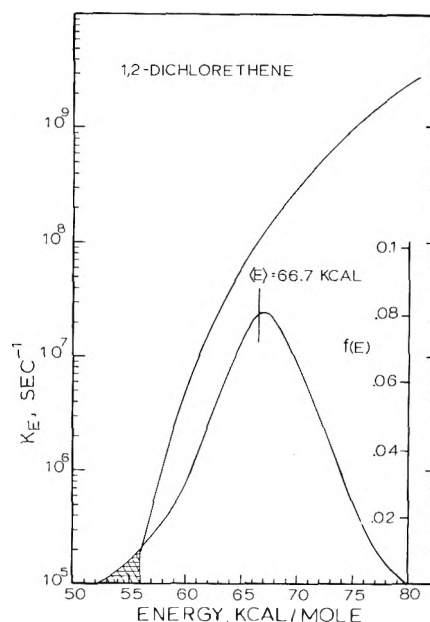


Figure 8. Specific rate constants for isomerization of *cis*-dichloroethene and the statistical energy distribution function for α elimination from $\text{CH}_2\text{ClC(DCl)}_2$ with case B thermochemistry. The energy scale is relative to $\Delta H_f^\circ(\text{DCl}) + \Delta H_f^\circ(\text{C}_2\text{H}_2\text{Cl}_2)$ as zero. The shaded part of the distribution lies below the threshold energy for isomerization; moving the distribution function to lower energy by 2 kcal moves 8% of the distribution below 56 kcal mol^{-1} .

tion of carbene to DCl. Case B corresponds to zero threshold energy for both addition and rearrangement, hence, no energy minimum. Case C has a small energy minimum but the threshold energy for rearrangement exceeds that for addition. The partitioning of the excess energy, E_x , can be estimated from the equation²⁴

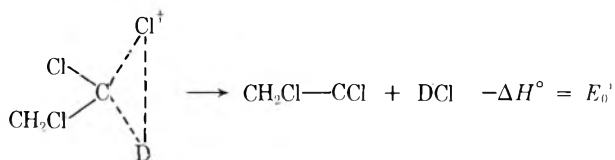
$$f(E_{01}) = \frac{D^+(E_{01}) \sum_{E=0}^{E_x - E_{01}} P_R^+(E)}{\sum_{E=0}^{E_x} P^+(E)}$$

if the statistical theory is adopted. The subscript 01 denotes the 12 frequencies of the α elimination transition state which correlate with the internal modes of the carbene; R denotes the remaining frequencies. The $D^+(E_{01})$ term is the density of states for the "carbene" frequencies; the sum of the eigenstates in the numerator, $P_R^+(E)$, is calculated from the five frequencies which do not correlate to internal modes of the carbene. The denominator is a normalization factor, the sum of eigenstates for the entire transition state. The form of the statistical energy distribution for the carbene fragment from $\text{CH}_2\text{Cl}-\text{CDCl}_2$ is shown in Figure 8. The distribution must be combined with the energy distribution arising from release of the potential energy associated with the thermochemistry of case A, B, or C.

Case B is the simplest and the full potential energy, E_p , is just added to the statistical distribution. Using $\Delta H_f^\circ(\text{C}_2\text{H}_2\text{Cl}_2) + \Delta H_f^\circ(\text{DF})$ as the energy reference, the distribution for case B begins at $51.5 \text{ kcal mol}^{-1}$ shown in Figure 8. Since the threshold energy for *cis* \rightarrow *trans* isomerization is 56 kcal mol^{-1} , a small fraction, $\sim 3\%$, of the molecules lack sufficient energy for isomerization. The situation shown in Figure 8 is unusually favorable for deducing $f(E)$ because the position of the energy distribution falls in the region where the energy dependence of k_E is greatest, *i.e.*, near the threshold energy. Three types of experimental information can be obtained: (i) the high-pressure values of the rate constants which give a measure of the average energy, (ii) the pressure dependence of the rate constants which give a measure of the width of the energy distribution, and (iii) failure of molecules with energy less than 56 kcal mol^{-1} to undergo the monitoring reaction. The calculated rate constants are sensitive to the average energy as

demonstrated by the curves of Figure 5; the 2 kcal mol^{-1} difference gives rate constants which differ by ~ 1.7 over the whole pressure range. As demonstrated in Figure 5, very good agreement between the calculated and experimental results was achieved for basically case B thermochemistry, but with E_p lowered by 2 kcal mol^{-1} . Moving the distribution downward by 2 kcal gives 8% of the distribution below 56 kcal mol^{-1} . This is consistent with the experimental low-pressure [*cis*]/[*trans*] limit, especially if the equilibrium ratio is, in fact, slightly less than unity. Although experimental limitations prevented accurate measurement of the high- and low-pressure rate constants, the variation of the rate constants with pressure certainly is consistent with the statistical distribution. Undue emphasis cannot be placed on the exact location of $f(E)$ because of the uncertainty in setting collision diameters for the experimental rates and because of uncertainty of the values of $R_c(E)$, especially near the threshold. We estimate an overall uncertainty of $\pm 3 \text{ kcal mol}^{-1}$ to $\langle E \rangle$.

For either case A or C, the average fraction of the potential energy partitioned to the carbene from the step



must be added to the statistical distribution. However, the energy released in the subsequent hydrogen migration step will be reduced from E_p (case B) by the full potential energy change (E_0') so the net effect is to reduce the average energy of the dichloroethene by that fraction of E_0' which was not released to the carbene in the DCl separation step. The favored energy distribution discussed above corresponds to case A with 2 kcal mol^{-1} released to relative translational and rotational energy of the carbene and DCl.

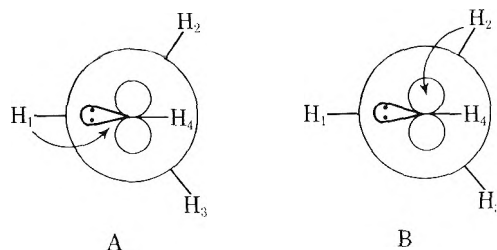
This would be consistent with a small, $<10 \text{ kcal mol}^{-1}$, activation energy for addition of carbenes to hydrogen halides.²⁵ In a more rigorous derivation the energy distribution associated with the release of the potential energy should be folded with the statistical distribution; however, this would have a minor effect on the final distribution since the statistical distribution is already quite broad.

The partitioning of energy for case C is complicated by the fact that not all of the carbene molecules will have sufficient energy for the hydrogen migration step. This appears to be inconsistent with the experimental observations and case C will not be considered further.

In addition to characterizing the energy partitioning pattern for $\alpha\alpha$ elimination, the average energy and the breadth of the distribution support a statistical distribution of internal energies in the microcanonical ensemble of systems crossing the transition-state configuration. Since E_0^\ddagger is quite small, the release mechanism of the potential energy plays a minor role and we conclude that these results provide additional⁷ support for energy randomization on the 10^{-8} – 10^{-9} sec time scale for the chemically activated halogenated alkanes. These internal energy partitioning data thus complement molecular beam measurements²⁶ of the translational product energies for cases which have small potential energy release after passing through the transition state. Although the statistical fraction of energy was retained as internal energy of the carbene, the data do not, of course, define the distribution within the modes of the polyatomic fragment.^{26d}

The foregoing treatment was repeated for the $\beta\alpha$ process. The energy distribution associated with the potential energy change ($\sim 49 \text{ kcal}$ of potential energy now is divided between HCl and CHClCDCl) was represented by a gaussian function plus the statistical energy distribution for E_x . Since $E_0(\alpha\alpha)$ and $E_0(\beta\alpha)$ are nearly equal, the statistical parts of the two distributions are virtually identical. The most probable energy, E_{mp} , and the σ of the gaussian distribution were varied in order to fit best the experimental rate constants in the way previously described.^{2b} The data are of poor quality and do not permit a reliable estimate of the shape of the energy distribution. Apparently somewhat less than half of the molecules are formed with energy greater than 56 kcal mol^{-1} which provides support for the previous estimate (which was based upon negative rather than positive evidence) that $\lesssim 2/3$ of the potential energy plus the statistical component of E_x is released to the olefin.

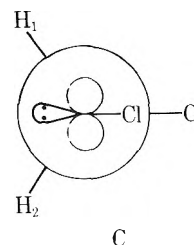
Stereochemistry of HX Eliminations. The explanation of the enhanced yield of *cis*-dichloroethene from $\alpha\alpha$ elimination must be sought from either the conformation of ethylidene or its rearrangement transition state. Conformations A (migration of H_1) and B (migration of H_2 or H_3)



have been studied²⁷ for the rearrangement of CH_3CH . According to the MINDO/2 method^{27a} rearrangement *via* B is highly favored and, in fact, no activation energy was found for migration *via* B, whereas, for A the energy raised stead-

ily as the H was transferred. Hoffman, *et al.*,^{27b} also have argued that the B-type transition state (but with H_2 being eclipsed by the p orbital) was favored over the A type. Extending those arguments to the dichloroethylidene suggests that conformation B with substitution of Cl at the 3 and 4 positions is greatly favored, relative to substitution at the 1 and 4 positions, in the transition-state geometry. An explanation for this preference may be the minimization of the dipole repulsion between the β chlorine and the electron pair on the carbene. On the other hand the more complex considerations outlined below may be important.

An alternative explanation is that conformation C of the



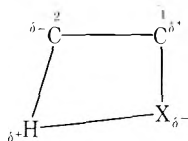
dichloroethylidene is significantly lower in energy than other possible conformations. Ethyl cations with electronegative groups are known^{27c} to favor C, rather than a conformation with the vacant p orbital and the group in an eclipsed geometry, and the situation may be similar for substituted ethylidene, which also has the vacant orbital. If C is the highly favored conformation, a natural favoring of the *cis* product will result *via* migration of either H_1 or H_2 toward the vacant p orbital, as in B, with subsequent twisting of the nonmigrating H atom. The difference between the explanations in these two paragraphs is the degree of stabilization for the *cis* conformation of the halogen atoms as the system changes from the carbene to the transition-state geometry. Since the difference in ΔH_f° of *cis*- and *trans*- $\text{C}_2\text{H}_2\text{Cl}_2$ is so small, the stabilization of the *cis* geometry may well arise in the carbene.

Both thermal²⁸ and chemical³ activation studies show that the four-centered HX elimination reactions yield *cis* and *trans* geometric isomers in general accord with thermodynamic predictions. The effect seems to be well established since elimination from 2-fluoro-³ and 2-chlorobutane²⁸ favors *trans*-butene-2, whereas, elimination from 1,1,2-trichloroethane favors *cis*-dichloroethene. If the same transition-state model is used for *cis* and *trans* $\beta\alpha$ elimination from $\text{CH}_2\text{Cl-CDCl}_2$, the observed $[\text{cis}]/[\text{trans}]$ ratio of 1.4–1.5 requires $E_0(\text{trans}) - E_0(\text{cis}) \approx 1 \text{ kcal mol}^{-1}$, which is slightly in excess of the difference ($0.4 \text{ kcal mol}^{-1}$) in the heats of formation of the olefins.

Additional Considerations about Four-Centered HX Elimination Reactions. The utility, as well as additional refinement of our transition-state model for HX elimination reactions, has been illustrated by the present application to the 1,1,2-trichloroethane. However, several questions about the four-centered elimination reactions are not answered by the model which provides a method for evaluating vibrational frequencies of the transition states. Three relevant questions are as follows. (a) What is the explanation for the small variation in the threshold energy upon multiple halogen substitution? (b) What is the role of orbital symmetry for the elimination reactions? (c) Where is the location of the potential barrier with respect to potential energy changes arising from the forming and breaking of bonds?

The first subject to be considered is the variation of the

threshold energy with halogen substitution. (We will use 1 and 2 to identify the carbon atoms to avoid confusion with our earlier α , β notation.)



The lowering of E_0 upon 1-methyl substitution indicates^{29a} a significant degree of charge separation in the transition state. Models incorporating varying degrees of charge separation have been used to calculate threshold energies²⁹ with mixed success. In general fluorine substitution raises E_0 , and the effect may be slightly greater for 1 substitution, than for 2 substitution (C_2H_5F , 58; 1,2- $C_2H_4F_2$, 62; 1,1- $C_2H_4F_2$, 61; 1,1,1- $C_2H_3F_3$, 68; 1,1,1,2- $C_2H_3F_4$, 69; 1,1,2,2- $C_2H_2F_2$, 68; C_2HF_5 , 70; all in kcal mol⁻¹).³⁰ In contrast the comparison between C_2H_5Cl and 1,1- and 1,2-dichloroethane indicates that substitutions of Cl at the 1 and 2 positions lower and raise the threshold energy, respectively (C_2H_5Cl , 55; 1,2- $C_2H_4Cl_2$, 60; 1,1- $C_2H_4Cl_2$, 52; 1,1,2- C_2H_3Cl , 59 \pm 2; all in kcal mol⁻¹).^{1,12,29} Extending this argument to the various channels of 1,1,2-trichloroethane would suggest that the threshold energy for the 1,1-dichloroethane channel (with two chlorine atoms at the 2 position) might be higher than the threshold energy for the 1,2-dichloroethane channel (with a chlorine at both the 1 and 2 positions). According to the present work little difference exists between them (if there is a difference $E_0(1,1\text{-dichloroethane}) < E_0(1,2\text{-dichloroethane})$) and the role of the 2 substituent in raising the threshold energy must be dominant, but not additive with additional substitution. Judging from the magnitude of the chemical activation rate constants, $E_0(1,1,2,2\text{-tetrachloroethane})$ is similar to $E_0(1,1,2\text{-trichloroethane})$ which further supports this conclusion. Maccoll²⁹ and others³¹ also have concluded that substitution of Cl or Br at the 1 and 2 positions lowered and raised E_0 , respectively. Chlorine is a strongly electron-accepting substituent and its expected effect might have been to destabilize the δ^+ for substitution at the 1 position and to stabilize the δ^- for substitution at the 2 position. The reverse is the case, which is an effect that has been observed for conjugated systems in which partial delocalization occurs between the chlorine nonbonded electrode and the conjugated system.³² Since the four-centered elimination transition states have partial double-bond character, the delocalization effect causes chlorine substitution at the 1 position to stabilize the δ^+ but the substitution at the 2 position destabilizes the δ^- . The delocalization argument also is consistent with the lowering of the threshold energy for the $\alpha\alpha$ elimination channel and explains the need for two halogen atoms on the same carbon.⁶ This reasoning suggests that for fluorine the inductive effect dominates at the 1 position but delocalization must have some importance at the 2 position if the E_0 is increased at both positions. Perhaps the most important deduction from the halogen substituent effect is that considerable charge difference as well as excess electron density (relative to a single bond) may exist between the carbon atoms at the potential barrier.

Whether or not the four-centered HX elimination proceeds by the orbital symmetry allowed process is an unresolved question. If the orbital symmetry pathway is followed, the hydrogen that is eliminated does not originate from the position adjacent to the halogen but rather from

the side opposite to the halogen. If the reaction pathway is symmetry allowed with the barrier being associated with the breaking of the C-H bond as the H moves to X, the force field at the transition state would differ little from that which we have termed the four-centered model. As has been previously discussed, the isotope effects for several examples, as well as for 1,1,2-trichloroethane- d_0 , $-d_1$, and $-d_2$ cases are only consistent with transition-state models which have a large component of H (D) motion in the reaction coordinate. Thus the frequencies we have assigned to the transition state should apply for either adjacent or nonadjacent elimination.

On the basis of our data and the infrared chemiluminescence results,¹⁰ a considerable fraction ($\geq 25\%$) of the potential energy must be released as relative translational or rotational energy of the olefin and HX. This approximate estimate is supported by kinetic energy measurements of HX eliminated from alkyl halide positive ions.¹¹ This pattern is not surprising when the detailed dynamics are examined. The motion of the H atom is necessarily rapid relative to the motion of the X atom. Hence the H will transfer to the X and the X subsequently recoils from the olefin taking H along with it. The dynamics of the first step may be somewhat analogous to H atom transfer in bimolecular $F + H - R$ reactions.³³ This particular mass combination leads to intermediate values of energy release to HF; complex and secondary encounters are also common because of the trapping of the light mass between two heavy masses.^{33,34} For HX elimination this effect plus the assumption that most of the potential energy release occurs during the departure of the X from the carbon and not as H moves to the X explains the small fraction (~ 0.13) of energy released to the internal energy of HX.¹⁰ If the potential energy is largely released as the X is ejected, the local potential surface will be repulsive and the final part of the reaction pathway may resemble that for $H + X_2$, which gives a high conversion to relative translational energy.^{35,36} Structural changes in the olefin fragment will occur as the bond between the HCl and olefin fragment breaks and some internal energy will be released to the olefin.

Summary

The unimolecular reaction kinetics associated with chemically activated 1,1,2-trichloroethane have been used to obtain the following results. (1) A characterization of the three-centered elimination process is accomplished by comparison with the four-centered reaction; detailed results including isotope effects are consistent with model calculations. (2) Since the three-centered elimination has zero or nearly zero activation energy for the reverse process, the energy partitioned to the product serves to characterize the distribution of excess energy at the barrier—and consistency with the predictions of statistical theory was found. (3) The energy partitioning of the potential energy (threshold energy for addition of HX to the olefin) by the four-centered reaction is explained by separating the dynamics into two parts. The first part consists of the rapid transfer of the light H fragment to the halogen. The second step is the separation of the two heavy fragments on the repulsive surface and appears to release a relatively large fraction of the energy to relative translation.

Acknowledgments. We wish to thank Mr. Bert Holmes for assistance with some of the calculations and for careful reading of the manuscript. Helpful discussions relating to

the stereochemistry were provided by Drs. Danen and McDonald of Kansas State University and Dr. Hoffmann of Cornell University. We are grateful for the support provided by the National Science Foundation (Grant No. 27536-X).

Appendix

The RRKM rate constants were calculated using the threshold energies of Table V and the models described in Tables VII and VIII. The basis for selection of these models already has been described. Computations were done using harmonic oscillator sums and densities of states in the usual way. The moments of inertia for the molecule or transition state depend strongly on conformation; therefore, for simplicity the ratios of moments of inertia were taken as unity in the calculation of rate constants for all channels. The only aspect of this application of the RRKM formulation that requires additional explanation is the choice for reaction path degeneracies. Since the experimental and calculated results were compared on the basis of unit reaction path degeneracy, the experimental rate constants of Table V must be scaled to a unit reaction path degeneracy basis. The densities of states were calculated for the asymmetric conformer of trichloroethane with the torsional mode treated as a vibration; however, the reaction path degeneracies were selected from the overall average of the three possible conformations, which gave $\frac{2}{3}$ for the $\beta\alpha$ process, $\frac{2}{3}$ for the $\alpha\beta$ process, and $\frac{6}{3}$ for the $\alpha\alpha$ process. Therefore, the average total path degeneracy is $\frac{16}{3}$. Our method, which weights the cis and trans isomers equally for the $\beta\alpha$ elimination, differs from the assignment of reaction degeneracies recently used for CH_2FCHF_2 .³⁷ Phillips and Trotman-Dickenson³⁸ used a reaction path degeneracy of 5 for the four-centered elimination pathways of $\text{CH}_2\text{F}-\text{CHF}_2$. The reaction path degeneracy of 5 arises by representing the torsion as a free rotor, the two fluorine atoms can eliminate with either of two H atoms for the $\alpha\beta$ channel but the fluorine atom can go with only one H atom for the $\beta\alpha$ channel. This method of counting does not include the possibility of optically active transition states, which increases the reaction path degeneracies to 8, 2, and 2 for the $\beta\alpha$, $\alpha\beta$, and $\alpha\alpha$ channels, respectively, for a free internal rotational model of 1,1,2-trichloroethane. The ratios of degeneracies for the $\beta\alpha$ and $\alpha\beta$ processes are 4:1 for either model. On the basis of relative reaction path degeneracies the four-centered pathways are weighted more heavily by the free-rotor model that includes the optically active channels; however, this weighting will be counterbalanced by the increase in N_E^* for treatment of the torsional mode of the molecule as a free rotor. Since the description of the torsional mode will be the same for the models of both the molecule and the three-centered transition state, the ratio of sums and densities for the $\alpha\alpha$ channel would be invariant to whether the torsional mode was described as a rotation or as a vibration.

References and Notes

- (1) D. W. Setser, *MTP (Med. Tech. Publ. Co.) Int. Rev. Sci.: Phys. Chem., Ser. One*, **9**, 1 (1972).
- (2) (a) W. G. Clark, D. W. Setser, and K. Dees, *J. Amer. Chem. Soc.*, **93**, 5328 (1971); (b) K. Dees and D. W. Setser, *J. Chem. Phys.*, **49**, 1193 (1968).

- (3) K. C. Kim and D. W. Setser, *J. Phys. Chem.*, **77**, 2021 (1973).
- (4) A. W. Kirk, A. F. Trotman-Dickenson, and B. L. Trus, *J. Chem. Soc. A*, 3058 (1968).
- (5) M. J. Perona, J. T. Bryant, and G. O. Pritchard, *J. Amer. Chem. Soc.*, **90**, 4782 (1968).
- (6) K. C. Kim, D. W. Setser, and B. E. Holmes, *J. Phys. Chem.*, **77**, 725 (1973).
- (7) K. C. Kim and D. W. Setser, *J. Phys. Chem.*, **76**, 283 (1972).
- (8) K. Dees, D. W. Setser, and W. G. Clark, *J. Phys. Chem.*, **75**, 2231 (1971).
- (9) The two-step model for energy disposal by a unimolecular reaction employed here differs from the restricted phase space model that was used to discuss the translational product energy distributions from a molecular beam study of F+ unsaturated compounds: J. M. Parsons, K. Shobatake, Y. T. Lee, and S. A. Rice, *J. Chem. Phys.*, **59**, 1402, 1427 (1973). On the other hand other molecular beam results frequently are interpreted using models similar to that employed in this paper: D. R. Herschbach, *Discuss. Faraday Soc.*, **No. 55**, 233 (1973).
- (10) (a) P. N. Clough, J. C. Polanyi, and R. T. Taguchi, *Can. J. Chem.*, **48**, 2919 (1970); (b) H. W. Chang, D. W. Setser, and M. J. Perona, *J. Phys. Chem.*, **75**, 2070 (1971).
- (11) K. C. Kim, J. H. Beynon, and R. G. Cooks, *J. Chem. Phys.*, **61**, 1305 (1974).
- (12) D. W. Setser and E. E. Siefert, *J. Chem. Phys.*, **57**, 3613, 3623 (1972).
- (13) J. C. Hassler and D. W. Setser, *J. Chem. Phys.*, **45**, 3237 (1966).
- (14) (a) W. G. Clark, D. W. Setser, and E. E. Siefert, *J. Phys. Chem.*, **74**, 1670 (1970); (b) F. S. Row and P. S. T. Lee, D. C. Montague, and R. L. Russel, *Discuss. Faraday Soc.*, **No. 53**, 111 (1972).
- (15) P. M. Jeffers, *J. Phys. Chem.*, **76**, 2829 (1973).
- (16) P. Goldfinger and G. Martens, *Trans. Faraday Soc.*, **57**, 2220 (1961).
- (17) (a) G. E. Millward and E. Tschuikow-Roux, *Int. J. Chem. Kinet.*, **4**, 559 (1972); (b) A. L. Englin, E. V. Sonin, and L. A. Petrukchina, U.S.S.R. Patent 130,894 (1960); *Chem. Abstr.*, **55**, 6373d (1961).
- (18) C. W. Larsen and B. S. Ratinovitch, *J. Chem. Phys.*, **51**, 2293 (1969).
- (19) (a) S. Furuyama, D. M. Golden, and S. W. Benson, *J. Amer. Chem. Soc.*, **91**, 7564 (1969); (b) G. D. Mendenhall, D. M. Golden, and S. W. Benson, *J. Phys. Chem.*, **77**, 2707 (1973).
- (20) (a) R. H. Harrison and L. A. Kobe, *J. Chem. Phys.*, **26**, 1411 (1957); (b) S. Saeki, *Nippon Kagaku Zasshi*, **80**, 238 (1959).
- (21) J. H. Schachtschneider, Technical Report No. 57-65, Shell Development Co., Emeryville, Calif., 1964.
- (22) T. Shimanouchi, *Nat. Stand. Ref. Data Ser., Nat. Bur. Stand.*, **39**, 80 (1972).
- (23) B. D. Neely and H. Carmichael, *J. Phys. Chem.*, **77**, 307 (1973).
- (24) Y. N. Lin and B. S. Rabinovitch, *J. Phys. Chem.*, **74**, 1769 (1970).
- (25) (a) T. Smali and F. S. Row and, *J. Amer. Chem. Soc.*, **92**, 1866 (1970); (b) J. W. Edwards and P. A. Small, *Nature (London)*, **202**, 1329 (1964).
- (26) (a) S. M. Friend, G. A. Fisk, D. R. Herschbach, and W. Klemperer, *J. Chem. Phys.*, **54**, 2560 (1971); (b) S. J. Riley and D. R. Herschbach, *ibid.*, **58**, 27 (1973); (c) K. Shobatake, Y. T. Lee, and S. A. Rice, *ibid.*, **59**, 6104 (1973); (d) J. G. Moehmann and J. D. McDonald, *ibid.*, **59**, 6683 (1973); **60**, 4790 (1974).
- (27) (a) N. Bodor and M. J. S. Dewar, *J. Amer. Chem. Soc.*, **94**, 9103 (1972); (b) R. Hoffmann, G. D. Zeiss, and G. W. VanDine, *ibid.*, **90**, 1485 (1968); (c) R. Hoffmann, L. Radom, J. A. Pople, P. R. Schleyer, W. J. Hehre, and L. Salem, *ibid.*, **94**, 6221 (1972); (d) J. A. Altmann, I. G. Cstzmadra, and K. Yates, *ibid.*, **96**, 4196 (1974).
- (28) H. Heydtmann and G. Rink, *Z. Phys. Chem. (Frankfurt am Main)*, **26**, 75 (1963).
- (29) (a) A. Maccoll, *Chem. Rev.*, **69**, 33 (1969); (b) K. R. Maltman, E. Tschuikow-Roux, and K. H. Jung, *J. Phys. Chem.*, **78**, 1035 (1974).
- (30) (a) G. E. Millward and E. Tschuikow-Roux, *J. Phys. Chem.*, **76**, 292 (1972); (b) W. Tsang, *Int. J. Chem. Kinet.*, **5**, 643 (1973); (c) J. A. Kerr and D. M. Timlin, *ibid.*, **3**, 427 (1971); (d) H. W. Chang, N. L. Craig, and D. W. Setser, *J. Phys. Chem.*, **76**, 954 (1972). The calculations for $\text{C}_2\text{H}_5\text{F}$ and 1,1,1- $\text{C}_2\text{H}_3\text{F}_3$ suggest that ~ 1.5 kcal mol⁻¹ should be subtracted from the Arrhenius activation energies to obtain threshold energies.
- (31) (a) G. J. Martens, M. Godfroid, and L. Ramoisy, *Int. J. Chem. Kinet.*, **2**, 123 (1970); (b) K. A. Holbrook and J. S. Palmer, *Trans. Faraday Soc.*, **67**, 1 (1971).
- (32) M. L. Poutsma, "Free Radicals," Vol. II, J. K. Kochi, Ed., Wiley-Interscience, New York, N. Y., 1973, p 190.
- (33) R. L. Johnson, K. C. Kim, and D. W. Setser, *J. Phys. Chem.*, **77**, 2499 (1973).
- (34) C. A. Parr, J. C. Polanyi, and W. H. Wong, *J. Chem. Phys.*, **58**, 5 (1973).
- (35) J. D. McDonald, P. R. LeBreton, Y. T. Lee, and D. R. Herschbach, *J. Chem. Phys.*, **56**, 769 (1972).
- (36) (a) K. G. Anlauf, P. J. Kuntz, D. H. Maylotte, P. D. Pacey, and J. C. Polanyi, *Discuss. Faraday Soc.*, **No. 44**, 183 (1967); (b) A. M. G. Ding, L. I. Kirsch, D. S. Perry, J. C. Polanyi, and J. L. Schreiber, *ibid.*, **No. 55**, 252 (1973).
- (37) M. V. C. Sekhar and E. Tschuikow-Roux, *J. Phys. Chem.*, **78**, 472 (1973).
- (38) D. C. Phillips and A. F. Trotman-Dickenson, *J. Chem. Soc. A*, 1144 (1968).

COMMUNICATIONS TO THE EDITOR

Infrared Spectra of Methane Adsorbed on NaA, CaA, and NaX Zeolites

Publication costs assisted by Université Paris VI

Sir: In the range of infrared spectra investigations of molecules physically adsorbed on zeolites,¹ we have studied the spectra of methane adsorbed on NaA, CaA, and NaX. After Hirschfelder, the collision diameter is 3.8 Å, but calculations from C-H bond lengths and van der Waals radii for C and H atoms actually yield approximately 4.6 Å. We know the effective diameter of the apertures of NaA (4.2 Å), CaA (5 Å), and NaX (8 Å) zeolite cavities;² therefore, it seems likely that adsorption of methane by the two latter molecular sieves occurs, but in the case of the NaA zeolite, this adsorption is expected to be restricted, due to the small pore size impeding diffusion.

The spectra of the three molecular sieves previously desorbed at 400° below 5×10^{-5} Torr¹ and then exposed to CH₄ at pressures greater than 500 Torr show no absorption bands when the zeolite pellet is at the same temperature as the beam of the spectrophotometer, *i.e.*, 313°K. At 173°K, however, under gas pressures of approximately 20 Torr, we have observed important intensities of CH₄ absorption bands in the case of NaX (Figure 1), slightly weaker intensities in the case of CaA, and very weak intensities in the case of NaA. CH₄ therefore penetrates the NaA cavities, but the adsorbed amount is very small.

There are four fundamental vibration frequencies for CH₄: in the gaseous phase, ν_3 and ν_4 are ir active, while ν_1 and ν_2 are only Raman active, although ν_2 has never been observed (likely its intensity is too weak). In the adsorbed state, besides the two allowed bands, the forbidden band ν_1 appears with approximately the same intensity as ν_3 and ν_4 , due to the dipole moment induced by the field existing in-

side the cavity. The intensity of ν_1 is proportional to $(\partial\mu_i/\partial q)^2$, *i.e.*, $E^2(\partial\alpha/\partial q)^2$, so it is proportional to the square of the field, and to the intensity of the Raman band (which accounts for the fact that the ν_2 band is not apparent in the adsorbed phase). The frequencies of CH₄ in the adsorbed and gas phases are given in Table I.

TABLE I: Methane Frequency (cm⁻¹)

Band	Gaseous state	Adsorbed on		
		NaA	CaA	NaX
ν_4 (F)	1306 (ir)	1312	1303	1306
ν_1 (A ₁)	2914 (R)	2890	2893	2888
ν_3 (F)	3020 (ir)	3000	3006	3000

The stretching bands ν_1 and ν_3 are shifted toward lower frequencies, as in the liquid and solid states,² while for the bending band ν_4 the shift toward high frequencies is less apparent (in the gaseous state, the central frequency is difficult to locate because of a strong Coriolis interaction).

Comparison of the profiles of the three bands shows that ν_1 is obviously narrower than ν_3 and ν_4 . Since the totally symmetrical Raman bands of a spherical rotator are not accompanied by rotational wings, we are able to infer that the ν_1 profile is strictly due to perturbations of the vibrational frequency; in this case, the motion of the molecule in a cavity where the field varies with the distance to the surface is responsible for the frequency distribution. In addition, the observed ν_1 band is entirely located below the gas-phase frequency; because its intensity is proportional to the square of the field, this band does not appear when the molecule is at the center of the cavity ($E = 0$) where its frequency would be the same as that observed for the gas.

On the contrary, ν_3 and ν_4 have broad profiles and over-

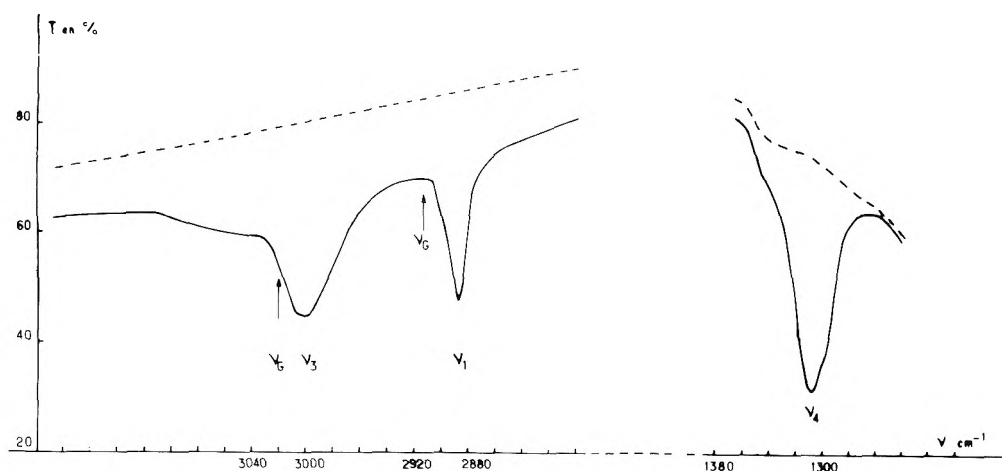


Figure 1. Infrared spectrum of CH₄ adsorbed on NaX.

lap the spectral range of the bands observed for the gaseous state. This observation, and the presence of a pronounced shoulder on the high-frequency side for ν_3 lead one to infer that CH_4 retains some rotational freedom inside the cavity, as has been observed for the molecule in the liquid state² and adsorbed on porous glass.³

References and Notes

- (1) E. Cohen de Lara, *Mol. Phys.*, **23**, 555 (1972).
- (2) G. E. Ewing, *J. Chem. Phys.*, **40**, 179 (1964).
- (3) N. Sheppard, and D. J. C. Yates, *Proc. Roy. Soc., Ser. A*, **238**, 69 (1956).

Service Infrarouge
 Département de Recherches Physiques
 Université Paris VI
 75230 Paris Cedex 05, France

E. Cohen de Lara*
 Y. Delaval

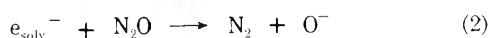
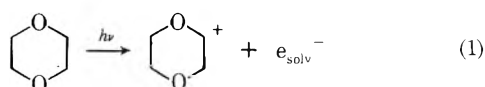
Received March 25, 1974

Solvated Electrons from Excited (λ 185 nm) *p*-Dioxane¹

Publication costs assisted by the Institut für Strahlenchemie im
 Max-Planck-Institut für Kohlenforschung

Sir: The photochemistry of *p*-dioxane has been studied in the gas and liquid phases. In the gas phase it decomposes (λ 147 nm) to give ethylene, hydrogen, carbon monoxide, and formaldehyde.² For the liquid phase (λ 185 nm) preliminary results indicate the formation of formaldehyde, ethylene, oxetane, acetaldehyde, 2-methyl-1,3-dioxolane, hydrogen, bis(dioxanyl), and some as yet unidentified products. CO, which is a major gas-phase photolysis product, is absent here.³ Although light is absorbed within a small layer next to the cell window photolysis of the products is negligible at the dose rate employed in these experiments (8×10^{15} quanta $\text{sec}^{-1} \text{cm}^{-2}$). Here, we wish to report evidence to the effect that the formation of solvated electrons is the major process in the 185-nm photolysis of liquid *p*-dioxane and, even more pronounced, in its aqueous solution

N_2O -saturated *p*-dioxane yields N_2 with a quantum yield of $\Phi(\text{N}_2) = 0.58$. This value increases with increasing water content, and in an aqueous solution containing 20 vol % ($\approx 2.35 \text{ M}$) *p*-dioxane $\Phi(\text{N}_2)$ approaches unity. Under these conditions neither water nor N_2O absorb to an appreciable extent since the molar extinction coefficients of water, N_2O , and *p*-dioxane at λ 185 nm are 0.026,⁴ 80,⁵ and ca. $3000^6 \text{ M}^{-1} \text{cm}^{-1}$, respectively. Quantum yields have been determined using $\Phi(\text{H}_2) = 0.47$ for the Farkas actinometer (5 M ethanol in water). The high yield of N_2 from N_2O -saturated solutions indicates that the photoexcited *p*-dioxane ejects an electron which reacts with N_2O according to eq 2.



Further to test this is a competition study was made with protons as scavengers. H_2SO_4 was chosen because of the

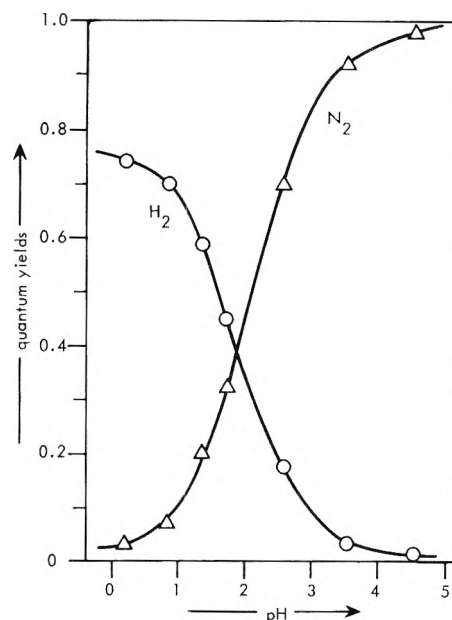


Figure 1. pH dependence of the quantum yields for H_2 (O) and N_2 (Δ) formation in N_2O -saturated solutions of *p*-dioxane in water (20 vol %).

low molar extinction coefficient ($24.3 \text{ M}^{-1} \text{cm}^{-1}$) of the HSO_4^- ion.⁸ The presence of acid leads to processes 3 and 4.

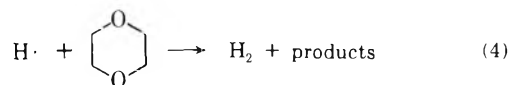


Figure 1 shows the competition of $\Phi(\text{N}_2)$ vs. $\Phi(\text{H}_2)$ at a constant N_2O concentration (saturated $\approx 2.5 \times 10^{-2} \text{ M}^{-1}$) as a function of pH. The half-values of the two curves coincide within experimental error at $\text{pH } 2 \pm 0.15$. Using published values⁹ for the rate constants of reactions 2 and 3 (k_2 (in water) = $5.6 \times 10^9 \text{ M}^{-1} \text{sec}^{-1}$, k_3 (in water) = $2.25 \times 10^{10} \text{ M}^{-1} \text{sec}^{-1}$) the half-value is calculated at $\text{pH } 1.85$. It is noted that even though $\Phi(\text{N}_2)$ reaches unity in this competition study, $\Phi(\text{H}_2)$ does not. The reason for this may be the reaction of the H atom with the *p*-dioxanyl radical which would not lead to hydrogen formation. Reaction 4 is expected to increase with increasing temperature. Indeed in accordance with this expectation $\Phi(\text{H}_2)$ rises with increasing temperature and at 80° a value of 0.85 has been found. There is no similar effect that could decrease the N_2 yield. We therefore conclude that in aqueous solution an electron is ejected on 185-nm irradiation with a quantum yield of unity. The gas-phase ionization potential of *p*-dioxane is 9.5 eV.¹⁰ The 185-nm quanta are equivalent to 6.7 eV. The energy gap of 2.8 eV will have to be filled by the solvation energy of the radical ions. The solvation free enthalpy of the electron in water is 1.8 eV.¹¹ In neat dioxane it is appreciably smaller.¹² The solvation free enthalpy of the radical cation is not known but larger positive ions such as Na^+ or Cs^+ ions have been reported to have solution free enthalpies of 4.25 and 2.95 eV, respectively,¹³ in water.¹⁴

Whereas no emission from 185-nm excited dioxane is observed in the gas phase,¹⁵ emission with λ_{max} 247 nm is observed in the liquid phase.^{15,16} The quantum yield for this emission has been reported to be 0.029. On dilution with isooctane this emission is blue-shifted and strongly re-

duced. On dilution with water or methanol the emission is red-shifted and also strongly reduced. In a 1:1 (vol/vol) mixture of dioxane-water the emission has nearly vanished. Similar results have been observed by pulse radiolysis.¹⁷ The emission found in the 185-nm photolysis of *p*-dioxane has been attributed to a fluorescence of an excimer species.¹⁵ Baxendale, *et al.*,¹⁷ have noted that N₂O suppresses strongly the fluorescence of anthracene in γ -irradiated *p*-dioxane. Since delayed charge neutralization had been excluded as the origin of the emission of neat *p*-dioxane under pulse radiolysis conditions the observed lifetime of about 2–3 nsec is believed to be due to fluorescent state formed by electron-radical cation recombination.¹⁷ It has been observed³ that the emission from the photoexcited *p*-dioxane can be suppressed by N₂O. Possibly the fluorescent state in the 185-nm photolysis also has a solvated electron-radical cation pair as its precursor.

References and Notes

- (1) Part V of the series "Strahlenchemie von Äthern." Part IV: S. Steenken, H.-P. Schuchmann, and C. von Sonntag, in press.
- (2) R. H. Hentz and C. F. Parrish, *J. Chem. Phys.*, **75**, 3899 (1971).
- (3) C. von Sonntag, H. Bandmann, and H.-P. Schuchmann, unpublished results.
- (4) J. Barrett and A. L. Mansell, *Nature (London)*, **187**, 138 (1960).
- (5) F. S. Dainton and P. Fowles, *Proc. Roy. Soc., Ser. A*, **287**, 295 (1965).
- (6) Gas-phase value from L. W. Pickett, N. J. Hoeflich, and T.-C. Lin, *J. Amer. Chem. Soc.*, **73**, 4865 (1951).
- (7) C. von Sonntag, H.-P. Schuchmann, and G. Schomburg, *Tetrahedron*, **28**, 4333 (1972).
- (8) J. Barrett, M. F. Fox, and A. L. Mansell, *J. Chem. Soc. A*, 483 (1967).
- (9) M. Anbar and P. Neta, *Int. J. Appl. Radiat. Isotopes*, **18**, 493 (1967).
- (10) H. F. Field and J. L. Franklin, "Electron Impact Phenomena," Academic Press, New York, N.Y., 1957, p 110.
- (11) A. Henglein, W. Schnabel, and J. Wendenburg, "Einführung in die Strahlenchemie," Verlag Chemie, Weinheim, 1969, p 142.
- (12) J. H. Baxendale and M. A. Rodgers, *J. Phys. Chem.*, **72**, 3849 (1968).
- (13) J. E. B. Randles, *Trans. Faraday Soc.*, **52**, 1573 (1956).
- (14) Lacking direct physical proof by *e.g.*, absorption or conductivity measurements a process involving solvated electrons cannot in principle be distinguished from a direct charge transfer from the excited dioxane molecule to N₂O or H⁺ respectively. However, the rate constants of such charge transfers would have to be in the same ratio as the rate constants for the reactions of solvated electrons with N₂O and H⁺.
- (15) F. Hirayama, C. W. Lawson, and S. Lipsky, *J. Phys. Chem.*, **74**, 2411 (1970).
- (16) A. M. Halpern and W. R. Ware, *J. Phys. Chem.*, **74**, 2413 (1970).
- (17) J. H. Baxendale, D. Beaumont, and M. A. J. Rodgers, *Chem. Phys. Lett.*, **4**, 3 (1969).

Institut für Strahlenchemie
Max-Planck-Institut für Kohlenforschung
D-4330 Mülheim a. d. Ruhr
West Germany

Clemens von Sonntag*
Heinz Bandmann

Received May 28, 1974

CHEMICAL AND BIOCHEMICAL APPLICATIONS OF LASERS

Volume 1

edited by C. BRADLEY MOORE

A Volume in the PHYSICAL CHEMISTRY Series

The book contains detailed, thoroughly documented descriptions of laser techniques. First, there is an introduction to the fundamental physics of lasers and to the properties of practical laser systems. Then the book examines the application of lasers to individual areas in spectroscopy, in the dynamics of small molecules, and in the kinetics of biochemical systems. This volume and the ones to follow are unique in that they discuss specific applications in chemistry and biochemistry, rather than being devoted to laser physics or to a particular chemical specialty.

1974, about 380 pp., in preparation

LOW ENERGY ELECTRON DIFFRACTION

The Theory and its Application to Determination of Surface Structure

by J. B. PENDRY

CONTENTS: Introduction. Scattering Processes for Low Energy Electrons. Principles of Diffraction at T=0°K. Schemes of Calculation. Perturbative Methods and Related Techniques. Temperature Effects. Applications of LEED to Surface Structure Analysis.

1974, 410 pp., \$22.25/£8.60

STATISTICAL THERMODYNAMICS

Volume 2

by ARNOLD MUNSTER

CONTENTS: THEORY OF CRYSTALS: Ideal Crystals. The Vapor Pressure Equilibrium; The Nernst Heat Theorem. Cooperative Phenomena in Crystals I: Elementary Theories of Superlattice Transformations. Cooperative Phenomena in Crystals II: Matrix Theory of the Ising Model. Critical Phenomena; Solid Solutions; Magnetic Systems; Rotational Transitions. THE THEORY OF LIQUIDS: Pure Liquids. Solutions of Non-Electrolytes. Solutions of Strong Electrolytes.

1974, in preparation

In Two Volumes

PHYSICAL CHEMISTRY OF MELTS IN METALLURGY

by F. D. RICHARDSON

Outlining our present knowledge concerning the chemistry of liquid metals, salts, matters and slags, this two volume publication forms a selective work aimed at highlighting those systems which exemplify important principles or which are of industrial importance. The work, divided into three sections, deals firstly with structure and kinetic properties, then with thermodynamic properties and equilibria and finally with interfacial phenomena and reaction kinetics. The third and final section of the book is concerned primarily with reactions proceeding across interfaces and deals with chemical kinetics, electrode kinetics and mass transfer and those interfacial phenomena which affect them. In addition, due to the growing importance of dispersed phases, which are now used to obtain high rates of processing per unit volume of reactor, particular attention is paid to reactions involving bubbles, drops and jets.

Volume 1/1974, 310 pp., \$19.50/£7.50

Volume 2/1974, 268 pp., \$19.50/£7.50

REACTIVE FREE RADICALS

by J. M. HAY

CONTENTS: Introduction. The Structure of Radicals. Bond Dissociation Energies. The Formation and Reactivity of Radicals: Non-polar Effects. The Formation and Reactivity of Radicals: Polar Effects. Author index.

1974 162 pp., \$11.50/£4.40

In Eleven Volumes

PHYSICAL CHEMISTRY:

An Advanced Treatise

Volume 6A: KINETICS OF GAS REACTIONS

edited by HENRY EYRING, DOUGLAS HENDERSON and WILHELM JOST

CONTENTS (TENTATIVE): W. JOST: Formal Kinetics. C. F. CURTISS: Survey of Kinetic Theory. H. EYRING and S. H. LIN: Potential Energy Surfaces. E. E. NIKITIN: Theory of Energy Transfer in Molecular Collisions. J. PETER TOENNIES: Molecular Beam Scattering Experiments on Elastic, Inelastic, and Reactive Collisions. J. C. POLANYI and J. L. SCHREIBER: The Dynamics of Bimolecular Reactions.

1974, 528 pp., \$43.00/£27.65; subscription price \$36.55

ACADEMIC PRESS

A Subsidiary of Harcourt Brace Jovanovich, Publishers



111 FIFTH AVENUE, NEW YORK, N. Y. 10003
24-28 OVAL ROAD, LONDON NW1 7DX

Recent advances and new applications for physical chemists

Advances in Radiation Chemistry, Volume 4

Edited by Milton Burton and John L. Magee, both of the University of Notre Dame

Here is the latest volume in a series that provides radiation chemists with recent theoretical and experimental advances in radiation chemistry. This particular volume reflects the current thrust toward a more refined understanding of the behavior of the displaced electron. As is customary in these volumes, the articles are by investigators who have made truly major contributions to the subject discussed.

Contents and Contributors

Ionization in Nonpolar Molecular Liquids by High-Energy Electrons—*A. Hummel*. Excess-Electron Processes in Radiation Chemistry of Disordered Materials—*K. Funabashi*. Trapped Electrons in Organic Glasses—*L. Kevan*. Radiation Chemistry of Polyethylene—*M. Dole*. Author Index. Subject Index.

1974 400 pages \$31.50

Experimental Electrochemistry for Chemists

By Donald T. Sawyer, *University of California, Riverside*, and Julian L. Roberts, Jr., *University of Redlands*

This book outlines the basic principles and modern methodology of electrochemistry. It is specifically intended for the research chemist who is unfamiliar with modern electrochemical methods and techniques and shows him how to select and use appropriate methods to characterize molecules and chemical systems. The approach is practical. The material is limited to those relationships that allow for successful and effective analysis and measurement of experimental data. Special topics include—

- the design and construction of electrodes and cells
- purification of solvents and electrolytes
- and a practical introduction to electrochemical instrumentation and electronics

1974 435 pages \$18.50

Finite Groups and Quantum Theory

By D. B. Chesnut, *Duke University*

This intermediate text gives graduate students and physical chemists competence in the use of point group theory to problems in quantum mechanics. To fill the gap between abstract theory and physical applications, mathematical definitions and terminology are carefully introduced and can be easily grasped by students and practitioners with the usual mathematical preparation given to chemistry and physics majors. The development flows logically from abstract theory to representations and finally to applications. In each chapter problems and exercises are provided to facilitate the learning process. Special topics include—

- mapping and permutation groups
- the construction of group representations and irreducible representations
- and projection operators and their application to the permutation symmetry of wave functions.

1974 240 pages \$14.95

Wiley-Interscience

a division of JOHN WILEY & SONS, Inc.
605 Third Avenue, New York, N.Y. 10016
In Canada: 22 Worcester Road, Rexdale, Ontario

Statistical Physics of Materials

By Louis A. Girifalco, *University of Pennsylvania*

Written by a well-known authority in the field, this book expands the role of statistical mechanics into a complete methodology that integrates equilibrium and transport properties in both perfect and defect crystals. In a clear and well organized manner that makes it suitable for self-study as well as classroom use, it introduces the principles of statistical mechanics and covers a broad range of crystal phenomena. To further aid understanding, it includes eight special appendices that highlight useful computational techniques—combinatorial problems in statistical mechanics, the method of undetermined multipliers, Stirling's approximation, sums and integrals and Fermi integrals—and pertinent theoretical considerations—Ferromagnetism and Order-Disorder Theory, The Einstein Function, Debye Energy and Heat Capacity Functions.

1973 346 pages \$24.25

William David Coolidge

A Centenarian and His Work

By Herman A. Liebhafsky, *Texas A&M University*

This book pays tribute to Dr. Coolidge and his long, distinguished career as an industrial researcher. It not only describes his well known work on ductile tungsten, but the numerous projects he was engaged in over the years that contributed to the success of the General Electric Research Laboratory.

1974 112 pages \$6.95

Mail this coupon to:

Wiley-Interscience, Dept. 322, Box 4569
Grand Central Station, New York, N.Y. 10017

Please send me the book(s) I have checked below.

- My check (money order) for \$ _____ is enclosed.
- Please bill me (Restricted to the continental United States.)
- Please send me a list of local bookstores carrying your titles.
- RADIATION CHEMISTRY, Vol. 4 (0 471 12543-1) @ \$31.50
- ELECTROCHEMISTRY (0 471 75560-5) @ \$18.50
- FINITE GROUPS (0 471 15445-8) @ \$14.95
- STATISTICAL PHYSICS (0 471 30230-9) @ \$24.25
- COOLIDGE (0 471 53430-7) @ \$6.95

Name _____ Title _____

Firm (College) _____

Address _____

City _____ State _____ Zip _____

Please add state and local taxes where applicable.

Prices subject to change without notice.

092 A4745-WI

